Journal of Heat Transfer

Published Monthly by ASME

VOLUME 127 • NUMBER 4 • APRIL 2005

Transactions of the ASME, Journal of Heat Transfer (ISSN 0022-1481) is published monthly by The American Society of Mechanical Engineers, Three Park Avenue, New York, NY 10016. Periodicals postage paid at New York, NY and additional mailing offices. POSTMASTER: Send address changes to Transactions of the ASME, Journal of Heat Transfer, c/o THE AMERICAN SOCIETY OF MECHANICAL ENGINEERS, 22 Law Drive, Box 2300, Fairfield, NJ 07007-2300. **CHANGES OF ADDRESS** must be received at Society headquarters seven weeks before they are to be effective. Please send old label and new address.

RESEARCH PAPERS

TECHNICAL NOTE

TECHNOLOGY REVIEW

(**Contents continued on inside back cover**)

This journal is printed on acid-free paper, which exceeds the ANSI Z39.48-1992 specification for permanence of paper and library materials. ♾™
♻ 85% recycled content, including 10% post-consumer fibers.

(**Contents continued**)

ANNOUNCEMENT

The ASME Journal of Engineering for Gas Turbines and Power is abstracted and indexed in the following:

AESIS (Australia's Geoscience, Minerals, & Petroleum Database), Applied Science & Technology Index, Aquatic Sciences and Fisheries Abstracts, Civil Engineering Abstracts, Compendex (The electronic equivalent of Engineering Index), Computer & Information Systems Abstracts, Corrosion Abstracts, Current Contents, Engineered Materials Abstracts, Engineering Index, Enviroline (The electronic equivalent of Environment Abstracts), Environment Abstracts, Environmental Science and Pollution Management, Fluidex, INSPEC, Mechanical & Transportation Engineering Abstracts, Mechanical Engineering Abstracts, METADEX (The electronic equivalent of Metals Abstracts and Alloys Index), Pollution Abstracts, Referativnyi Zhurnal, Science Citation Index, SciSearch (The electronic equivalent of Science Citation Index), Shock and Vibration Digest

Journal of Heat Transfer

Preface

Special Issue on Gas Turbine Heat Transfer: Part 1

It is with great pleasure that we present the next two issues of the ASME J. of Heat Transfer to the heat transfer community dedicated to *Gas Turbine Heat Transfer*. Gas turbines are used in military and commercial aircraft, and for land-based power generation, and contribute significantly to the nation's economy. In modern gas turbine engines, the turbine inlet temperatures exceed the operating limits of the turbine blades, and one of the major technical challenges is the ability to effectively cool the turbine components with minimum coolant usage. Improvements in turbine efficiencies can be achieved with higher turbine inlet temperatures, and therefore, there is a significant ongoing effort in the gas turbine community (industry, academia, and federal laboratories) to explore new materials and material coatings that can withstand higher temperatures, and to explore more effective cooling strategies.

The special issues are an effort to communicate to the larger heat transfer community the opportunities and challenges in gas turbine heat transfer. The issues consist of 2 Technology Reviews (one on film cooling and the other on impingement cooling), 14 full-length Research Papers, and 2 Technical Briefs. The topics covered run the gamut of cooling strategies, both internal and external, and the authors represent researchers from both academia and industry. It is our hope that these issues will serve as a resource for researchers in the gas turbine field and that it will motivate new researchers looking for challenging problems. Part 2 will appear as the May 2005 issue.

This preface ends with a note of thanks to all of the contributing authors in this special issue on *Gas Turbine Heat Transfer*. It is no coincidence that so many papers in one topic area become available for publication simultaneously. This requires considerable effort and discipline on the part of the authors and reviewers, as well as the ASME Journal of Heat Transfer publishing staff. Accordingly, we acknowledge the enthusiastic support and help we received from many reviewers who worked hard to meet the stringent deadlines of the review process for these issues. We also acknowledge the continuous encouragement and support we received from Professor Vijay Dhir in bringing out these special issues, and the wonderful help provided by Jenell Rae, Editorial Assistant for the ASME Journal of Heat Transfer, who patiently guided us and the authors from start to finish. All must be commended and we hope that you, the reader, will benefit from, and appreciate, these efforts.

Sumanta Acharya
Louisiana State University

Phil Ligrani
University of Utah

Andrew C. Chambers
e-mail: ac@chambersandrew.com

David R. H. Gillespie

Peter T. Ireland

Department of Engineering Science,
University of Oxford,
Parks Road, Oxford, OX1 3PJ, United Kingdom

Geoffrey M. Dailey
e-mail: geoffrey.dailey@rolls-royce.com
Rolls-Royce CAEL,
Derby, UK

The Effect of Initial Cross Flow on the Cooling Performance of a Narrow Impingement Channel

Impingement channels are often used in turbine blade cooling configurations. This paper examines the heat transfer performance of a typical integrally cast impingement channel. Detailed heat transfer coefficient distributions on all heat transfer surfaces were obtained in a series of low temperature experiments carried out in a large-scale model of a turbine cooling system using liquid crystal techniques. All experiments were performed on a model of a 19-hole, low aspect ratio impingement channel. The effect of flow introduced at the inlet to the channel on the impingement heat transfer within the channel was investigated. A novel test technique has been applied to determine the effect of the initial cross flow on jet penetration. The experiments were performed at an engine representative Reynolds number of 20,000 and examined the effect of additional initial cross flow up to 10 percent of the total mass flow. It was shown that initial cross flow strongly influenced the heat transfer performance with just 10 percent initial cross flow able to reduce the mean target plate jet effectiveness by 57 percent. [DOI: 10.1115/1.1800493]

Introduction

Many modern high pressure turbine blades are cooled by passing air bled from the compressor through the blade, before feeding it to the surface to form cooling films. The heat removed by convection is dependent on both the temperature of the flow and the heat transfer coefficient. Cooling by impingement is of particular interest as it provides heat transfer coefficient enhancement over an ordinary plane passage, while the continual injection of coolant keeps the driving gas temperature difference high to ensure locally high heat fluxes. Improvements in casting technology have increased the useful heat transfer area and flow path length of impingement cooling systems while maintaining a robust design. Figure 1 indicates a typical cross section of a turbine blade cooled using impingement channels integrally cast into the blade wall.

Frequently, the experimental heat transfer data required for the design of such internal cooling systems are obtained from tests performed on large-scale Perspex models under flow conditions which achieve engine representative Reynolds numbers. This report concerns experiments performed on a low aspect ratio ($z/d = 1.54$) impingement channel. Earlier impingement channel cross sections have tended to be of high aspect ratio and had several rows of impingement holes spread across their width [1–3].

Recent developments in soluble core casting technology at Rolls Royce have allowed very intricate internal passages to be manufactured. This has opened up the possibility of casting small diameter (<1 mm) low aspect ratio impingement passages into turbine blades. Such passages would be of a race track geometry and typically include about 19 impingement holes. This is much longer than impingement passages previously tested and results in changed flow conditions.

In some cases it may be possible to introduce additional cross flow at a different temperature to the main impingement flow. This further increases the range of possible flow characteristics. To correctly model the heat transfer process, the adiabatic wall temperature, related to the source of the coolant flow, is required. This paper details experimental measurement of both the heat transfer coefficient and the adiabatic wall temperature.

Contributed by the Heat Transfer Division for publication in the JOURNAL OF HEAT TRANSFER. Manuscript received by the Heat Transfer Division January 12, 2004; revision received June 7, 2004. Associate Editor: P. M. Ligrani.

Test Facility

Figure 2 shows details of the impingement cooling channel geometry used in the current series of tests. The channel is constructed from Perspex and coated with a single narrow band thermochromic liquid crystal which displays peak intensity at 313.3 K. Cross flow is introduced at one end of the channel and air impinges from a separate source through a staggered row of 19 evenly spaced holes along the length of the channel. All the impingement jets are supplied from a common plenum and thus the same total pressure. The stream wise hole spacing is $x_n/d = 4.36$ and the hole offset is $y/d = 1.8$ (Fig. 2). The air exhausts at the far end of the channel to a vacuum pump. The total mass flow through the channel is controlled using a valve between the channel exit and the vacuum pump. A photograph of the impingement channel undergoing a heat transfer test is shown in Fig. 3 (no cross flow case). The proportion of cross flow is controlled by a variable speed blower. Independent heating of each gas stream is achieved by passing the air through two planar mesh heaters, Gillespie et al., [4], powered from two transformers. A timer that delays the power to the cross flow heater is used to ensure simultaneous arrival of both heated streams at the working section. The transit delays within the channel itself are in the order of 0.1 seconds ensuring they have negligible effect on the experimental results. Each of the impingement holes has a length to diameter ratio of 1.25 and an inlet and exit chamfer of 0.167 diameters. The hole average Reynolds number (Re) is calculated from the total mass flow rate and the impingement hole diameter.

$$\mathrm{Re} = \frac{4\dot{m}}{\pi n d \mu} \tag{1}$$

Engine representative Reynolds numbers in the range 10,000–35,000 can be reproduced with up to 10 percent of the total mass flow introduced as initial cross flow. The effects of initial cross flow are examined in this paper and the results are presented for an average hole Reynolds number of 20,000.

Instrumentation

The power supplied to the heater mesh is calculated from the mesh voltage and current measurements. Gas temperatures are based on these power measurements and verified using a set of gas thermocouples placed in the plenum upstream of the channel. Seven thermocouples equally distributed along the length of the

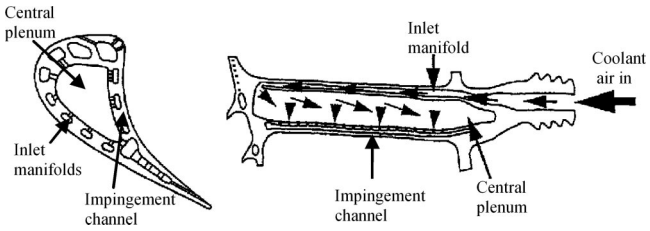

Fig. 1 Schematic diagram of the cross section of a turbine blade cooled by impingement channels (Dailey, [1])

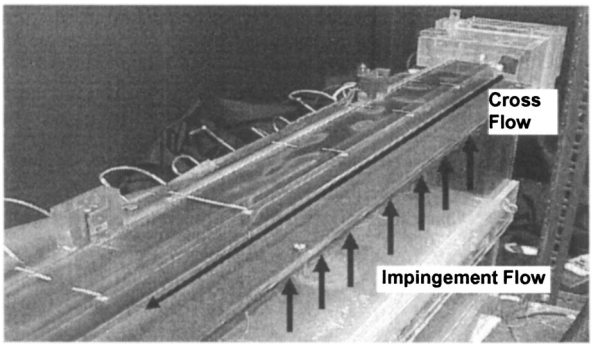

Fig. 3 Snapshot of a heat transfer test with no initial cross flow. Note the upstream areas where simple impingement occurs before cross flow dominates the heat transfer.

impingement plenum allow confirmation of the gas temperature uniformity. Additional flow resistance was required to achieve a spanwise temperature uniformity of ±0.5°C. The thermocouples were logged using a PC. *Labview* software controls the data acquisition card and 16 temperature channels at a sample rate of 10 Hz are recorded in each test. The total exit mass flow rate and the cross flow mass flow rate are measured using BS ISO TR 15377 orifice meters. The experimental procedure was cross checked by showing that in the steady state the gas temperature predicted by an energy balance matched the measured gas temperature. The color change in the liquid crystal is monitored using 2 PAL video cameras coupled to VHS recorders. Surface thermocouples were embedded in both measurement plates to facilitate calibration of the crystal coating. Uniform lighting was provided along the length of the channel by a pair of fluorescent lights (color =''white'') positioned on either side of the channel to prevent reflection.

Measurement Requirements

The flow introduced at the beginning of the passage and the flow from impingement introduced along the passage are not necessary at the same temperature in the engine. To scale results between the model and the engine conditions, the Nusselt number and impingement effectiveness (defined in Eq. (2)) distributions are required. The Nusselt number is calculated from the heat transfer coefficient based on the local adiabatic wall temperature, while the impingement effectiveness is the dimensionless adiabatic wall temperature. The effectiveness lies between 0 and 1, where 0 indicates that the local adiabatic wall temperature equals the cross flow temperature, and 1 that it is equal to the impingement flow temperature.

$$\varepsilon = \frac{T_{aw} - T_c}{T_i - T_c} \tag{2}$$

Both the heat transfer coefficient and the local effectiveness values are deduced from the interpretation of a series of transient liquid crystal tests using the ''3 Test Strategy'' developed by Chambers et al. [5].

Review of Measurement Technology

Due to the complex impingement channel geometry and the need for full surface data, liquid crystal measurement techniques are best suited to this application. Thermochromic liquid crystals have provided experimenters with the ability to measure entire surface temperature events essentially noninvasively. The first application of this to impingement cooling was by den Ouden and Hoogendoorn, [6], who used a steady-state technique to measure impingement heat transfer from a fully developed turbulent jet. Subsequent developments in steady-state techniques allowed the investigation of three temperature problems such as the influence of the impingement plate (contains the impingement holes) temperature on heat transfer to the target plate (parallel to the impingement plate), Lucas et al., [7].

Transient liquid crystal techniques for the measurement of heat transfer have been used since the 1980s. As the basic technique, first applied to internal cooling by Ireland and Jones, [8], it is well known, so only a brief description is given here. In the heat transfer experiments, scale models of engine components are manufac-

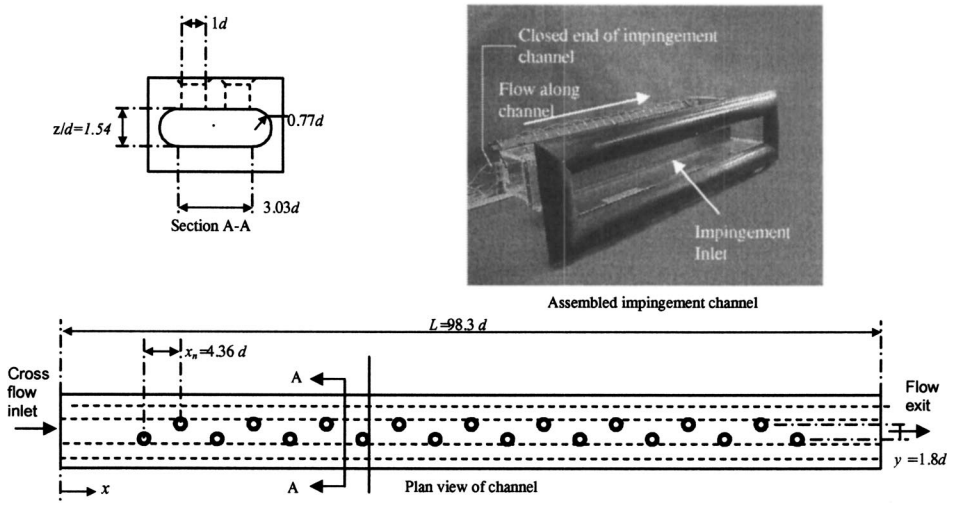

Fig. 2 Impingement channel geometry

tured from a poor thermal conductor such as Perspex; a transparent plastic that allows excellent optical access. The liquid crystal coating (typically of thickness ~10 microns) is applied to the substrate using a small air brush, although the optical response is insensitive to coating thickness. When a flow temperature transient is initiated the model temperature starts to change. The liquid crystal color play is recorded yielding the temperature history of the model surface, and hence the local heat transfer coefficient distribution. It is the ease with which the surface coating can be prepared, even if the model surface has compound curvature, which makes the method particularly suitable to the measurement of heat transfer coefficients on complex surfaces (Chyu et al., [9] and Gillespie et al., [10]). Wide band liquid crystals provide more surface temperature data than narrow band crystals, but are subject to a shift in the temperature/color calibration, as the angle of viewing and the angle of illumination are altered (Farina and Moffat, [11]). This means that in situations where the model cannot be calibrated by isothermal heating (Guo et al., [12]), it is desirable to use several narrow banded liquid crystals (color play $<1°C$) to obtain multiple temperature events based on relative intensity of illumination rather than a color index signal as is used with a wide band crystal. Compared to infrared thermography or the use of multiple surface thermocouples, liquid crystals provide a cheap and accurate way of attaining full surface temperature measurements. In the two temperature situation there has recently been much effort to increase the speed of data reduction. Of particular note is the work of Baughn et al., [13], and Turnbull and Oosthuizen, [14], whose novel techniques involved subjecting the model to a periodically varying heat flux, and inferring the heat transfer coefficient from the attenuation of the signal and the phase delay in the corresponding local surface temperature response, respectively.

Work by Lucas et al. [7] and Van Treuren et al. [15] has previously shown good agreement between work from steady state experiments and transient experiments. Similarly Son et al. [16] showed that transiently heated impingement flow and a pre-heated working section produced identical heat transfer coefficient measurements and equivalent adiabatic wall temperatures. Tsang et al. [17] outlined a detailed procedure for assessing the effects of upstream wall temperature and the associated uncertainty in heat transfer coefficient measurements.

The work of Florschuetz and Su [18] and Goldstein et al. [19] who investigated the effect of entrainment on a single jet in a series of steady state heated plate tests showed that the heat transfer coefficient obtained was independent of the relative magnitude of the jet temperature and ambient temperature, when the adiabatic wall temperature is used as a reference. Thus, it is concluded that the heat transfer coefficient may be correctly deduced from low temperature tests without having to match temperature ratios.

The transient liquid crystal technique has also been employed in three temperature problems to simultaneously obtain two unknown parameters over all the model surfaces in a single test. Here, two surface temperature events are required for solution. This may be straightforwardly implemented by applying a mixture of two or more narrow banded liquid crystals to the model surface; however, this problem remains only well conditioned if at least one of the parameters varies over a fairly small range, and the liquid crystal color play temperature ranges are carefully chosen (Ireland and Jones [20]). The technique can be extended using additional liquid crystals, the reduced amount of each crystal can adversely affect the quality of each of the color plays. Post processing of narrow band crystals may yield one temperature event for each liquid crystal used. Alternatively, at each point, the full intensity-time signature (Ling and Ireland, [21]) may be compared to those predicted for all possible values of heat transfer coefficient and driving gas temperature to obtain a ''best fit'' value. This approach provides many degrees of redundancy, and unlike wide band crystal techniques (Camci et al. [22], van Treuren et al. [23]) is not subject to problems of lighting and viewing angle.

Table 1 Test permutations

Test Name		Upstream Cross Flow	Impingement Jets
Heat transfer coefficient test		Hot	Hot
Effectiveness Tests	A	Hot	Cold
	B	Cold	Hot

Vedula and Metzger [24], proposed a two test strategy for film-cooling configurations to allow the determination of both film-cooling effectiveness and heat transfer coefficient. These techniques were further expanded by Chambers et al. [5], who proposed the three test strategy for internal cooling geometries, which enabled both the heat transfer coefficient and the full range of effectiveness to be assessed in a manner that is relatively insensitive to experimental uncertainty.

Extensive studies of large impingement arrays were performed by Gillespie et al. [23] and Son et al. [25]. Son et al. [25], looked at the heat transfer on both the target plate and the impingement plate. The experiments were performed with an aspect ratio (z/d) of between 1.875 and 3. The maximum hole to cross flow velocity ratio achieved was 0.36. Van Treuren [15], performed a series of experiments for both inline and staggered impingent arrays measuring the target surface heat transfer for aspect ratios (z/d) of 1, 2, and 4 in the presence of initial cross flow. Florschuetz et al. [26], performed a series of tests on a wide range of impingement geometries and produced correlations that are widely used for impingement arrays. The current study differs from preceding research as the channel studied has an oval cross section and a high open area ratio (total impingement hole area/channel cross sectional area). This results in the mass flux ratio, G_c/G_j, approaching its asymptotic limit of 0.707 in the downstream of the channel and impingement flow under these conditions has not been previously reported.

Technique

The experiments are performed using the three Test Strategies developed by Chambers et al. [5]. This strategy was developed by the author to enable processing of the three temperature problem with minimal sensitivity to experimental errors. Other techniques were initially applied to the problem such as the complete curve fit strategy developed by Ling et al. [21] and multiple narrow band crystal techniques developed by Ireland and Jones [20]. It was found that these techniques were too sensitive to small errors in gas temperatures and experimental start times to be of use with this impingement channel problem. The three test technique uses a single narrow band liquid crystal and compares crystal transition times between the three separate experiments detailed in Table 1.

Provided that the gas temperatures are correctly chosen for the expected heat transfer coefficient and the known liquid crystal transition temperature, the liquid crystal on the entire test surface exhibits color play during the HTC test. Furthermore, any position on the surface of interest can undergo a crystal transition during either effectiveness test. The heat transfer coefficient and effectiveness may then be determined by comparing the transition times between the heat transfer coefficient test and either of the effectiveness tests. Using a combination of results from two separate tests allows a well-conditioned solution to the two unknowns in this problem. In the simplest case, where both gas streams are at the same temperature the heat transfer coefficient will be determined solely from the heat transfer coefficient test, the gas temperature being known. The effectiveness may then be determined from the second test, which is now well conditioned, as the heat transfer coefficient is known at all points on the surface. Figure 4 shows that if either the heat transfer coefficient or the driving gas temperature is fixed then the other parameter becomes a strong function of the crystal transition time leading to a well conditioned solution for the other unknown parameter.

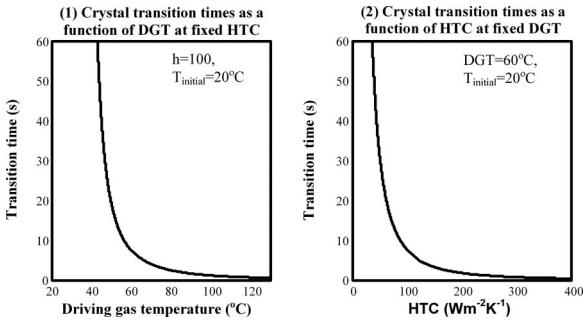

Fig. 4 Variation of liquid crystal transition times for the case of (1) fixed heat transfer coefficient with varying driving gas temperature and (2) fixed driving gas temperature with varying heat transfer coefficient

The three tests required are performed using step changes in the driving gas temperature. This is achieved through using the heater mesh developed by Gillespie [23]. Thermocouples measured the time-temperature profiles at the inlet to the apparatus and a heater mesh time constant of less than 0.25 seconds was measured. This was sufficiently fast to allow approximation of an ideal step and enable application of a uniform temperature model. Gas temperature rises were subsequently calculated from the mass flow rate and the heater mesh power. The calculations were confirmed by thermocouple measurements. The response of the Perspex model is described by the solution to the one-dimensional Fourier equation.

$$\theta = 1 - e^{\beta^2}\,\mathrm{erfc}(\beta) \tag{3}$$

where

$$\theta = \frac{T - T_0}{T_{\mathrm{gas}} - T_0} \quad \text{and} \quad \beta = h\sqrt{\frac{t}{\rho c k}}. \tag{4}$$

Solution, subject to the appropriate boundary conditions as described by Chambers et al. [5], yields the analytical solution for the heat transfer test.

$$\frac{T_{\mathrm{crystal}} - T_{0h}}{(T_{ih} - T_{0h})\varepsilon + (T_{ch} - T_{0h})(1-\varepsilon)} = 1 - e^{h^2 t_h/\rho c k}\,\mathrm{erfc}\left(h\sqrt{\frac{t_h}{\rho c k}}\right) \tag{5}$$

Similarly for the A test

$$\frac{T_{crystal} - T_{0A}}{(T_i - T_{0A})\varepsilon} = 1 - e^{h^2 t_A/\rho c k}\,\mathrm{erfc}\left(h\sqrt{\frac{t_A}{\rho c k}}\right), \tag{6}$$

and for the B test

$$\frac{T_{\mathrm{crystal}} - T_{0B}}{(T_c - T_{0B})(\varepsilon - 1)} = 1 - e^{h^2 t_B/\rho c k}\,\mathrm{erfc}\left(h\sqrt{\frac{t_B}{\rho c k}}\right). \tag{7}$$

Solution of these equations yields the heat transfer coefficient and the driving gas effectiveness.

Uncertainty Analysis

An estimate of the uncertainties associated with these experiments has been made using the method of small perturbations described by Moffat [27]. Calculations were performed to gauge the effect of uncertainties in experimental parameters at test conditions typical of those found in the impingement channel. The effect of each type of measuring error is considered, in isolation. The typical experimental error has been estimated by considering the RSS of the component errors. The error analysis was performed by applying small perturbations about a typical heat transfer coefficient of 85 $\mathrm{Wm^{-2}K^{-1}}$ and an effectiveness of 0.5. The results of the error analysis are presented in Table 2.

Table 2 Contributors to uncertainties in heat transfer coefficient and effectiveness

Test Condition	Typical Value	Typical Error	Error in HTC	Error in Effectiveness
Start Temperature T_0, °C	20	0.5	5.88%	15.4%
Crystal Temperature $T_{crystal}$, °C	33	0.3	4.03%	2.09%
Gas Temperature T_{gas}, °C	50	0.5	1.47%	4.5%
Transition Time t (s)	10	0.04	0.59%	2.5%
Perspex Properties ($\sqrt{\rho c k}$)	569	29	5.00%	0%
RSS Error			8.85%	16.37%
Maximum Error			16.97%	24.49%

Experimental Results and Interpretation

The experiments were performed at a fixed hole average engine representative Reynolds number of 20,000 and between 0 and 10 percent of the total mass flow was introduced upstream of the first hole as initial cross flow. Full surface heat transfer measurements were performed using the liquid crystal techniques described above. A liquid crystal coated target plate was used to obtain data on the target surface. This was replaceable by a clear plate to allow viewing through the channel onto the impingement plate enabling measurements on this surface.

The flow field within the channel was modelled using a momentum based approach similar to that adopted by Florschuetz et al. [3]. It was shown that the impingement hole discharge coefficient had little influence on the overall channel pressure drop as the dominant loss mechanism was the mixing of the impingement flow and the cross flow. A constant discharge coefficient of 0.85 was chosen based on the work of Florschuetz et al. [3] and the mass flux ratio was calculated for various initial cross flow conditions. The flow field predictions were cross checked with respect to the channel static pressure and shown to be accurate within 6 percent.

Figure 5 shows the target plate heat transfer results for an average hole Reynolds number of 20,000 and no initial cross flow. It should be noted that, without initial cross flow, the effectiveness is not defined. The first three upstream holes are subject to low cross flow and show almost symmetric impingement patterns. There is no measurable heat transfer coefficient due to the stagnant, or very low velocity, secondary flows upstream of the first impingement region. Beyond the third hole, the peak heat transfer levels initially reduce, even though both the jet and the channel flow velocities are increasing. This is due to increasing cross flow counteracting the impingement mechanism by preventing the jet reaching the surface. A similar pattern, but at increasing heat transfer levels, is repeated throughout the channel as both the jet and the channel velocities rise and the mass flux ratio approaches its asymptotic limit of 0.707. Figure 6 details the mass flux ratios within the channel. In the downstream of the channel when there is nearly an asymptotic mass flux ratio the local maximum heat transfer coefficient as influenced directly by an individual jet occurs approximately four jet hole diameters downstream of the impingement hole centerline. This indicates deflection of the jet before impinging on the target plate and this deflection causes a considerable reduction in the peak heat transfer coefficient. Without cross flow this would be predicted to be 317 $\mathrm{Wm^{-2}K^{-1}}$ (Van Treuren, [15]) for the furthest downstream impingement hole. The cross flow causes the maximum measured heat transfer coefficient for this hole to be just 141 $\mathrm{Wm^{-2}K^{-1}}$.

Figure 7 shows the target plate heat transfer and the effectiveness results for an average hole Reynolds number of 20,000 and 5 percent of the total flow introduced as initial cross flow. Upstream, a very different pattern from that of the zero cross flow case is observed with the channel acting as a plain duct and no impingement enhancement occurring. Only by the 5th hole downstream is the effect of flow injection through the jet evident in the effective-

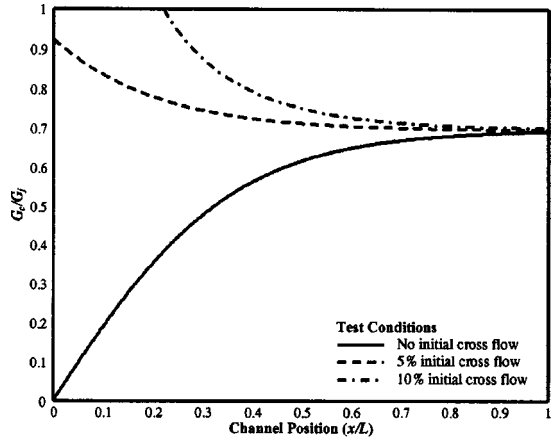

Fig. 5 Mass flux ratios as a function of hole position within the channel

ness plots, indicating that the jet flow is responsible for a local increase in heat transfer coefficient. This is explained through interpretation of the mass flux ratio graph for 5 percent initial cross flow (Fig. 5). In this case, with the initial ratio of $G_c/G_j=0.92$, the impingement flow is unable to penetrate the cross flow. Only further downstream, as the G_c/G_j ratio decreases towards its asymptotic limit of 0.707, is the impingement enhancement observed. The first enhancement occurs at a G_c/G_j ratio of 0.81 and a local jet Reynolds number of 6000 (the average jet Reynolds number is 20,000). As well as Reynolds number, the mass flux ratio and the channel aspect ratio are likely to be the primary factors that determine the performance of a racetrack impingement channel.

The effectiveness results provide further insight into the flow mechanisms present. At the point where enhancement in heat transfer by impingement first occurs, there is also a step in effectiveness. This shows that the impingement flow is striking the surface, leading to the enhanced heat transfer coefficient. It is also of interest to note that the effectiveness under the jets is not unity, as would be expected if pure impingement occurred. Instead, at each impinging hole there is a step rise in effectiveness of between 0.1 and 0.2. This implies that the jet mixes with the surrounding cross flow before impacting the wall and the impingement heat transfer enhancement is a consequence of the disruption of the boundary layer caused by turbulence from the jet wake region striking the surface rather than through impingement of the

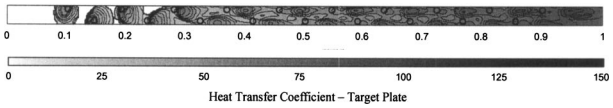

Fig. 6 Heat transfer coefficient for target plate, Re=20,000 and no initial cross flow

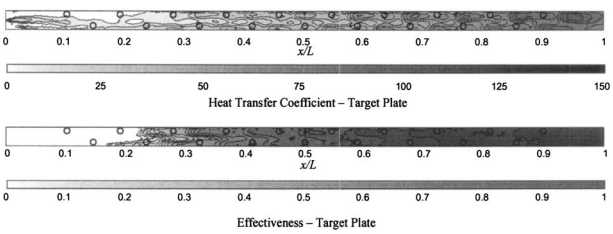

Fig. 7 Heat transfer coefficient and effectiveness for target plate, Re=20,000 and 5 percent initial cross flow

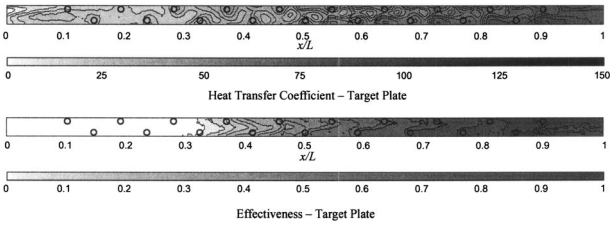

Fig. 8 Heat transfer coefficient and effectiveness for target plate, Re=20,000 and 10 percent initial cross flow

potential core. The mean plate effectiveness is 0.61. This could initially be considered surprisingly low considering that only 5 percent of the total mass flow is introduced as initial cross flow. It is explained by the way in which the mass flow through the channel increases dramatically downstream. This means that 5 percent initial cross flow corresponds to a significant portion of the total mass flow in the upstream regions of the channel. This figure could be compared to a theoretical area-averaged, mixed-out effectiveness value of 0.66, which was calculated using the equation.

$$\varepsilon_{\text{mean}}=\frac{1}{A}\int_A \frac{\dot{m}-m_0}{\dot{m}}\,dA \tag{8}$$

Figure 8 shows the heat transfer and effectiveness results for an average hole Reynolds number of 20,000 and 10 percent of the total flow introduced as initial cross flow. The upstream heat transfer in this case is much higher than would be expected. It is thought that this is a Reynolds number dependent entrance effect as the streak of high transfer coefficient decays away from the channel entrance. The contribution of the jet to the driving gas temperature is first evident in the effectiveness plot at the ninth hole downstream. Similar effectiveness patterns are seen to the 5% initial cross flow case, but the patterns are displaced further downstream by the increased initial cross flow. The jet flow first strikes the target surface at a mass flux ratio of 0.76 and a local jet Reynolds number of 10,400. This may be compared to the mass flux ratio of 0.81 at which the impingement jet first strikes the surface with 5 percent initial cross flow. This indicates that the impingement properties are primarily a function of the mass flux ratio for a fixed channel aspect ratio. The mean channel effectiveness is 0.53 with 5 percent initial cross flow and 0.43 with 10 percent initial cross flow. This shows that the initial cross flow drives a disproportional degree of the overall heat transfer.

An overall comparison of the span-wise average heat transfer and effectiveness is found in Figs. 9 and 10 respectively. For the target surface, it can be concluded that small quantities of initial cross flow have a large influence on both the heat transfer and effectiveness over a large area. It was not possible to perform tests with higher that 10 percent initial cross flow, as ingestion occurs in the upstream holes. This would have serious consequences on the heat transfer levels for a real engine and proves a design limit with which care must be taken. Also, it should be noted that it is not possible to predict the occurrence of such ingestion in frictionless channel models and channel friction needs to be taken into account when high initial cross flow rates are concerned. Overall it could be concluded that the channel is not of optimum design as the majority of the cooling is provided by the flow injected in the upstream portion of the channel. The last few holes in the downstream portion of the channel are responsible for a substantial portion of the flow consumption, but these holes do not contribute much to the channel cooling.

The impingement plate heat transfer and effectiveness tests were performed at a hole average Reynolds number of 20,000 and with initial cross flow proportions of 0, 5, and 10 percent. The results for the test with no initial cross flow are found in Fig. 11. There was no measurable heat transfer until the 4th hole at $x/L=0.24$. There was no sign of any re-impingement in the region

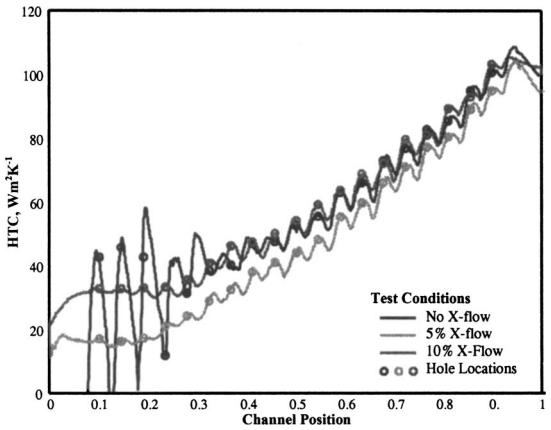

Fig. 9 Span wise average HTC for the target plate at an average jet Reynolds number of 20,000

equivalent to the impingement plate as observed in large impingement arrays by Son et al. [16]. Measurable heat transfer first occurs downstream of the 4th hole and is observed as a wake region of increased heat transfer coefficient downstream of the jet. The mass flux ratio is 0.42 and the cross flow velocity is 5.2 m s^{-1} at this location. By the time the 5th hole is reached, at a position of $x/L=0.29$ downstream the cross flow velocity has increased significantly to produce measurable heat transfer across the entire region of the channel. Downstream of each hole there is a wake region of locally increased heat transfer. This is thought to be due to the high turbulence causing a local region of increased heat transfer. Similar patterns are observed in pedestal banks where the presence of the pedestal causes local downstream increases in the heat transfer coefficient (Ireland and Jones [28]). Such patterns are repeated at progressively increasing heat transfer levels as the down stream channel region approaches its asymptotic G_c/G_j ratio and the flow velocities increase nearly exponentially.

When 5 percent of the total flow is introduced as initial cross flow, the impingement plate heat transfer and effectiveness patterns found in Fig. 12 are observed. There are no longer any regions of negligible heat transfer within the channel. Upstream, there is an almost uniform heat transfer coefficient due the presence of cross flow. The upstream jet velocities are low, but there are still small regions of increased heat transfer downstream of the upstream jets. The downstream jets have a similar effect on heat transfer to that seen in the no initial cross flow case. This is to be expected, as the G_c/G_j ratios asymptote to the same value in both cases. The effectiveness results provide further insight into the flow mechanisms. All but the upstream 3 holes produce downstream wake regions of high effectiveness. It is speculated that the upstream holes do not produce wake regions as the jet velocities through these holes are too small when compared to the cross flow velocity. The rest of the holes act as pedestals, enhancing downstream heat transfer while also being stripped by the cross flow, producing regions of high effectiveness downstream of the holes even when the jet flow is not attached to the surface. There are many similarities to film cooling scenarios, which have been extensively studied. Future comparisons with these results would be beneficial to attaining further understanding of this topic.

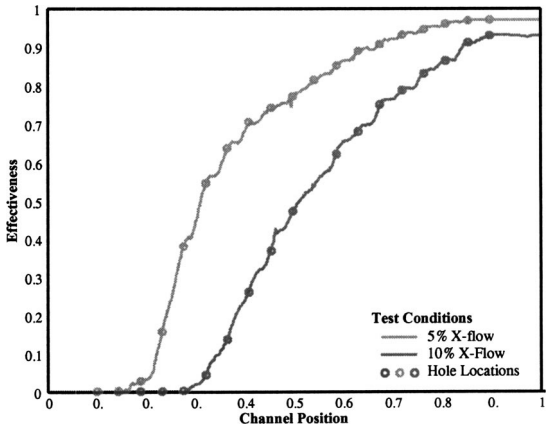

Fig. 10 Span wise average effectiveness for the target plate at an average jet Reynolds number of 20,000

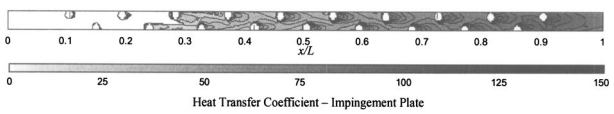

Fig. 11 Heat transfer coefficient for the impingement plate, Re =20,000 and no initial cross flow

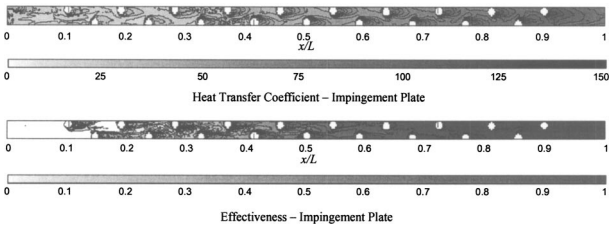

Fig. 12 Heat transfer coefficient and effectiveness for the impingement plate, Re=20,000 and 5 percent initial cross flow

The results for 10 percent of the total flow introduced as initial cross flow is found in Fig. 13. Similar heat transfer patterns are observed to those of the 5 percent cross flow case, but shifted downstream by approximately 9 jet diameters. This is explained by examination of the G_c/G_j graph. The effect of 10 percent additional cross flow causes a higher initial G_c/G_j ratio than in the 5 percent case. After 9 jet diameters, this ratio becomes approximately equal to the initial ratio in the 5 percent initial cross flow case. No entrance effects, as noted on the target plate, are seen on the impingement plate. Overall comparisons of the hole surface results for heat transfer and effectiveness are found in Figs. 14 and 15, respectively.

Figure 16 shows the method of solution used in different regions of the channel for the Reynolds number=20,000 with 10 percent initial cross flow case. Near the entrance of the channel, the cross flow dominates, the effectiveness is low and the transition times from the heat transfer test are used in conjunction with effectiveness test B (cross flow heated) to determine the heat transfer parameters. Far downstream and away from the inlet, effectiveness test A (impingement flow heated) is used. Over a limited region in the center of the channel, results are available from

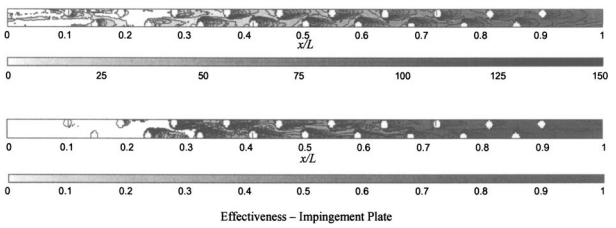

Fig. 13 Heat transfer coefficient and effectiveness for the impingement plate, Re=20,000 and 10 percent initial cross flow

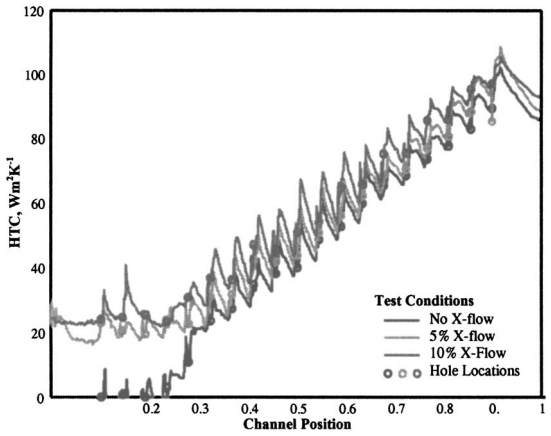

Fig. 14 Span wise average HTC for the impingement plate at an average jet Reynolds number of 20,000

both tests, A and B. The same heat transfer coefficients and effectiveness values were found in the latter region giving confidence in the experimental technique.

Summary and Conclusions

A comprehensive study of the effects of initial cross flow on heat transfer and effectiveness within a racetrack impingement channel has been made. These results have been interpreted using established flow field models. The knowledge of the effectiveness allows the application of these results to engine representative conditions where the initial cross flow and impingement coolant can be at different temperatures. The effectiveness data also provide valuable insight into the impingement properties of the jets. It is seen that at low mass flux ratios the classic impingement patterns are observed with the potential core striking the target surface. As the mass flux ratios increase, the jet potential core is no longer able to traverse the channel and instead heat transfer enhancement occurs when the mixed out jet wake strikes the target surface. At still higher mass flux ratios, no impingement enhancement is evident. Impingement plate data show regions of both high heat transfer and effectiveness values downstream of the impingement holes. On this surface an analogy may be drawn to film cooling situations with orthogonal holes and high blowing ratios. The introduction of small quantities of initial cross flow significantly affects the channel behavior due to the near exponential increase in both the impingement hole velocity and the cross flow velocity. Initial cross flow is able to produce fairly uniform upstream heat transfer on all surfaces, but not the high peak values associated with the impingement that occurs in the no cross flow case. It was also found that a disproportionately large fraction of the total heat transfer could be driven by a small quantity of initial cross flow. Just 5 percent initial cross flow would reduce the mean target plate effectiveness to 0.61, while 10 percent initial cross flow would reduce the mean target plate mean to only 0.43. This represents a large portion of the total heat transfer driven by a small portion of the total flow and suggests the possibility for future optimization of the channel geometry.

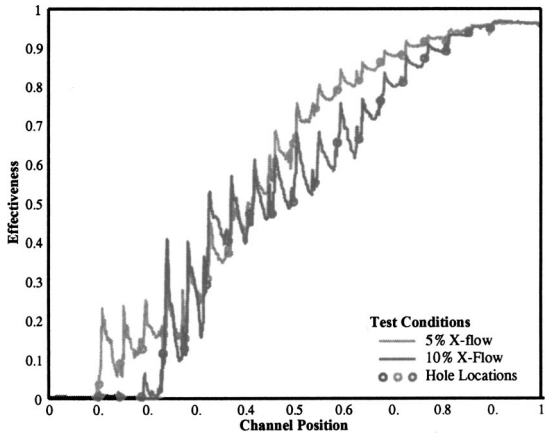

Fig. 15 Span wise average effectiveness for the impingement plate at an average jet Reynolds number of 20,000

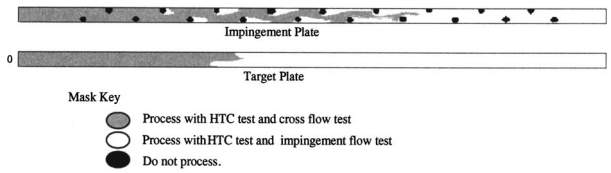

Fig. 16 Processing mask for Re=20,000 and 10 percent cross flow

Acknowledgments

This work has been carried out with the support of Rolls-Royce plc., QinetiQ, DTI CARAD and MOD ARP26c, the continuance of which is greatly appreciated by the authors. The experimental apparatus was expertly manufactured by Mr. Pat Timms.

Nomenclature

A = area, m^2
c = specific heat capacity of Perspex, $JK^{-1}kg^{-1}$
c_p = specific heat capacity of air, $JK^{-1}kg^{-1}$
d = hole diameter, m
DGT = driving gas temperature, K
G_c/G_j = mass flux ratio
h, HTC = heat transfer coefficient, $Wm^{-2}K^{-1}$
k = conductivity, $Wm^{-1}K^{-1}$
L = channel length, m
$\dot{m}$ = mass flow, $kg\,s^{-1}$
Re = Reynolds number
RSS = route sum square
t = time, s
T = temperature, K
T_c = temperature of the initial cross flow, K
T_{crystal} = crystal transition temperature, K
T_i = temperature of the impingement flow, K
$\_T$ = temperature, K
$\overline{V}_{\text{jet}}$ = mean jet velocity, $m\,s^{-1}$
x = longitudinal distance, m
y = span wise hole offset, m
z = channel height, m
x_n = jet spacing, m

Definitions

Impingement holes = the plate which contains the impingement plate
Nu = $h\overline{d}/k$
Re = $r\overline{V}_{jet}d/m$
Target plate = the plate upon which the jets impinge

Greek

ε = effectiveness
ρ = density, $kg\,m^{-3}$
μ = viscosity, $Nm^2\,s^{-1}$

Subscripts

0 = initial condition
aw = adiabatic wall conditions
A = impingement test
B = cross flow test
gas = mixed bulk gas temperature
h = heat transfer coefficient test
j = impinging jet
mb = mixed bulk conditions
mean = mean conditions
surface = surface

References

[1] Dailey, G. M., 2000, ''Aero-Thermal Performance of Integral Cooling Systems in Turbomachines: Design and Calculation Issues,'' VKI Lecture Series, February 28th–March 3rd, 2000.

[2] Kercher, D. M., and Tabakoff, W., 1970, ''Heat Transfer by a Square Array of Round Air Jets Impinging Perpendicular to a Flat Surface Including the Effect of Spent Air,'' ASME J. Eng. Power, pp. 73–82.

[3] Florschuetz, L. W., Metzger, D. E., and Truman, C. R., 1981, ''Jet Array Impingement With Crossflow Correlation of Streamwise Resolved Flow and Heat Transfer Distributions,'' NASA Contractor Report 3373.

[4] Gillespie, D. R. H., 1996, ''Intricate Internal Cooling Systems for Gas Turbine Blading,'' D. Phil thesis, Department of Engineering Science, Oxford University.

[5] Chambers, A. C., Gillespie, D. R. H., and Ireland, P. T., 2002, ''A Novel Transient Liquid Crystal Technique to Determine Heat Transfer Coefficient Distributions and Adiabatic Wall Temperature in a Three Temperature Problem,'' ASME Paper 2002-GT-30533.

[6] den Ouden, C., and Hoogendoorn, C. J., 1974, ''Local Convective Heat Transfer Coefficients for Jets Impinging on a Plate: Experiments Using a Liquid Crystal Technique,'' *Proceeding of the 5th Heat Transfer Conference*, **5**, ASME, New York, pp. 293–295.

[7] Lucas, M. G., Ireland, P. T., Wang, Z., and Jones, T. V., 1993, ''Fundamental Studies of Impingement Cooling Thermal Boundary Conditions,'' AGARD CP-527, Paper No. 14.

[8] Ireland, P. T., and Jones, T. V., 1986, ''Detailed Measurements of Heat Transfer on and Around a Pedestal in Fully-Developed Channel Flow,'' *Proc. 8th Int. Heat Trans. Conf.*, San Francisco, pp. 975–986.

[9] Chyu, M. K., Ding, H., Downs, J. P., van Sutendael, A., and Soechting, F. S., 1997, ''Determination of Local Heat Transfer Coefficient Based on Bulk Mean Temperature Using a Transient Liquid Crystals Technique,'' ASME Paper 97-GT-489.

[10] Gillespie D. R. H., Ireland, P. T., and Dailey, G. M., 2000, ''Detailed Flow and Heat Transfer Coefficient Measurements in a Model of an Internal Cooling Geometry Employing Orthogonal Intersecting Channels,'' ASME 2000-GT-653.

[11] Farina, D. J., and Moffat, R. J., 1994, ''A System for Making Temperature Measurements Using Thermochromic Liquid Crystals,'' Stanford University Department of Engineering Report No. HMT-48.

[12] Guo, S. M., Lai, C. C., Jones, T. V., Oldfield, M. L. G., Lock, G. D., and Rawlinson, A. J., 2000, ''Influence of Surface Roughness on Heat Transfer and Effectiveness for a Fully Film Cooled Nozzle Guide Vane Measured by Wide Band Liquid Crystals and Direct Heat Flux Gauges,'' ASME Paper 2000-GT-0204.

[13] Baughn, J. W., Mayhew, J. E., Anderson, M. R., and Butler, R. J., 1998, ''A Periodic Transient Method Using Liquid Crystals for the Measurement of Local Heat Transfer Coefficients,'' ASME J. Heat Transfer, **120**, pp. 772–775.

[14] Turnbull, and Oosthuizen, 1999, ''Theoretical Evaluation of New Phase Delay Methods for Measuring Local Heat Transfer Coefficients,'' Trans. Can. Soc. Mech. Eng., **23**(3–4), pp. 361–376.

[15] Van Treuren, K. V., 1994, ''Impingement Flow Heat Transfer Measurement of Turbine Blades Using a Jet Array,'' D.Phil thesis, University of Oxford.

[16] Son, C., Gillespie, D., and Ireland, P., 2001, ''Heat Transfer Characteristics of an Impingement Plate Used in a Turbine Vane Cooling System,'' Proceedings of ASME TURBO EXPO, Paper No. 2001-GT154.

[17] Tsang, C. L. P., Gillespie, D. R. H., and Ireland, P. T., 2001, ''Analysis of Transient Heat Transfer Experiments,'' The 8th International Symposium on Transport Phenomena and Dynamics of Rotating Machinery (ISOMAX-8).

[18] Florschuetz, L. W., and Su, C. C., 1987, ''Effects of Cross Flow Temperature on Heat Transfer Within An ~Array of Impinging Jets,'' ASME J. Heat Transfer, **109**, pp. 74–82.

[19] Goldstein, R. J., Sobolik, K. A., and Seoal, W. S., 1990, ''Effect of Entrainment on the Heat Transfer to a Heated Circular Air Jet Impinging on a Flat Surface,'' ASME J. Heat Transfer, **112**, pp. 608–611.

[20] Ireland, P. T., and Jones, T. V., 1987, ''Note on the Double Crystal Method of Measuring Heat Transfer Coefficient,'' OUEL Report 1710/87.

[21] Ling, J., and Ireland, P. T., 2001, ''Film Cooling Research For DLE Combustor Discharge Nozzles,'' OUEL report 2244/01 (restricted).

[22] Camci, C., Kim, K., and Hippensteele, S. A., 1991, ''A New Hue Capturing Technique for the Quantitative Interpretation of Liquid Crystal Images Used in Convective Heat Transfer,'' ASME Paper 91-GT-122.

[23] Van Treuren, K. W., Wang, Z., Ireland, P. T., and Jones, T. V., 1994, ''Detailed Measurements of Local Heat Transfer Coefficient and Adiabatic Wall Temperature Beneath an Array of Impinging Jets,'' ASME J. Turbomach., **116**, pp. 369–374.

[24] Vedula R. J., and Metzger, D. E., 1991, ''A Method for Simultaneous Determination of Local Effectiveness and Heat Transfer Distribution of Local Effectiveness and Heat Transfer Distributions in Three-Temperature Convection Situations,'' ASME 91-GT-345.

[25] Son, C., Gillespie, D., Ireland, P., and Dailey, G. M., 2001, ''Heat Transfer and Flow Characteristics of an Engine Representative Impingement Cooling System,'' ASME J. Turbomach., **123**, pp. 154–160.

[26] Florschuetz, L. W., and Su, C. C., 1985, ''Heat Transfer Characteristics Within an Array of Impinging Jets—Effects of Crossflow Temperature Relative to Jet Temperature,'' NASA Contractor Report 3936.

[27] Moffat, R. J., 1982, ''Contributions to the Theory of Single Sample Uncertainty Analysis,'' ASME J. Fluids Eng., **104**, pp. 250.

[28] Ireland, P. T., and Jones, T. V., 1985, ''The Measurement of Local Heat Transfer on and Around a Pedestal in Fully Developed Passage Flow,'' Proceedings of the 8th International Heat Transfer Conference, **3**, Hemisphere, pp. 975–980.

Discrete Green's Function Measurements in a Single Passage Turbine Model

Debjit Mukerji
e-mail: debjit@stanfordalumni.org
119 Loma Vista St. #4,
El Segundo, CA 90245
Telephone: (650) 906-2745

John K. Eaton
e-mail: eaton@vk.stanford.edu
Department of Mechanical Engineering,
Stanford University,
Stanford, CA 94305-3030
Telephone: (650) 723-1971
Fax: (650) 723-4548

The superposition-based Discrete Green's Function (DGF) technique provides a general representation of convective heat transfer that can capture the numerous flow and thermal complexities of the gas turbine environment and provide benchmark data for the validation of computational codes. The main advantages of the DGF technique are that the measurement apparatus is easier to fabricate than a uniform heat flux or uniform temperature surface, and that the results are applicable to any choice of discretized thermal boundary condition. Once determined for a specific flow condition, the DGF results can be used, for example, with measured surface temperature data to estimate the surface heat flux. In this study, the experimental DGF approach was extended to the suction side blade surface of a single passage model of a turbine cascade. Full-field thermal data were acquired using a steady state, liquid crystal-based imaging technique. The objective was to compute a 10×10 one-dimensional DGF matrix in a realistic turbomachinery geometry. The inverse 1-D DGF matrix, G^{-1}, was calculated and its uncertainties estimated. The DGF-based predictions for the temperature rise and Stanton number distributions on a uniform heat flux surface were found to be in good agreement with experimental data. The G matrix obtained by a direct inversion of G^{-1} provided reasonable heat transfer predictions for standard thermal boundary conditions. [DOI: 10.1115/1.1844537]

Introduction

In the area of turbine blade heat transfer analysis, a fundamental goal is to predict the blade temperature distribution under various operating conditions. This requires a fully coupled numerical analysis to solve the convection/conduction problem including the external convective heat transfer, the heat conduction in the blade metal, the internal cooling heat transfer, and the film cooling physics. However, such a computational evaluation is far beyond the current state of the art. The external and internal heat transfer predictions are subject to very large uncertainties because modern turbulence models are not yet capable of handling the highly complex, strongly interdependent physics of the turbine environment.

As a consequence, experimental methods are required that can provide accurate, spatially-resolved heat transfer measurements in a reasonable time frame such that they can be used to qualify CFD codes or provide design data for a particular turbine geometry. Time is a critical factor because ideally, the results should be able to impact the design evolution of the engine. The testing of a full-scale engine at the prototype stage, while perhaps yielding useful data, occurs at too late a development phase to permit any significant design changes to the overall blade cooling system. Small-scale experiments performed at the benchtop level, in contrast, can be executed quickly and at minimal cost, and can yield reliable, high-resolution data.

A basic objective in convective heat transfer research is to determine, for a given set of flow and thermal boundary conditions, the relation between surface heat flux and temperature rise at a given point on the object of interest. The heat flux out of a heated surface is proportional to the temperature difference between the surface and an appropriate reference:

$$q'' = h(T_{\text{surf}} - T_{\text{ref}}) \tag{1}$$

where the constant of proportionality is the heat transfer coefficient, h. The surface heat transfer is governed by the shape of the temperature profile near the wall, which is a reflection of the local skin friction, the thermal transport in the boundary layer, and the upstream wall temperature history. Hence, the heat transfer coefficient is strongly dependent on both hydrodynamic and thermal boundary conditions. Despite its very specific representation, h has traditionally been used as the primary descriptor of convective heat transfer.

For turbomachinery flows, where the thermal boundary conditions are highly complex, experiments are often run as simplified representatives of actual engine operation. In these experiments, measurement of h is useful only if there is confidence that the experimental boundary conditions are substantially similar to those expected under full-scale operational conditions. Because the actual thermal boundary conditions are difficult to reproduce and are rarely known at test time, experiments are usually run with either uniform temperature or uniform heat flux boundary conditions. Without a direct method to apply the resulting h measurements to cases with arbitrarily specified wall temperature or heat flux distributions, representative of the application of interest, the experiments remain of limited value. In this context, an improved experimental method is required, the results of which can be applied for general thermal boundary conditions.

Superposition-based methods, which rely on the linearity of the energy equation, have been applied successfully in simple geometry flows including fully developed pipe flow (Sellars et al. [1]) and flat plate boundary layers (Reynolds et al. [2,3]), where semi-analytical solutions for the case of a sharp step in wall temperature are available. While linearity is not strictly applicable in flows with large temperature variations, superposition techniques have been remarkably successful even in electronics cooling cases with strong natural convection effects (Ortega and Moffat [4]).

Hacker and Eaton [5] introduced a superposition-based description of convective heat transfer, the Discrete Green's Function (DGF) method. The DGF basis functions quantify the thermal response to discrete square pulses in either wall temperature or heat flux. This method is more amenable to experimental evaluation of the basis functions than other superposition methods. Hacker and Eaton [5] developed one technique to measure the DGF in a backward-facing step flow and demonstrated that it

Contributed by the Heat Transfer Division for publication in the JOURNAL OF HEAT TRANSFER. Manuscript received by the Heat Transfer Division February 4, 2004; revision received November 2, 2004. Review conducted by: S. Acharya.

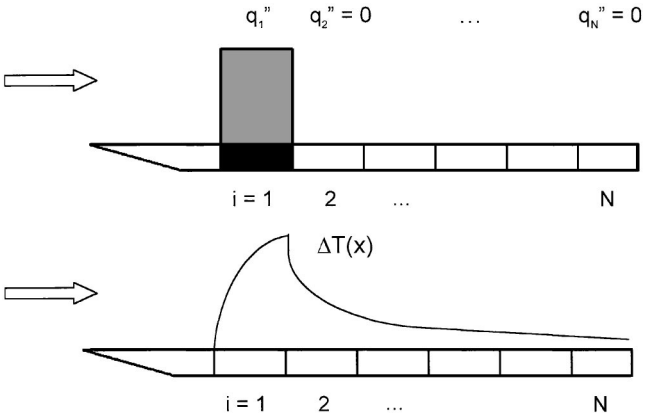

Fig. 1 Discretization of heat transfer surface and measurement of inverse DGF matrix

could be used to accurately calculate the heat transfer rate with complex boundary conditions. Batchelder and Eaton [6] developed a much simpler DGF measurement technique for a steady-state boundary layer, and coupled the DGF into a conjugate heat transfer analysis system. They showed that in a flat plate boundary layer, it is sufficient to heat only a few discrete elements of the surface while measuring the global temperature distribution. This technique offers the possibility of considerably simplifying convective heat transfer measurements in complex geometries where fabrication of uniform heat flux or uniform temperature surfaces is difficult.

The objective of the present work was to extend the experimental, one-dimensional DGF technique to a practical complex geometry, namely, a benchtop-scale, two-dimensional turbine cascade. The DGF technique as explored here could potentially evolve into a supporting tool for turbomachinery hardware development. A full-field, steady state wideband liquid crystal imaging technique was used to calculate a 10×10 DGF matrix for the suction side boundary layer in a single passage turbine model. Uniform heat flux data also were obtained to provide baseline comparisons to the DGF results.

The Discrete Green's Function Approach. The Discrete Green's Function (DGF) technique provides a general description of convective heat transfer that is flow-specific but independent of the thermal boundary conditions. The DGF is effectively a ''thermal influence'' function that carries complete information about the flow. The 1D DGF accounts only for streamwise variations along the surface, whereas the 2D DGF includes both spanwise and streamwise effects. 1D DGF measurements are appropriate in simple 2D flows, whereas 3D flows may demand a 2D DGF treatment. The formulation of the 1D DGF will be reviewed here. Batchelder and Moffat [7] provide details regarding development of the 2D DGF methodology.

The 1D DGF approach conceptually divides the heat transfer surface into a series of equal-sized, discrete elements (strips). The DGF relates the heat transfer rate on each of these strips to the temperature rise (relative to a suitable reference) on all of the others. The division of the surface into N discrete elements is depicted in Fig. 1. The discretization implies that heat transfer rate and temperature rise must be spatially averaged over the length l of each element. The continuous heat transfer and temperature distributions are represented as a series of discrete square pulses. As the discretization becomes finer, the spatial resolution of the DGF measurement increases. Ideally, the discretization size should be sufficiently small to resolve anticipated temperature and heat flux variations. The average heat transfer rate per unit length at element i is related to the average temperature rise at element j through the DGF term g_{ij}, with units of W/m-K:

$$q'_{ij}=g_{ij}\Delta T_j \tag{2}$$

Equation (2) describes only the influence of one element on another. In practice, the heat transfer at one element i depends on thermal conditions at all of the elements. The combined effect of all N elements on element i may be found by performing a summation:

$$q'_i=\sum_{j=1}^{N} g_{ij}\Delta T_j \tag{3}$$

In practice, it is difficult to apply a square pulse in temperature rise at one location and measure the heat transfer rate at all other locations. In the laboratory, it is more convenient to instead apply a square pulse in surface heat flux over one element (while maintaining the remainder of the surface adiabatic) and measure the global temperature distribution. It is thus advantageous to measure the inverse DGF elements, defined as

$$\Delta T_i=\sum_{j=1}^{N} g_{ij}^{-1}q'_j \tag{4}$$

This may be expressed compactly in matrix form as:

$$\mathbf{\Delta T}=\mathrm{G}^{-1}\mathbf{q}' \tag{5}$$

In attached flows, the effects of downstream elements on upstream elements are negligible, so that the matrix is lower triangular ($g_{ij}^{-1}=0$ for $j>i$). The main diagonal terms represent the thermal effects of ''self-heating.'' The off-diagonal terms capture the influence that other elements in the array have on the element of interest; in the case of attached flows this is the ''upstream heating'' effect.

Measurement of the first column of G^{-1} is depicted in Fig. 1. The top diagram shows the heat flux distribution, with a single element heated (element 1) on an otherwise adiabatic wall. The bottom diagram illustrates the resulting rise in the surface temperature due to the uniform heat flux boundary condition on element 1. To obtain the full $N\times N$ G^{-1} matrix directly, each of the N elements would be heated and the resulting N surface temperature distributions measured.

Because the matrix G^{-1} (or G) relates the heat flux and temperature rise distributions on a general level, it can be used to yield the conventional heat transfer coefficient, h, for arbitrarily complex thermal boundary conditions. Hence, even though the DGF description and h are both flow-specific, the DGF formulation is more versatile than h.

One of the great advantages of the DGF experimental approach, as presented here, is that the DGF measurements themselves do not need to be made under complex thermal boundary conditions. Rather, the wall boundary conditions during the experiment are very simple, as discussed above. Once the DGF basis functions have been carefully determined for a given flow, they can be used, for example, to estimate surface heat flux for highly complex surface temperature distributions, which are common in turbomachinery applications. A priori knowledge of the actual thermal boundary conditions is not strictly necessary, though expected spatial variations may have a role in setting the DGF discretization.

Experimental System

Single Passage Model. The DGF experiments were performed in a scale model, originally used by Buck and Prakash [8], of the single passage between two adjacent blades in a turbine cascade. The original single passage model, designed for film cooling tests, was modified significantly for the current experiments. The inlet design featured an elliptical bellmouth upstream of the airfoil surfaces and a circular arc bellmouth on the top and bottom inlet walls. The original model featured individually adjustable tailboards on pressure and suction sides, which pivoted

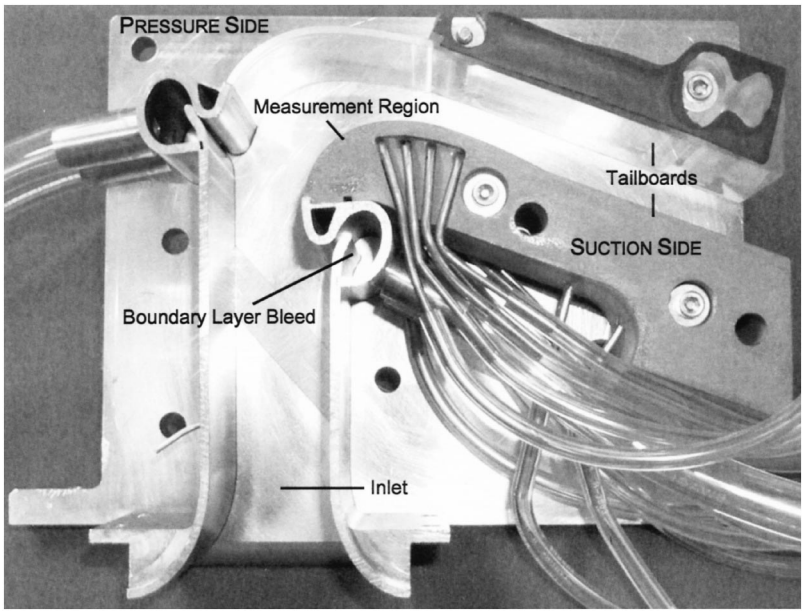

Fig. 2 Cross-sectional view of modified single passage model

around the trailing edges of the airfoils and guided the flow out to the model exit. On both pressure and suction sides, the flow encountered bleed slots that ''restarted'' the boundary layer near the stagnation point of the airfoils. Further details regarding the single passage model design can be found in Buck and Prakash [8].

In the original model, a film cooling plenum (containing a single row of film cooling holes) and airfoil were integrated into a single piece, on suction and pressure sides. The present objective was to retain the original film cooling plenum and hole hardware for an associated series of film cooling tests, not discussed here. The airfoils were thus EDM-cut just downstream of the film cooling holes. The original pressure side airfoil was replaced with a thin, transparent Plexiglas window of identical shape, through which imaging could be performed. The pressure side tailboard was replaced with an adjustable Plexiglas piece. On the suction side, a new, integrated airfoil and tailboard was constructed out of a single piece of Ren Shape 450 (Ciba Specialty Chemicals, Inc./Vantico), a resin-based tooling foam that is relatively easy to machine and features a low thermal conductivity. Three such Ren Shape components were constructed: one for pressure measurements, and one each for uniform heat flux and DGF measurements. The interface between the metal film cooling plenum piece (containing the film holes) and the Ren Shape airfoil/tailboard surface was sealed flush with silicone rubber adhesive sealant, creating a smooth transition and tight bond between the adjoining surfaces.

A cross-sectional photograph of the modified single passage model is provided in Fig. 2. The figure shows the Plexiglas window and tailboard on the pressure side, and integrated Ren Shape pressure measurement piece on the suction side. The section of the Ren Shape piece corresponding to the DGF measurement region is roughly identified. The bellmouth-shaped flow inlet, suction side boundary layer bleed, and tailboards are also indicated.

Flow System and Instrumentation. The airflow to the single passage model was supplied by a large rotary screw compressor and passed through the flow system shown schematically in Fig. 3. The compressor supplied air to a thermal mass air dryer followed by a large tank and a chilled water-to-air heat exchanger. The flow then passed through a length of copper pipe wrapped with heating tape and fiberglass insulation. The heating tape and heat exchanger maintained the stagnation temperature of the air in the model constant to within ± 0.2°C.

The mass flow rate was measured with an ASME-certified orifice plate. The orifice plate measurements were compared to mass flow predictions from pressure data at the inlet of the single passage model, assuming a one-dimensional velocity profile. The two independent mass flow measurements agreed to within $\pm 3\%$. This indicated a high level of mean flow uniformity at the model inlet.

The flow entered the single passage setup shown schematically in Fig. 4, passing first through a diffuser and then turning vertically into a 0.40 m square plenum. A 67 mm$\times$75 mm opening at the center of the plenum lid accommodated the bellmouth inlet of the single passage model. The center of the plenum was instrumented with two thermocouples that were within 0.1°C agreement for all experimental cases. The plenum was also tapped for total pressure measurements.

Pressure measurements were made with a 48-port Scanivalve system connected to a differential pressure transducer. Type K thermocouples were used for all temperature measurements. An insulated thermocouple ice bath was equipped with two reference thermocouples inserted in a glass tube. All thermocouples were connected through an insulated zone box to a data acquisition unit and digital multimeter.

DGF and Uniform Heat Flux Measurement Surfaces. The DGF and uniform heat flux surfaces were each constructed from a layer of coated polyester film affixed to a Ren Shape substrate. Two identical Ren Shape integrated airfoil and tailboard components were fabricated, with 180 μm recesses on the portion of the surface corresponding to the original airfoil. The recess accommodated a thin film heater without creating local steps on the surface. The heater for both heat transfer surfaces was a 125 μm thick polyester film with a sputter-deposited indium/tin oxide (ITO) layer (CP Films, Inc.). The nominal coating resistance was 100 ohms/square and was, according to the manufacturer, spatially uniform to within 5%. The film was fixed to the Ren Shape substrate with a pressure-sensitive adhesive layer. The recess accommodating the film started 2.8 mm downstream of the interface between the stainless steel upstream component and the Ren Shape piece.

The imaged DGF surface was divided conceptually into 10 discrete elements in the streamwise direction, each nominally $l = 3.5$ mm in extent. This discretization length was chosen on the basis of practical considerations, including measurement uncertainty and ease of fabrication.

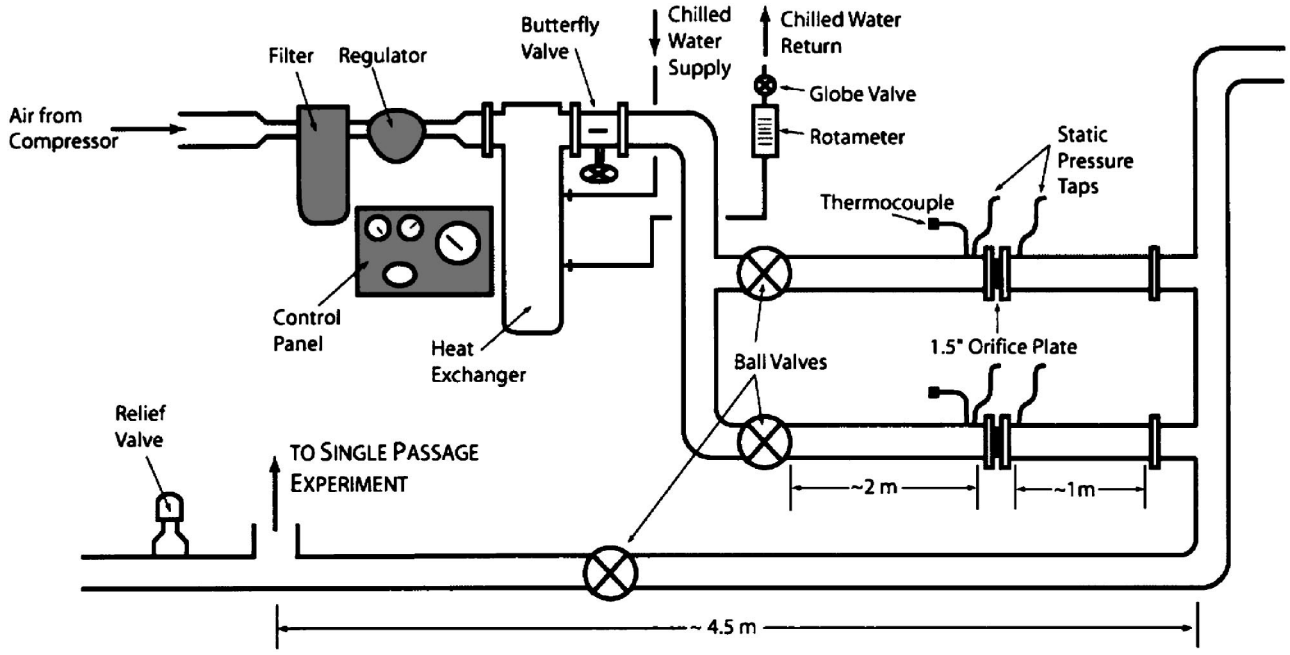

Fig. 3 Schematic diagram of air flow system preceding single passage model

The heater for the DGF surface was divided into five distinct discrete regions (3 active, 2 inactive) by scoring the surface of the film lightly. The electrical resistances of the active elements were measured with a four-wire technique. The 3% agreement between the resistance values confirmed that the elements were cut to virtually identical dimensions. The surface for the uniform heat flux measurements was left unscored. Power connections to both surfaces were made using 1/8 in. wide 3M copper tape, bonded to the active regions of each surface using two-part silver epoxy (SPI Supplies). A Hewlett-Packard 6034A dc power supply provided current to the heat transfer surfaces. The electrical current input was deduced by measuring the voltage across a precision 1% current sense resistor (Caddock Electronics, Inc.) in series with the heated element.

Three Type K, 36-gauge thermocouples were embedded with thermally conductive epoxy into 0.050 in. diameter holes along the centerline of each Ren Shape component, at a subsurface depth of 5 mm. The readings from these thermocouples provided rough estimates of conduction back losses, serving as reference data for the numerical conduction solver discussed later.

The DGF and uniform heat flux surfaces were coated with approximately 0.01-mm-thick layers of nonconductive black ink and

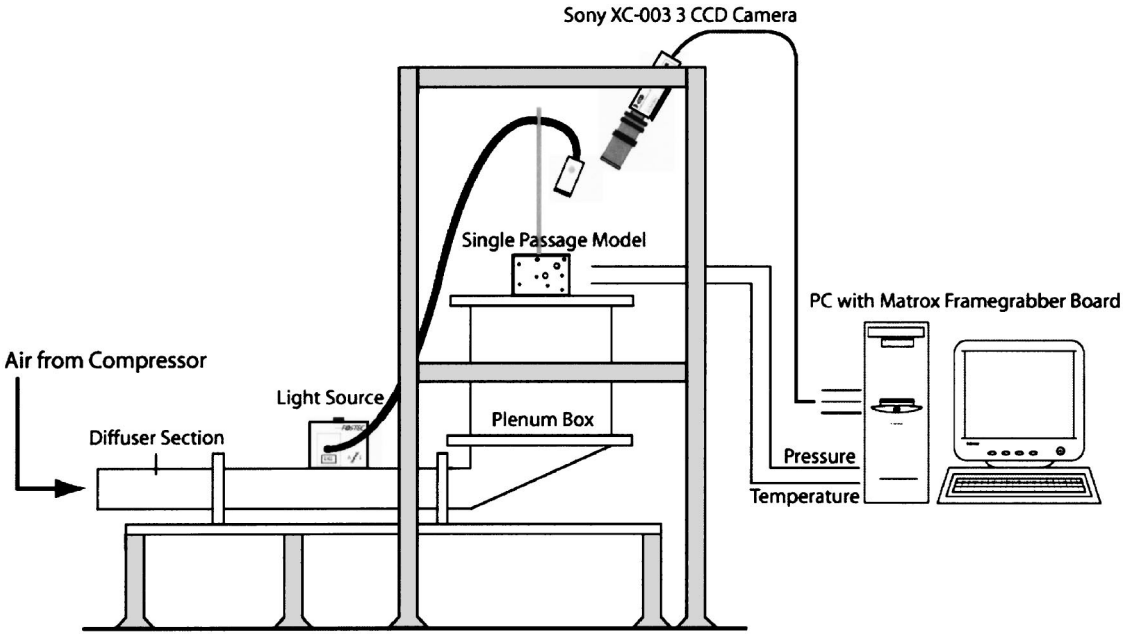

Fig. 4 Single passage facility and imaging system schematic

thermochromic liquid crystal (TLC) paint (Hallcrest 25C5W). When painting each film-covered heat transfer surface, a copper calibrator (discussed in the next section) was coated simultaneously, using the identical TLC mixture and airbrushing technique. Masking of the calibrator and heat transfer surfaces produced a set of precision fiducial marks on each, providing accurate spatial referencing on the highly curved geometry.

Thermochromic Liquid Crystal Imaging

Spatially-Varying Hue-Temperature Calibration. The temperature distributions on the DGF and uniform heat flux surfaces were measured using thermochromic liquid crystal imaging, following the general procedures used by Farina et al. [9] and Hacker and Eaton [5]. A schematic diagram of the imaging setup is shown in Fig. 4. The TLC imaging was performed through the Plexiglas window on the pressure side of the model. The measurement surface was illuminated using a Fostec Ace I halogen light source fitted with a fiberoptic gooseneck cable. TLC images were acquired using a Sony XC-003 3-CCD camera with 8-bit resolution. The image data were transferred to a Matrox frame grabber board installed in a PC.

The strong curvature of the measurement surface caused two major difficulties. First, there were strong variations in the image intensity, requiring the use of three different camera aperture settings to obtain useful data over the entire imaged area. The image data from individual aperture settings were assembled into a single composite temperature map during postprocessing. Also, true color TLC measurements are very sensitive to the incidence angle of the camera and lighting relative to the imaged surface (Farina et al. [9]). A spatially-varying calibration procedure was developed to address this problem.

The TLC paint was calibrated using an oxygen-free high-conductivity (OFHC) copper piece cut to the exact shape of the measurement surface. The calibrator was mounted in grooves in the single passage endwalls to insure precise positioning and identical imaging conditions under calibration and measurement. The calibrator was instrumented with six Type K, 36-gauge thermocouples and was heated by a Kapton heater (Minco, Inc.). The heater was mounted to the back surface of the calibrator and controlled by a PC-based closed loop controller.

Figure 5 displays an image of the painted calibrator surface with an overlaid TLC calibration grid. The calibration area was divided into fourteen nonuniform sections in the streamwise direction (from bottom to top), as shown. Smaller streamwise dimensions were used at the leading edge, where the spatial variation in hue was the greatest due to the large surface curvature. The regions selected for the TLC calibration were the fourteen, 10-mm-wide center elements shown in Fig. 5, which were directly over the calibrator thermocouple positions. An independent calibration was performed for each of these regions. The large variation in light intensity over the surface is also evident in Fig. 5. Additionally, the square fiducial mark patterns are visible on the spanwise limits of the imaged area.

The ⟨R G B⟩ values captured by the CCD camera were averaged for each of the fourteen calibration regions over the entire zone (spatially) and over the specified number of image frames (temporally). These mean ⟨R G B⟩ values for each of the calibration regions were converted to hue and plotted against temperature to yield calibration curves. Hue, or hue angle, is a commonly used tristimulus value that provides a one-to-one conversion of measured ⟨R G B⟩ components to temperature. The hue formulation used here was presented by Farina et al. [9]:

$$Q = \frac{255}{2\pi} \arctan\left(\frac{\frac{1}{2}R - \frac{1}{2}G}{-\frac{1}{4}R - \frac{1}{4}G + \frac{1}{2}B} \right) \tag{6}$$

The temperature value associated with the image data was the average of two thermocouple readings, acquired immediately before and after imaging at each calibration point. This helped to compensate for thermal drift during the imaging procedure.

A representative pair of calibration curves for the TLC paint applied to the DGF surface, corresponding to two different camera aperture settings, is shown in Fig. 6. Regions 1 and 14 were at the

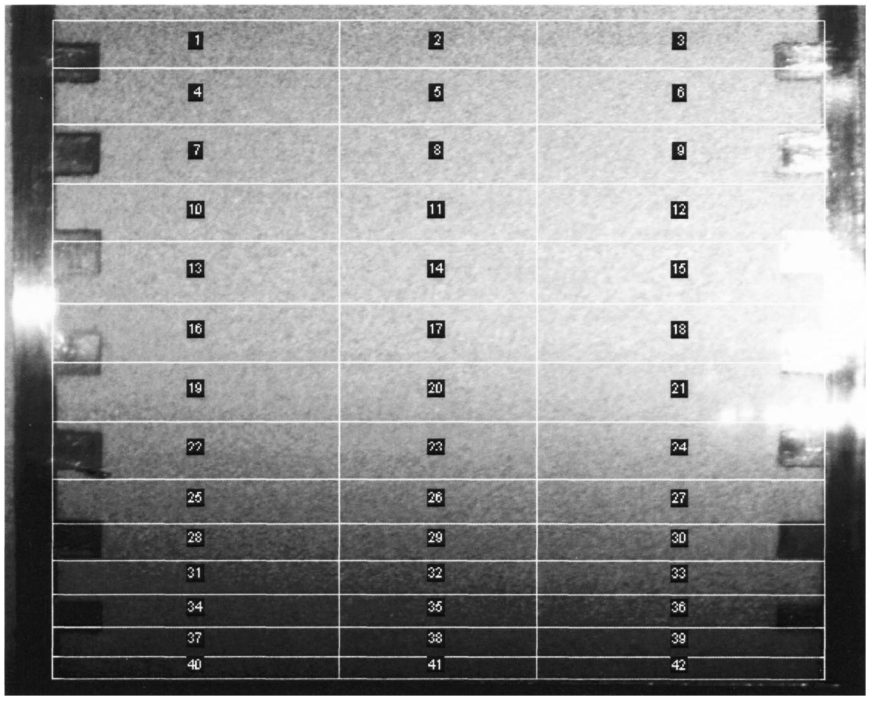

Fig. 5 DGF calibration regions and light intensity variation

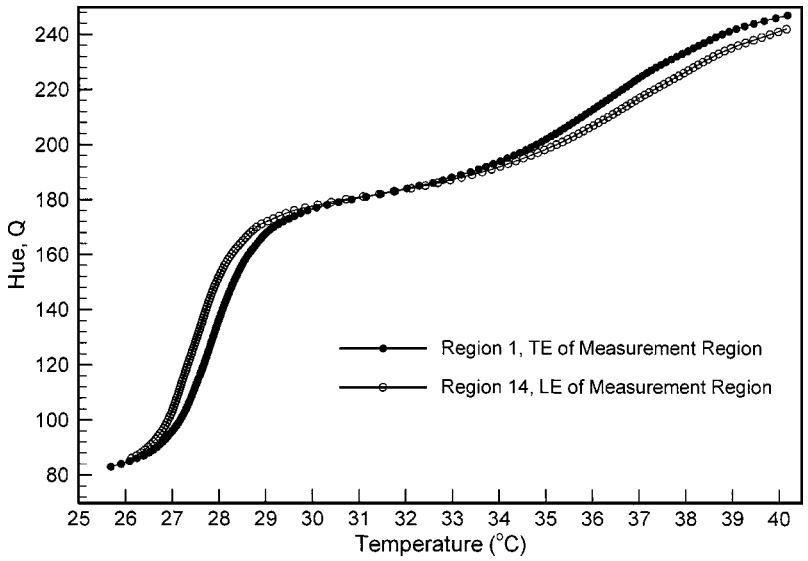

Fig. 6 Spatial variation of thermochromic liquid crystal (TLC) paint calibration

streamwise limits of the imaged area, with Region 14 corresponding to the leading edge of the airfoil. The data illustrate the spatial dependence of the calibration due to surface curvature. Between hue values of 100 and 175, the difference in corresponding temperatures between Region 1 and Region 14 was between 0.3°C and 0.4°C. The temperature disparity was also significant at hue values above 190, and exceeded 1.0°C at hue values above 240. The maximum measurement resolution was found over a temperature range of roughly 27–29°C, near the activation temperature of the TLCs. Repeatability between independent calibrations over the full temperature range was within 0.2°C.

The uncertainty in the TLC measurements was assessed by performing a redundant check on the calibration. The calibrator was set to specified temperatures and the surface imaged. The TLC-indicated temperatures on the surface were then checked against the thermocouple readings. Combining the deviations with the uncertainty of the thermocouple measurement, the maximum uncertainty of the TLC measurements was estimated to be 0.35°C. Because the calibration was performed in-situ, the angular dependence of the TLC measurement was not factored into the uncertainty.

Hysteresis in TLCs is the phenomenon by which the paint can register different hue values for a given temperature, depending on whether the test point is approached from below (by heating) or from above (by cooling). Depending on the absolute temperature, the measurement can shift by as much as 0.6–0.7°C for the type of liquid crystal paint studied here. Uncertainty due to hysteresis was excluded from the calculations, as all experimental conditions were approached (as in the calibration) by heating.

Discrete Green's Function Measurements

As demonstrated in Batchelder and Eaton [6], it is generally unnecessary to measure the heat transfer characteristics at every DGF element in the array. Rather, because of smooth variations in attached boundary layers, only a few elements need to be active (powered). Each active element, in the absence of significant conduction effects, generates a single column of the DGF matrix. The other columns may be found by interpolation or extrapolation. Batchelder and Eaton [6] obtained an accurate DGF matrix by measuring only the first and last columns of a 15×15 matrix and interpolating the remaining columns. A minimum of three heated elements was deemed necessary in the present case due to the increased complexity of the flow. The active elements corresponded to regions 1, 4, and 7, with element 1 at the leading edge. These three columns of the 10×10 inverse DGF matrix were measured directly. Columns 2, 3, 5, and 6 were interpolated, and columns 8, 9, and 10 were extrapolated from the measured data.

DGF Data Acquisition and Analysis. Each of the three active elements on the DGF surface was powered in isolation in separate experimental runs. The nominal thermal boundary condition was uniform heat flux on the powered element and adiabatic elsewhere. TLC imaging was used to measure the complete wall temperature profile and the average temperature rise at each element was related to the average heat flux distribution through Eq. (4).

The heat flux expressed in the DGF definition is the convective term only. The DGF calculations thus required corrections for heat conduction and radiation effects. The conduction losses within the Ren Shape substrate material were estimated using a numerical approach. The analysis used a steady state, two-dimensional conduction code with a uniformly-spaced 40×90 Cartesian grid that approximated the shape of the measurement piece. A stair-step and half-node (cut diagonally) pattern was fit to the curvature on the airfoil surface. The thermal conductivity of the Ren Shape 450 material was specified to be 0.2 W/m-K, based on the manufacturer's estimates. Experimental TLC measurements were used as input to the code, specifying the surface temperature boundary condition. The complete temperature distribution in the numerical domain was then solved using an initial temperature guess and Gauss–Seidel iteration. Back loss thermocouple data from the experiments were used for validation of the computational results. The numerical and back loss thermocouple temperatures agreed to within ±0.3°C for all cases. Conduction loss profiles for individual heating of DGF elements 1, 4, and 7 are provided in Fig. 7. The plot shows the conduction heat flux out of each element, normalized by the nominal heat flux generated in the active element. Note that a negative conduction heat flux indicates heat inflow to the element.

The only elements notably influenced by conduction were the heated element itself and its two adjacent neighbor elements. The element downstream of the heated element was predicted to have a lower influx of heat by conduction than the element immediately upstream due to the thermal wake effect. All of the other DGF elements have less than 1% influx of heat by conduction. The data reduction was simplified by considering these elements adiabatic.

Radiation corrections were calculated only for the main diago-

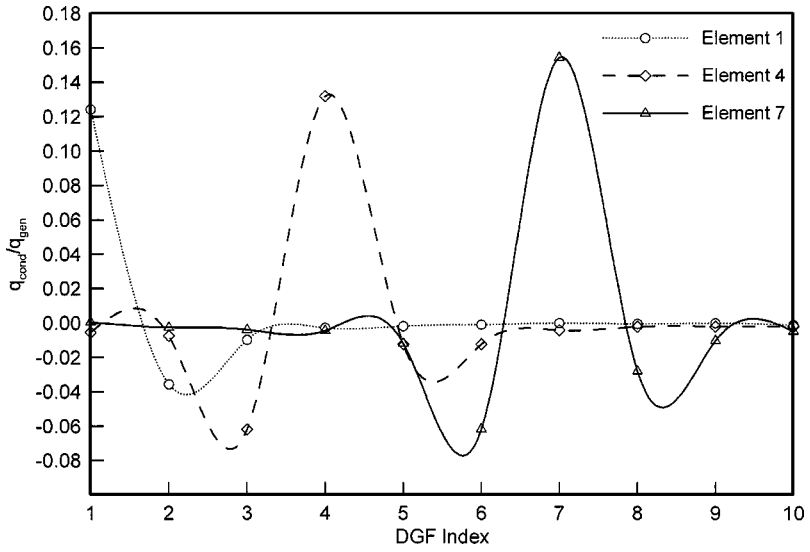

Fig. 7 Profiles of conduction heat loss for DGF elements

nal and first off-diagonal elements. The emissivity of the black paint- and TLC-coated heat transfer surface was estimated to be $\varepsilon=0.9$. This value was determined by emissivity measurements on a similarly-prepared flat surface. Radiation heat loss accounted for only $\approx$1% of the generated heat flux for the main diagonal elements.

The overall uncertainty estimates for the DGF measurements accounted for uncertainties in wall and recovery temperatures, film power measurements, active element dimensions, and conduction and radiation heat loss terms. Due to the small temperature rise values on the elements far downstream of the heated region, the uncertainties for these far off-diagonal elements was large. To generate higher temperature signal, ''overheat'' cases were run in which the powered element was heated beyond the upper limit of the TLC temperature range. This improved measurement quality substantially for the off-diagonal terms of G^{-1}. For example, for the first element heated to near the upper limit of the TLC range, the uncertainties in the $g_{8,1}^{-1}$, $g_{9,1}^{-1}$, and $g_{10,1}^{-1}$ terms were 109%, 127%, and 151%, respectively. By using overheat conditions, the final uncertainties in these terms were reduced to less than 30%.

When computing the total uncertainty of the measured DGF matrix elements, the variable uncertainty from data set to data set was considered. The individual uncertainty sources were divided into bias (systematic) errors and random errors. Columns 1, 4, and 7 of the G^{-1} matrix were calculated by averaging 4–6 independent data sets. The final reported uncertainties combined the random and systematic errors in a root-sum-square fashion, as suggested by Kline and McClintock [10] and Moffat [11].

The columns of G^{-1} were obtained first by determining the main diagonal elements for each of the three active columns, and then using spline interpolation and extrapolation to yield the remaining main diagonal terms. These were then used to compute the first off-diagonal terms for the active columns, with the remaining first off-diagonal terms again found by spline interpolation and extrapolation. This ''cascading'' solution procedure proceeded, from the main diagonal to the furthest off-diagonal, until the full matrix was obtained. For consistency, the G^{-1} matrix has the same units as the DGF formulation described in Batchelder and Eaton [6]. The matrix elements have units of temperature rise over heat flux, divided by DGF discretization length l (m-K/W).

The conduction code results and radiation loss estimates were used to make second-order corrections to the DGF terms. The uncertainty of each of the interpolated or extrapolated elements was computed by sequentially perturbing the relevant measured values by their individual uncertainties and observing the deviation in the inferred terms. These deviations were combined using the root-sum-square approach to deduce a matrix of uncertainties associated with G^{-1}, δG^{-1}.

Results and Discussion

Discrete Green's Function Heat Transfer Results. The full-field TLC images of the DGF surface contained 448 streamwise $\times$420 spanwise pixels, with corresponding physical dimensions 40 mm long and 30 mm wide. Continuous streamwise profiles of temperature rise were obtained by spanwise-averaging the full-field TLC images over the center 15 mm (200 pixels). Mean temperature rise and heat flux values on each DGF element were calculated by averaging the streamwise temperature and heat flux profiles over the element lengths ($l=3.5$ mm).

Figure 8 shows a sample spanwise-averaged temperature profile with element 4 powered, at a nominal heat flux of $q_4''=4460$ W/m^2. The plot indicates a clearly defined leading edge region (characterized by a sharp streamwise temperature gradient) and distinct thermal wake. No corrections were made for thermal conduction in the film. The conduction resistance through the film

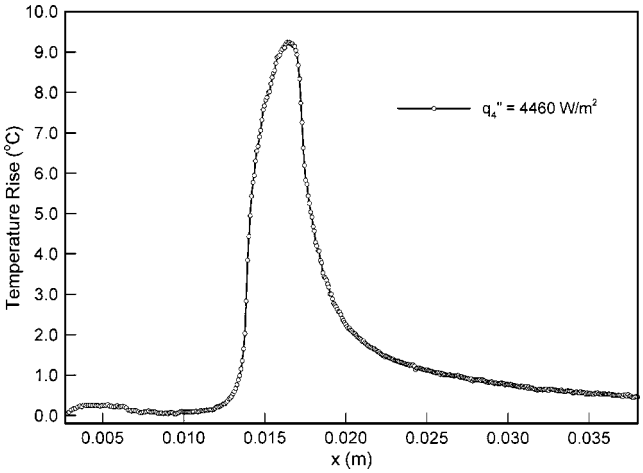

Fig. 8 Spanwise-averaged temperature rise profile with DGF element 4 heated

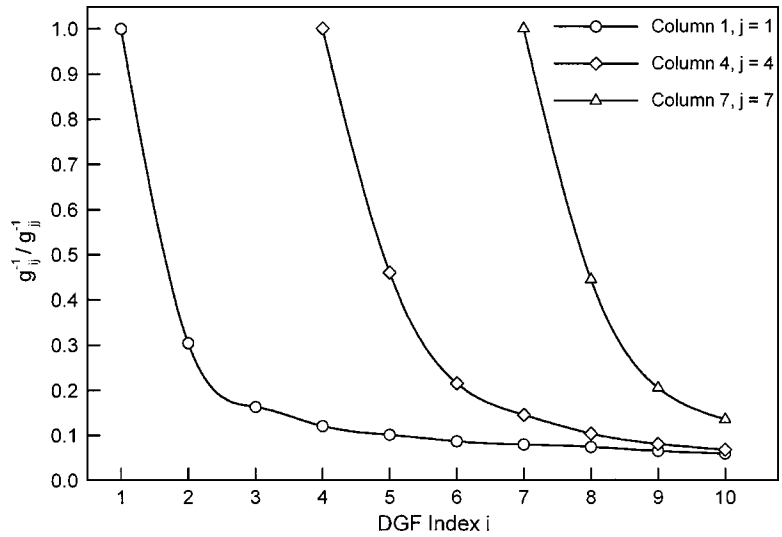

Fig. 9 Measured columns of the G^{-1} matrix

was high due to the small dimension of the film (0.005 in. thick) and the low thermal conductivity of the constituent polyester.

A plot of each of the measured DGF columns, with each element normalized by its corresponding main diagonal, is shown in Fig. 9. The ratios of the first two off-diagonals to the main diagonal in columns 4 and 7 are in good agreement with the results of Batchelder and Moffat [7]. The sharp drop-off for the first off-diagonal in the first column is probably fluid mechanics-related. It is possibly influenced by surface roughness at the interface between the Ren Shape surface and the film cooling plenum. Although the experimental uncertainty was relatively high for the far off-diagonal terms, the results from columns 1 and 4 of G^{-1} show the off-diagonals far downstream of the heated element asymptotically approaching a value that is approximately 6% of the magnitude of the main diagonal. Additionally, the fourth off-diagonal term for columns 1 and 4 is roughly 10% of the main diagonal element. This information may be useful in developing scaling laws for far off-diagonal terms rather than relying on global temperature measurements. These terms do not contribute appreciably to the overall uncertainty in the heat transfer solution, so estimating them is a justifiable approach.

The measured and inferred values of the main diagonal elements of G^{-1} are shown in Fig. 10. The trend is one of steady increase in g_{ii}^{-1} near the leading edge followed by a tapering off with downstream distance. The primary contributor to this trend is the growing momentum boundary layer and the resulting decrease in skin friction for the downstream elements.

Thermal Predictions Using the DGF Method. The uniform heat flux results represent a baseline data set against which the DGF predictions can be compared. The measured G^{-1} matrix was used to predict the experimentally-determined temperature rise for this boundary condition. The DGF ΔT prediction is displayed in Fig. 11, plotted along with the measured, spanwise-averaged temperature profile and the measured temperatures averaged over the DGF discretization. The nominal heat flux for this case, prior to heat loss corrections, was $q''=1510\,\mathrm{W/m^2}$. The DGF prediction was obtained using a matrix multiplication of G^{-1} with the experimental conduction- and radiation-corrected heat flux vector, $\mathbf{q}'$, as expressed in Eq. (5). The uncertainties in the elements of the heat flux vector were calculated to be approximately 5%. The overall uncertainty in the DGF prediction was a combination of

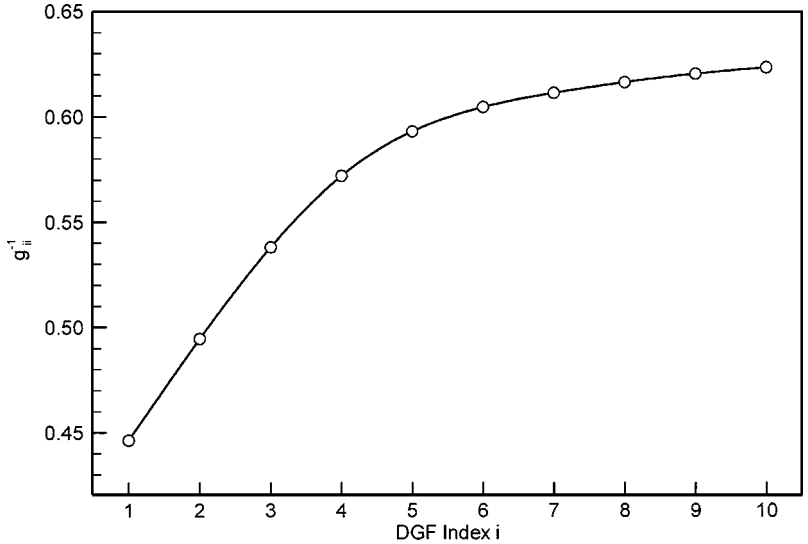

Fig. 10 Main diagonal elements of the G^{-1} matrix

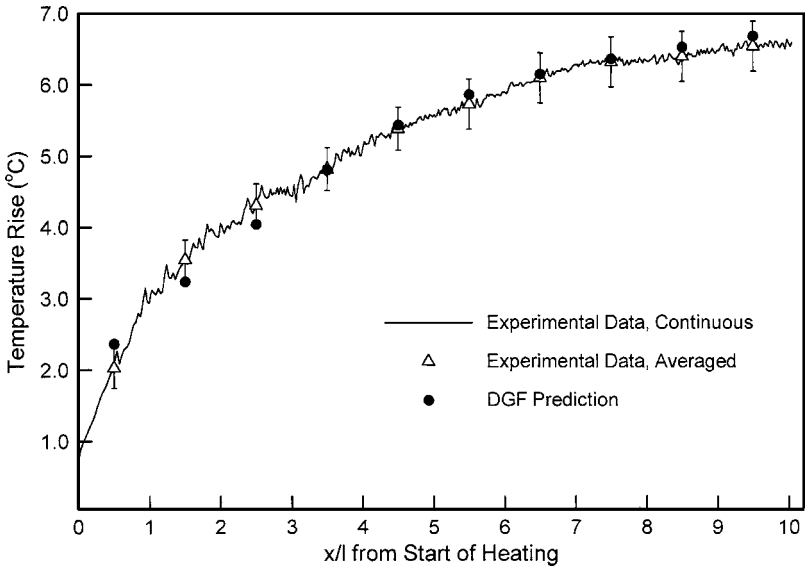

Fig. 11 DGF temperature rise prediction using the G^{-1} matrix

the uncertainties of the DGF elements, given by the matrix δG^{-1}, and the uncertainties in the heat flux measurements.

The results show excellent agreement overall. The error bars for the DGF prediction have not been plotted because for points near the trailing edge, they are appreciably larger than the difference between prediction and experiment and distort the vertical scale. Table 1 contains a breakdown of the uncertainty in the DGF prediction on a point-by-point basis. The notably increased uncertainties for points 8–10 are due to extrapolation error in the DGF matrix elements. The error bars in Fig. 11 are for the temperature measurement alone, representing only the uncertainty incurred by the TLC imaging procedure and varying between 0.28°C and 0.35°C. The point of largest disagreement between the prediction and experiment is at the first element, where the DGF solution overpredicts the temperature rise by 0.34°C, or 17%. The DGF prediction overestimates ΔT_1 but slightly underpredicts ΔT_2 and ΔT_3. Because columns 2 and 3 of G^{-1} were interpolated, this implies that in the first column, the magnitude of the main diagonal element is probably high relative to the first two off-diagonal terms.

The DGF temperature prediction is excellent over the rest of the surface, with less than 0.2°C disagreement with points 4–10. The results are particularly encouraging at the furthest downstream point, which has the highest DGF prediction uncertainty (about 12%) due to the large uncertainty in the extrapolated 10th main diagonal element. The disagreement between the predicted and measured average temperature rise value at this location is only 2%. Apart from the first point, the DGF prediction points fall within the uncertainty band for the TLC measurement alone. At all locations, the uncertainty intervals for the experimental temperature rise distribution and the DGF measurement overlap.

Table 1 DGF uncertainties for temperature rise prediction

DGF Index	ΔT_{pred} (°C)	$\delta\Delta T_{pred}$ (°C)	% Uncertainty
1	2.37	0.24	10.2
2	3.23	0.24	7.5
3	4.04	0.29	7.1
4	4.80	0.35	7.2
5	5.43	0.36	6.7
6	5.86	0.36	6.2
7	6.15	0.42	6.8
8	6.36	0.53	8.4
9	6.52	0.68	10.4
10	6.68	0.81	12.1

The temperature rise predictions can be used with the known heat flux distribution to predict the Stanton number over the surface. The DGF St prediction is shown in Fig. 12, along with the averaged and continuous experimental distributions. Uncertainty intervals for the St measurements alone are shown at the DGF locations. The DGF prediction uncertainty margins are considerably larger, particularly at the trailing edge, and are outlined in Table 2. The error trends are consistent with the observations for the temperature rise comparisons. The heat transfer measurements near the leading edge have the greatest uncertainty because the difference between the wall and recovery temperatures approaches zero. Apart from the first data point, the agreement between predicted and measured *St* is better than 10%, and the DGF predictions lie within the uncertainty band of the experimental St measurement.

Knowledge of G (rather than G^{-1}) is required to determine the heat flux profile for a specified temperature rise distribution, a capability of particular relevance to turbomachinery applications. Direct inversion of the measured G^{-1} matrix resulted in slight nonphysical oscillations in the off-diagonal terms of the G matrix, consistent with the observations of Batchelder and Eaton [6]. The oscillations did not lead to significantly erroneous results for relatively simple thermal boundary condition cases. The G matrix was used with the experimental temperature rise distribution for a uniform heat flux boundary condition to approximate the averaged surface heat flux, shown in Fig. 13. The uncertainty intervals for the experimental heat flux measurement are included. The predicted q'' falls outside the uncertainty limits for the first three DGF locations, but within the brackets for the remaining locations. The DGF prediction underestimates the heat flux by 14% at the first location and overestimates it by 16% at the second location. By the third DGF location, the disagreement is only 6%. By many standards, these errors are not unacceptable, suggesting that the admittedly imperfect practice of directly inverting G^{-1} to obtain G may be of practical value.

Despite these promising results, there are limitations to the DGF technique. Because it is superposition-based, the DGF approach relies on the linearity of the energy equation. In many realistic environments, including turbomachinery flows, strict linearity is often violated due to extreme wall-to-mainstream temperature differences and viscous dissipation in high-speed flows, either of which may induce temperature-dependent property varia-

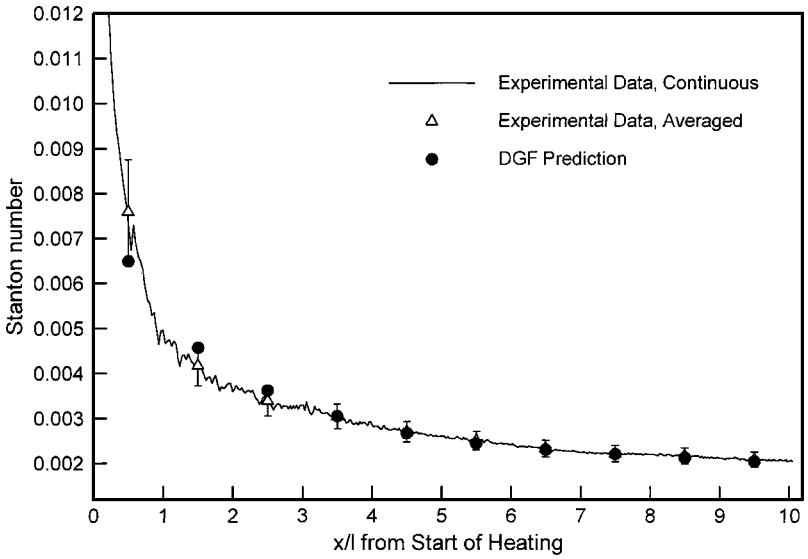

Fig. 12 DGF Stanton number prediction using the G^{-1} matrix

tions in the fluid. While such nonlinearities may be accounted for using simple property-ratio type corrections as suggested in Kays and Crawford [12], they do complicate the DGF representation. Further, as mentioned above, nonphysical oscillations can arise during direct inversion of the measured DGF matrix, due to discretization effects. Batchelder and Eaton [6] suggest one way to address this issue, by using a numerical technique to artificially increase the size of the DGF matrix and allow it more nearly represent the continuous heat transfer behavior. Another approach is to physically improve the spatial resolution through direct reduction of the DGF discretization size. However, as the size of the individual DGF elements decreases, the measurement uncertainty correspondingly increases as secondary heat loss terms become important. There exists, in this sense, the concept of an ''optimum'' DGF discretization size that strikes a balance between spatial resolution and measurement uncertainty.

Table 2 DGF uncertainties for Stanton number prediction

DGF Index	St_{pred} $\times 10^{-3}$	δSt_{pred} $\times 10^{-4}$	% Uncertainty
1	6.49	7.33	11.3
2	4.57	4.19	9.2
3	3.62	3.18	8.8
4	3.05	2.69	8.8
5	2.67	2.24	8.4
6	2.44	1.98	8.1
7	2.30	1.97	8.6
8	2.20	2.17	9.9
9	2.12	2.47	11.7
10	2.04	2.69	13.2

The principal advantage of the DGF technique is its applicability to a wide variety of thermal boundary conditions. As a test of the versatility of the DGF approach, the Stanton number distribution for a uniform surface temperature boundary condition was computed and is shown along with predictions for a uniform heat flux boundary condition in Fig. 14. The expectation that St should be consistently higher for the uniform heat flux boundary condition is confirmed. At all but the first DGF location, the uniform

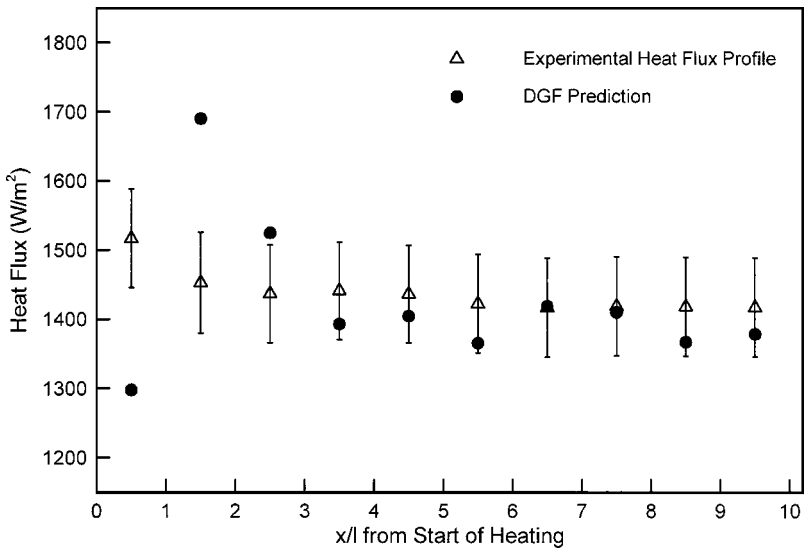

Fig. 13 DGF heat flux prediction using the G matrix

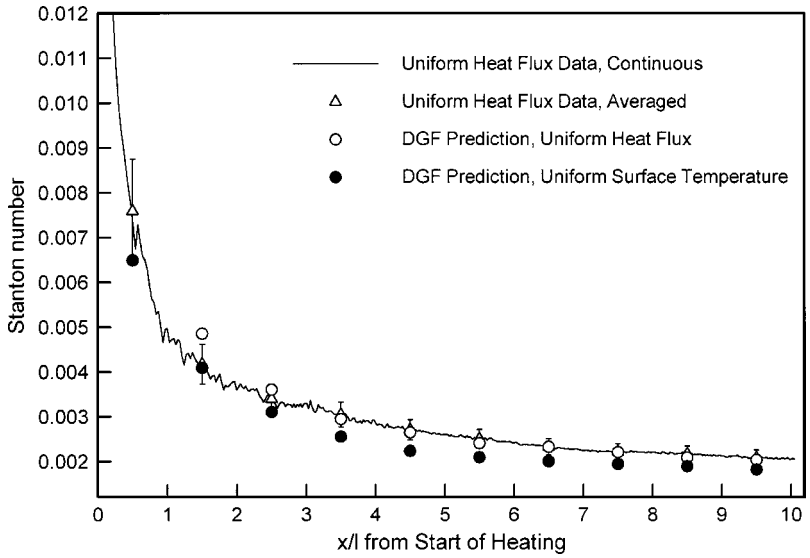

Fig. 14 DGF Stanton number prediction using the G matrix for two thermal boundary conditions

heat flux results are between 10% and 19% higher than the uniform surface temperature St values.

Conclusions and Future Prospects

The current experiments showed that DGF elements, covering only 30% of the area of the uniform heat flux surface, could be used reliably for thermal predictions for a uniform heat flux boundary condition. Beyond this relatively standard capability, the same DGF results could be used to determine the heat transfer for a thermal boundary condition of arbitrary complexity. It may be necessary to measure only the main diagonal and the first two or three off-diagonal terms of the DGF matrix, and extrapolate the remaining terms or perhaps use a correlation to scale them. The primary limitation for a well-resolved prediction is that the spatial variations in surface temperature or heat flux should not be appreciably smaller than the DGF discretization size. This may be a challenging task given the thin boundary layers and steep thermal gradients common to turbomachinery environments. Microfabrication techniques may play a prominent role in the development of future DGF surfaces for such applications.

It is probably easier, in a complex geometry, to develop a compact DGF device for measuring local heat transfer rather than constructing a uniform heat flux type of device covering the entire surface. By determining the local heat transfer characteristics through the DGF approach, the global temperature or heat flux distribution may be evaluated through interpolation or extrapolation of elements of the DGF matrix and/or through the use of correlations or scaling guidelines. Most importantly, DGF measurements have the significant advantage that they are applicable to any choice of discretized thermal boundary condition.

Realistic turbomachinery flows are inherently complex, featuring rotation effects and wakes from upstream stator or blade rows. In light of these conditions, extending the 1D DGF concept to a 2D formulation may prove worthwhile. Because the magnitude of the temperature rise for off-diagonal elements can be very small, it is important to design a surface capable of sustaining a large heat flux, so that ''overheating'' the main element to generate higher temperature signal evolves into standard practice for data acquisition. One of the challenges in producing a high-quality DGF surface remains the elimination of conduction losses in the substrate. The fact, however, that most turbomachinery flows are characterized by very high heat transfer rates makes such environments particularly suitable for future exploration of the DGF concept.

Acknowledgments

The authors gratefully acknowledge the financial support of General Electric Aircraft Engines (GEAE) through the University Strategic Alliance Program.

Nomenclature

C_p = Specific heat at constant pressure
δG^{-1} = Matrix of uncertainties for elements of G^{-1}
ΔT_i = Temperature rise relative to reference temperature on DGF element i
ΔT = Temperature rise
$\mathbf{\Delta T}$ = Temperature rise vector
ε = Emissivity
g_{ij} = Element of G matrix in ith row and jth column
g_{ij}^{-1} = Element of G^{-1} matrix in ith row and jth column
G = DGF matrix
G^{-1} = Inverse DGF matrix
h = Heat transfer coefficient, based on local heat flux and difference between freestream temperature and local surface temperature
l = DGF discretization length, streamwise direction
L = Length of DGF domain
N = Number of discrete elements on DGF domain
q_i' = Heat transfer rate per unit length on DGF element i
q_{ij}' = Heat transfer rate per unit length on DGF element i due to temperature rise on element j
$\mathbf{q}'$ = Heat transfer rate per unit length vector
q'' = Heat flux, or heat transfer rate per unit area
Q = Hue or hue angle
ρ = Local flow density
St = Stanton number$=h/\rho U_\infty C_p$
T_{surf} = Surface temperature
T_{ref} = Reference temperature
U_∞ = Local flow velocity
x = Coordinate in streamwise direction

References

[1] Sellars, J. R., Tribus, M., and Klein, J. S., 1956, ''Heat Transfer to Laminar Flow in a Round Tube or Flat Conduit—the Graetz Problem Extended,'' Trans. ASME, **78**, pp. 441–448.
[2] Reynolds, W. C., Kays, W. M., and Kline, S. J., 1958a, ''Heat Transfer in the

Turbulent Incompressible Boundary Layer—Step Wall-Temperature Boundary Conditions,'' NASA Memo 12-2-58W, Washington, D.C.
[3] Reynolds, W. C., Kays, W. M., and Kline, S. J., 1958b, ''Heat Transfer in the Turbulent Incompressible Boundary Layer—Arbitrary Wall Temperature and Heat Flux,'' NASA Memo 12-3-58W, Washington, D.C.
[4] Ortega, A., and Moffat, R. J., 1986, ''Experiments on Buoyancy-Induced Convection Heat Transfer From an Array of Cubical Elements on a Vertical Channel Wall,'' Technical Report No. HMT-38, Mechanical Engineering Department, Stanford University, Stanford, CA.
[5] Hacker, J. M., and Eaton, J. K., 1997, ''Measurements of Heat Transfer in a Separated and Reattaching Flow With Spatially Variable Thermal Boundary Conditions,'' Int. J. Heat Fluid Flow, **18**, pp. 131–141.
[6] Batchelder, K. A., and Eaton, J. K., 2001, ''Practical Experience With the Discrete Green's Function Approach to Convective Heat Transfer,'' ASME J. Heat Transfer, **123**, pp. 70–76.
[7] Batchelder, K. A., and Moffat, R. J., 1997, ''Towards a Method for Measuring Heat Transfer in Complex 3-D Flows,'' Technical Report No. TSD-108, Mechanical Engineering Department, Stanford University, Stanford, CA.
[8] Buck, F. A., and Prakash, C., 1995, ''Design and Evaluation of a Single Passage Test Model to Obtain Turbine Airfoil Film Cooling Effectiveness Data,'' ASME Paper No. 95-GT-19.
[9] Farina, D. J., Hacker, J. M., Moffat, R. J., and Eaton, J. K., 1994, ''Illuminant Invariant Calibration of Thermochromic Liquid Crystals,'' Exp. Therm. Fluid Sci., **9**, pp. 765–775.
[10] Kline, S. J., and McClintock, F. A., 1953, ''Describing Uncertainties in Single Sample Experiments,'' Mech. Eng. (Am. Soc. Mech. Eng.), **75**, pp. 3–8.
[11] Moffat, R. J., 1988, ''Describing the Uncertainties in Experimental Results,'' Exp. Therm. Fluid Sci., **1**, pp. 3–17.
[12] Kays, W. M., and Crawford, M. E., 1993, *Convective Heat and Mass Transfer*, 3rd ed., McGraw-Hill Book Co., NY.

Influence of Entrance Geometry on Heat Transfer in Rotating Rectangular Cooling Channels (AR=4:1) With Angled Ribs

Lesley M. Wright

Wen-Lung Fu

Je-Chin Han*

Turbine Heat Transfer Laboratory,
Department of Mechanical Engineering,
Texas A&M University,
College Station, TX 77843-3123

The effect of entrance geometry on the heat transfer in rotating, narrow rectangular cooling channels is investigated in this study. Both smooth channels and channels with angled ribs are considered with three different entrance conditions: fully developed, sudden contraction, and partial sudden contraction. The rectangular channel has as aspect ratio of 4:1, and it is oriented at 135° with respect to the plane of rotation. In the test section with angled ribs, the ribs are angled at 45° to the mainstream flow. The rib height-to-hydraulic diameter ratio (e/D_h) is 0.078, and the rib pitch-to-height ratio (P/e) is 10. The range of flow parameters includes Reynolds number ($Re=5000–40,000$), rotation number ($Ro=0.0–0.302$), and inlet coolant-to-wall density ratio ($\Delta\rho/\rho=0.12$). The heat transfer at the entrance of the heated portion of the smooth channel is significantly enhanced with the sudden contraction and partial sudden contraction entrances. In the smooth rotating channels, the effect of the entrance geometry is also present; however, as the rotation number increases, the effect of the entrance geometry decreases. It was also found in this study that the sudden and partial sudden contraction entrances provide higher heat transfer enhancement than the fully developed entrance through the first three to four hydraulic diameters of the channels with angled ribs. Again, the effect of the entrance geometry is greater in the stationary channels with angled ribs than the rotating channels with ribs. In both stationary and rotating channels, the influence of the entrance geometry on the heat transfer is more apparent in the smooth channels than in the ribbed channels. [DOI: 10.1115/1.1860564]

Introduction

There is an increasing demand for energy throughout the world, and to meet this increasing demand, the turbomachinery industry has been led to develop more efficient ways of generating power. One method of increasing the efficiency of these turbines is to increase the gas inlet temperature; however, by raising the gas temperature, the structural integrity of the turbine blades is compromised. In order for the blades to withstand the extremely high inlet temperatures, they must be manufactured from superior materials, have an excellent cooling design, or both. One method for cooling the blades is internal cooling. With internal blade cooling, a small amount of air is extracted from the compressor, and the air is injected into the blades. Through forced convection, the coolant air removes heat from the wall of the blade.

Numerous techniques have been employed to enhance the heat transfer within the internal cooling passages. The channel walls are typically lined with turbulence promoters to increase the heat transfer from the channel walls to the coolant. The cooling passages may utilize rib turbulators (trip strips), pin fins, or dimples to enhance the heat transfer. Rib turbulated cooling is commonly used in modern engines, and because ribs are widely used for heat transfer enhancement, many experimental investigations have been completed to examine the level of heat transfer enhancement in ribbed channels. To begin to understand the complexities of internal cooling in turbine blades, many experiments have been performed that model the internal cooling passages as stationary channels, and the interested reader is referred to *Gas Turbine and Cooling Technology* [1] for a comprehensive review of internal cooling. However, the flow field through a rotating channel exhibits different characteristics than the flow field through a stationary channel. This is due to the forces generated by rotation. These Coriolis and rotational buoyancy forces shift the peak velocity of the coolant toward the trailing surface of the blade. Therefore, the coolant is forced away from the leading surface (suction side) of the channel to the trailing surface (pressure side). Typically, under rotation, the trailing surface experiences heat transfer enhancement, while the leading surface experiences a reduction in heat transfer.

The duct orientation and aspect ratio also have an effect on the coolant flow through the channel. As shown in Fig. 1, as one moves from the mid-chord of the blade toward the trailing edge, the blade becomes thinner; therefore, cooling channels must become more narrow (the aspect ratio increases). Moving toward the trailing edge of the blade also alters the orientation angle (β) of the cooling channel. Moving from the mid-chord toward the trailing edge, the orientation angle (measured from the direction of rotation to the midpoint of the channel) increases. For narrow ducts with large orientation angles, the coolant is forced away from the leading and inner surfaces toward the trailing and outer surfaces of the channel during rotation. Figure 1 also shows the orientation of a 4:1 aspect ratio channel within the trailing edge of a turbine blade.

As the need for heat transfer data in rotating channels was realized, investigations shifted from nonrotating channels to rotating cooling channels. Investigations of rotating cooling channels provide turbine blade designers with heat transfer data that is more applicable to actual engine conditions. Johnson et al. [2,3] investigated the effect of buoyancy and Coriolis forces on the heat transfer coefficient in a square four-pass channel with 45° angled ribs. Dutta and Han [4] studied the regionally averaged heat transfer enhancement in two-pass smooth, rotating square channels, and two-pass rotating square channels with ribs; three different

Manuscript received October 27, 2003; revision received March 24, 2004. Review conducted by: P. M. Ligrani.

*Marcus Easterling Endowed Chair, jchan@mengr.tamu.edu

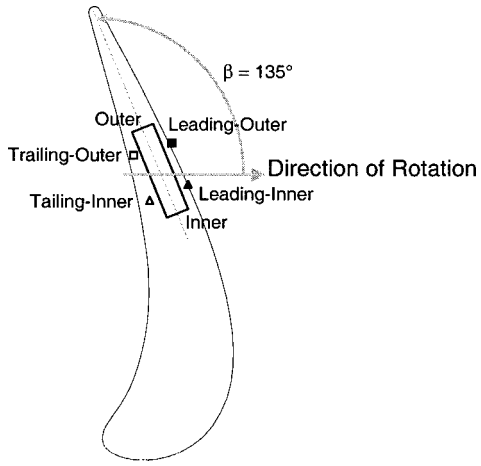

Fig. 1 Orientation of a narrow rectangular channel in a gas turbine blade

channel orientations were investigated in this study. Taslim et al. [5,6] also investigated the heat transfer distributions in square, rib-roughened rotating channels. All of these studies showed significant difference between the heat transfer coefficient on the leading surface and that on the trailing surface. However, the difference is dependent on the orientation of the channel with respect to rotation, and the blockage of the ribs.

As shown previously, cooling channels located in the trailing edge of the blade are typically very narrow. Therefore, it is necessary to study the heat transfer enhancement of cooling channels with large aspect ratios, rather than only square channels (AR =1:1). The effect of rotation on the heat transfer distribution in a rotating, rectangular (AR=2:1), two-pass channel with ribs was experimentally investigated by Azad et al. [7] and numerically simulated by Al-Qahtani et al. [8]. They showed the heat transfer coefficients decrease from the leading surface and increase from the trailing surface in the first pass of the channel. They also concluded that the effect of rotation is more apparent in the channel oriented at 90° than the channel oriented at 135° with respect to the direction of rotation.

Single-pass rectangular (AR=4:1) channels were studied by Griffith et al. [9] and Lee et al. [10]. Griffith et al. [9] concluded that this narrow rectangular passage creates more heat transfer enhancement than the smaller aspect ratio channels. They also found that significant spanwise variation is present across the width of the channel, and this variation is amplified by the use of angled ribs. Lee et al. [10] investigated six different rib configurations. They found in the rib-roughened channels all surfaces undergo heat transfer enhancement, which increases with rotation. They also confirmed the finding of Griffith et al. [9]: significant spanwise variation is present in the channels with angled ribs.

The cross section of the internal cooling passages is limited by the size and shape of the turbine blade. Just as the cross section of the cooling passages are adapted to fit the cross section of the blade, the length of the cooling channel must also be adapted to meet spatial limitations in the streamwise direction. In other words, the coolant used to internally cool the blade typically does not travel through a single, straight, constant diameter duct. The coolant could be forced to travel through any of a variety of entrance sections, within the dovetail of the blade, before entering the actual cooling channel. Rather than flow being developed upon entering the blade (as in the studies listed above), in most cases the flow must develop both thermally and hydrodynamically within the turbine blade.

A number of studies have investigated the developing flow in various channels. Studies have involved the development of both the thermal and hydrodynamic boundary layers in smooth channels and channels with various rib configurations. However, the studies that involve the entrance effect within cooling channels with rib turbulators are limited to flow through a sudden contraction. Furthermore, all the previous studies of developing flow have a common tie: the effect of the entrance geometry is investigated for nonrotating cooling channels.

Kays and Crawford [11] summarized and presented the work of Boelter et al. [12] regarding developing flow. In this study, the heat transfer within a nonrotating circular tube was measured for various entrance configurations. The entrance length of the heated circular tube is dependent upon the selected entrance geometry. The local Nusselt number ratio for flow through bends or an abrupt contraction is substantially greater than hydrodynamically fully developed flow. The effect of the entrance also has as a substantial effect on the mean Nusselt number ratio in the smooth channels. The mean Nusselt number ratio for flow through the abrupt contraction can be six percent greater than fully developed flow; this increase is primarily attributed to the entrance of the channel, where both the thermal and hydrodynamic boundary layers are developing.

Burggraf [13] investigated the effect of entrance flow on the heat transfer in both nonrotating smooth square channels and square channels with rib turbulators oriented 90° to the mainstream flow. The entrance geometries of this study consisted of a long unheated duct that allowed the flow to hydrodynamically develop before entering the heat test section, a short entrance duct (which is similar to a contraction), and a 180° turn positioned immediately upstream of the heated test section. These results showed the heat transfer distributions in the channel with a long entrance and a channel with a short entrance follow the same trends. The heat transfer coefficients (for both cases) are elevated at the cooling channel entrance, and the coefficients decrease to the fully developed value, which is achieved approximately 3.3 hydraulic diameters downstream of the start of the heated test section. His results also showed that the heat transfer coefficients in the channel with the short entrance are approximately 5% greater than those of the long entrance. However, the heat transfer coefficients at the entrance of the channel with the bend can be up to 38% greater than those of the long entrance. This study also showed the heat transfer coefficients within the channel with the bend were always greater than those of the long channel. The results also show as the Reynolds number increases, the difference between the long entrance and the other two entrances decreases.

Han and Park [14] investigated developing heat transfer in nonrotating rectangular channels. In this study, a variety of rib configurations and channel cross sections were studied. The coolant flowed through a plenum and into the rectangular test section. The plenum was sufficiently larger than the test section, so the fluid was forced through a contraction and into the test section. From this study they found that in a stationary rectangular (AR=4:1) channel with angled ribs, the Nusselt number decreases in the streamwise direction from the sharp entrance but increases again at $x/D_h \approx 3$ because of the secondary flow induced by the rib angle. The Nusselt number then remains relatively constant throughout the remaining length of the channel.

Liou and Hwang [15] also investigated the effect of entrance geometry in nonrotating rectangular channels with rib turbulators. They found for ribbed channels the first 12%–18% of the channel is affected by the abrupt contraction. From this study, they also developed a correlation for developing flows in a ribbed channel with an abrupt contraction. This correlation is independent of the Reynolds number and the rib pitch-to-height ratio.

Park et al. [16] investigated the heat transfer performance of various rib configurations in nonrotating rectangular cooling channels; five different aspect ratio channels were studied with a variety of rib orientations for each channel. The coolant was forced through a contraction before entering the heated test section. The Nusselt number ratio gradually decreases in the entrance portion

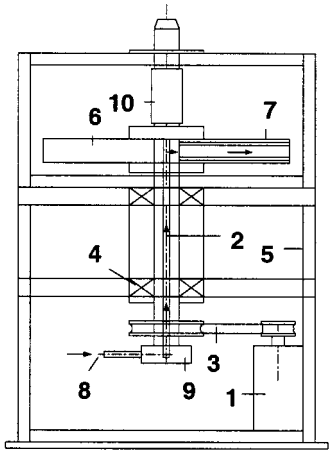

1- Variable Speed Electric Motor
2- Hollow Rotating Shaft
3- Belt-Driven Gear System
4- Bearing Support System
5- Steel Work Table
6 - Rotating Arm
7 - Test Section
8 - Compressor Air
9 - Rotary Seal
10 - Slip Ring Assembly

Fig. 2 Rotating test facility

of the heated test section. In the rib-roughened channels, the ratio becomes fully developed approximately two diameters downstream of the entrance.

Each of the above-mentioned studies focuses on the entrance effect within nonrotating channels. However, in the present study we explore the effect of entrance geometry on the regionally averaged heat transfer coefficients in rotating, narrow rectangular channels. The varying entrance geometry is applied to both smooth channels and channels with angled ribs. The effect of three different entrance conditions on the regionally averaged heat transfer is investigated, i.e., flow that is fully developed, flow through a sudden contraction, and flow through a sudden partial contraction. The latter two cases present entrance conditions that are close to the actual turbine blade cooling channel configurations. Therefore, the results will be useful for the design of the actual internal cooling passages of the blade. In the study we address the spanwise heat transfer variation on both the leading and trailing surfaces, as well as the streamwise variation due to the varied entrance geometry and the angled ribs.

Experimental Facility

The experimental test rig used for this study was previously used by Lee et al. [10] and is shown in Fig. 2. A gear attached to the shaft of a variable frequency motor is connected to a gear located at the base of a hollow shaft via a timing belt, so the variable frequency motor is used to rotate the hollow shaft. The hollow shaft extends from the base of the test rig to the work platform. A hollow rotating arm is attached orthogonal to the rotating shaft; the test section is inserted into this rotating arm. Thermocouple and heater wires are connected to a 100-channel slip ring assembly that is mounted to the rotating shaft. The thermocouple output is monitored using commercially available software. The temperature data is displayed using the virtual instrument format, and the data is written to a data file specified by the user. Power is supplied through the slip ring to the heaters using variable transformers. Cooling air is pumped to the test rig using a steady flow air compressor. The air flows through an ASME square-edge orifice meter, upward through the hollow rotating shaft, around a 90° bend, through two mesh screens, and into the rotating arm and test section. After flowing through the test section, the air is expelled to the atmosphere.

The test section is a one-pass rectangular channel. The ratio of mean rotating arm radius-to-channel hydraulic diameter ($\bar{R}/D_h$) is 33.0 for the 4:1 channel. Likewise, the heated channel length-to-hydraulic diameter ratio (L/D_h) is 7.5. The air flows radially outward from the axis of rotation through the test section. Figure 3 shows a schematic of the test section used in the present study. The test section consists of the leading, trailing, inner, and outer surfaces. The inner and outer surfaces each consist of six plates in the streamwise direction. The leading and trailing surfaces each consist of 12 plates. The cross section of the test section contains two plates for the leading surface, two plates for the trailing surface, one plate for the inner surface, and one plate for the outer surface. A total of 36 copper plates make-up the entire test section. Each plate is 0.9375 in.×0.9375 in. (2.38 cm×2.38 cm) and is surrounded by a 0.0625 in. (0.159 cm) strip of nylon to prevent conduction between the plates. This method provides a grid for an analysis of the spanwise as well as the streamwise variation in the regionally averaged heat transfer coefficients. In order to maintain approximately the same circumferential wall temperature the power supplied to the heaters is varied. While maintaining the same temperature at two adjacent copper plates, the net heat flux can vary by 45%. Therefore, the nylon strip is effectively limiting the conduction between adjacent copper plates.

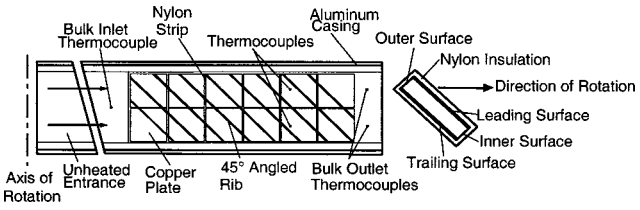

Fig. 3 Schematic of the heated portion of the 4:1 test section

Each 0.125 in. (0.318 cm) thick copper plate has a 0.0625 in. (0.159 cm) deep blind hole drilled in its backside. The temperature of each copper plate is measured using a 36 gauge, type T thermocouple. The thermocouple is secured in the blind hole using thermally conducting glue. With this setup, the thermocouple junction is located 0.0625 in. (0.159 cm) from the surface of the copper plate.

A nylon substrate serves as the support for the test section; each of the copper plates is mounted into this substrate. The nylon substrate forms a 3.25 in. (8.26 cm) diameter cylinder, and this test section is placed inside the aluminum, rotating arm of the test rig (Fig. 2). Flexible heaters are installed beneath the leading and trailing surfaces, two for each surface. Thermal conducting paste is applied between the heater and copper plates to minimize contact resistance and promote heat transfer from the heater to the plates. The leading and trailing surfaces of the cooling channels of actual blades see the greatest heat loads. Because the heat transfer from the inner and outer surfaces is much less than the contribution of the leading and trailing surfaces, in the present study, the inner and outer wall (sidewalls) were left unheated.

Angled ribs are widely used as turbulence promoters within the cooling channels of turbine airfoils. Therefore, the rib configuration of the present study is parallel, 45° angled ribs. The rib turbulators are placed on both the leading and trailing surfaces of the channel; the sidewalls remain smooth. This configuration results in a rib height-to-hydraulic diameter ratio (e/D_h) of 0.078 and a pitch-to-rib ratio (P/e) of 10, and the rib orientation angle is maintained at 45°. The ribs are made of brass, and they are glued to the copper plates of the leading and trailing surfaces. The thickness of the glue is less than 0.01 cm and creates negligible thermal resistance between the ribs and the copper plates.

Figure 4 shows the three entrance geometries investigated in this study. Figure 4(*a*) shows the case of fully developed flow. For the fully developed case the cross section of the entrance section is identical to that of the heated test section, and the entrance duct is 11.25 hydraulic diameters in length. Figure 4(*b*) shows a channel in which the fluid is forced through a sudden contraction. As shown in this figure, the height of the entrance duct is three times

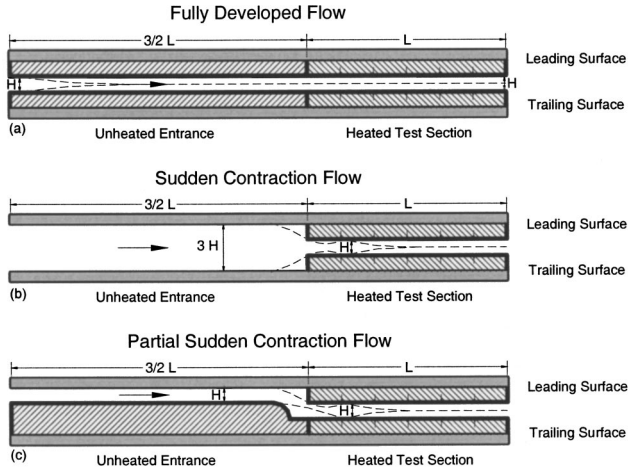

Fig. 4 Cross-sectional view of the various entrance configurations

greater than that of the heated test section. Therefore, the coolant is forced through the sudden contraction into the heated test section. Figure 4(*c*) shows the cross section of a channel that contains a partial sudden contraction. In this case, the cross section of the entrance duct is identical to the heated test section. However, the entrance duct does not allow the coolant to flow directly into the heated test section; the coolant is redirected just before entering the heated test section. As with the fully developed case, the entrance duct of the latter two cases is 11.25 hydraulic diameters long. The entry of the channel is altered using pieces of nylon, which can be moved to create various entry scenarios (only the entrances of the leading and trailing surfaces are altered to create the various entrances).

The test section is oriented at 135° from the direction of rotation. The experiments are conducted at Reynolds numbers (based on the hydraulic diameter) of 5000, 10,000, 20,000, and 40,000. For the rotation cases, the rotation speed remains constant at 550 rpm. This combination of Reynolds number and constant angular velocity results in the rotation number (Ro) varying from 0.037–0.302, which are applicable to aircraft engines. Constant heat flux is supplied to the test section by each of the heaters. The maximum wall temperature is maintained at approximately 70°C, and the inlet coolant temperature is approximately 29°C, yielding an inlet coolant-to-wall density ratio ($\Delta\rho/\rho$) of approximately 0.12 for all cases.

Data Reduction

Our purpose in this investigation is to study the regionally averaged heat transfer coefficient at various locations within the narrow rotating duct. The heat transfer coefficient is determined by the net heat transferred from the heated plate, the surface area of the plate, the regionally averaged temperature of the plate, and the local bulk mean temperature in the channel. Therefore, the heat transfer coefficient is given as

$$h = \frac{Q_{\text{net}}/A}{(T_w - T_{b,x})}. \tag{1}$$

The net heat transfer is calculated using the measured voltage and current supplied to each heater from the variac transformers multiplied by the area fraction of the heater exposed to the respective plate minus the external heat losses escaping from the test section. The heat losses are predetermined by performing a heat loss calibration for both the rotational and stationary experiments. The heat loss calibration is performed by inserting insulation into the channel to eliminate natural convection. During the calibration, the heat transfer (in the form of power from the variac transformers) and wall temperature of each plate are measured. Two sets of heat loss data are obtained for each point, so the wall temperature measured during the actual heat transfer experiment is between the two wall temperatures measured in the calibration. Using linear interpolation and the conservation of energy principle, it is possible to know how much heat is being lost to the environment at each location in the channel. At a Reynolds number of 5000, heat losses account for 25% of the heat put into the test section. However, at the highest Reynolds number of 40,000, just less than 10% of the heat input is lost by conduction through the test section.

To express the heat transfer enhancement over a smooth channel, the surface area used in this study is the projected surface area of the channel (i.e., the surface area of a smooth channel); the area increase of 24% due to the ribs is neglected. The regionally averaged wall temperature (T_w) is directly measured using the thermocouple installed in the blind hole on the backside of each copper plate. Because the plates are made of copper, which has a high thermal conductivity, the temperature of each plate is assumed uniform. Linear interpolation is used to determine the local bulk temperature. One thermocouple at the inlet and two thermocouples at the outlet of the test section measure the inlet and outlet bulk temperatures, respectively. At a Reynolds number of 5000, the average rise in the bulk coolant temperature is 26% from the inlet to the exit, and at Re=40,000, the rise is approximately 15%. Therefore, the bulk temperature at any location in the test section can be calculated using linear interpolation. The results presented from this study are based on the linear interpolation method. However, the local bulk temperature can also be calculated using the conservation of energy principle. For the present study, both methods compare very well. The energy balance equation is

$$T_{b,x} = T_{\text{in}} + \sum_i (Q - Q_{\text{loss}})/\dot{m}c_p, \quad x = 1,2,\ldots,6. \tag{2}$$

The Dittus-Boelter/McAdams correlation for heating ($T_w > T_{b,x}$) is used in this study to provide a basis of comparison. The Dittus-Boelter/McAdams correlation is used to calculate the Nusselt number for fully developed turbulent flow through a smooth stationary circular tube. Therefore, the Nusselt number ratio is given as

$$\frac{\text{Nu}}{\text{Nu}_0} = \frac{hD_h}{k}\frac{1}{0.023\,\text{Re}^{0.8}\,\text{Pr}^{0.4}}. \tag{3}$$

All air properties are taken based on the bulk air temperature with a Prandtl number (Pr) for air of 0.71.

The experimental uncertainty for the presented results was calculated using the method developed and published by Kline and McClintock [17]. The estimated uncertainty in the temperature measurements is 0.5°C for all cases. At the Reynolds number of 5000, where the most uncertainty exists in the measured quantities, the overall uncertainty in the Nusselt number ratio is approximately 23% of the presented values. At this lowest Reynolds number, a greater percentage of the heat input is lost (25%). Due to the estimation of these heat losses, the experimental uncertainty increases. However, at the higher Reynolds numbers, the percent uncertainty of the individual measurements decreases and the percentage of heat losses decreases (10%). Therefore, the overall uncertainty in the Nusselt number ratio decreases to approximately 11% of the calculated value at the highest Reynolds number of 40,000.

Results and Discussion

The legend for the present channel is shown in Fig. 1. The inner surface is the surface located closest to the mid-chord of the blade, and the outer surface is the surface located closest to the trailing edge of the blade. The leading and trailing surfaces are each subdivided into two surfaces. The leading surface is divided into the

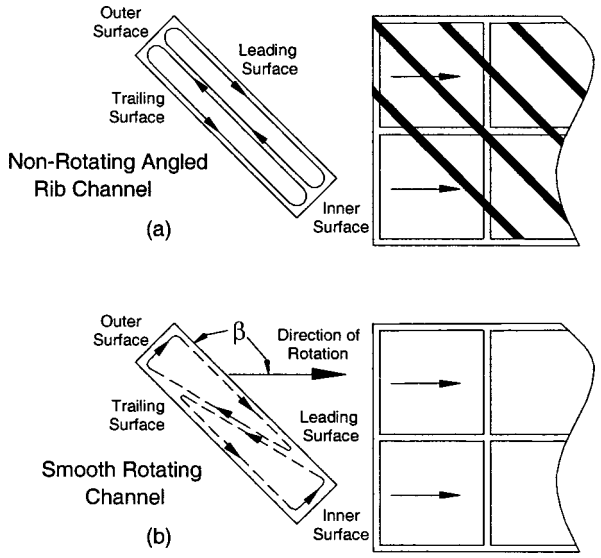

Fig. 5 Flow conceptualization: (*a*) secondary flow induced by 45° angled ribs; and (*b*) vortices induced by rotation in a narrow, rectangular channel

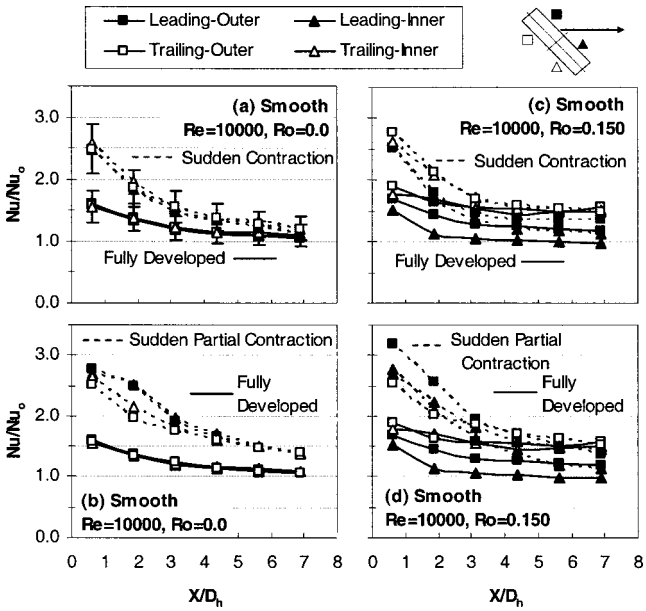

Fig. 6 Nusselt number ratios in smooth channels with Re =10,000

leading-inner surface and the leading-outer surface, and the same is done for the trailing surface. As stated previously, the inner and outer surfaces were left unheated.

Secondary Flow Behavior. Figure 5 shows conceptual views of the secondary flow behavior within the cooling channel. As shown in Fig. 5(*a*), the secondary flow induced by the 45° angled ribs, in the fully developed channel, moves parallel to the ribs from the outer surface to the inner surface and returns back to the outer surface. Thus, the angled ribs create two counter-rotating vortices rotating parallel to the angled ribs in the cross section of the channel. As the coolant travels along the rib, it gradually becomes warmer. Therefore, the heat transfer enhancement for the leading and trailing-outer surfaces is expected to be greater than the leading and trailing-inner surfaces.

The Coriolis and buoyancy forces, induced by the rotation, affect the flow through a rotating channel. Two counter-rotating vortices are created in a rotating channel, as shown in Fig. 5(*b*). The vortices are created as a result of the coolant being forced from the leading-inner corner to the trailing-outer corner. The trailing surfaces experience enhanced heat transfer as the coolant is forced to the trailing side of the channel, and the trailing-outer surface typically experiences the greatest enhancement. However, due to the rectangular channel and orientation angle, the leading surface should also experience heat transfer enhancement.

For the channel shown in Fig. 4(*a*), the flow is hydrodynamically developed when it enters the heated portion of the test section, and the dashed line shown in this figure represents the hydrodynamic boundary layer. Therefore, only the thermal boundary layer develops within the heated test section. However, for flow through a sudden contraction and flow through a partial sudden contraction, both the thermal and hydrodynamic boundary layers are developing in the heated test section.

As the coolant is forced through the sudden contraction, flow separation occurs at the entrance of the heated test section; this separation is associated with the vena contracta that occurs just downstream of the sharp entrance. Therefore, at the entrance of the heated test section, the turbulence intensity of the flow increases due to the area of separation and flow recirculation. With the increased turbulence, the heat transfer will also increase. Also associated with the flow separation and reattachment is development of the boundary layer. After the flow separates and reattaches past the vena contracta, the boundary layer develops and begins to grow. Therefore, the boundary layer at the beginning of this heated test section is much thinner than the boundary layer of the fully developed channel (the boundary layer extends to the middle of the channel). The development of the hydrodynamic boundary layer is represented in Fig. 4(*b*) by the dashed line. The thinner boundary layer results in greater heat transfer from the channel walls. Downstream when the flow becomes developed, the heat transfer trends are expected to be similar to those of the fully developed flow.

As the coolant travels through the partial sudden contraction, areas of separation and recirculation form. The phenomenon occurring along the upper (leading) surface is similar to that of the sudden contraction. The flow separates as it passes the sharp entrance into the heated test section. Again, there is the area of recirculation associated with the vena contracta downstream of the entrance. On the trailing surface, the flow advances down a rounded step before entering the heated test section. The flow also separates as it passes over the step. Therefore, on the trailing surface an area of flow separation and recirculation exists. As with the sudden contraction entrance geometry, the turbulence at the beginning of the heated test section is increased, and associated with the increased turbulence is an increase in the heat transferred from the channel walls. As with the flow through the sudden contraction, the boundary layer begins to develop and grow just inside the heated test section. In this developing region, the boundary layer is relatively thin [as represented by the dashed line in Fig. 4(*c*)], and there is more heat transferred from the walls.

Within the stationary channels, the turbulent mixing is increased by both the rib turbulators, as well as the various entrance geometries. Therefore, it is expected that the varied entrance geometries will increase the heat transfer at the entrance of the channel. In the rotating channels with angled ribs, there is an increased turbulence due to the ribs, the entrance geometry, and rotation. Therefore, it is conjectured that the effect of the various entrance geometries will be less significant in the rotating channel than in the stationary channel.

Smooth Channel Results. Figure 6 contains the stationary Nusselt number ratio results for the smooth channel with varying entrance geometry. The solid lines represent the data for the fully developed flow, and the dashed lines represent the data for flow through the sudden contraction or partial sudden contraction. Both

nonrotating and rotating experiments are shown for Re=10 000, with Ro=0.150 for the rotating channels. Figures 6(*a*) and 6(*b*) show the Nusselt number ratio for stationary channels, and Figs. 6(*c*) and 6(*d*) show the results for the rotation channels.

Figure 6(*a*) shows the heat transfer enhancement for the fully developed entrance geometry and the sudden contraction entrance geometry applied to the smooth channel. As shown by the solid lines in the figure, the Nusselt number ratio for the smooth channel with the fully developed entrance approaches a thermally developed value of unity. The values at the entrance of the channel are elevated above the value of one due to the development of the thermal boundary layer. The dashed lines in Fig. 6(*a*) show the Nusselt number ratios for flow through the sudden contraction. As clearly seen in this figure, the ratios at the entrance of the heated test section are elevated above those within the fully developed channel. Due to the contraction, both the hydrodynamic and thermal boundary layers are developing at the beginning of this channel. With this relatively thin boundary layer, the heat transfer is enhanced above that in the fully developed channel. At the Reynolds numbers greater than 10,000, the entrance condition has less of an impact on the downstream heat transfer enhancement.

Figure 6(*b*) compares the heat transfer enhancement of the fully developed flow to that of flow through a partial sudden contraction. Similar to the sudden contraction, at the entrance of the channel, the Nusselt number ratios are elevated above those of fully developed flow. The heat transfer coefficients are also elevated above those of the sudden contraction geometry (Fig. 6(*a*)). However, for this geometry all surfaces do not exhibit the same level of enhancement; at the entrance of the channel, the leading surfaces are enhanced more than the trailing surfaces. This is due to the nonsymmetrical entrance condition (as shown in Fig. 4). With the high Nusselt number ratios at the entrance, the Nusselt number ratios for flow through this partial sudden contraction do not reach the fully developed value of unity. As the Reynolds number increases, the trends begin to approach one, but they remain greater than one. Therefore, this nonsymmetrical partial sudden contraction has a more significant impact on the heat transfer throughout the entire channel than the sudden contraction entrance.

As shown in Fig. 6(*c*), the general trends of the data for the smooth, rotating channel are the same as for the stationary cases. However, there exists spanwise variation, and as one may anticipate, the surface that undergoes the least enhancement is the leading-inner surface. As explained previously, this is due to the rotation-induced vortices that shift the coolant away from the leading-inner corner to the trailing-outer corner of the channel. As the rotation number decreases (Reynolds number increases), rotation has less of an effect on the coolant flow through the channel. At the highest Reynolds number of 40,000 (Ro=0.038), the spanwise variation is very small, and the flow in the smooth rotating channel exhibits the same trend as the flow in the smooth stationary channel: a gradual decrease until the fully developed value of unity is achieved.

Also shown in Fig. 6(*c*) are the Nusselt number ratios for the flow through the sudden contraction. As with the stationary channel, the Nusselt number ratio of the first point for all surfaces is elevated above the fully developed values. Spanwise variation is also present in this channel; however, it is clear that the amount of variation is less than that in the fully developed channel.

Figure 6(*d*) shows a similar trend as Fig. 6(*c*). The heat transfer from the channel walls is elevated above the enhancement created with the fully developed geometry. From the stationary results it was shown that the leading surfaces underwent more enhancement than the trailing surfaces. This is trend is also apparent at the entrance of these rotating channels. As one moves downstream, the effect of rotation is more pronounced as there is more enhancement from the trailing surfaces than the leading surfaces.

Figure 7 compares data from the current study to that of Boelter et al. [12] as presented by Kays and Crawford [11]. This data

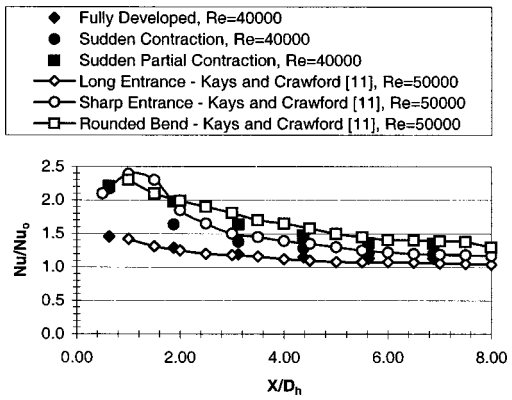

Fig. 7 Nusselt number ratio comparison of smooth channels with varied entrances

from Kays and Crawford [12] corresponds to a Reynolds number of 50,000, and from this present study, a Reynolds number of 40,000 is shown. The results from the present study for the fully developed, sudden contraction, and partial sudden contraction are compared to flow through a long entrance, sharp entrance, and rounded bend, respectively. The Nusselt number ratios for fully developed flow follow the results from the previous study along the entire length of the channel. For flow through a sudden contraction, the Nusselt number ratio is slightly less than ratios for flow through the sharp entrance. Because in the present study we focus on the regionally averaged heat transfer, the detailed distribution of the increase then decrease within in the channel is not captured. Overall, throughout the channel, in the present study we follow the same trend as the well-known literature. Similar to the sudden contraction, the values for the sudden partial contraction are less than those of the rounded bend. However, the values are comparable to those of the accepted literature.

Angled Rib Channel Results. Figure 8 contains the stationary Nusselt number ratio results for the channels with angled ribs and varying entrance geometry. Figure 8(*a*) shows the heat transfer enhancement for the fully developed entrance geometry and the sudden contraction entrance geometry. For the present angled

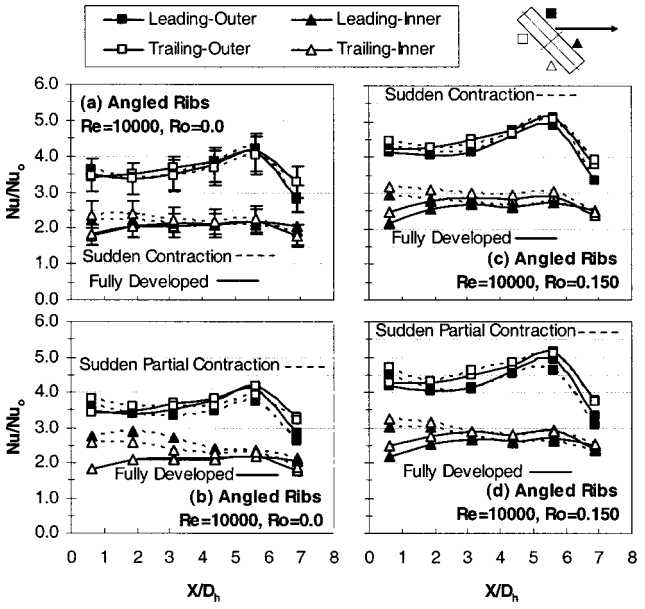

Fig. 8 Nusselt number ratios in angled rib channels with Re =10,000

rib configuration, the leading-outer and trailing-outer surfaces undergo significantly higher heat transfer enhancement than the leading and trailing-inner surfaces. With this 45° angled rib geometry, the first interaction between the rib and the coolant occurs on the leading- and trailing-outer surfaces, near the corner of the channel. When the coolant contacts the rib, the hydrodynamic boundary layer of the fluid is tripped, and the coolant near the surface is forced to traverse along the length of the rib from the outer surface toward the inner surface. As the coolant follows the rib, the secondary fluid velocity is decreasing. More heat is convected away from the channel along the leading- and trailing-outer walls due to the increased secondary flow velocity of the coolant and relatively thin boundary layer. As the velocity decreases (and the boundary layer grows thicker), less heat is convected from the surface, and thus the leading- and trailing-inner surfaces undergo less heat transfer enhancement than the leading- and trailing-outer surfaces. Also, as the coolant travels along the length of the rib turbulators, there is a rise in the coolant temperature. Therefore, the heat transfer enhancement is greatest along the leading- and trailing-outer surfaces where the coolant temperature is the lowest. As the coolant temperature rises along the length of the rib, less heat is transferred from the hot leading- and trailing-inner surfaces to the relatively warm coolant.

The Nusselt number ratios continue to increase until approximately 4.5 hydraulic diameters downstream of the entrance, as the rib induced secondary flow gains strength. As the Reynolds number increases, the effectiveness of the ribs decreases. From the Dittus–Boelter correlation, the Nusselt number (Nu_0) increases as the Reynolds number increases, and this results in a decrease in the Nusselt number ratio. Also as the Reynolds number increases, the Nusselt number ratio difference between the outer surfaces (leading and trailing) and inner surfaces (leading and trailing) decreases.

As also shown in Fig. 8(*a*), fully developed flow and flow through a sudden contraction undergo relatively the same amount of heat transfer enhancement for the majority of the channel. The difference in the two channels occurs at the beginning of the channel. As with the smooth stationary channel, the Nusselt number ratios of the sudden contraction begin to converge to the ratios of the fully developed channel. For this angled rib case, the values of the sudden contraction converge to the fully developed values at approximately two hydraulic diameters; in the smooth channel, at least five hydraulic diameters are required for sudden contraction values to meet the fully developed values.

Figure 8(*b*) shows a similar trend as Fig. 8(*a*). However, the entry length for flow through a sudden partial contraction is much longer than flow through a sudden contraction. As shown in Fig. 8(*b*), the flow through the partial sudden contraction requires almost two-thirds of the channel to reach the Nusselt number ratio of the fully developed flow (leading-inner and trailing-inner surfaces); this is unlike the smooth channel, where the ratios of the partial sudden contraction never decrease to the fully developed values. In addition, the heat transfer enhancement in the entrance of the channel is increased by as much as 52% (on the leading- and trailing-inner surfaces) when compared to the fully developed channel. As the Reynolds number increases the effect of the entrance geometry decreases. With the increasing Reynolds number, the flow becomes more turbulent, therefore the additional effect created by the entrance geometry has less of an impact on the flow.

Figures 8(*c*) and 8(*d*) show the rotational Nusselt number ratio results for the channels with angled ribs and varying entrance geometry. As shown in Fig. 8(*c*), the heat transfer distributions in the rotating channel with fully developed flow are similar to those of the stationary channel (Fig. 8(*a*)). When the Nusselt number ratios are compared to those of the stationary channel (Fig. 8(*a*)), it can be seen that all surfaces in the rotating channel undergo heat transfer enhancement. As shown in Fig. 5, the vortices induced by rotation circulate in the same direction as those induced by the angled ribs. Therefore, rotation strengthens the secondary flow, and thus all surfaces experience heat transfer enhancement when compared to the stationary channel. As the Reynolds number increases, rotation number decreases, the heat transfer enhancement decreases, and there is less variation between the surfaces.

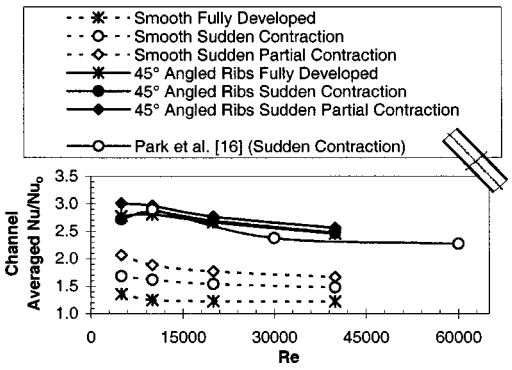

Fig. 9 Channel-averaged nusselt number ratio for stationary cases

Also shown in Fig. 8(*c*) are the Nusselt number ratios for the flow through the sudden contraction. The values for flow through the contraction are slightly elevated above the ratios for the fully developed flow. The ribs induce counter-rotating vortices that increase the mixing of the coolant. Rotation also induces counter-rotating vortices, which strengthen the rib-induced vortices, and more mixing occurs. Therefore, the effect of any additional mixing introduced by the varied entrance geometry has a decreased effect on the heat transfer enhancement in the rotating channel.

Figure 8(*d*) shows a similar trend as Fig. 8(*b*). The heat transfer from the channel walls is elevated above the enhancement created with the fully developed geometry. However, the difference between the fully developed flow and the flow through a partial sudden contraction is less in the rotating channel than in the stationary channel. In the rotating channel, the maximum variation is 40% along the leading- and trailing-inner surfaces, compared to a difference of 52% from the stationary channel. Again, rotation induces more turbulent mixing in the channel, so the additional turbulence created by the varying entrance geometry has less of an effect in the rotating channel.

Figure 9 shows the channel-averaged Nusselt number ratios for the smooth and angled rib stationary channels with the given entrance geometries. This figure clearly shows for the smooth channels, the greatest channel enhancement occurs in the channel with the partial sudden contraction entrance, and this is followed by the sudden contraction entrance. The fully developed values are elevated above the ratio of one due to the entrance region of the channel where the thermal boundary is developing. Although the channels with the sudden contraction and partial sudden contraction approach values of one (Figs. 6(*a*) and 6(*b*)), the ratios at the entrance of these channels are much greater than those for the fully developed channel. Therefore, the averages are significantly greater than the fully developed channel.

As also shown in this figure, over the specified range of Reynolds numbers, the angled rib channel with the partial sudden contraction experiences greater heat transfer enhancement than the other ribbed channels. As the Reynolds number increases, the difference between the three geometries decreases. At a Reynolds number of 5000, the difference between the partial sudden contraction and the fully developed case is approximately 9%, and at the Reynolds number of 40,000, the difference is only 4%.

Figure 9 also compares the stationary results of the present study to those of the previous study by Park et al. [16]. This previous study involved flow through an abrupt contraction with various rib configurations. The curve shown in this figure is for 45° angled ribs with a height-to-hydraulic diameter ratio (e/D_h)

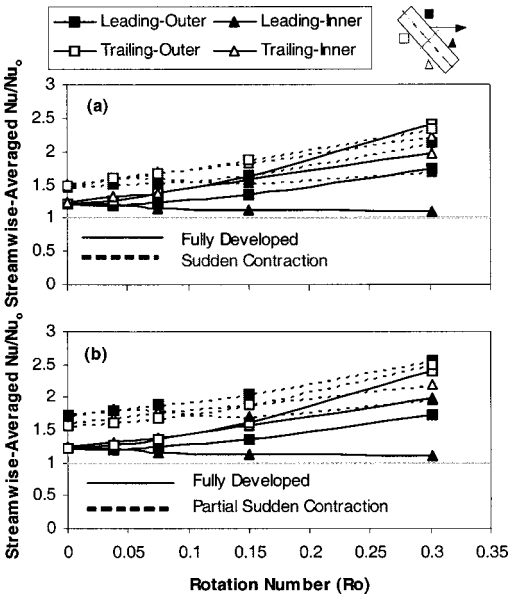

Fig. 10 Streamwise-averaged Nusselt number ratios in smooth channels

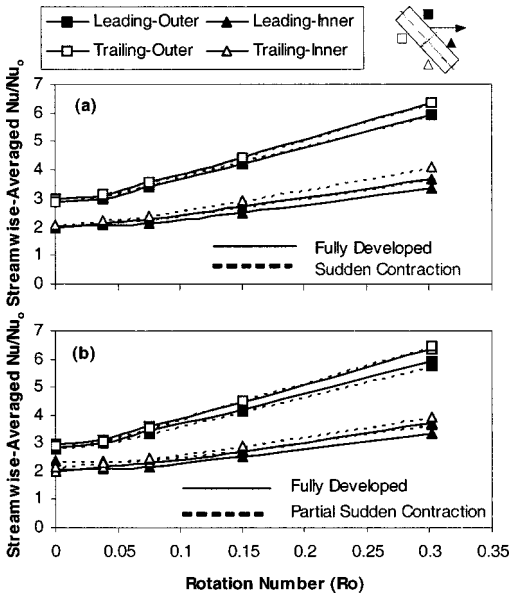

Fig. 11 Streamwise-averaged Nusselt number ratios in angled rib channels

of 0.078 and a pitch-to-rib ratio (P/e) of 10, and the channel aspect ratio is 4:1. At the lower Reynolds numbers, almost no difference exists between the present and previous studies (less than 1% difference). However, as a Reynolds number increases, the trends of the two studies show variation. Although the present study does not directly involve a Reynolds number of 30,000, the data trends show a variation of approximately 8% between the present and previous studies (which is within the experimental uncertainties of the two investigations). Again, from the data trends, as the Reynolds numbers continue to increase past 30,000, the variation between the two studies decreases. Therefore, the stationary results of the present study are comparable to previous studies involving similar channel geometry.

Streamwise-Averaged Results. Figure 10 shows the streamwise-averaged Nusselt number ratios in the smooth channel for fully developed flow, flow through a sudden contraction, and flow through a sudden partial contraction. The solid lines represent fully developed flow, and the dashed lines represent flow through a sudden contraction and flow through a sudden partial contraction in Figs. 10(a) and 10(b), respectively. The results shown in Fig. 10(a) clearly indicate that the coolant is being forced away from the leading-inner surface toward the trailing-outer surface. Due to the channel orientation and aspect ratio, the trailing-outer, trailing-inner, and leading-outer surfaces experience heat transfer enhancement and the leading-inner surface experiences a declination in the heat transfer with the increasing effect of rotation. The spanwise variation is also clearly seen in this figure. As the rotation number continues to increase the separation between the surfaces increases. The greatest enhancement due to rotation occurs on the trailing-outer surface, followed by the trailing-inner, and leading-outer, respectively.

Figure 10(a) also shows the difference between the fully developed flow and the flow through a sudden contraction. At the lower rotation numbers, the entrance condition is the dominant factor in determining the level of heat transfer enhancement; all surfaces in the channel with the contraction are greater than those of the fully developed channel. However, as the rotation number increases, the surfaces in the fully developed channel are affected more than the surfaces in the channel with the contraction. As with the fully developed channel, all surfaces undergo enhancement with the addition of rotation, but the enhancement due to rotation is less in the channel in the sudden contraction than the fully developed channel.

Figure 10(b) shows interesting trends for enhancement in the channel with the partial sudden contraction. Again, at low rotation numbers, the entrance condition is the primary factor influencing the level of enhancement. At the low rotation numbers, the greater enhancement of the leading surfaces is clearly seen. However, as the rotation number increases, the effect of rotation begins competing with the effect of the entrance geometry. The leading-inner surface experiences the least enhancement at the highest rotation number. The effect of the entrance does not totally diminish at the higher rotation numbers, and this is seen with the leading-outer surface experiencing the greatest enhancement.

Figure 11 shows the streamwise-averaged Nusselt number ratios in ribbed channels with fully developed flow, as well as flow through a sudden contraction and flow through a sudden partial contraction, in Figs. 11(a) and 11(b), respectively. As shown in Fig. 11(a), all surfaces in the rib channel with a fully developed entrance experience heat transfer enhancement with rotation. As the rotation number increases (Reynolds number decreases), the variation between the leading outer and trailing outer surfaces increases, and the same is true for the leading and trailing inner surfaces. Due to the nature of the rotation-induced vortices, the trailing-outer surface undergoes greater heat transfer enhancement than the leading-outer surface because the vortices are forcing the coolant from the leading-inner surface toward the trailing-outer surface. Likewise the trailing-inner surface experiences greater enhancement than the leading-inner surface.

Figure 11(a) also shows that there is little difference between the fully developed flow and the flow through a sudden contraction. The trailing surfaces of the channel with the sudden contraction undergo more heat transfer enhancement than the trailing surfaces of the fully developed channel. Figure 11(b) shows similar trends for flow through a partial sudden contraction.

Figure 12 shows the channel-averaged Nusselt number ratios for both the rotating and nonrotating channels with the various entrance geometries. This figure clearly shows the entrance geometry has a more profound effect on the heat transfer in the smooth channels than the ribbed channels. For both rotating and nonrotating channels, there is a clear distinction between the partial sudden contraction, sudden contraction, and fully developed values.

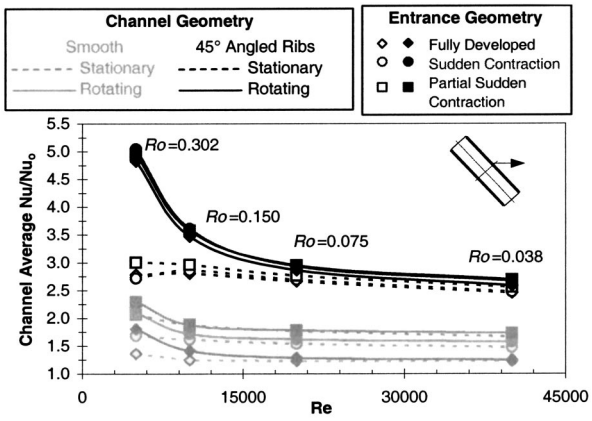

Fig. 12 Channel-averaged Nusselt number ratios in rotating and stationary channels with varying entrances

For the rotating channels, the increasing Reynolds number corresponds to a decreasing rotation number. In this figure, the effect of rotation is clearly seen at the given Reynolds numbers. At the lowest Reynolds number of 5000, the greatest variation exists between the stationary and rotating results. In the ribbed channel, at this highest rotation number, the rotating channel results can be up to 1.75 times greater than the stationary results. However, at the highest Reynolds number (lowest rotation number) the enhancement within the rotating channel is only 1.10 times greater than the stationary channel. It can also be seen in this figure that the flows through the sudden contraction and partial sudden contraction experience greater heat transfer enhancement than the fully developed flow.

Conclusions

The geometry of internal cooling passages in modern gas turbine blades is limited to by the blade profile. The cross section of the cooling channels varies to meet the cross section of the blade from the leading edge to the trailing edge. Channels with large aspect ratios and large orientation angles are typically located near the trailing edge of the blade. The coolant entering the blade does not travel through a straight constant cross-section channel; the entrance of the cooling channel is manufactured to meet the space limitations in the dovetail of the blade. This study experimentally investigated the effect of entrance geometry on heat transfer in rotating cooling channels with smooth walls and angled ribs. In the study we present designers with new heat transfer data applicable to the design of cooling channels. From the results, the main conclusions are as follows.

1. The entrance geometry has a significant effect on the heat transfer in smooth rotating and nonrotating channels. In the smooth channel with a sudden contraction, the Nusselt number ratios are elevated above the fully developed values for the first 5 hydraulic diameters of the channel. The Nusselt number ratios in the channel with the partial sudden contraction are elevated above the fully developed values for the entire length of the channel.
2. The effect of the entrance condition is also seen in the smooth rotating channel. However, as the rotation number increases, the effect of rotation is more dominant than the effect of entrance geometry. For all three entrance conditions, all surfaces within the channels experience heat transfer enhancement with the increasing effect of rotation.
3. For the present 45° angled rib geometry, significant spanwise variation exists due to rib turbulators. The leading- and trailing-outer surfaces experience significantly greater enhancement than the leading- and trailing-inner surfaces.
4. Due to the large aspect ratio of the channel and the orientation of the channel, all surfaces in the ribbed cooling channel experience heat transfer enhancement with the increasing effect of rotation.
5. Sudden and partial contraction entrances provide higher heat transfer enhancement than the fully developed entrance from the entrance of the channel through the first three to four hydraulic diameters of the channels with angled ribs.
6. The effect of the varying entrance geometry is more prominent in the stationary cooling channels with angled ribs than the rotating channels.

Acknowledgment

This publication was prepared with the support of the U.S. Department of Energy, Office of Fossil Energy, National Energy Technology Laboratory through AGTSR project 00-01-SR082. However, any opinions, findings, conclusions, or recommendations expressed herein are those of the authors and do not necessarily reflect the views of the DOE.

Nomenclature

A = surface area of copper plate (m^2)
AR = channel aspect ratio
c_p = coolant specific heat (kJ/kg K)
D_h = hydraulic diameter (m)
e = rib height (m)
H = duct height (m)
h = heat transfer coefficient (W/m^2 K)
k = thermal conductivity of coolant (W/m K)
L = length of duct (m)
$\dot{m}$ = coolant mass flow rate (kg/s)
Nu = regionally averaged Nusselt number, hD_h/k
Nu_0 = Nusselt number for flow in fully developed turbulent nonrotating smooth tube
P = rib pitch (m)
Pr = Prandtl number
Q = rate of heat transfer (W)
Q_{loss} = rate of heat loss from the test section (W)
Q_{net} = net rate of heat transfer (W)
R = mean rotating arm radius (m)
Re = Reynolds number based on hydraulic diameter, $\rho V D_h/\mu$
Ro = Rotation number, $\Omega D_h/V$
$T_{b,x}$ = local coolant bulk temperature (K)
T_w = wall temperature (K)
V = bulk velocity in streamwise direction (m/s)
x = streamwise location (m)
α = rib angle
β = angle of channel orientation
ρ = density of coolant (kg/m^3)
$\Delta\rho/\rho$ = inlet coolant-to-wall density ratio, $(\rho_{b,i}-\rho_w)/\rho_{b,i} = (T_w-T_{b,i})/T_w$
Ω = rotational speed (rad/s)

References

[1] Han, J. C., Dutta, S., and Ekkad, S. V., 2000, *Gas Turbine Heat Transfer and Cooling Technology*, Taylor and Francis, New York.
[2] Johnson, B. V., Wagner, J. H., Steuber, G. D., and Yeh, F. C., 1994a, "Heat Transfer in Rotating Serpentine Passage With Trips Skewed to the Flow," ASME J. Turbomach., **116**, pp. 113–123.
[3] Johnson, B. V., Wagner, J. H., Steuber, G. D., and Yeh, F. C., 1994b, "Heat Transfer in Rotating Serpentine Passage With Selected Model Orientations for Smooth or Skewed Trip Walls," ASME J. Turbomach., **116**, pp. 738–744.
[4] Dutta, S., and Han, J. C., 1996, "Local Heat Transfer in Rotating Smooth and Ribbed Two-Pass Square Channels With Three Channel Orientations," ASME J. Heat Transfer, **118**, pp. 578–584.
[5] Taslim, M. E., Rahman, A., and Spring, S. D., 1991a, "An Experimental Investigation of Heat Transfer Coefficients in a Span-Wise Rotating Channel With Two Opposite Rib-Roughened Walls," ASME J. Turbomach., **113**, pp. 75–82.
[6] Taslim, M. E., Bondi, L. A., and Kercher, D. M., 1991b, "An Experimental

Investigation of Heat Transfer in an Orthogonally Rotating Channel Roughened With 45° Criss-Cross Ribs on Two Opposite Walls,'' ASME J. Turbomach., **113**, pp. 346–353.
[7] Azad, G. S., Uddin, M. J., Han, J. C., Moon, H. K., and Glezer, B., 2002, ''Heat Transfer in a Two-Pass Rectangular Rotating Channel With 45° Angled Rib Turbulators,'' ASME J. Turbomach., **124**, pp. 251–259.
[8] Al-Qahtani, M., Jang, Y. J., Chen, H. C., and Han, J. C., 2002, ''Prediction of Flow and Heat Transfer in Rotating Two-Pass Rectangular Channels With 45° Rib Turbulators,'' ASME J. Turbomach., **124**, pp. 242–250.
[9] Griffith, T. S., Al-Hadhrami, L., and Han, J. C., 2002, ''Heat Transfer in Rotating Rectangular Channels (AR=4) With Angled Ribs,'' ASME J. Heat Transfer, **124**, pp. 617–625.
[10] Lee, E., Wright, L. M., and Han, J. C., 2003, ''Heat Transfer in Rotating Rectangular Channels (AR=4:1) With V-Shaped and Angled Rib Turbulators With and Without Gaps,'' ASME Paper No. 2003-GT-38900.
[11] Kays, W. M., and Crawford, M. E., 1993, *Convective Heat and Mass Transfer*, 3rd ed., McGraw-Hill, New York, pp. 345–348.
[12] Boelter, L. M. K., Young, G., and Iverson, H. W., 1948, ''An Investigation on Aircraft Heaters—Distribution of Heat Transfer Rate in the Entrance Section of a Circular Tube,'' NACA Technical Note No. 1451.
[13] Burggraf, F., 1970, ''Experimental Heat Transfer and Pressure Drop With Two-Dimensional Turbulence Promoter Applied to Two Opposite Walls of a Square Duct,'' in *Augmentation of Convective Heat and Mass Transfer*, edited by A. E. Bergles and R. L. Webb, ASME, New York, pp. 70–79.
[14] Han, J. C., and Park, J. S., 1988, ''Developing Heat Transfer in Rectangular Channels With Rib Turbulators,'' Int. J. Heat Mass Transfer, **31**, pp. 183–195.
[15] Loui, T. M., and Hwang, J. J., 1992, ''Developing Heat Transfer and Friction in a Ribbed Rectangular Duct With Flow Separation at Inlet,'' ASME J. Heat Transfer, **114**, pp. 565–573.
[16] Park, J. S., Han, J. C., Huang, Y., and Ou, S., 1991, ''Heat Transfer Performance Comparisons of Five Different Rectangular Channels With Parallel Angled Ribs,'' Int. J. Heat Mass Transfer, **35**, pp. 2891–2902.
[17] Kline, S. J., and McClintock, F. A., 1953, ''Describing Uncertainties in Single-Sample Experiments,'' Mech. Eng. (Am. Soc. Mech. Eng.), **75**, pp. 3–8.

Unsteady Effects on Trailing Edge Cooling

G. Medic

P. A. Durbin

Mechanical Engineering Department,
Stanford University,
Stanford, CA 94305-3030

It is shown how natural and forced unsteadiness play a major role in turbine blade trailing edge cooling flows. Reynolds averaged simulations are presented for a surface jet in coflow, resembling the geometry of the pressure side breakout on a turbine blade. Steady computations show very effective cooling; however, when natural—or even moreso, forced—unsteadiness is allowed, the adiabatic effectiveness decreases substantially. Streamwise vortices in the mean flow are found to be the cause of the increased heat transfer. [DOI: 10.1115/1.1860565]

1 Introduction

The trailing edges of high pressure turbine blades are subjected to substantial heat loads. For this reason cooling air is blown from breakouts on the pressure side, jetting toward the trailing edge. A computational analysis has tended to significantly overestimate the cooling effectiveness of these jets. Indeed, adiabatic effectiveness, η, is found to be nearly 1 to the trailing edge; at least, that is so when the predictions in question are steady, Reynolds-averaged (RANS) computations. Unfortunately, lab tests show that the effectiveness starts to drop after about four jet nozzle diameters, and might fall to about 0.5 near the trailing edge, at typical blowing ratios. It has been suggested that the discrepancy between prediction and observation might be due to coherent unsteadiness [1].

In the present paper, we describe unsteady RANS computations of a flow that is representative of the pressure-side, trailing edge. Some interesting phenomenology is observed. It is this, not applied prediction methods, that is the subject of this article. We find that natural unsteadiness does arise, due to three-dimensional vortex shedding from the upper lip of the breakout (Fig. 2, later). This mean flow unsteadiness causes some extra mixing, and causes the time-averaged η to decrease noticeably below 1; however, it does not seem to drop as much as lab tests lead one to expect. Pulsations added to the upstream plenum cause a more substantial drop in η. Adiabatic effectiveness then mimics that observed experimentally. It is unclear whether the pulsations have any analogy to conditions that occur in lab tests; so they are presented here simply as a study in the effect of forcing. A fascinating change in the mean vortical structure is seen under the imposition of periodic forcing. The shed vortices become more three-dimensional, forming into loops, which are the cause of greatly enhanced mixing.

The rationale for unsteady RANS is sometimes a cause of confusion. There is no inconsistency between representing turbulent mixing by a statistical closure, while computing an unsteady mean flow [2]. In the presence of coherent, periodic unsteadiness, the energy spectrum will look like Fig. 1. Mixing due to the broadband portion of the spectrum is represented by the closure model. The spike is due to mean flow unsteadiness. This *must be computed* by an unsteady simulation. It is a source of additional mixing—mixing that is not due to turbulence, but rather, to vortices in the mean flow.

Holloway et al. [3] have previously suggested a role of unsteadiness in the pressure-side bleed problem. Indeed, the present is a follow-on to their study, and is motivated by the same experiments. Those experiments are described in Holloway et al. [1]. The papers by Holloway et al. appear be the only previous computational studies of coherent unsteadiness in external trailing edge film cooling. Computations addressing the passages internal to the trailing edge are discussed in Rigby and Bunker [4]. A recent article by Martini and Shultz [5] describes experiments and computations of a trailing edge geometry, cooled by a row of jets, without lands. They found unsteadiness due to random coalescence between the jets. However, unsteadiness was not important in their CFD analysis. Their geometry differs substantially from the present, because of the lands.

Manuscript received January 21, 2003; revision received November 8, 2004. Review conducted by: S. Acharya.

2 Computations

The commercial code, CFX, was used for the present simulations. Second-order time stepping must be used for this code to capture the coherent unsteadiness. With that switched on, we conducted a number of grid- and time-step refinements to be convinced that the observed unsteadiness is not a numerical artifact. In fact, we ran a few simulations with a different code, Star-CD, with similar results. Hence, the numerical accuracy appears to be sufficient for the task at hand.

The present computations invoke the SST model, as implemented in CFX. The broad features of these simulations are insensitive to the particulars of the turbulence closure; similar results were seen with the two-layer RNG and Chen $k-\epsilon$ models.

Figure 2 shows the computational domain. It consists of an upstream plenum, a land that channels the flow into jets, and an external region of coflowing fluid. At the breakout the internal flow exits through a rectangular nozzle. The thickness of the upper lip of the nozzle is equal to the height of the jet. The land protrudes downstream from the nozzle, in a wedge shape, to the trailing edge. The lower part of Fig. 2 shows a geometry constructed from four images of the domain.

The flow is from left to right, in two streams: the wall jet exits from the plenum and is channeled by the land; the external flow enters in the upper portion. Generally, the two streams have different bulk velocities; their ratio, $U_{\text{jet}}/U_{\text{free-stream}}$ is the blowing ratio, since we consider constant density, incompressible flow. A few compressible simulations showed the same vortical flow components and heat transfer that are described herein.

The geometry is subject to a symmetry condition on the left and the right lateral sides of the domain. This emulates a series of jets, blowing toward the trailing edge. The computational domain contains only one-half of the jet exit; hence the second symmetry condition is at the center of the jet. Computations with a full jet cross section produced very similar results to those shown herein. In the presence of forcing, the flow becomes quite complex. That was the primary motive for testing the validity of the symmetry assumption. The present forcing was plane wave; hence, it is consistent with the symmetry, but it was uncertain whether the flow respects that symmetry—it appears that it does. Therefore, we present results only for the geometry of Fig. 2. The Reynolds number based on free-stream velocity and nozzle lip thickness is 5×10^4.

The final grid consisted of 0.75 million cells, in a block structured form. The solver treats it as fully unstructured, but block

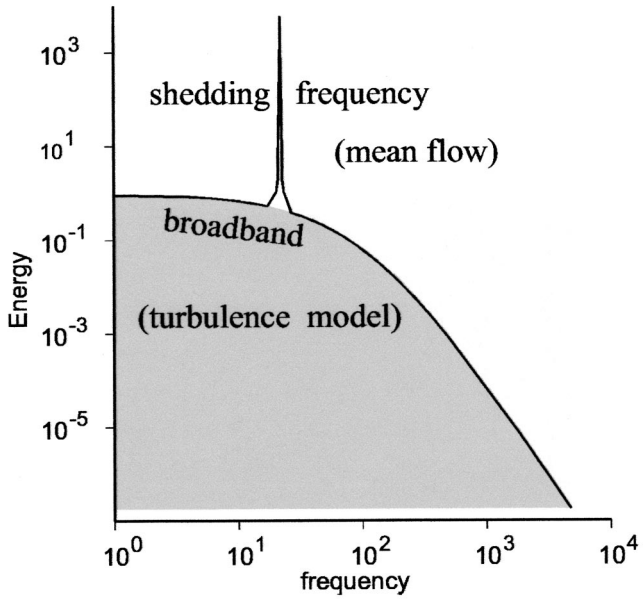

Fig. 1 The form of an energy spectrum with broadband and coherent frequencies. Units are arbitrary.

structured gridding produced a smooth grid, with good resolution near surfaces and in the wake of the upper nozzle lip. A grid refinement study was conducted, with a special focus on the grid blocks in the shedding region. The resolution in those blocks was successively doubled in the streamwise and spanwise direction. The finest grid had 1.25 million cells. Coarsening the grid in the same manner led to a loss of accuracy for grids with approximately 0.25 million cells. The 0.75 million cell mesh was designed from these studies, to provide grid insensitivity.

For the time-accurate computations, the time step was adjusted to provide about $50\Delta t$ per period. In the natural case, no forcing was applied. The flow was allowed to develop a self-sustained unsteadiness. A large number of simulations, not reported herein, were conducted at various blowing ratios. It was found that coherent unsteadiness developed spontaneously for all simulations with a blowing ratio larger than 0.35 (simulations for very low blowing ratios were not performed). For blowing ratios larger than 1.5, the unsteadiness was damped down and the flow became steady. To confirm the computational results, lab tests were conducted on the rig described in Holloway et al. [1] solely to determine whether or not coherent unsteadiness occurred. The results were positive: a frequency was seen corresponding to a Strouhal number of about 0.2.

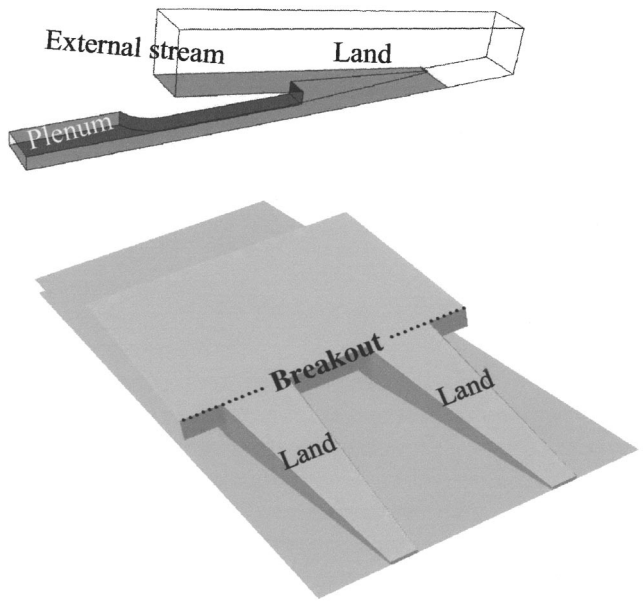

Fig. 2 The computational geometry

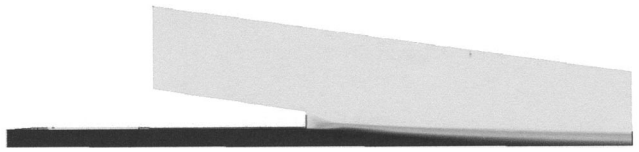

Fig. 3 Temperature contours in steady flow

3 Results

Observations will be summarized for steady, unsteady, and forced simulations. To an extent, we are using a RANS simulation to understand the averaged mixing processes of the pressure-side cooling jets.

Temperature contours in a vertical section through the mid plane of the nozzle shows how a layer of cool fluid lies next to the wall in the steady flow calculation: see Fig. 3. The same midplane section through an unsteady computation shows vortex shedding from the upper nozzle lip: see Fig. 4.

Comparing the temperature contours from the steady (Fig. 3) and unsteady solutions (Fig. 4) shows that the mean flow vortices cause substantial additional mixing. However, a layer of cool air persists next to the wall for a distance of about eight jet heights. The cooling effectiveness,

$$\eta \equiv (T_{\text{hot}} - T_{\text{wall}})/(T_{\text{hot}} - T_{\text{cool}}), \tag{1}$$

depends only on the adiabatic surface temperature. Despite the enhanced mixing away from the wall, in the unsteady simulation η remains near unity until near the trailing edge.

In these incompressible computations, temperature is a passive scalar. The contour levels in the figures could be regarded as ranging from 0 in the coolant stream to 1 in the gas stream. Dark regions show where the temperature is low.

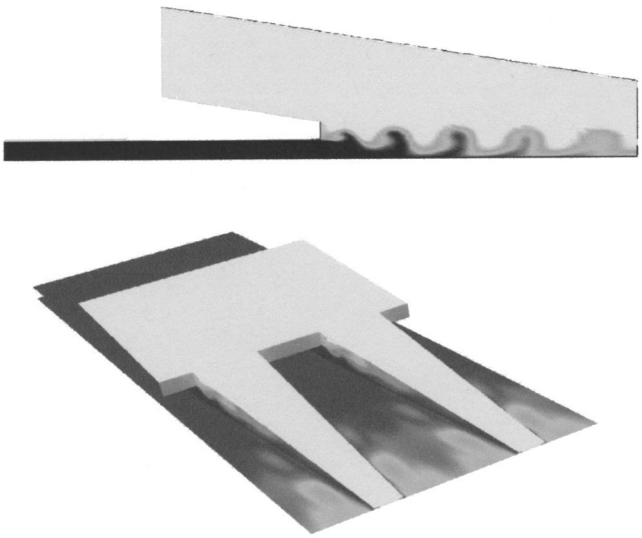

Fig. 4 Temperature contours illustrating natural unsteadiness. Side view and wall temperature under natural unsteadiness.

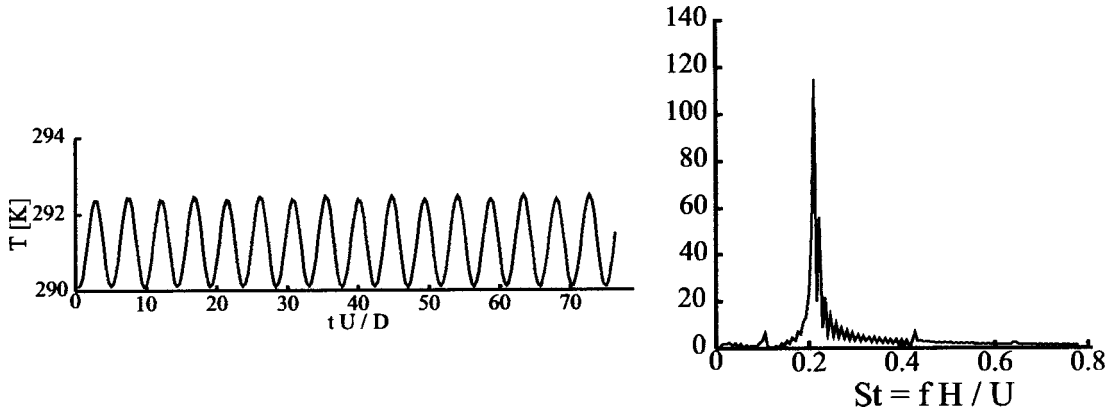

Fig. 5 A sample time history and spectrum

The plan form in Fig. 4 illustrates this more completely. Hot fluid is seen on top of the land. This is carried over the land, and is not cooled by mixing with the jet; but the lower surface, between the lands, remains near the jet temperature to the trailing edge. Hot fluid begins to impinge near the vertical walls of the land.

Time histories of temperature near the lower wall show the strict periodicity. This demonstrates that the computation has converged to a limit cycle. Spectra contain a sharp peak at a Strouhal number of 0.2 based on the nozzle lip thickness (Fig. 5). In reference to Fig. 1, the spike in Fig. 5 is the coherent unsteadiness; it is resolved as part of the mean flow. The broadband is not simulated; it is represented by the Reynolds-averaged turbulence model.

The extra mixing due to unsteadiness motivated a further study in which the velocity at the inlet to the plenum was pulsated:

$$U_{\text{in}} = U_0(1 + A \sin \omega_f t).$$

Although the forcing frequency, ω_f, was varied, the largest and most interesting response was for $\omega_f H/U = 0.2$; i.e., forcing with the natural shedding frequency. A was also varied. The value $A = 0.1$ is selected as representative of cases where forcing has a pronounced effect.

Figure 6 contains a time history and spectrum for the flow produced by inlet pulsations. Rather curiously, the response contains a strong subharmonic of the forcing frequency, and even a sub-subharmonic. The period is four times that of the forcing. On close inspection, a very weak subharmonic is seen, even in the natural case of Fig. 5; it becomes quite pronounced with forcing. The flow structure responsible for the appearance of subharmonics will be discussed below.

Again, the time history in Fig. 6 shows that we are simulating a periodic, ensemble-averaged flow. The chaotic, broadband component is represented by the closure model. There is no randomness in the time history; in particular, this is not a turbulent eddy simulation. That point should be emphasized: there is no connection between the present unsteady RANS computations and large eddy simulation (LES). The latter simulates random fields and would have to be phase averaged to extract coherent unsteadiness. That would require an extremely expensive computation, that included several hundred periods to obtain statistical convergence.

The influence of the plenum pulsations on mixing is protrayed in Fig. 7. Mixing now brings heated fluid to the wall a couple of nozzle diameters downstream. The pattern of wall temperature, in the lower part of Fig. 7, shows a distinct change in the distribution of mixing. The highest temperature now occurs on the midline, between the lands. The warmer fluid is swept down in the central region of the lower wall, leaving a small region next to the lands at the cold temperature.

The centerline effectivenesses for the three cases of steady, natural unsteadiness, and forced unsteadiness are plotted in Fig. 8 versus the distance between the slot breakout and trailing edge. The forced case shows a significant decline in effectiveness, beginning shortly after the nozzle exit. It was the intention of this simulation to produce mixing that resembled lab tests. The data in Fig. 8 are from Holloway et al. [1].

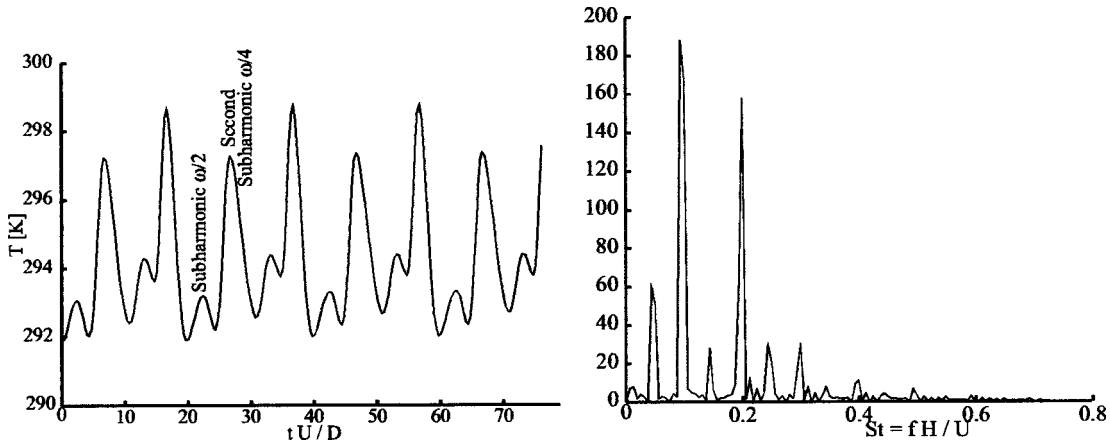

Fig. 6 A sample time history and spectrum, with forcing

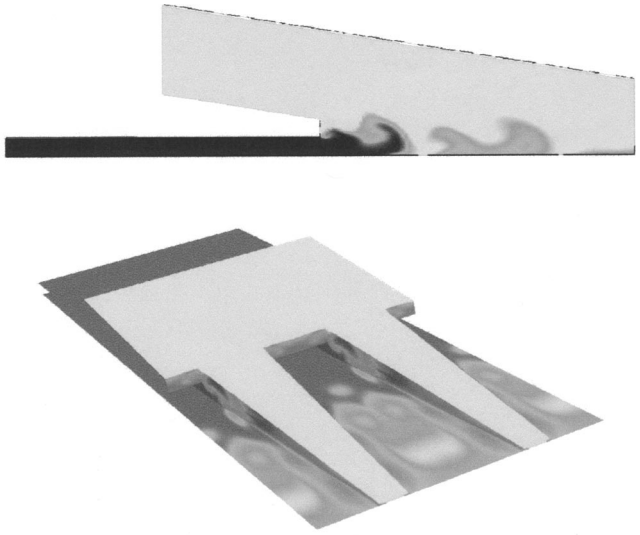

Fig. 7 Temperature contours with forced unsteadiness. Side view and wall temperature under forcing.

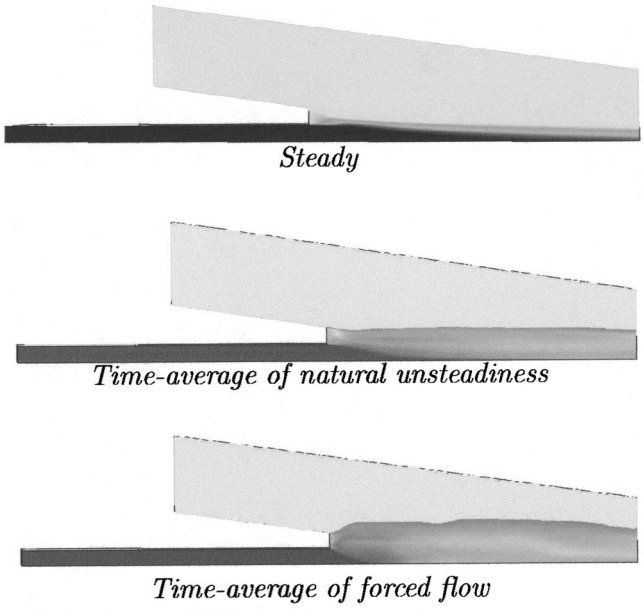

Fig. 9 Time-averaged temperature contours in a midspan plane

While it is unlikely that simple, plane wave forcing occurred in the lab, both η and the spatial pattern of heating in Fig. 7 very closely mirror those seen in experiments. To repeat a previous disclaimer, this simulation is not being presented as a prediction method. It illustrates the role that mean flow unsteadiness and three-dimensionality can play in trailing edge coolant flows.

The time-averaged, unsteady midspan temperature fields are compared to the steady computation in Fig. 9. The contribution of coherent unsteadiness is enhanced mixing. The steady computation represents mixing by broadband turbulence alone (via the turbulence model). The natural vortex street wafts the mixing layer, spreading the time-averaged temperature field. The evolution is similar to the steady case, but with faster spreading. Forcing produces stronger periodic, steamwise vortices. These change the nature of mixing. Heat disperses more quickly and the layer between free-stream and jet temperature is disrupted. A well-mixed region forms near the wall.

The drastic change in mixing that accompanies unsteadiness warrants explanation. Its origin is in the vortical features that occur in the jet. The following observations are presented for the purpose of uncovering some of the physical mechanisms that are at work.

The unsteadiness is associated with quite complex flow patterns. The midspan sections (Figs. 4, 7) are misleading in their simplicity: the flow is highly three-dimensional. The midspan sections have the appearance of shedding from a blunt trailing edge. While it is obvious that a two-dimensional geometry will produce a von Kàrmàn vortex street, it is far from obvious in three dimensions; indeed, three-dimensionality can suppress coherent shedding. In fact, a modification to the present geometry produced that effect.

The question arose as to whether the natural frequency is peculiar to the present geometry. To an extent it is. The present geometry was simplified to a series of rectangular wall jets in coflow by removing the protruding section of the lands. Simulations then converged to steady flow, even though they were computed with time accuracy. Grid- and time-step refinements on the truncated land geometry always converged to steady flow.

These results are consistent with the observation by Martini and Shultz [5] that coherent unsteadiness was not significant in their geometry—which did not have lands. This might not be surprising. The unsteadiness originates at the upper wall of the breakout. The jets are not the cause of unsteadiness; rather, they break up

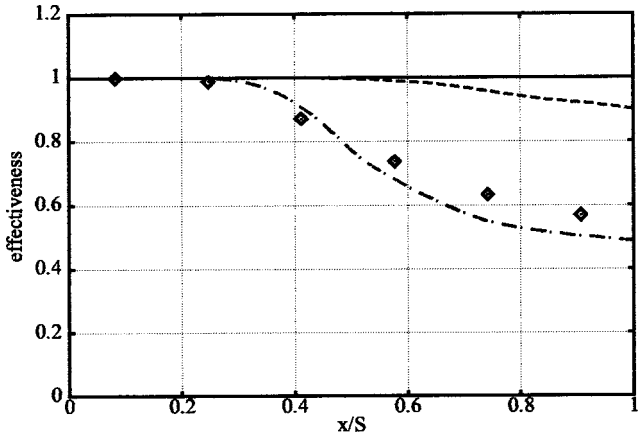

Fig. 8 Centerline adiabatic effectiveness. —, steady; ----, natural shedding; – – –, forced. ♦, experiments from Holloway et al. [1].

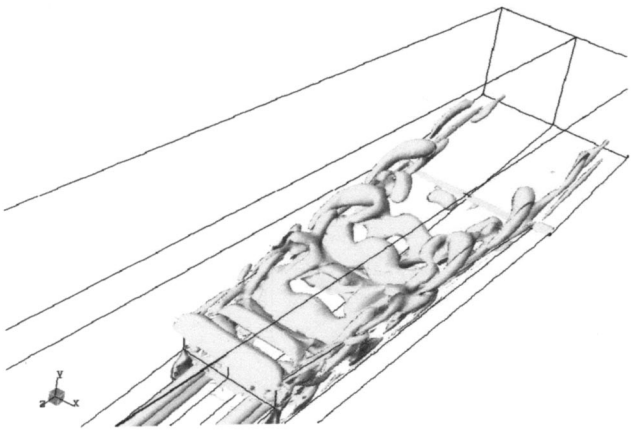

Fig. 10 Vortices with natural unsteadiness

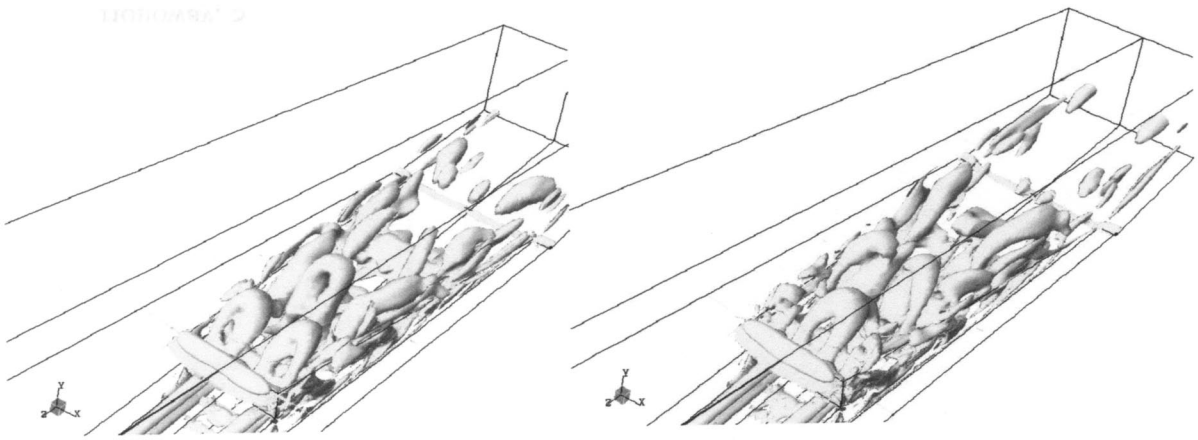

Fig. 11 Vortices with forced unsteadiness. Two instants, showing the origin of subharmonics.

the spanwise coherence of the flow leaving the upper surface, above the nozzles; i.e., three-dimensionality suppresses unsteadiness. The surprising observation is that the protruding lands restores coherent unsteadiness. The protruding section seems to impose a spanwise periodicity that resynchronizes the vortex shedding from the upper and lower surfaces of the nozzle lip.

A perspective on the flow complexity is provided by vortex visualization. Figures 10 and 11 show the three-dimensional vortex streets with natural and forced unsteadiness. A surface $Q>0$ is plotted, where $Q \equiv |\Omega|^2 - |S|^2$, with S and Ω being the rate of strain and rate of rotation tensors. Inside these surfaces, the rate of rotation is larger than the rate of strain: that is the sense in which Q detects vortices. Note that a full jet nozzle was created in these figures by reflecting the computational domain across the symmetry plane—solely for the purpose of display. As complex as the vortical structure appears to be, this is not a turbulent eddy simulation: the vortex pattern repeats periodically and represents the ensemble-averaged flow.

The natural unsteadiness (Fig. 10) takes the form of vortex tubes, with strong three-dimensionality only occurring near the vertical walls of the lands. The connection to a two-dimensional, von Kàrmàn street is apparent. The three-dimensionality due to the wall jets is not disruptive of shedding.

A horseshoe vortex wraps around the junctions between the upstream edge of the land and the upper and lower walls in the plenum portion of Fig. 2. This vortex can be seen exiting the jet at the bottom of Fig. 10. These horseshoe vortices may contribute to the distortion of the shed vortices near the end walls in the case of natural unsteadiness. However, they do not seem to make a major contribution to mixing beyond the nozzle exit.

The forced case, in Fig. 11, is more intriguing. The shedding now breaks into vortex loops. The subharmonic component in the spectrum seems to be due to the loops appearing alternatively at the sides and in the middle of the slot. This can be seen by comparing the figures at the left and the right; they are one natural period apart in time. Again, it must be emphasized that, as complex as the flow may seem to be, it repeats periodically; this is not a LES.

The mean flow vortices now have a stronger streamwise component than in the unforced case. Streamwise vorticity is known to greatly enhance mixing in shear layers [6]. The surface temperature patterns in Figs. 4 and 7 reflect the role of streamwise vortices. In Fig. 4, higher wall temperatures occur near the lands because that is where the streamwise vortices occur. In the forced case, Fig. 7, vortex loops in the middle of the flow result in the higher wall temperatures.

These simulations raise the intriguing possibility of reducing mixing and improving cooling via control of the unsteadiness. Because the mean flow unsteadiness is at issue, this does not require suppression of turbulence; the broadband, turbulent component does not mix the hot stream to the wall. Passive devices might be able to break the coherence and suppress mixing. We have seen that modifications to the land geometry downstream of the nozzle breakout can have this effect.

Acknowledgment

This work was sponsored by General Electric aircraft engines through their Universities Strategic Alliance. We are especially grateful to Scott Hunter, Fred Buck, and Ganesh Kumar for their advice.

References

[1] Holloway, S. D., Leylek, J. H., and Buck, F. A., 2002, "Pressure-Side Bleed Film Cooling: Part I, Steady Framework for Experimental and Computational Results," ASME Turbo Expo 2002; papers GT-2002-30471.
[2] Iaccarino, G., Ooi, A., Durbin, P. A., and Behnia, M., 2003, "Reynolds Averaged Simulation of Unsteady Separated Flow," Int. J. Heat Mass Transfer, **24**, pp. 147–156.
[3] Holloway, S. D., Leylek, J. H., and Buck, F. A., 2002, "Pressure-Side Bleed Film Cooling: Part 2, Unsteady Framework for Experimental and Computational Results," ASME Turbo Expo 2002, papers GT-2002-30472.
[4] Rigby, D. L., and Bunker, R. S., 2002, "Heat Transfer in a Complex Trailing Edge Passage for a High Pressure Turbine Blade," NASA/CR 2002-211701.
[5] Martini, P., and Shultz, A., 2004, "Experimental and Numerical Investigation of Trailing Edge Film Cooling by Circular Coolant Wall Jets Ejected From a Slot With Internal Rib Arrays," ASME J. Turbomach., **126**, pp. 229–236.
[6] Moser, M. M., and Rogers, R. D., 1991, "Mixing Transition in the Cascade to Small Scales in a Plane Mixing Layer," Phys. Fluids A, **3**, pp. 1128–1134.

Effect of Elevated Free-Stream Turbulence on Transitional Flow Heat Transfer Over Dual-Scaled Rough Surfaces

Ting Wang
Energy Conversion and Conservation Center,
University of New Orleans,
New Orleans, LA 70148-2220

Matthew C. Rice
Borg Warner Turbo Systems,
1849 Brevard Road,
Arden, NC 28704

The surface roughness over a serviced turbine airfoil is usually multiscaled with varying features that are difficult to be universally characterized. However, it was previously discovered in low free-stream turbulence conditions that the height of larger roughness produces separation and vortex shedding, which trigger early transition and exert a dominant effect on flow pattern and heat transfer. The geometry of the roughness and smaller roughness scales played secondary roles. This paper extends the previous study to elevated turbulence conditions with free-stream turbulence intensity ranging from 0.2% to 6.0%. A simplified test condition on a flat plate is conducted with two discrete regions having different surface roughness. The leading-edge roughness is comprised of a sandpaper strip or a single cylinder. The downstream surface is either smooth or covered with sandpaper of grit sizes ranging from 100 to 40 ($R_a = 37-119\ \mu m$). Hot wire measurements are conducted in the boundary layer to study the flow structure. The results of this study verify that the height of the largest-scale roughness triggers an earlier transition even under elevated turbulence conditions and exerts a more dominant effect on flow and heat transfer than does the geometry of the roughness. Heat transfer enhancements of about 30–40%-over the entire test surface are observed. The vortical motion, generated by the backward facing step at the joint of two roughness regions, is believed to significantly increase momentum transport across the boundary layer and bring the elevated turbulence from the freestream towards the wall. No such long-lasting heat transfer phenomenon is observed in low free-stream turbulence cases even though vortex shedding also exists in the low turbulence cases. The heat transfer enhancement decreases, instead of increases, as the downstream roughness height increases. [DOI: 10.1115/1.1861920]

Introduction

The effects of elevated free-stream turbulence and roughness on flow and thermal structures can exert a significant impact on turbine performance through profile losses from increased aerodynamic drag as well as reduced airfoil life from enhanced external heat transfer. Roughened surface conditions affect the performance of gas turbines through altering the fundamental nature of the flow. This presence can cause decreases of the engine performance below design objectives for new turbine systems or alter the longevity, reliability, and durability of the airfoils for in-service systems. To protect the airfoil material from the hot gas flow, a thin coat of thermal barrier coating (TBC) is applied to extend blade life for new engines. This process entails a trade-off between manufacturing costs and engine performance for a new engine. The roughness of TBC surface condition affects aerodynamic performance and in-turn will affect the manufacturer's guaranteed initial overall engine performance. For in-service engines, the presence of protrusion or recess of surface due to deposits, corrosion, and erosion can significantly increase especially when an early laminar-turbulent transition is triggered by surface roughness. Generally, in-service turbines incur roughness in the form of pitting or deposition, which can cause significant variation in the surface finish of a used airfoil.

In this paper, the ''rough scales'' are defined as ''rough height scales'' which could be expressed in terms of k^+, k_s, R_a, or R_z, as defined in the nomenclature. The surface roughness structure was examined by Tarada [1] who analyzed 50 different turbine blades (both new and used) with a typical range in roughness from 2 to 160 μm [root-mean-square (rms) roughness value]. Following Tarada's investigation, Taylor [2] conducted a detailed study of the physical features and effects of surface roughness on used gas turbine blades. Vital observations during Taylor's experiment include: *the leading edge of the blade incurred the greatest roughness*, and nonuniformities in roughness distribution along blade contours were rare. Boynton et al. [3] and Tarada and Suzuki [4] showed that an increase in surface roughness decreased overall turbine performance. Suder et al. [5] found that decreasing the roughness of coated compressor blades of the finished coating from 3.1 to 0.6 μm increased overall compressor efficiency three percentage points. Blair [6] reported that a tenfold increase in surface roughness doubled the rate of heat transfer. He also reported that the correlations commonly used in industry overpredicted suction side blade heat transfer and underpredicted heat transfer on the pressure side.

Combined Effects of Surface Roughness and Turbulence Intensity. Recent experiments conducted by Bunker [7,8] have demonstrated that both surface roughness and free-stream turbulence were major contributors to undesirable but inevitable increase in airfoil heat loads. Using a centerline surface roughness level from $R_a = 0.5\ \mu$m to $R_a = 4.5\ \mu$m and a free-stream turbulence from 4% to 13%, Bunker demonstrated that in both elevated roughness and free-stream turbulence the airfoil heat transfer distribution depended on Reynolds number and showed an increase in surface heat transfer up to 30%. This study also indicated that at higher roughness levels the roughness tended to dominate the turbulence effects in most regions except the leading edge. Gibbings and Al-Shukri [9] demonstrated that combining free-stream turbulence and surface roughness caused a net increase in the skin friction, an increase in the momentum thickness, and a decrease in

Manuscript received March 21, 2004; revised manuscript received September 27, 2004. Review conducted by: S. Acharya.

the shape factor. The result included the forward movement of the start of transition even though the basic mechanism of transition (bypass transition mode) was unchanged with imposition of both sandpaper and free-stream turbulence.

Bons [10] conducted heat transfer experiments employing plastic roughness models with roughness distributions obtained from land-based turbine airfoils. The free-stream turbulence intensity (FSTI) ranged from 1% to 11% and roughness k^+ from 0.66 to 515. He reported that the standard Stanton number (St) and skin friction coefficient (C_f) correlations severely underpredicted the effect of roughness for $k^+<70$, but overpredicted St by 10% when $k^+>70$.

Measurements and Simulations of Turbine Airfoil Roughness. To simulate the physical properties of a surface located inside a gas turbine, previous researchers have used several approaches. Typically, the roughness was characterized in terms of roughness scale and geometry. The common ways of specifying the scale include rms or arithmetical mean of peak-to-valley values. The familiar technique to designate geometry encompasses shape type, frequency of shape, and blockage. The type of shapes could include frustum, cylinder, cubic, sphere, etc. Numerous approaches have been used to describe the structure of rough surfaces. Two of these structures, skewness and kurtosis, were measured on the blades of gas turbine by Taylor [2] and Tarada [1]. Taylor [2] reported values for R_a, skewness, kurtosis, and autocorrelation; and Tarada [1] presented some rms results for several different types of turbine blades. Using suggestions by Sigal and Danberg [11], Bogard et al. [12] utilized profilometry measurement of conical elements in an array that provided centerline average, average peak values, and roughness shape/density parameters in the roughness scale of turbine blades. These estimates of the roughness scale parameters have laid the groundwork for improved understanding of roughness measurement.

Belnap et al. [13] recently investigated the Reynolds analogy of convective heat transfer over a surface with roughness similar to that exists on some of the external surfaces gas turbine airfoils. They developed a modified Reynolds analogy equation which is different from the Reynolds analogy equation for surfaces with uniformly shaped elements arranged in a regular, periodic pattern.

Recently, Bons et al. [14] assembled and measured nearly 100 land-based turbine components. Significant spatial variations were evidenced and transitions from rough to smooth surface conditions were shown to be remarkably abrupt in some cases. They found consistently high roughness existing in the trailing edge near tip, and in the leading edge and trailing edge near hub. The spanwise trace indicated abrupt drop in roughness from leading hub to midspan on the pressure side of the airfoils. Finally, they concluded that no one characterization can accurately capture the range of features exhibited by the various forms of surface roughness. From the experimental results of St and C_f values, Bons et al. [14] further concluded that results of simulated roughness is fundamentally different from roughness on real engine airfoils.

The above conclusions are not unexpected. In addition, we need to further realize that even though the real surface roughness over a serviced turbine airfoil could be precisely captured, it is usually multiscaled with varying features, and it is difficult to be universally characterized. Respecting the difficulties and complexity to simulate the real roughness, especially the geometries of roughness, Pinson and Wang [15] wondered if the height of the roughness (ie. the vertical scale of the roughness) is the predominant factor that would affect the flow pattern and structures, while the geometries and the precise distribution of roughness are less important. Furthermore, motivated by the measurements made by Taylor [2], Finson [16], and Sigal and Danberg [11], who documented that the leading edge was found to be one of the two areas that possessed the largest roughness, Pinson and Wang [15] initiated a study to investigate the effect of single-scaled leading-edge roughness on flow and heat transfer behavior on a smooth flat surface. Using the roughness Reynolds numbers ranging from 2 to 2480 at the leading edge and low free-stream turbulence intensity less than 0.5%, they were able to observe that the maximum roughness height is the primary contributing factor that controls the onset of transition and downstream heat transfer. The geometry of roughness (sand papers, cylinders, and strips) plays a secondary role. The result of the leading edge roughness was used as a reference for the next step studies of two-scale roughness.

With their earlier study of leading edge roughness paving the way, Pinson and Wang [17] studied the effects of leading roughness accompanied by a region of downstream roughness. They approached the study by investigating whether the leading edge roughness overshadows the downstream roughness. They observed an unexpected phenomenon: With a fixed leading edge roughness of 60-grit sandpaper, increasing the downstream surface roughness from smooth to 100-grit sandpaper significantly delays transition, rather than trigger an earlier transition. This observation was exactly opposite to their common intuition. From this phenomenon, they concluded that the primary mechanism that triggers transition in the dual-scale roughness condition is caused by the flow separation and vortex shedding produced by the backward-facing step at the joint of two different scales of roughness. The geometry of the roughness has only a secondary effect. A rough/smooth condition can trigger much earlier transition than a rough/small-rough condition. With the onset of transition being triggered earlier, significant changes of C_f and heat transfer occurs. They also reported that even though when the roughness scales ($k^+<0.7$) were significantly less than the hydraulically smooth value ($y^+<4$), the onset of transition is triggered significantly earlier under low FSTI conditions.

Pinson and Wang's studies [15,17] were performed in low FSTI conditions. To be useful for real engine applications, the effect of elevated FSTI is essential and needs to be further investigated. It has been known that both elevated FSTI and surface roughness can trigger earlier onset of transition, which in turn, significantly alters the flow structure, surface friction, and surface heat transfer. However, it has not been clear which one plays a more dominant role or if the combined effects are additive. Furthermore, it is not known if the dominant effect of the leading edge roughness would diminish under elevated FSTI conditions. These unknowns motivate the present study.

Roughness and FSTI effects on an actual gas turbine blade are undoubtedly functions of many parameters. To fundamentally understand the combined effects of roughness and FSTI effect on the transition process, this study focuses on free-stream turbulence from 0.2% to 6%, with roughness from $R_a=37$ to 119 μm over a flat plate without a pressure gradient. Using of a flat surface serves to isolate the effect of roughness scales from more complex conditions of turbine airfoils including other length scales such as radii of convex and concave curvature. Although this study does not simulate all the complexities of the gas turbine environment, it will serve as an important reference for more complicated situations.

Experimental Program

Wind Tunnel. The test facility employed in this study was constructed by Pinson [18] as shown in Fig. 1(*a*). It is an open-circuit, blowing-type wind tunnel. Air enters the system by passing through a filter designed to remove all particles larger than 5 μm. A honeycomb passage is used to straighten the flow. A heat exchanger is used to control the steadiness of the free-stream temperature to within 0.05°C over a 20 h period. Suction is employed upstream of the flat, heated test surface to facilitate the formation of a boundary layer from zero thickness at an elliptic leading edge.

The test section itself is a channel that measures 2.3 m in the streamwise (x) direction, 0.92 m in the spanwise (z) direction (parallel to the leading edge), and 0.15 m in the cross-stream (y) direction (perpendicular to the heated test surface). Opposite to the test surface is a flexible acrylic sheet that can be adjusted to

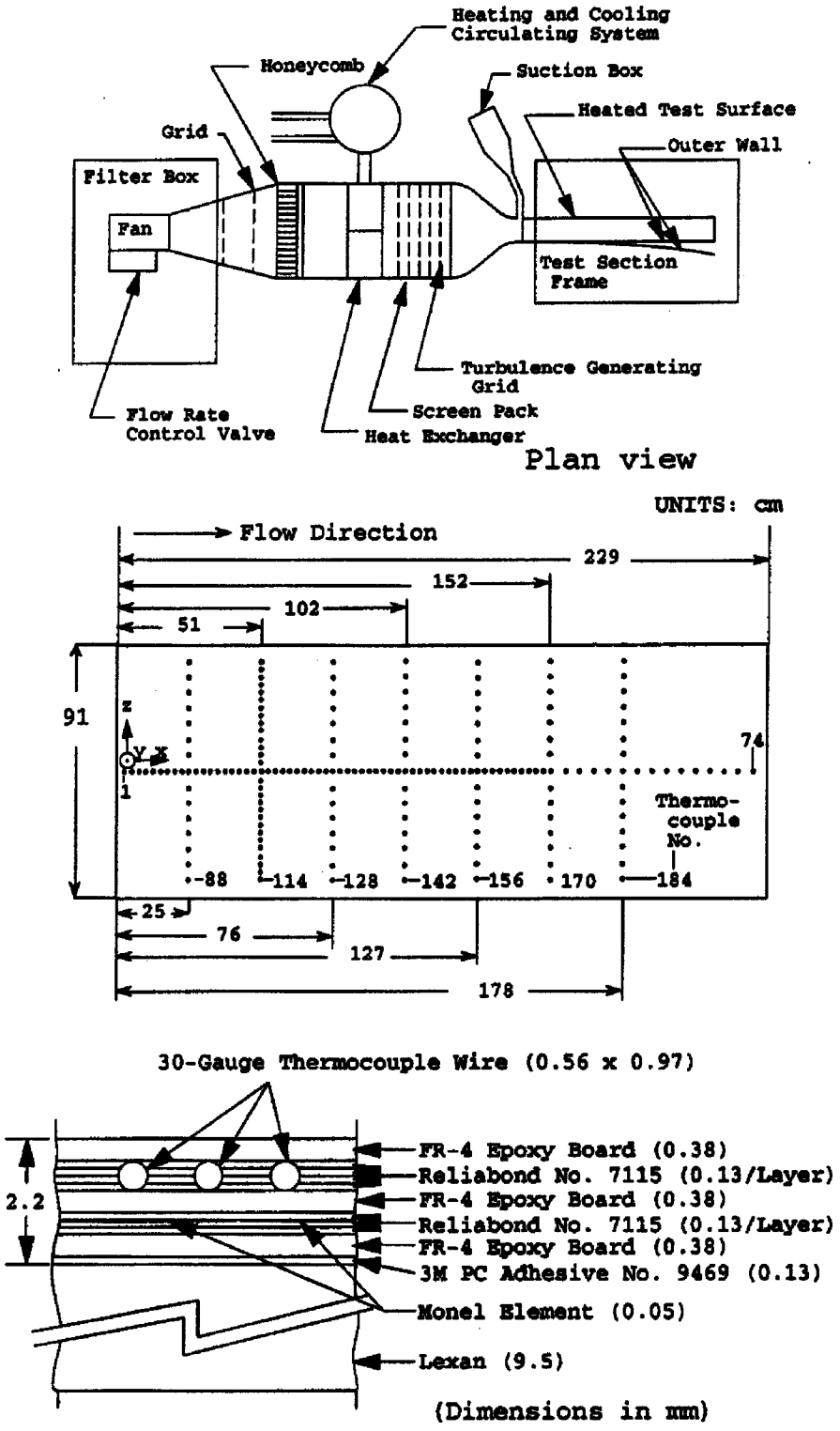

Fig. 1 Schematic diagrams of experimental facility: (*a*) overview of wind tunnel and test section; (*b*) thermocouple layout on test surface; (*c*) cross-section detail of heated test surface

provide the pressure gradient desired within the test section. In the present study, the pressure gradient is adjusted to be nearly zero.

The heated test surface is a composite design comprised of several layers as depicted in Fig. 1(*c*). At its lowest level, a layer of Lexan provides structural support. The upper portions of the test surface contain the monel heating elements and a series of *E*-type thermocouples that are positioned along the length and height of the surface as shown in Fig. 1(*b*). A total of nine monel sheets (0.05 mm thick, 25 cm×91 cm pieces spaced 0.8 mm apart) are connected in series to form the active heating elements within the surface. A layer of 30-cm-thick fiberglass insulation is placed behind the heated surface. The typical range of heat flux

Table 1 Surface conditions and roughness levels

Surface conditions	Roughness level
100-grit sandpaper	37 μm (R_a) 122 μm (R_z)
40-grit sandpaper	119 μm (R_a) 360 μm (R_z)
Cylinder	1 mm (diameter)
Paper backing of sandpapers	330 μm

convected into the air flow is between 88 and 210 W/m^2. The wall surface temperature is typically 3–13°C above the free-stream value. The thermocouples were calibrated against a RTD at ten temperature points between the ice point and the boiling point of water.

The turbulence-generating grids are made of rectangular biplane bar array grids consisting of approximately 69% open area. Two grids are used; grid 1 has a mesh width of 19 cm producing a FSTI of about 4%, and grid 2 has 33 cm mesh width producing a FSTI of about 6%, respectively. To maintain a nearly constant FSTI along the test section, turbulence-generating grids are positioned at the entrance of the main tunnel contraction. This allows sufficient distance for the grid-generated turbulence to reach the final stage dissipation.

In the present study, random sand-grain roughness is employed. The rms values of roughness heights are measured by a profilometer. Table 1 provides the surface conditions and roughness information.

Experimental Approach. The experiments are undertaken at two free-stream velocities, 4.6 and 7.0 m/s, respectively. Six smooth-wall cases are conducted first (see column 3 in Table 2). Then the leading edge is roughened by placing a 1 mm diameter cylinder or a 50 mm wide strip of 40-grit sandpaper, followed by a smooth surface (see column 4 in Table 2). Finally, sand papers with 40 or 100 grits are glued downstream from the leading edge roughness (see Fig. 2 and column 5 in Table 2). In total, 33 cases are conducted as shown in Table 2. The nomenclature used in each surface measurement is as follows: leading edge condition/surface condition/inlet FSTI percent. For instance, 40/100/5.0, corresponds to a roughened leading edge with a 5 cm band of 40-grit sand paper, followed by a region of 100-grit sand paper with a FSTI level of 5.0%, accordingly. The location of the end of the 5 cm band coincides with the location of the second thermocouple. The FSTI levels listed in column 2 of Table 2 represent nominal values for the group of cases in the same row. The actually measured FSTI value can be a little different and is indicated in each case's identification.

Table 2 Summary of test conditions

Free-stream velocity (m/s)	FSTI (%)	Baseline smooth wall	Leading-edge roughness only	Leading-edge and downstream roughness
4.6	0.2	0/0/0.2	cyl/0/0.2 40/0/0.3	cyl/100/0.2 40/40/0.2 40/100/0.2
4.6	3.3	0/0/3.3	cyl/0/3.3 40/0/3.3	cyl/100/3.3 40/40/3.3 40/100/3.3
4.6	5.0	0/0/5.0	cyl/0/5.2 40/0/4.9	cyl/100/5.0 40/40/5.2 40/100/5.0
7.0	0.4	0/0/0.4	40/0/0.4	cyl/100/4.0 40/40/4.1 40/100/4.2
7.0	4.0	0/0/4.1	40/0/3.9	cyl/100/4.0 40/40/4.1 40/100/4.2
7.0	6.0	0/0/5.9	40/0/5.9	cyl/100/6.0 40/40/6.0 40/100/6.0

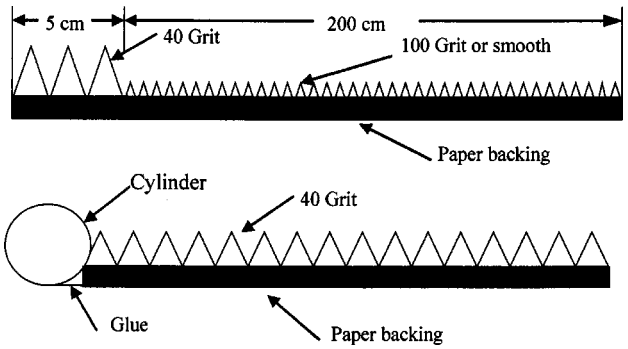

Fig. 2 Layout of roughness conditions. The step change between two roughness regions is near the second thermocouple location for 40-grit sand paper cases and is upstream of the first thermocouple for the cylinder cases.

Surface Heat Transfer Measurements. To normalize the presentation of the surface heat transfer, the Stanton number is used. It is defined as

$$\mathrm{St} = \frac{q_w''}{\rho_\infty C_{p,\infty} U_\infty (T_w - T_\infty)} \tag{1}$$

Since the thermocouples are buried 0.38 mm beneath the surface, the surface temperatures are calculated by employing a one-dimensional energy balance in the y direction. Corrections of radiation and backlosses are made. The rough wall case involved more layers between the heating element and the air stream, so additional thermal resistances are added to the analysis. The radiant loss from the test surface is deducted from q_w'' by assuming the outer wall opposite to the test surface is opaque to the infrared and has a temperature equal to the free-stream flow temperature. The test surface is assumed nonreflective, diffuse, and gray. The measured free-stream temperature is corrected for effects of recovery factor and relative humidity. The detailed analysis is documented by Rice [19].

Flow Measurements. A standard boundary layer type TSI crosswire is used to measure flow and turbulence information in the boundary layer. The crosswire is TSI (model 1243-T1.5, with 3.8 mm platinum coated tungsten material and a length/diameter ratio of 334.) The crosswire is operated at an overheat ratio of 1.5 in the constant temperature mode using TSI IFA-100 constant temperature anemometers. A sampling rates of 4 kHz and sampling duration of 30 s are employed. To remove aliasing, the Nyquist principle is employed by setting a low pass filter at 2 kHz on a third order (−18 db/octave) Sallen-Key type filter. The sample rate of 4 kHz is experimentally determined to sufficiently capture the content of 95% of the turbulence energy. The sampling duration of 30 s is found to provide a stable estimate for the mean and rms values. Sixteen measurements are taken at eight locations along the streamwise direction of the test section. At each x location, measurements are made at two y locations. One measurement is inside the boundary layer at approximately 1 mm from the test surface, and the second measurement is at the centerline, $y = 7.5$ cm, of the test section. The boundary layer thickness is about 2 mm at $x = 10$ cm and grows to about 50 mm at $x = 200$ cm with a free-stream velocity of 7 m/s. When the free-stream velocity is reduced to 4 m/s, the corresponding boundary layer thickness values are approximately 2.8 mm at $x = 10$ cm and 58 mm at $x = 200$ cm, respectively.

Uncertainty. The uncertainty analysis is conducted based on the theory of the Moffat [20] and closely follows the method used by Wang and Simon [21]. Twenty-four independent parameters are evaluated. The results of the uncertainty analysis for 7 m/s

Table 3 Summary of six largest contributions to uncertainty in Stanton number

Parameters	Individual uncertainty (%)
Epoxy resin thickness	2.03
k—epoxy resin	2.05
Test surface emissivity	1.72
Heater area	1.39
Free-stream velocity	1.07
Heater input	3.6
Total uncertainty (%)	5.67

with 40-grit surface roughness are summarized in Table 3. Only the six largest contributors are shown. The detailed analysis can be found in Rice [19].

Six sets of Stanton number data are taken for each case in a 14 hour period. The first set is obtained after a 3 h stabilization period followed by five sets, obtained at the 5th, 7th, 10th, 12th, and 14th h, respectively. The maximum unsteadiness in Stanton numbers during the period between the 5th and the 14th h period is approximately $\pm 2\%$. Including this unsteadiness, the uncertainty is 5.2% overall the smooth surface and 5.7% overall on the rough surfaces.

Results and Discussion

Surface Heat Transfer Measurements. The heat transfer results were presented in terms of Stanton number versus Reynolds number. Two baseline cases taken at 4.6 and 7.0 m/s at low FSTI (i.e., 0.2% and 0.4%) over a smooth surface are all laminar flow, as shown in Figs. 3 and 4. Both figures show that the smooth-wall results agree very well with the theoretical Blasius flow heat transfer correlation. The difference in transition onset point is due to reduced FSTI from 0.4% to 0.2% as air speed decreases from 7.0 to 4.6 m/s. The laminar and turbulent correlations for a uniformly heated smooth surface with unheated starting length are adopted from Kays and Crawford [22] as Eqs. (2) and (3). It should be noted that the laminar correlation with an unheated starting length appears different for various free-stream velocities when plotted in Fig. 3. This difference is attributed to the term, (x_{UHSL}/x). For example, if we look at Stanton numbers of two cases in Fig. 3 with different velocities at $\mathrm{Re}_x=10^5$, the Reynolds numbers are the same but the x values are different. This results in different Stanton numbers at the same Reynolds number for two cases with different velocities. To keep the figure clear, the correlations are plotted for the baseline smooth wall cases only

$$\mathrm{St}_{\mathrm{lam}}=0.453\mathrm{Pr}^{-0.67}\,\mathrm{Re}_x^{-0.5}\left[1-\left(\frac{x_{\mathrm{UHSL}}}{x}\right)^{0.75}\right]^{-0.333} \tag{2}$$

and

$$\mathrm{St}_{\mathrm{turb}}=0.0287\mathrm{Pr}^{-0.4}\,\mathrm{Re}_x^{-0.2}\left[1-\left(\frac{x_{\mathrm{UHSL}}}{x}\right)^{0.9}\right]^{-0.111} \tag{3}$$

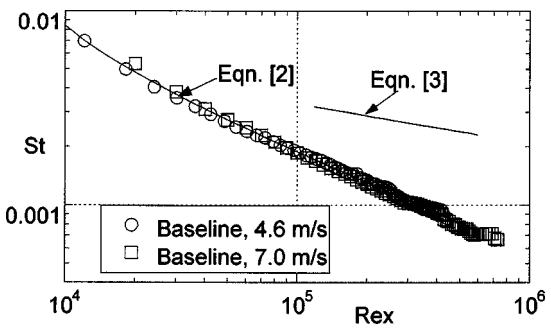

Fig. 3 Baseline cases

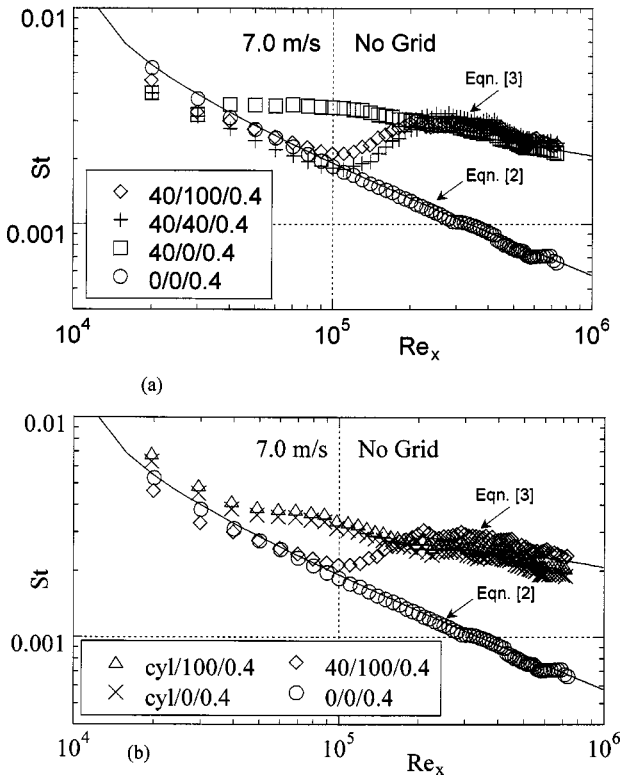

Fig. 4 (*a*) and (*b*) Comparison of leading edge and downstream surface roughness cases at 7.0 m/s without a grid

As shown in Fig. 3, the Stanton number distributions of the 4.6 and 7.0 m/s cases suggest that the flow is laminar for almost the entire length of the test surface. The laminar portion of the distributions is within an average of 3.5% of the correlation. The 4.6 m/s case has the largest deviation at an average of 2.5% above the correlation, while the data of 7.0 m/s case range from 1.5% below to 1.8% above the correlation. Overall, the agreement is considered good in light of the 5.27% uncertainty estimated for the smooth-wall heat transfer data.

Rough Surfaces at Low FSTI (no grid) Conditions. First, four rough surface conditions with no turbulence grid are conducted to duplicate the results of Pinson and Wang [17], as shown in Fig. 4(*a*). Recalling the naming scheme (''40/40/0.4'') means that both the leading edge and the downstream portion of the surface are covered with 40-grit sand paper with an R_a roughness level of 119 μm and with an inlet FSTI=0.4%. The onset of transition (observed by the location where the Stanton number starts to deviate from the laminar correlation) occurs at $\mathrm{Re}_x=0.25\times 10^5$, which was 72% earlier than the transition onset of the corresponding smooth-wall case. When the downstream portion of the 40-grit sandpaper is replaced by a decreasing roughness strip of 100-grit sandpaper ($R_a=37$ μm), i.e., the 40/100/0.4 case, an earlier transition onset is triggered at a $\mathrm{Re}_x=7.0\times 10^4$. Recall that the location of the end of the 5 cm 40-grit band coincides with the location of the second thermocouple. The combination of a rough leading edge and a smaller downstream roughness introduces a larger backward-facing step, which triggers stronger instability. This result successfully duplicates the experiments performed by Pinson and Wang [17].

An examination of the 40/0/0.4 case, which is obtained by removing the downstream 100-grit sandpaper, shows that transition occurs much earlier at $\mathrm{Re}_x=2.84\times 10^4$ than either in the 40/100/0.4 or the 40/40/0.4 cases. This agrees with the results observed by Pinson and Wang [17]. This implies that increasing the step

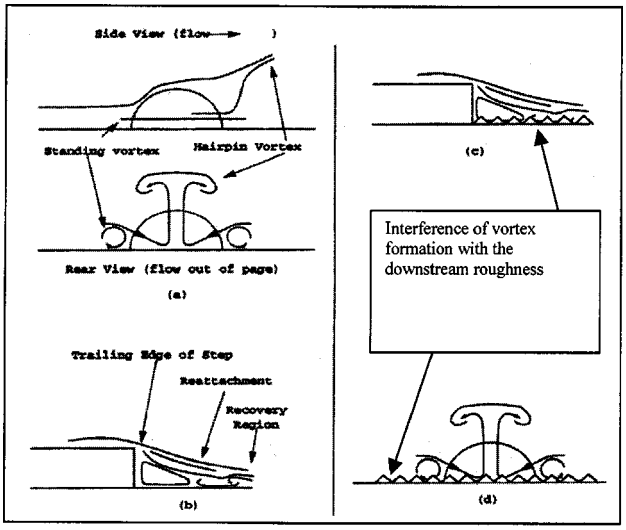

Fig. 5 Conceptual drawings of flow past two different flow disturbances: (*a*) flow past an isolated hemisphere (Acarlar and Smith [23]); (*b*) flow past a backward-facing step (Ruderich and Fernholz [24]); (*c*) flow past backward-facing step with downstream roughness, (*d*) flow past a hemisphere and surrounding roughness

height by reducing the downstream surface roughness is more effective than increasing the downstream roughness to trigger an earlier transition.

Pinson and Wang [17] hypothesized that the source of increased instability in the flow was caused by the step change at the joint between the 100-grit and 40-grit sandpaper. To illustrate this concept, Pinson and Wang applied conceptual drawings of flows past a hemispherical disturbance [23] and a backward-facing step [24] to a dual-scale roughness surface as shown in Fig. 5. Acalar and Smith [23] documented a standing vortex forms near its base as the flow moves around the hemisphere, and joining of the two halves behind the hemisphere forms the formation of a hairpin type vortex. The reduction in the step size by adding additional roughness [Figs. 5(*c*) and 5(*d*)] around the base of the object reduces the opportunity for them to form.

Reviewing the major features of the flow past the step, Eaton and Johnston [25] suggested that the foremost aspects are a separation bubble and a recovery region, which cause a region with the characteristics of an unseparated boundary layer. Upon the separation bubble forming immediately downstream of the trailing edge of the step, the separated shear layer reattaches downstream of the bubble. The reattachment of the shear layer is very complicated and location of the exact streamwise reattachement point is unsteady with the shedding of the turbulent structures downstream. Immediately following the reattachement, the boundary layer undergoes a recovery from the effects of the upstream step and eventually regains the characteristics of an unseparated boundary layer condition. The earlier investigations support that the addition of a small roughness behind a backward facing step substantially change the separation bubble behavior and point of reattachment of the shear layer as a result of the reduction in step scale. This change of flow structure reduces the disturbances to the surrounding boundary layer flow.

Once the present study verifies Pinson and Wang's *first hypothesis that the backward facing height was the primary factor controlling the onset of transition*, more experiments are conducted in the present study to verify their second hypothesis, which would establish a firm background for further studies in elevated FSTI conditions. *Their second hypothesis states that if the scale of the step height is the dominant factor, then the geometry of this step only plays a secondary role*. To verify this second hypothesis, a 1

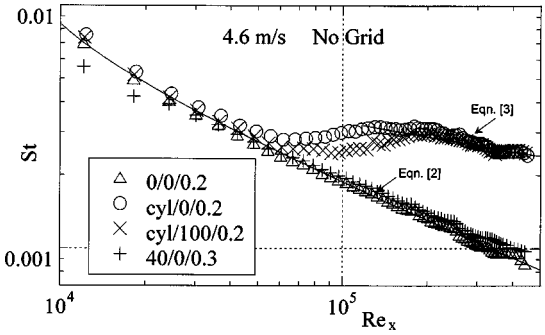

Fig. 6 Comparison of leading edge roughness for 4.6 m/s without a grid

mm diameter cylinder is deployed at the leading edge. At 7.0 m/s, the cyl/0/0.4 case seems to only slightly lead 40/0/0.4 case in starting transition [Fig. 4(b)]. This minor difference on onset of transition can be seen more clearly by reducing the flow speed to 4.6 m/s. As shown by Fig. 6, the two-dimensional cylinder case certainly triggered an earlier transition than the three-dimensional sand grains of the sandpaper. This verifies that geometry of the roughness still matters but only plays a secondary role. This is consistent with the findings of [17] and Braslow [26], who observed the difference between two- and three-dimensional disturbances showing those three-dimensional disturbances are less effective in destabilizing a laminar layer than two-dimensional disturbances.

A comparison between cases cyl/0/0.4 and cyl/100/0.4 also indicates that at 7.0 m/s the difference on onset of transition is minor; however, when the flow speed is reduced to 4 m/s, cyl/0/0.4 case shows an earlier transition (see Fig. 6). The cylinder diameter used during investigation was 1 mm, which is a trace larger than the thickness of the roughness (0.87 mm) of the strip. This addition of 100-grit sandpaper does not change the surface roughness too much but it does affect the step height at the joint between the strip and the 100-grit sandpaper.

To this point, the low FSTI cases performed by the present study have verified Pinson and Wang's two hypotheses and will be used as the reference for elevated FSTI studies.

Elevated Free-Stream Turbulence. In this section, the results of wall heat transfer measurements and two-point cross-wire measurements are presented with elevated free-stream turbulence intensities of 3.3–4.2% for grid 1, and 5.0–6.0% for grid 2 at zero pressure gradient.

Smooth Wall at Elevated FSTI. The centerline Stanton number distribution for the four smooth-wall cases at different FSTI (3.3–6.0%) and two different free-stream velocities are shown in Figs. 7 and 8. For both grid 1 (FSTI=3.3%) and grid 2 (FSTI=5.0%) cases in Fig. 7, the transition point occurs approxi-

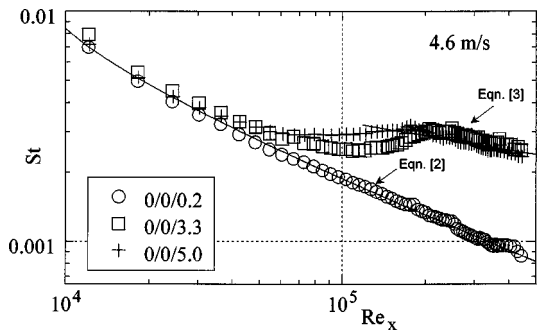

Fig. 7 Effect of FSTI on smooth wall cases at 4.6 m/s

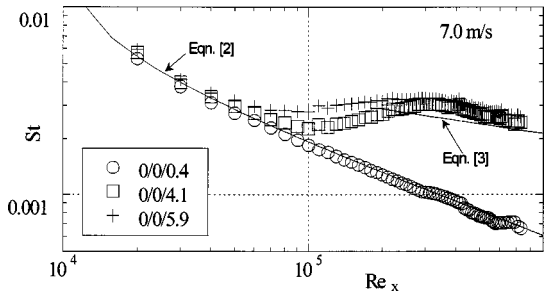

Fig. 8 Effect of FSTI on smooth wall cases at 7.0 m/s

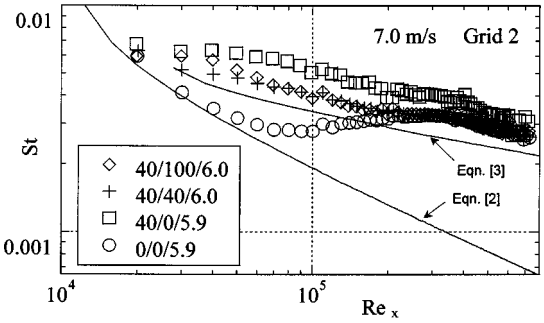

Fig. 10 Comparison of smooth and rough wall cases with grid 2 (FSTI~6%) at 7.0 m/s

mately at $Re_x=5\times10^4$. In the laminar part, the Stanton numbers are about 10% higher than the zero-turbulence laminar correlations. In the turbulent region, the Stanton number follows the low-FSTI turbulent correlation, i.e., the effect of elevated FSTI is not shown to increase heat transfer in the turbulent region at the low speed of 4.6 m/s. For the smooth wall cases at 7.0 m/s as shown in Fig. 8, the onsets of transition are located at $Re_x=7\times10^4$ for grid 1 case (0/0/4.1) and at $Re_x=6\times10^4$ for grid 2 case (0/0/5.9), respectively. The end of transition is found to be at $Re_x=3\times10^5$ and $Re_x=2\times10^5$ for grids 1 and 2, accordingly. The increase in free-stream turbulence intensity causes a quicker onset of transition and shorter length of transition. Zhou and Wang [27] provided a detailed report of the effects of FSTI on transitional boundary layer flow, thermal structures, and heat transfer on the wall using this same test facility.

Rough Walls With Elevated FSTI. The heat transfer results of four rough surfaces using grid 1 at 7.0 m/s are shown in Fig. 9. By adding 40-grit roughness over the entire surface (40/40/4.1), the transition point moves from $Re_x=7\times10^4$ of the 0/0/4.1 case to near the leading edge. The flow is immediately triggered to turbulent flow within the first two inches of the leading edge. This indicates that even under elevated FSTI at 4%, the 40-grit roughness with $R_a=119\,\mu$m can still significantly trigger much earlier transition. Replacing the downstream portion of the sandpaper with the 100-grit sandpaper (the 40/100/4.2 case), a maximum Stanton number is induced at $Re_x=3.0\times10^4$ as a result of the step height between the 40- and 100-grit surface. When further removing the downstream portion of the 100-grit sandpaper for case 40/0/4.0, Stanton numbers are significantly enhanced about 30–40% above the values of the 40/100/4.2 case all the way downstream. This heat transfer augmentation between the 40/0/4.0 and 40/100/4.2 cases is not seen in low FSTI cases shown in Fig. 4. It seems that elevated FSTI is able to continuously feed energy to the disturbance produced by the backward facing step and exerts a long-lasting heat transfer enhancement downstream. It could also be interpreted that the vortical motion generated by the backward facing step significantly increases momentum transport across the boundary layer and bring the elevated turbulence from the freestream to the wall. This results to a significantly enhanced wall heat transfer. No such long-lasting heat transfer phenomenon is observed in low FSTI cases even though vortex shedding also exists in the low turbulence cases. A further increase of the FSTI to 5.9, using grid 2, produces similar results as shown in Fig. 10. The heat transfer of the case with a large step height 40/0/5.9 is about 30–40% higher than the 40/40/6.0 and 40/100/6.0 cases. These results imply that the hypothesis of step-height playing a dominant role on affecting transitional flow and downstream heat transfer was not only valid in low FSTI conditions, as observed by Pinson and Wang [17], but also valid in elevated FSTI conditions.

At a low air velocity of 4.6 m/s, the FSTI effect becomes more dominant than the roughness effect, as can be seen in Fig. 11. The surface roughness and step change between two regions of roughness does not trigger much earlier transition as they did at 7.0 m/s (Fig. 10). The effects of step height and surface roughness are minor but can still be seen in Fig. 11 because the onset of transition moves earlier following the order of 40/0/4.9, 40/100/5.0, and 40/40/5.2. This can be explained as that at low air velocities, the boundary layer is thicker and the viscous effect is important, so the viscous damping effect is stronger. Therefore, the separation triggered by the backward facing step is less vigorous, and the effect of the leading edge roughness is reduced. Although the step height does not trigger much earlier transition in low velocity, the effect of step height is still fairly pronounced, as can be evidenced by the fact that the Stanton numbers of case 40/0/4.9 are about 20% higher than other cases.

To further examine the effect of geometry, a 1 mm diameter cylinder is used. The results shown in Fig. 12 do not clearly indicate that cyl/0/5.2 case triggers an earlier transition than the cyl/100/5.0 case does, but it is clearly shown that cyl/0/5.2 case has 10% higher Stanton numbers than cyl/100/5.0 and 40/0/4.9 cases have. The cyl/0/5.2 case seems to have a bit earlier onset of transition than 40/0/4.9 case, but the difference is very small. In Fig.

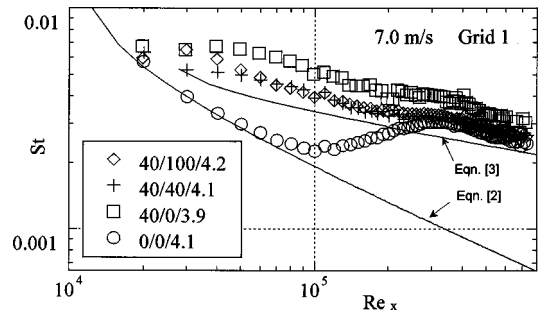

Fig. 9 Comparison of smooth and rough wall cases at 7.0 m/s with grid 1 (FSTI ~4%)

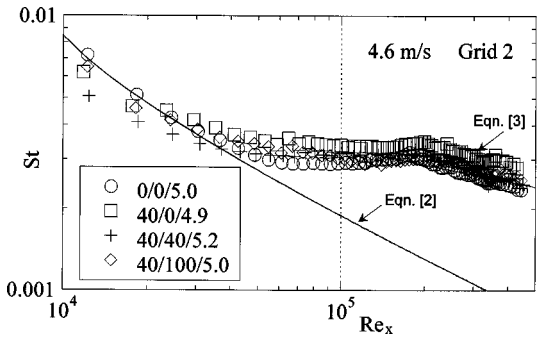

Fig. 11 Comparison of smooth and rough wall cases at 4.6 m/s with grid 2 (FSTI~5%)

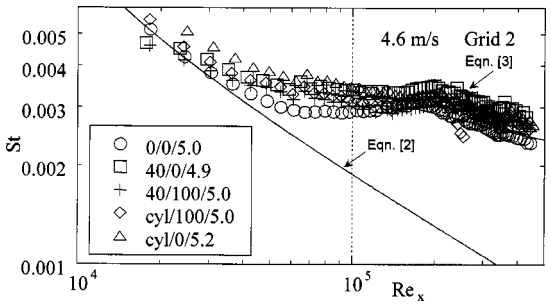

Fig. 12 Comparison of smooth and rough wall cases at 4.6 m/s with grid 2 (FSTI~5%)

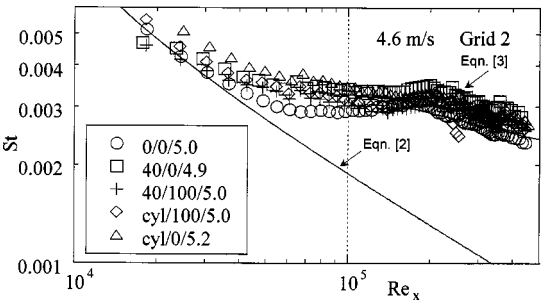

Fig. 14 Free-stream integral length scale distributions

12, the heat transfer enhancement of cyl/0/5.2 case is highest in the disturbed laminar boundary layer and transitional region. This implies that the leading-edge cylinder has induced larger disturbances than a strip of rough sandpaper has even at elevated FSTI conditions. Pinson and Wang's second hypothesis is proved marginally valid at elevated FSTI conditions but its importance is not as significant as in the low FSTI and low free-stream velocity conditions.

Discussion of Flow Measurements

To gain some insight into the effects of the leading-edge and surface roughness on the flow structure and surface heat transfer, two-point flow measurements are taken by using a hot-wire probe. One measurement is taken in the free stream and the second measurement is taken at 1 mm from the test surface. The five representative conditions (40/0, 40/100, 40/40, cyl/0, cyl/100 at 4.6 and 7.0 m/s, respectively) are investigated with different free-stream turbulence levels ranging from 0.2% to 6.0%. All cases are compared to the baseline smooth wall case at low FSTI. Figures 13–15 represent the free-stream condition in terms of FSTI, integral length scale, and u'/v'.

Free-Stream Turbulence. The FSTI distributions along the streamwise direction in the test section are calculated based on the two components of the velocity fluctuations. Figure 13 shows the baseline (no grid) condition where the FSTI stays at about 0.2% for 4.6 m/s and about 0.4% for 7.0 m/s, respectively. For the elevated FSTI cases, the FSTI remains almost constant with only slight variations throughout the test section.

Integral Length Scale. The integral length scales, Λ_f, are calculated by integrating the streamwise autocorrelation coefficient to the first zero crossing with the abscissa. As shown by Fig. 14, the integral length scale increases downstream from the leading edge and increases as the speed is decreased. The Λ_f values are 1.5–2.5 cm for the baseline no-grid case, 2–3 cm for the grid 1 case, and 4–6 cm for the grid 2 case. As expected, the integral length scales downstream of the grids are controlled by the grid sizes. Also as expected, the average integral length scales (Λ_f) are close to the actual grid size values. For example, the average integral length scale of the grid 1 case is 3.5 cm which corresponds to the grid size of 3.7 cm and for the grid 2 case, they are 5 cm (Λ_f) vs 7.62 (grid size) accordingly.

The value of v'/u', shown in Fig. 15, indicates that the grid-generated turbulence achieves better isotropy at 1.2–0.8 than no-grid case at 0.3–0.8.

Normalized Streamwise Velocity Fluctuations (u'/U_{inf}) Figure 16 shows the distribution of the normalized streamwise velocity fluctuations, u'/U_{inf}, along the streamwise distance of the test surface at 4.6 m/s with grid 1. Typically u'/U_{inf} value increases from the leading edge to a maximum value of about $x = 30$ cm and then levels off downstream. By comparing u'/U_{inf} distributions with the Stanton number distributions, the increasing trend of the u'/U_{inf} values from the leading edge indicates laminar-turbulent transition. Among these cases, the cyl/100/3.26 case distinctively shows an increased u' distribution. This could be contributed by a highly concentrated vortex-shedding energy,

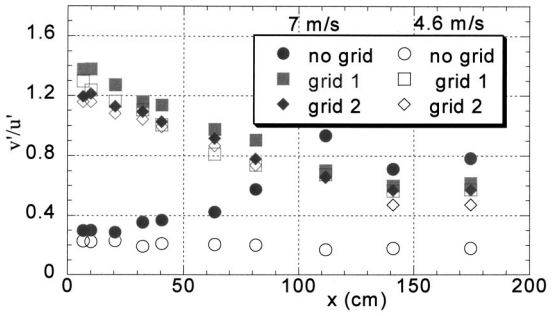

Fig. 15 Free-stream distributions of v'/u'

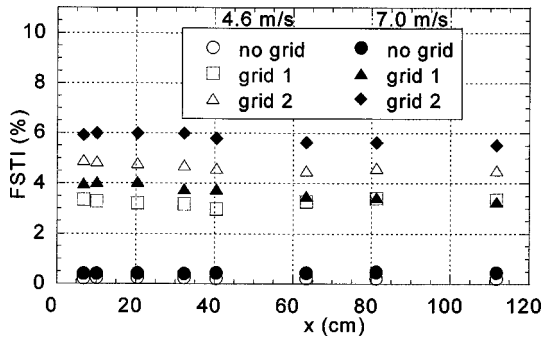

Fig. 13 Comparison of smooth and rough wall cases at 4.6 m/s with grid 2 (FSTI~5%)

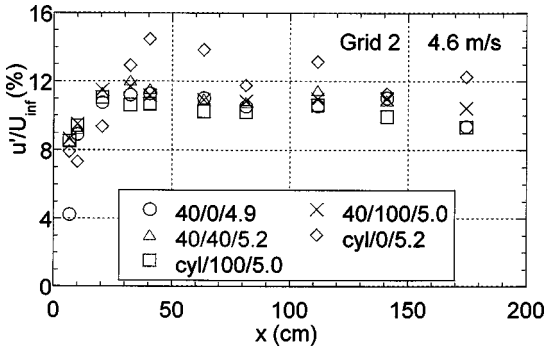

Fig. 16 Streamwise velocity fluctuation distributions in boundary layer at $y=1$ mm with grid 2 at 4.6 m/s

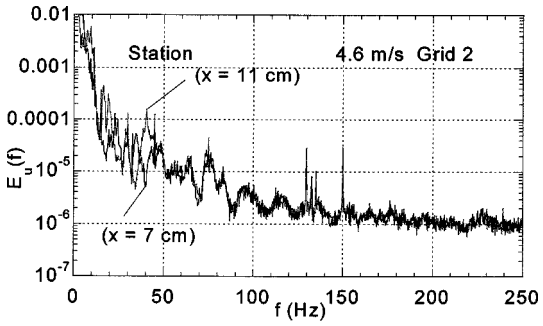

Fig. 17 Power spectrum density (PSD) function of the 40/0/4.9 case in boundary layers at $y=1$ mm with grid 2 at 4.6 m/s

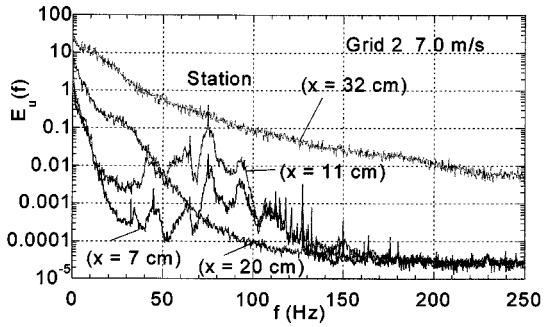

Fig. 19 PSD function of 40/100/6.0 case in boundary layers at $y=1$ mm with grid 2 at 7.0 m/s

as previously suggested by Pinson and Wang [17] in low turbulence conditions. This separation-induced vortex shedding also seems to occur in the present high FSTI cases. To further investigate the possible vortex shedding in elevated FSTI conditions, the power spectra of the first two measuring points downstream of the leading edge of the 40/0/3.3 cases are produced and shown in Fig. 17. In a frequency range lower than 50 Hz; discrete energy peaks are randomly distributed across the 50 Hz band for both stations 1 and 2. Above 50 Hz, the spectrum of these two stations coincide and exhibit multiple peaks and humps containing discrete concentrations of spectral energy. These peaks and humps do not follow simple harmonic and subharmonic traits but manifest a multimode unsteadiness, which was not seen in the low FSTI cases in this study or in Ref. [17].

It is speculated that elevated FSTI is generating more complex multimodes of vortex shedding than the simple mode observed in the low FSTI cases. A further investigation of this phenomenon is performed at a higher velocity. Figure 18 shows u'/U_{inf} distributions for various cases at 7.0 m/s using grid 2. The u'/U_{inf} value of the case with the cylinder continues to exceed those of all other cases at high speed.

The PSD function of the 40/100/6.0 case is produced and shown in Fig. 19. Similar to the low speed case in Fig. 17, multiple peaks occur in Fig. 19 at frequencies of 35, 45, 65, 75, 95, 105 Hz, and other frequencies until about 135 Hz. Again these multimode disturbances were different from the concentrated vortex shedding frequency observed by Pinson and Wang [17] in low FSTI study. Since there was only one point measurement in the boundary layer at each station, the vortex-shedding phenomenon was not captured in all cases.

Normalized Cross-Stream Velocity Fluctuations (v'/U_{inf}) The distributions of v'/U_{inf} at 4.6 and 7.0 m/s for all representative cases are shown in Figs. 20 and 21, accordingly. Similar to the trend of u'/U_{inf}, the cylinder cases have higher u'/U_{inf} values than the 40-grit cases have. In Figs. 16 and 18, the v'/U_{inf} values of the cylinder cases are about 10–20% higher than those of the 40-grit cases, but in Figs. 20 and 21, v'/U_{inf} values are about 30–50% higher than those of the 40-grit cases. This implies that the cylinder cases introduce higher cross-stream fluctuations than the 40-grit cases. Figure 21 represents the leading edge and downstream roughness for v'/U_{inf} at 7.0 m/s. At the lower speed of 4.6 m/s, the v'/U_{inf} decreases almost immediately with a steep slope near the leading edge instead of increasing to a maximum and gradually decaying afterwards as typically occurs in the transitional boundary layer flow. This implies a much quicker (or shorter) transition at 7.0 m/s than that at 4.6 m/s.

Normalized Reynolds Shear Stress ($-\overline{uv}/U_{\text{inf}}^2$). The distribution of the normalized Reynolds shear stress, $(-\overline{uv}/U_{\text{inf}}^2)$, for all representative cases are shown in Figs. 22 and 23 for 4.6 and 7.0 m/s, respectively. In these two figures, the cylinder cases have much larger values than the 40-grit case does for both 4.6 and 7.0

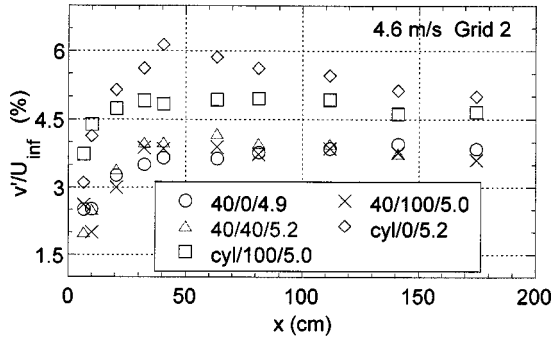

Fig. 20 Cross-stream velocity fluctuations in boundary layers at $y=1$ mm with grid 2 at 4.6 m/s

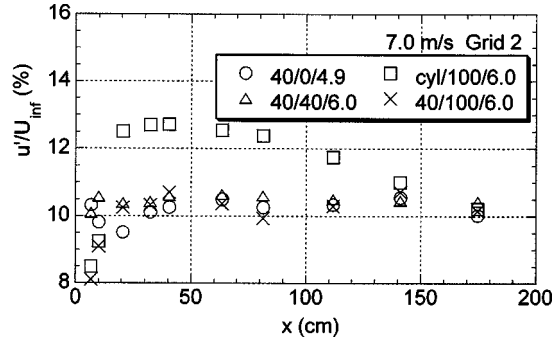

Fig. 18 Streamwise velocity fluctuation distributions in boundary layer at $y=1$ mm with grid 2 at 7.0 m/s

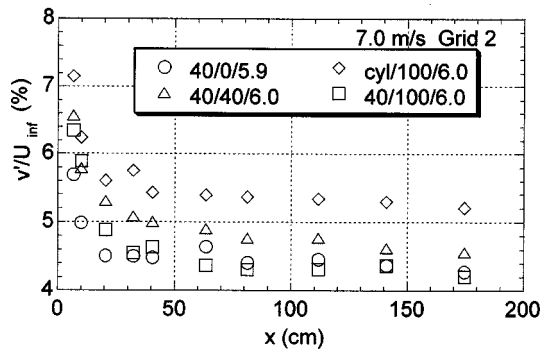

Fig. 21 Cross-stream velocity fluctuations in boundary layers at $y=1$ mm with grid 2 at 7.0 m/s

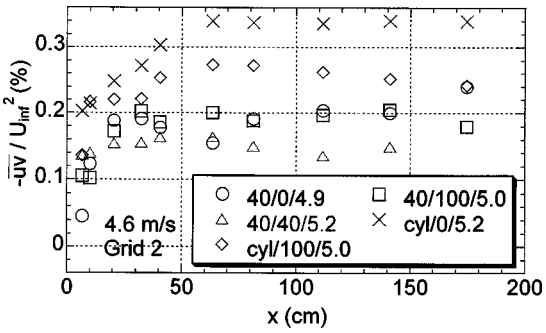

Fig. 22 Normalized Reynolds shear stress distributions in boundary layers at $y=1$ mm with grid 2 at 4.6 m/s

m/s. This implies that the multimode unsteadiness, which are produced by various sizes of vortices, is turbulent in nature and produces high Reynolds shear stress and turbulent transports. All the earlier analyses in the boundary layer support the vortex shedding hypothesis, as a result of flow separation behind roughness step change.

Conclusions

This paper extends the previous study of investigating the effects of dual-scale roughness on laminar-turbulent transition and heat transfer into flows with elevated free-stream turbulence. The results are as follows.

(1) This study duplicates previous cases in lower FSTI conditions; the results are consistent with those reported by Pinson and Wang [17].

(2) Rough walls, even under elevated FSTI conditions, can trigger significantly much earlier transition.

(3) Similar to in the low FSTI cases, the scale of the step change of roughness height is proven to be the primary cause of earlier transitions in elevated FSTI cases. The two cases studied suggest that geometry of the roughness plays a less important role in affecting laminar-turbulent transition and heat transfer downstream if the height scales of the roughness geometries are different.

(4) Similar to in the low FSTI cases, adding second roughness scale downstream of the initial leading edge roughness does not increase disturbances, instead it reduces disturbances. This is believed to be caused by the reduced step height and suppressed vortex dynamics.

(5) The relatively small scale of the roughness geometries tested does not induce any significant deviation of Stanton number from the smooth-wall laminar correlations in the low free-stream turbulence cases, but heat transfer enhancement of various degrees are observed in the turbulent boundary layer. This phenomenon is not seen in low FSTI cases.

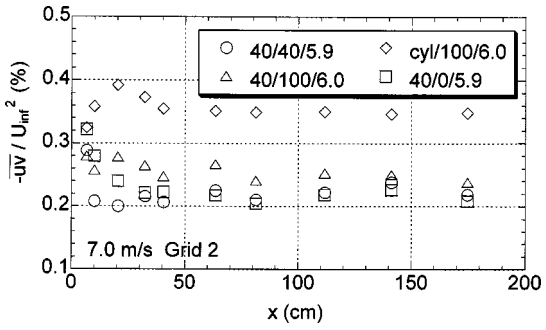

Fig. 23 Normalized Reynolds shear stress distributions with grid 2 at 7.0 m/s

(6) Under elevated FSTI conditions, the cases having a large roughness step change produce a heat transfer enhancement of 30–40%, along the entire test plate, above cases having a small step change. This enhancement could be explained in two plausible ways: (a) the elevated FSTI is able to continuously feed energy to the disturbance produced by the backward facing step and exerts a long-lasting heat transfer enhancement downstream. (b) The vortical motion generated by the backward facing step significantly increases momentum transport across the boundary layer and brings the elevated turbulence from the freestream to the wall. This results to a significantly enhanced wall heat transfer. No such long-lasting heat transfer phenomenon is observed in low FSTI cases even though vortex shedding also exists in the low turbulence cases.

(7) This separation-induced vortex shedding is confirmed by power spectra analysis in the boundary layer. However, in elevated FSTI cases, miltimode disturbances are observed, which are different from the concentrated vortex shedding frequency observed in low FSTI study.

(8) The data of u'/U_{inf} and v'/U_{inf} support the fact that the two-dimensional roughness (cylinder cases) introduced higher cross-stream fluctuations than the three-dimensional roughness (40-grit cases).

(9) At the higher speed (7 m/s), the roughness effect is more pronounced, whereas, at a lower speed (4.6 m/s), FSTI effect is dominant due to a thicker boundary layer, which reduces the effect of geometry-introduced disturbance via viscous damping.

The discovery in this paper is important because it implies that time and effort could be saved for predicting heat transfer over multiscale rough surface by focusing on the effect of the height of the larger-scale roughness and relaxing the needs for obtaining precise geometries and patterns of the roughness of small scales.

Nomenclature

$C_{p,\infty}$ = free-stream specific heat
$E(f)$ = power spectral density
FSTI = free-stream turbulence intensity
k = roughness height or roughness
k^+ = kU_τ/ρ, nondimensional roughness
k_s = equivalent sand grain roughness height
L = length of surface profile
Pr = Prandtl number
q''_{conv} = convective heat flux to free-stream
R_a = $(1/L)\int_{x=0}^{x=L}|y(x)|dx$, average roughness level—$y(x)$ is measured from the midpoint between the average peak and valley heights
R_z = average peak-valley roughness level
Re = xU_∞/ν, Reynolds number
St = Stanton number [see Eq. (1)]
T_W = wall surface temperature
T_∞ = free-stream temperature
u' = rms streamwise velocity fluctuation
$\overline{uv}$ = Reynolds shear stress
U_∞ = mean free-stream velocity
U_τ = $(\tau_w/\rho)^{0.5}$, friction velocity
v' = rms cross-stream velocity fluctuation
x_{UHSL} = unheated starting length of test surface (2.5 cm)

Greek symbols

Λ_f = integral length scale
ν = kinematic viscosity
ρ_∞ = free-stream air density
τ_w = wall shear stress

References

[1] Tarada, F. H. A., 1987, "Heat Transfer to Rough Turbine Blading," Ph.D. Disertation, University of Sussex, England.
[2] Taylor, R. P., 1990, "Surface Roughness Measurements on Gas Turbine Blades," ASME J. Turbomach., **112**, pp. 175–180.

[3] Boynton, J. L., Tabibzadeh, R., and Hudson, S. T., 1993, ''Investigation of Rotor Blade Roughness Effects on Turbine Performance,'' ASME J. Turbomach., **115**, pp. 614–620.
[4] Tarada, F., and Suzuki, M., 1993, ''External Heat Transfer Enhancement to Turbine Blading Due to Surface Roughness,'' ASME paper 93-GT-74.
[5] Suder, K. L., Chima, R. V., Strazisar, A. J., and Roberts, W. B., 1995, ''The Effect of Adding Roughness and Thickness to a Transonic Axial Compressor Rotor,'' ASME J. Turbomach., **117**, pp. 491–505.
[6] Blair, M. F., 1994, ''An Experimental Study of Heat Transfer in a Large-Scale Turbine Rotor Passage,'' ASME J. Turbomach., **116**, pp. 1–13.
[7] Bunker, R. S., 1997, ''Effect of Discrete Surface Disturbances on Vane External Heat Transfer,'' ASME paper 97-GT-134.
[8] Bunker, R. S., 1997, ''Separate and Combined Effects of Surface Roughness and Turbulence Intensity on Vane Heat Transfer,'' ASME paper, 97-GT-135.
[9] Gibbings, J. C., and Al-Shukri, S. M., 1997, ''Effect of Sandpaper Roughness and Stream Turbulence on the Laminar Layer and Its Transition,'' Aeronaut. J., **101**, pp. 17–24.
[10] Bons, J. P., 2002, ''St and C_f Augmentation for Real Turbine Roughness With Elevated Freestream Turbulence,'' Proceedings of ASME Turbo Expo 2002, GT-2002-30198, Amsterdam, Netherlands.
[11] Sigal, A., and Danberg, J. E., 1990, ''New Correlation of Roughness Density Effect on the Turbulent Boundary Layer,'' AIAA J., **28**, pp. 554–556.
[12] Bogard, D. G., Schmidt, D. L., and Tabbita, M., 1996, ''Characterization and Laboratory Simulation of Turbine Airfoil Surface Roughness and Associated Heat Transfer,'' ASME paper 96-GT-386.
[13] Belnap, B. J., van Rij, J. A., and Ligrani, P. M., 2002, ''A Reynolds Analogy for Real Component Surface Roughness,'' Int. J. Heat Mass Transfer, **45**, pp. 3089–3099.
[14] Bons, J. P., Taylor, R., McClain, S., and Rivir, R. B., 2001, ''The Many Faces of Turbine Surface Roughness,'' ASME J. Turbomach., **123**(4), pp. 739–748.
[15] Pinson, M. W., and Wang, T., 1997, ''Effects of Leading-Edge Roughness on Fluid Flow and Heat Transfer in the Transitional Boundary Layer Over a Flat Plate,'' Int. J. Heat Mass Transfer, **40**, pp. 2813–2823.
[16] Finson, M. L., 1975, ''A Reynolds Stress Model for Boundary Layer Transition With Application to Rough Surfaces,'' Physical Sciences, Inc., TR-34.
[17] Pinson, M. W., and Wang, T., 2000, ''Effect of Two-Scale Roughness on Boundary Layer Transition Over a Heated Flat Plate: Part 1: Surface Heat Transfer and Part 2: Boundary Layer Structure,'' Int. J. Heat Mass Transfer, **122**, pp. 301–307, 308–316.
[18] Pinson, M., 1992, ''The Effects of Initial Conditions on Heat Transfer in Transitional Boundary Layers,'' M.S. Thesis, Department of Mechanical Engineering, Clemson University, Clemson, SC.
[19] Rice, M. C., 1999, ''Effect of Elevated Free-Stream Turbulence on Heat Transfer Over Two-Scaled Rough Surfaces,'' Master Thesis, Dept. of Mechanical Engineering, Clemson University, Clemson, SC.
[20] Moffat, R. J., 1982, ''Contributions to the Theory of Single-Sample Uncertainty Analysis,'' ASME J. Fluids Eng., **104**, pp. 250–260.
[21] Wang, T., and Simon, T. W., 1989, ''Development of a Special Purpose Test Surface Guided by Uncertainty Analysis,'' J. Thermophys., **3**(1), pp. 19–26.
[22] Kays, W. M., and Crawford, M. E., 1993, *Convective Heat and Mass Transfer*, 3rd ed., McGraw-Hill, New York, pp. 175, 179, and 281.
[23] Acarlar, M. S., and Smith, C. R., 1987, ''A Study of Hairpin Vortices in a Laminar Boundary Layer. Part 1. Hairpin Vortices Generated by a Hemisphere Protuberance,'' J. Fluid Mech., **175**, pp. 1–41.
[24] Ruderich, R., and Fernholz, H. H., 1986, ''An Experimental Investigation of a Turbulent Shear Flow With Separation, Reverse Flow, and Reattachment,'' J. Fluid Mech., **163**, pp. 283–322.
[25] Eaton, J. K., and Johnston, J. P., 1981, ''A Review of Research on Subsonic Turbulent Flow Reattachment,'' AIAA J., **19**, pp. 1093–1100.
[26] Braslow, A. L., 1960, ''Review of the Effect of Distributed Surface Roughness on Boundary-Layer Transition,'' Advisory Group for Aeronautical Research and Development, Report 254.
[27] Zhou, D., and Wang, T., 1996, ''Combined Effects of Elevated Free-Stream Turbulence and Streamwise Acceleration on Flow and Thermal Structures in Transitional Boundary Layers,'' Exp. Therm. Fluid Sci., **12**, pp. 338–35.

Roland S. Muwanga
Department of Mechanical and Industrial Engineering, Concordia University, 1455 de Maisonneuve Boulevard W., Montreal, Quebec, H3G 1M8, Canada
e-mail: roland.muwanga@pwc.ca

Sri Sreekanth[1]
Turbine Module Center, Pratt and Whitney Canada, 1801 Courtney Park Drive, Mississauga, Ontario, L5T 1J3, Canada
e-mail: sri.sreekanth@pwc.ca

Daniel Grigore
Product Reliability and Safety, Pratt and Whitney Canada, 1000 Marie Victorin Boulevard, Longueuil, Quebec, J4G 1A1, Canada
e-mail: daniel.grigore@pwc.ca

Ricardo Trindade[2]
e-mail: ricardo.trindade@pw.utc.com

Terry Lucas
e-mail: terry.lucas@pwc.ca

Turbine Module Center, Pratt and Whitney Canada, 1000 Marie Victorin Bouelvard, Longueuil, Quebec, J4G 1A1, Canada

Effect of Input Variability on the Performance of Turbine Blade Thermal Design Using Monte Carlo Simulation: An Exploratory Study

A probabilistic approach to the thermal design and analysis of cooled turbine blades is presented. Various factors that affect the probabilistic performance of the blade thermal design are grouped into categories and a select number of factors known to be significant, for which the variability could be assessed are modeled as random variables. The variability data for these random variables were generated from separate Monte Carlo simulations (MCS) of the combustor and the upstream stator and secondary air system. The oxidation life of the blade is used as a measure to evaluate the thermal design as well as to evaluate validity of the methods. Two approaches have been explored to simulate blade row life variability and compare it with the field data. Field data from several engine removals are used for investigating the approach. Additionally a response surface approximation technique has been explored to expedite the simulation process. The results indicate that the conventional approach of a worst-case analysis is overly conservative and analysis based on nominal values could be very optimistic. The potential of a probabilistic approach in predicting the actual variability of the blade row life is clearly evident in the results. However, the results show that, in order to predict the blade row life variability adequately, it is important to model the operating condition variability. The probabilistic techniques such as MCS could become very practical when approximation techniques such as response surface modeling are used to represent the analytical model. [DOI: 10.1115/1.1861922]

1 Introduction

The fundamental function of a turbine blade is to extract work efficiently and, hence, the aerodynamic efficiency of the blade is the prime objective in its design. Modern blades, however, work in a high temperature/high speed regime making the durability of the blade itself a prime concern to the blade designers. The durability of the blade is achieved by appropriate thermal design of the blade, which incorporates a combination of internal and film cooling, as well as choosing appropriate material/coating for oxidation resistance and thermal protection. The thermal design of a turbine blade will have to cater to often conflicting requirements of aerodynamic performance targets, manufacturing constraints, and restrictions on the thermodynamic performance of the engine (cooling air requirements), yet meet the durability requirements.

The parameters which influence the turbine blade thermal design have a significant variability associated with them. The variability originates for a plethora of reasons. For example, the operating turbine entry temperature (TET) is a strong function of the ambient temperature for a given thrust and, hence, fluctuates with it. The manufacturing and build tolerances of various components of the engine result in engines requiring different TET for a given thrust and ambient temperature. In order to ensure a robust design of the turbine blade from the durability point of view, it is imperative to understand the variability associated with the blade design parameters and its impact on the blade metal temperature. In the absence of this understanding the designer will have to consider a conservative theoretically defined worst-case scenario. This is not always possible and therefore the designer will at other times consider trade-offs based on the nominal and worst case condition [1]. This worst-case condition is in general specific to the company, department, or problem. In the present work the worst case is taken as twice the standard deviation from the mean, in the direction of undesirable effects. Such worst-case scenarios severely compromise the cost and/or the performance of the engine. As well they are not always the best, as they do not shed light on the reliability of a particular design. Finally, understanding the variability will drive the designers towards more robust blade designs.

In order to assess the reliability of the turbine blade thermal design, the input variability needs to be understood and this variability should be allowed to propagate through the design process, so that the variability in the blade life can be captured. Probabilistic techniques such as Monte Carlo simulations have been traditionally applied in similar situations.

Lykins and Thompson [2] describe the initiative taken by the US Air Force to develop a probabilistic design system for the design of turbine disks at Pratt and Whitney and at General Elec-

[1]To whom correspondence should be addressed.
[2]Present address: Turbine Durability, Pratt and Whitney, 400 Main St., East Hartford, CT 06108.

Manuscript received April 8, 2004; revised manuscript received October 20, 2004. Review conducted by: P. M. Ligrani.

tric. While no results are presented in the paper, they recognize the need for a probabilistic approach to the design of gas turbine engines. Pomfret [3] has emphasized the need for utilization of probabilistic approach for risk management in gas turbine engines. They have reported that 82 lb of engine weight could have been saved by designing the turbine disk alone using probabilistic approach as opposed to deterministic worst-case scenario design—without any increase in the risk of failure. This translates into a life cycle cost saving of $490 million. Ghiocel and Rieger [4] applied probabilistic approach to model a gas turbine fan blades high cycle fatigue (HCF) life. Shen [5] used fast probability integration technique to develop a probabilistic HCF life prediction of a turbomachinery blade. In his paper, the damping distributions were obtained from the measured vibratory stress distributions and the resulting probabilistic damping data was used to assess the probability of failure of the blade. Liu et al. [6] have outlined a method for making assessment of residual creep life of gas turbine components using Monte Carlo simulation. Their method focuses on using a response surface method to simplify the model and a Monte Carlo simulation (MCS) of the response surface using online measured data with its uncertainty to get a probabilistic assessment of the creep life. Garzon and Darmofal [7] assessed the impact of the blade geometry variability on the compressor performance. In short, they showed that the input variability has a profound impact on not only the variability of the compressor performance, but also on the mean (expected) performance of the compressor. They used principle component analysis (PCA) to characterize the blade geometry variability from the measured data.

The aforementioned papers have highlighted the importance of the probabilistic approach to the design of mechanical components. The focus has been largely on structural analysis and fatigue life (high and low cycle) and very little information [8] is available on the probabilistic analysis of a cooled turbine blade. Also, the main focus of the aforementioned papers has been to lay out the methodology showing little, if any, validation data to support their findings. Very little information is also available regarding how to assess or even obtain the input parameter uncertainty (PCA based method [7] is an exception) and or the distribution.

Sidwell and Darmofal [8] idealized the entire blade cooling system as a flow network comprised of chambers interconnected by restrictors. All the cooled blades of a turbine blade row are modeled as restrictors with their flow area as normally distributed random variables. They related the blade temperature to the blade flow through a simple relationship in which the cooling effectiveness (η) is proportional to the cooling air flow (W) through the blade. They presented field data for an engine from two operators and tried to validate their method with some degree of success. To the best knowledge of the authors of this paper, the work of Sidwell and Darmofal [8] is likely the only published work which directly addresses the probabilistic nature of a cooled blade in a realistic situation.

Similar to the work of Sidwell and Darmofal [8], the following paper presents the probabilistic analysis of a cooled turbine blade, however, with three improvements. First, no assumption has been made between the relation of cooling effectiveness and coolant airflow. Rather, the effectiveness is evaluated by a full blade thermal analysis throughout the simulation. Second, variability of input parameters is obtained through simulation of physics based models of the upstream flow domain. Unlike the work of Sidwell and Darmofal [8], these upstream models have their variability obtained directly from blue print tolerances as opposed to any experienced-based knowledge. Third, the effect of the gas path radial temperature profile variation has been accounted for rather than just its mean variation. This aspect is important as the radial profile is a significant contributor to the variability of the blade life. One of the major effects of the radial profile variability can be shifting of the life-critical locations on the blade. In addition to the above improvements, three different approaches for considering the robustness of a thermal design through the blades life are explored. These are the life of a single blade, the life of a blade row from a single blade analysis, and the life of a blade row separating blade-to-blade variability from blade row to blade row variability.

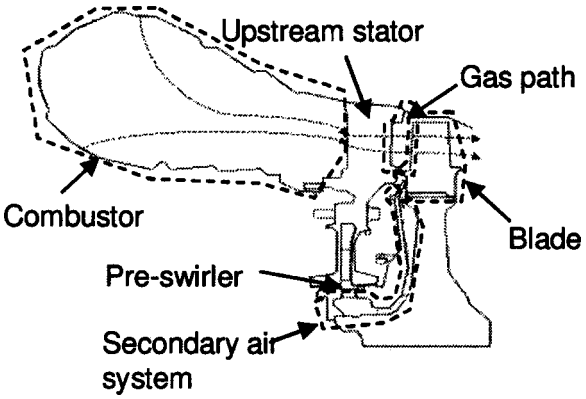

Fig. 1 Simulation model domain

2 Analytical Models

2.1 Problem Description. The domain considered for simulation is depicted in Fig. 1. It consists of the combustion chamber, the gas path upstream of the blade, the secondary air systems passage feeding the blade, and the blade itself. The focus here is to do a probabilistic analysis of the blade thermal design. The thermal analysis of the blade needs information regarding the gas path thermodynamic and fluid dynamic quantities to calculate the heat load, as well as sink pressure for the blade internal fluid flow model. The blade feed pressure and temperature are also needed for the thermal analysis. The subdomains surrounding the blade (combustor, secondary air systems, and gas path) are modeled and simulated separately to obtain input variability for the blade thermal analysis. Ideally, these models should be treated as a single integrated entity to account for dependencies that may be present between the proposed random variables. This was not possible in the present work, primarily because of the computational expense it would incur. Further, for the random variables selected, the effect of their dependencies on the accuracy of the results is expected to be negligible. The details of these subdomains will be described in detail later in the paper.

2.2 Deterministic Thermal and Lifing Analysis. The thermal analysis of the blade is done using a finite element method. The blade's internal (cold side) boundary conditions in the model are generated using an internal flow solver that calculates the heat transfer coefficient and bulk temperature. The blades external (hot side) boundary conditions are generated using a boundary layer code that calculates the heat transfer coefficient and the thermal boundary layer along a streamline for a given set of inlet conditions and a surface static pressure distribution. The static pressure distribution on the blade surface that is needed for the boundary layer code and internal flow solver (sink pressure) is extracted from a viscous solution of a multistage Navier–Stokes code.

The thermal analysis is carried out at a design point condition and the resulting temperatures are normalized as follows:

$$\eta = \frac{T_{\text{AvgGas}} - T_{\text{surface}}}{T_{\text{AvgGas}} - T_{\text{feed}}} \tag{1}$$

The blade surface temperature distribution is scanned for critical locations and the effectiveness (η) based on the critical location is carried to the lifing analysis tool. These critical locations are the life-limiting locations on the blade, which have been determined through evaluation of field components. Several locations may

Table 1 Thermal analysis parameters modeled as random variables thermal analysis parameters modeled as variable

Group	Parameter	Uncertainty sources modeled
Gas path parameters	P_{Trel}	Combustor hole areas, combustor outlet pressure, upstream stator stagger angle, upstream vane coolant flow
	T_{TrelAvg}	
	$T_{\text{Trel,Local}}$	Radial gas path temperature profile
Coolant side	P_{feed}	Fixing leakage, blade restriction, blade feed slot area and leakage, preswirler flow area and leakage, leakage sink pressures
	T_{feed}	
Geometric parameters	FF_{Dim}	Film hole area change due to machining tolerances
	RF_{Dim}	
	CT_{Dim}	Core thickness variations in casting

exist on a single blade and in the present problem four such locations existed. As well for the present problem these locations are specifically oxidation life-limiting locations. This tool calculates the time to part replacement, which is equivalently the life of the blade. In this particular analysis the tool calculates the life due to oxidation of the blade. The oxidation life of the blade is calculated at a given condition based on the following expression and is the same as that adopted by Sidwell and Darmofal [8]:

$$\text{tcond} = L_1 e^{L_2(T_{\text{surface}} - L_3)} \tag{2}$$

The exponents and constants in Eq. (2) are obtained from a proprietary database and are the result of several burner rig tests and field observation. The life (tcond) is for a given condition in the mission and the contribution of all the mission conditions is summed through the use of Miner's rule. The lifing analysis tool requires the information about the cooling effectiveness and the material/coating information. It also requires a mission profile (time spent at different events) and the average temperatures in front of the blade at various mission conditions. As seen from this relationship the oxidation life is directly related to the surface temperature of the aerofoil. In other words by tracking the oxidation life of a population of components, the performance of a thermal design can be equivalently tracked. In this case the longer the time to part replacement the better the thermal design is. These points are important for the current work, as there is no direct thermal data available to compare the developed probabilistic thermal analysis technique with. Instead we have available time to part retirement of a sample population of components from the field. These components being the blade row for a specific stage in the engine. With this information we evaluate the accuracy and effectiveness of the probabilistic technique applied to thermal design.

2.3 Probabilistic Thermal and Lifing Analysis

2.3.1 Random Variables Definition. Cooled blade thermal analysis requires various inputs which can be classified into three groups

- gas path parameters
- coolant side parameters
- geometric parameters

Upwards of 100 parameters are incorporated in the thermal analysis, though not all are independent. In narrowing down the random variables to incorporate in the simulation, parameters were identified from experience-based observation of their likely impact on the blade life. Further criterion included readily available variability information that was derived from blue print tolerances. Table 1 shows the parameters belonging to the above groups that are modeled as random variables and the sources of uncertainty that are captured in the current analysis.

Apart from the parameters mentioned in Table 1, several other parameters (turbulence intensity, the surface roughness, curvature, and others) influence the heat load on the blade. While these are modeled in the thermal analysis they are not treated as random variables mainly due to the lack of available data on their variability.

As shown in Table 1, the two major parameters on the coolant side captured as random variables are the feed pressure and feed temperatures. There are several other parameters such as discharge coefficients, entry losses, bend losses, and others that are not modeled as random variables, for the same reasons as noted previously.

Several geometric parameters affect the blade thermal performance. These include the cooling passage areas, film hole diameters, and the trailing edge slot ejection widths. These are modeled as random variables and a description of the methodology used follows. The uncertainty in the blade cooling flow at a given pressure ratio between the feed to the exit of the blade comes from manufacturing variability. In reality the manufacturing variability affects cast dimensions (coolant passages, heat transfer augmentation features, trailing edge ejection areas, and others) and machined dimensions (film holes) of the flow passages. In this study one parameter called CT_{Dim} is defined as a random variable to account for casting variability. This parameter represents the ratio of the core thickness at a given location to the nominal core thickness at the same location. The nominal core thickness at every location is scaled with this factor in every MCS cycle. In other words all the passage areas increase or decrease from their respective nominal at the same time and do not behave independently. Similarly, for the film holes, two film hole factors, FF_{Dim} and RF_{Dim}, are defined for two different film hole groups in the blade. These factors are modeled as random variables. As a result of the film hole area changes, the film effectiveness and the heat pickup in the film hole changes. This effect is also modeled.

2.3.2 Statistical Description of Thermal Analysis Input Parameters. It is important to provide realistic values of the variability and distribution type for each of the random variables. Ideally, one would like to measure these parameters for various builds of engines and fit in proper distributions. However, some of the parameters are almost impossible to measure on a routine basis in an actual engine. In this study, the probability distribution of all the random variables listed in Table 1 have been generated through Monte Carlo simulations of physics based analytical models. These will be called peripheral models in this paper. Four such models were used and are described in the following.

(1) Gas path model: This model is used to determine the probability distribution for the blade leading edge average total pressure and average relative temperature and comprises of two submodels. The first one determines the pressure drop across the combustor. This model uses the compressor exit pressure and the dilution and cooling hole geometry of the combustor as input to determine the pressure drop across the combustor for a given flow. The second one is a turbine meanline program that is used to generate the average conditions at the blade leading edge. This uses the pressure at the exit of the combustor, stator cooling flows, and stator stagger angle as input random variables in a Monte Carlo simulation to generate the probability density functions for the blade leading edge relative pressure and temperatures.

(2) Secondary air systems model: This model is used to generate the probability density function of the coolant feed pressure and temperature to the blade. It uses the preswirler throat area, several leakage areas, gas path pressures (sink pressures), and the blade cooling flow as the random variables to generate a response of the blade feed pressure and temperature.

(3) Cold flow model: It is a general practice in the industry to measure the flow through each blade under ambient conditions with a predetermined pressure ratio for quality control purposes. These measurements are termed cold flow measurements. In this study, the measured cold flow data is used to determine the probability density functions of the casting (CT_{Dim}) and film hole (FF_{Dim},RF_{Dim}) dimensional variations. This is done by a separate Monte Carlo simulation of the internal flow solver model under

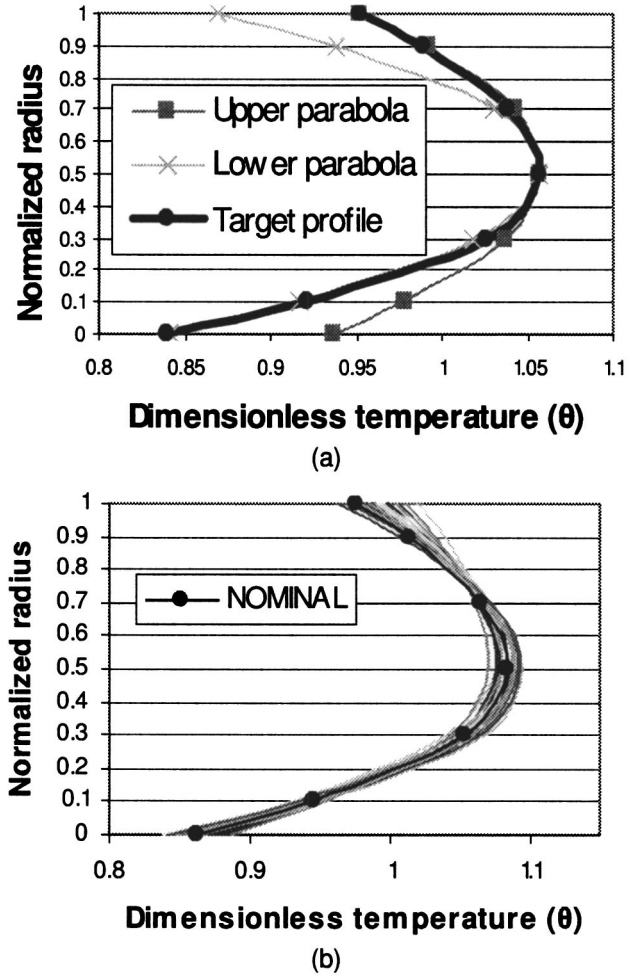

Fig. 2 (*a*) Nominal radial profile definition and (*b*) radial profile variation

the same conditions at which the cold flows are measured. The CT_{Dim}, FF_{Dim}, and RF_{Dim} factors are used as input random variables that are assumed to be normally distributed. This assumption is verified in the results section. The blade flow is the response (output) from the simulation. The standard deviations of the random variables are adjusted such that the response statistic characteristics of the simulated flows match those of the measured data. It should be noted that the actual blade flow variation might be due to a large number of dimensions, which are modeled here as just three parameters.

(4) Spanwise variation of the gas path temperature: It is almost impossible to have a uniform temperature in front of the blade and it is not desirable in many situations. This variability is a result of the upstream component variability and should ideally be captured through a physics based model of the combustor and upstream vane. Such a model though would be quite complex and in this study, a numerical approach is chosen instead. The gas path temperature, as seen by the rotating blade, can be expressed as a function of the radius. These local gas path temperatures are normalized appropriately such that the following constraint is met

$$\int \theta(r)dr = 1 \tag{3}$$

This is required to respect the average value of the TET, which is fixed for a given thermodynamic cycle. In this approach, the target radial temperature profile (nondimensional) as shown in Fig. 2(*a*) is parameterized with four parameters and two parabolic curves are fit [one for the lower part, $F(a)$, and another for the upper part, $F(b)$] to it. It can be seen from the figure that the representation is very good. The parametric equation has the following form:

$$F_a(r) = F_{\text{peak}} - \varphi_a(C_a, F_{\text{peak}}, r_{\text{peak}}) \times (r_{\text{peak}} - r)^2$$
$$F_b(r) = F_{\text{peak}} - \varphi_b(C_b, F_{\text{peak}}, r_{\text{peak}}) \times (r_{\text{peak}} - r)^2 \tag{4}$$

F_{peak} is the peak temperature in the profile and r_{peak} is its radial location. C_a and C_b are the normalized temperatures at the hub and tip, respectively. The relations for The constants r_{peak}, C_a, and C_b are used as input random variables during the Monte Carlo thermal analysis simulation, and were provided with variability values based on proprietary data. The fourth parameter, F_{peak}, is allowed to depend on the other three parameters such that the integration of the radial profile with the radius is unity. At each simulation cycle the radial profile then varies from variation in the profile coefficients as shown in Fig. 2(*b*).

Where applicable in the above model definitions, the random variables are assumed to be normally distributed as a first approximation and the blue print tolerances are used as 2σ limits in this exploratory study. Investigation of the influence of additional distribution types will be considered in future work.

2.3.3 Lifing Model. Table 2 describes the various parameters that are required to perform an oxidation lifing analysis on the blade. As can be seen from the table, not all the parameters are modelled as random variables. Only the parameters for which the variability is known or may be assumed with a reasonable confidence are used as input random variables while the remaining ones are left as constants.

2.3.4 Simulation Execution. With the peripheral models described earlier, an overall simulation was executed as shown in Fig. 3. The gas path peripheral model was completed first; its results provided boundary conditions for both the secondary air systems model as well as the thermal analysis. The coolant feed passage model correspondingly provided boundary conditions for the thermal analysis. The cold flow model was initiated separately to provide the geometrical boundary conditions for the thermal analysis. On completion of the thermal analysis, its output, the blade effectiveness was passed to the blade life analysis simulation model. After each peripheral model simulation the best-fit distribution was determined using @Risk/BestFit software, produced by Palisade Corporation.

3 Results and Discussion

3.1 Results of Peripheral Models

3.1.1 Gas Path Model. As mentioned earlier the gas path model takes into account the variations in the combustor hole sizes, the stagger angle in the vane, and the vane cooling flow variations, then determines the variability in the relative pressure and temperatures at the blade leading edge. The outputs considered are the total relative pressure (P_{Trel}) and temperature (T_{Trel}) upstream of the blade. Figures 4(*a*) and 4(*b*) show histograms of P_{Trel} and T_{Trel} resulting from the Monte Carlo simulation of the gas path model (note: the figures are put in nondimensional form with their mean values). Also shown in the figure is a normal distribution curve that fits the data. For the blade thermal analysis, the P_{Trel} and T_{Trel} were consequently normally distributed with the coefficient of variation as indicated in the figures. Plotted in Fig. 5 are 1-CDF (cumulative distribution function) curves for P_{Trel} and T_{Trel}. Shown in the figure are the values of P_{Trel} and T_{Trel} that would result from a worst-case analysis of the gas path model. It is interesting to see that the probability of occurrence of worst-case P_{Trel} is only 0.04% and that of T_{Trel} is only 0.19%. This implies that the worst-case scenario is very conservative.

Table 2 Parameters that affect the blade life

Parameters	Description	Sources of variability captured
Mission profile	Consists of time spent at various events such as take-off, climb, cruise, and others	Not modeled as a random variable in the current study
Mission conditions	Thermodynamic conditions at different mission events	Considered constant for an average new engine and two standard ambient temperatures (ISA and ISA+20°C)
Mix of ambient conditions	Percent mixture of missions at the ISA and ISA+20°C	Random variable: Mean value of this variable matches with the mean ambient temperature. Variability is derived from the field data for a given operator
Deviations from average new engine	An engine fresh out of the box has some variability in TET at which it operates for a given thrust	Random variable: Based on the engine experience data
Cooling scheme effectiveness	Nondimensional temperature used to scale the blade metal temperatures to different conditions	Random variable: Based on the probabilistic analysis of the thermal design of the blade
Material properties	Material properties upon which lifing curves are based	Random variable: Based on proprietary data

3.1.2 Secondary Air Systems Model. The results from the Monte Carlo simulation of the secondary air systems model are shown in Figs. 6 and 7. P_{feed} and T_{feed} are the output variables from this simulation. Figures 6(*a*)–6(*b*) show histograms of P_{feed} and T_{feed} (put in nondimensional form with their mean values). Figure 7 shows the CDF values for the P_{feed} and T_{feed}. Based on these results, the blade thermal analysis utilized P_{feed} and T_{feed} are normally distributed with the coefficient of variation as indicated in Figs. 6(*a*)–6(*b*) and the mean value obtained from the analysis.

3.1.3 Cold Flow Model. Figures 8(*a*)–8(*c*) show the results from the cold flow analysis. In these figures the probability distribution function of the measured flows is compared with that of the simulated flows. Three different flows were measured for each blade and each flow represents a different combination of inlet and or exit locations. Through variation of the CT_{Dim}, FF_{Dim}, and RF_{Dim} parameters, the variability observed in the measured flows is reproduced fairly accurately in the simulated flows as shown in the figures. As is further seen from the figures, the difference in the mean and standard deviation between the measured and simulated flows is less than 1% of the mean value for all the three cases. It should be noted that the measured flow variations result from a large number of dimensional variations on the blade and incorporate the flow measurement uncertainty as well. In this study all these dimensional variations have been represented by three factors. In this sense, the simulation results compare reason-

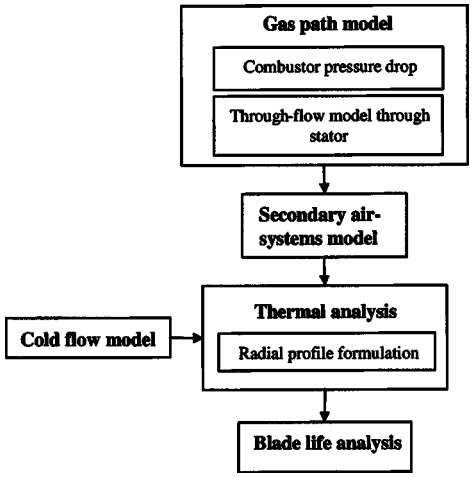

Fig. 3 Overall simulation execution

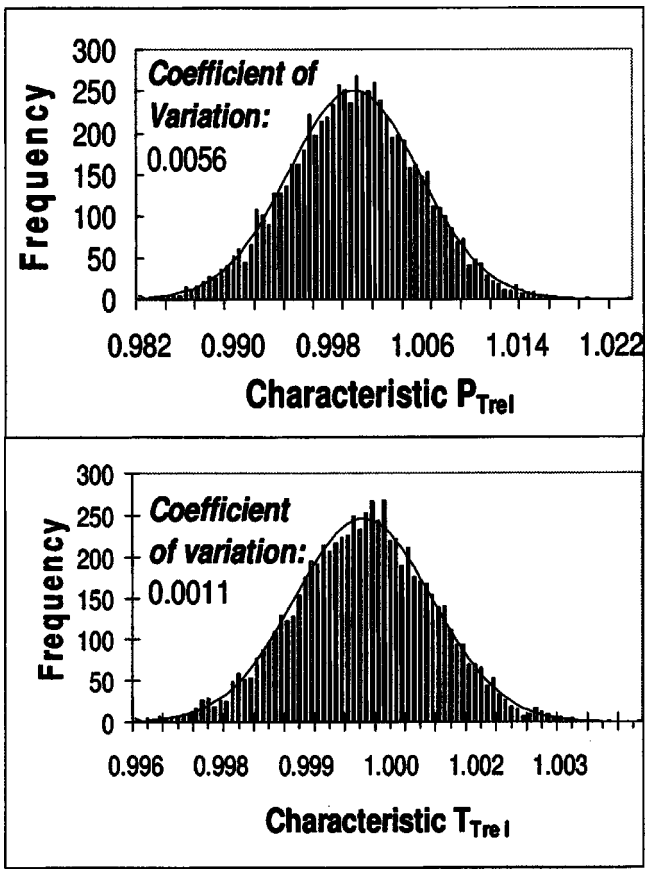

Fig. 4 P_{Trel} results and T_{Trel} results

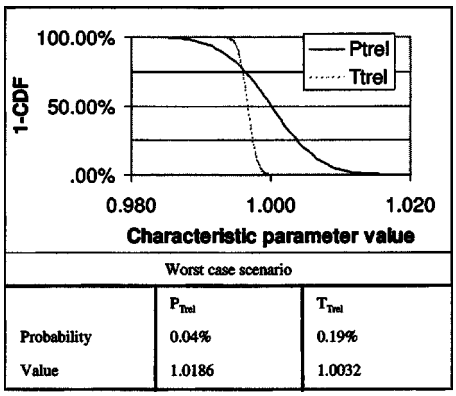

Fig. 5 P_{Trel} and T_{Trel} 1-CDF plots

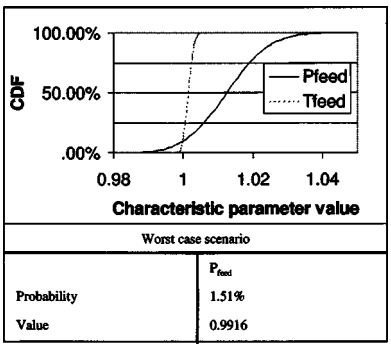

Fig. 7 P_{feed} and T_{feed} CDF plots

ably well with the measured data. Figures 9(*a*)–9(*c*) show the histograms for the three geometric factors representing the cooling passage and sink areas (CT_{Dim}, FF_{Dim}, and RF_{Dim}). The best-fit line applied to the data in Figs. 9(*a*)–9(*c*) is a normal distribution since it was the inputted probability distribution type. The good correspondence of measured to simulated flow results in Figs. 8(*a*)–8(*c*) validates the assumption of a normal probability distribution type for the inputted geometric parameters.

3.2 Notes on the Field Data. The field data collected represent a sample of 51 engine blade rows from a particular stage of an aero engine turbine. It should be noted that among these 51 engines 19 engines had the blade rows retired for reasons other than oxidation deterioration, and these have been appropriately censored in the data presented. The remaining 32 engines had the blade rows retired based on the established oxidation criterion. All the engines considered are from a single operator in order to minimize the effect of operating and mission condition variability. The time to retirement of the blade row is considered as the lifespan of the blade row in the current work. Through a separate internal initiative the engine data has been statistically characterized and is used for comparison here in its best-fit form.

3.3 Single Blade MCS. The previous sections dealt with the generation of the distribution type and variability for the input random parameters of the blade thermal analysis. Using these random variables and their input uncertainty, a Monte Carlo simula-

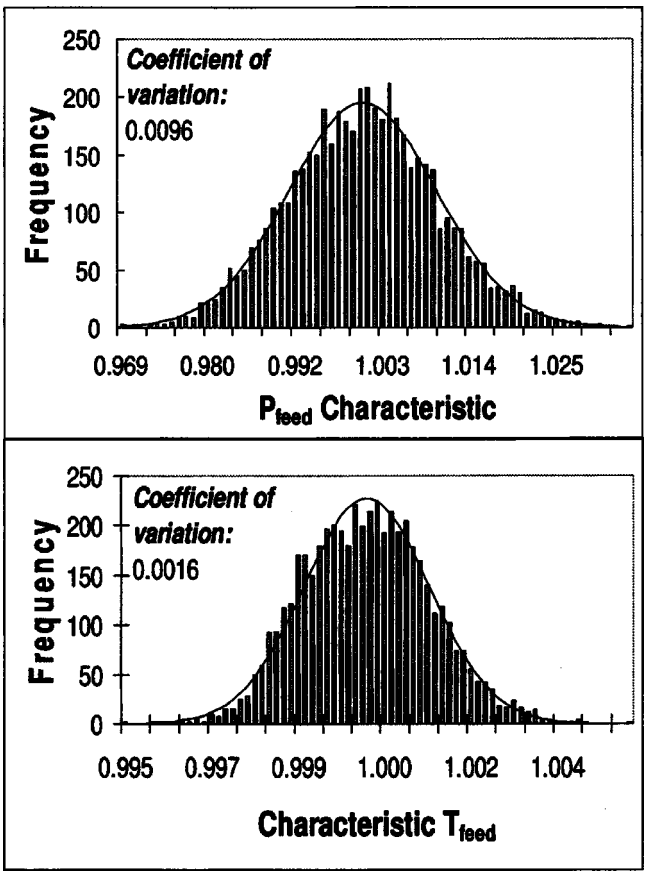

Fig. 6 P_{feed} and T_{feed} results

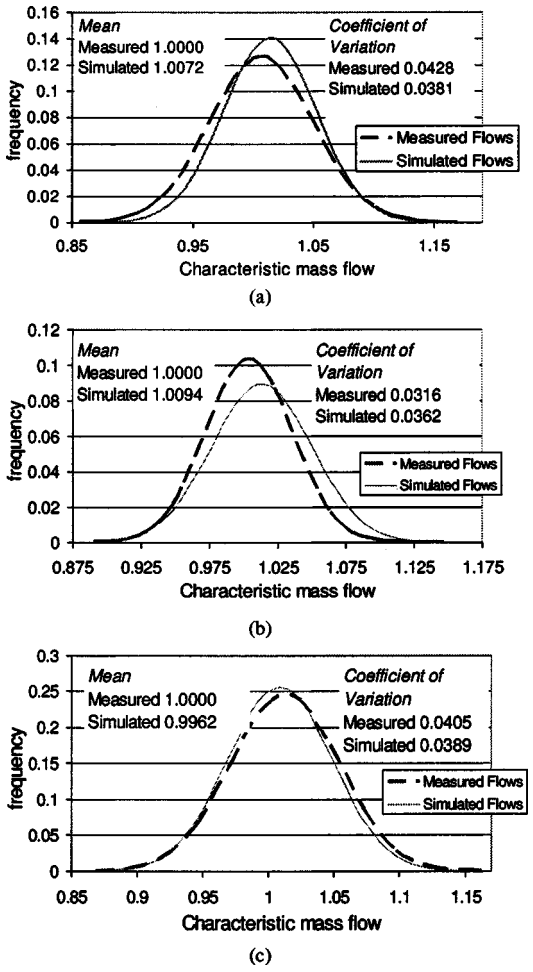

Fig. 8 Measured vs simulated cold flow probability distribution plots

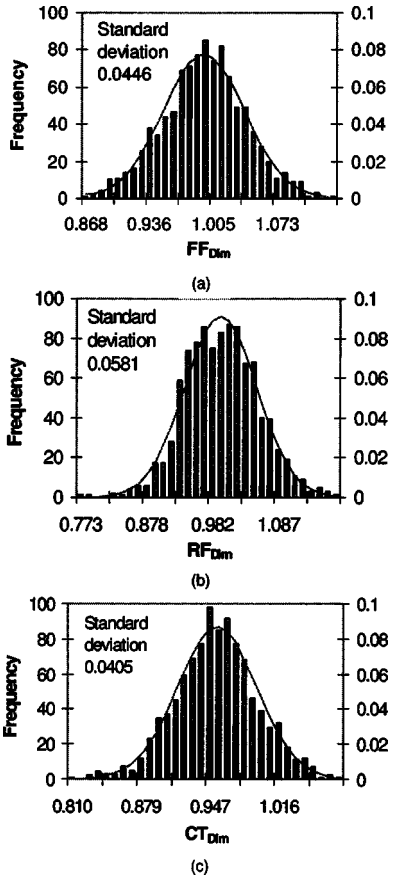

Fig. 9 Geometric parameter histograms

tion of the blade thermal analysis was performed. In this analysis, it is assumed that a given blade sees a random value of any of the input random parameters while respecting the distribution type and the coefficient of variation for that parameter. Blade metal temperatures at critical locations were tracked for each run and the most critical (highest) temperature was chosen to the output random variable (response) from the thermal analysis MCS. The simulation of the thermal analysis is repeated, each time with new random values of the input random parameters for a predetermined number of steps. The blade metal temperatures were then converted into their nondimensional form (η). Figure 10 shows the histogram of the life critical effectiveness resulting from the

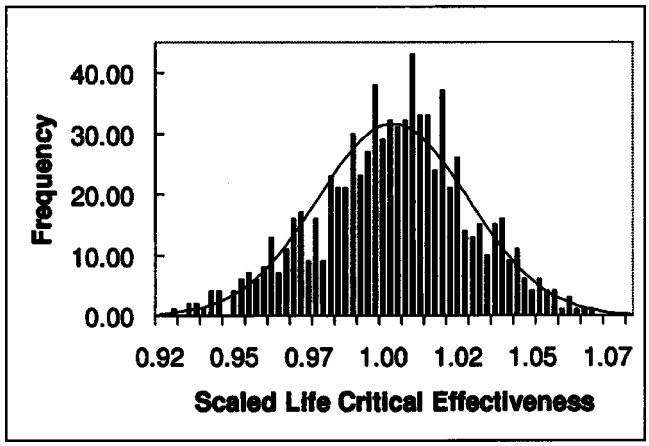

Fig. 10 Life critical effectiveness histogram

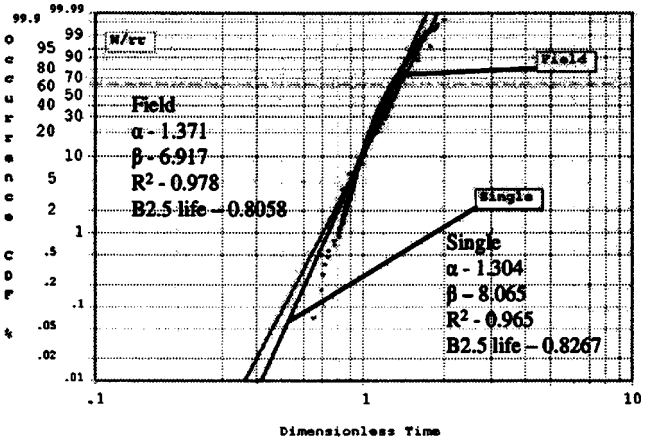

Fig. 11 Single blade-Weibull plot of cumulative probability of occurrence of a given life single blade life MCS results

blade thermal analysis. The effectiveness as determined is well represented by a normal distribution and this distribution was therefore carried to the Monte Carlo simulation of the lifing model. The results from the Monte Carlo simulation of the lifing analysis is shown in Fig. 11 plotted on a Weibull scale. The abscissa is dimensionless time (lifespan of the blade as defined earlier) and has been put in nondimensional form with respect to a reference life. The ordinate represents the percentage of blades from the entire population expected to be retired at or below a certain time. For any given value of the time (abscissa), the ordinate represents the probability that the blade life is equal or smaller than that value. Reliability of the blade life is 1 minus the value displayed on the ordinate.

Figure 11 shows a very good comparison between the analytical prediction and the field data. The R^2 value of the Weibull fit is comparable between the field data and the analytical prediction although the analytical prediction has a slightly lower R^2 value. The characteristic life, α (which represents $\sim B63.2$ life), of the distribution is very much comparable between the field data and the analytical prediction. While MCS is a good tool to predict the effects of variability such as Weibull slopes, the characteristic life prediction is only as good as the deterministic model, this is discussed later. The Weibull slope appears to be not too far from the field data, giving an impression that the analytical prediction is very good. It should be noted that though the single blade MCS data has been plotted on a Weibull scale in Fig. 11, this is done only for comparison with the field data. This data, however, are actually best fit to a lognormal distribution type rather than the Weibull distribution type.

3.4 Blade Row Analysis. In the above the results were presented for an analysis considering a single blade. The life statistics from the field, however, are for the life of a blade row (rotor). Hence, even though the agreement with the field data appears to be good, it cannot be considered to be an appropriate comparison. To evaluate the life of a blade row two approaches were considered. They are detailed below along with the results.

3.4.1 Blade Row Life With Single Blade MCS. In this approach the single blade life's response statistics as predicted from the MCS in the previous section was considered applicable to all the blades in a blade row. A fleet of 10,000 engines are considered. For each engine, the life of each of the blades on a rotor was randomly evaluated from the Monte Carlo simulation results of the single blade analysis of previous section. The life of the blade row as a whole was considered to be the minimum of all the blades of the row. This was repeated for each of the engines in the fleet and a population is thus generated. It is recognized at this point that such an analysis assumes each blade as an independent

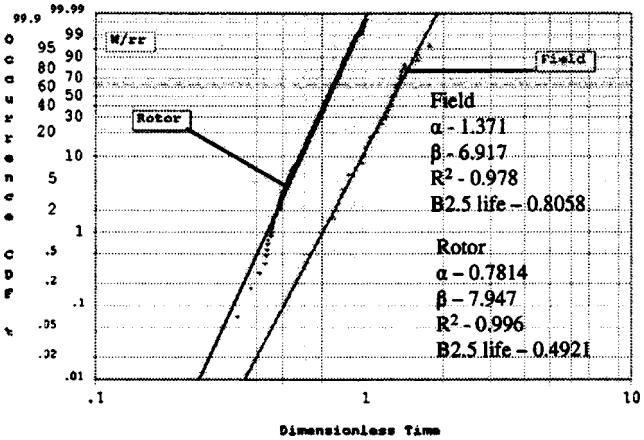

Fig. 12 Blade row (rotor) results from single blade MCS-Weibull plot of cumulative probability of occurrence of a given life blade row (rotor) life MCS from single blade MCS results

entity, particularly dependencies due to gas path conditions are ignored. However, the value in such an approach is the minimal computational effort required (on the order of hours as opposed to days). Figure 12 shows the results of this analysis. It should be noted that these results represent a sample of 1000. To verify this sample as representative of the population, three separate random samplings were performed and the error observed between samples was negligible.

Figure 12 reveals some interesting aspects. First of all, the analytical data represent a far superior Weibull fit compared to that of the single blade MCS data of Fig. 11. This is evident from the R^2 value of the fit. Second, the Weibull slope does not change from that of the single blade analysis (Fig. 11). This is expected as the data for Fig. 12 are basically derived from the same population as those of Fig. 11. More interestingly, there is a significant reduction in the α value. The characteristic life reduces from 1.304 for the single blade MCS to 0.7814 for the blade row analysis. This is expected because the blade row analysis calculates a minimum life for every blade row and, hence, filters out the higher blade life data from the single blade MCS population. This value should be further reduced if blade-to-blade dependencies are accounted for. Particularly a given blade may underflow due to another blade on the same rotor overflowing because of differences in restriction. Such results would be important to obtain, however, due to the computational effort as mentioned earlier and the added complexity this was not explored in the current work, but will be part of a future effort.

It is noted at this point that the α value is well below the field data α value, however, matching the characteristic life is not critical to this study. This is because it is generally the practice of the turbine industry to calibrate the life from the nominal deterministic analysis with that of the field data. The approach is mainly due to the fact that the probabilistics are not available to assess the rotor life and then calibrate the analysis. Hence, at the start of this probabilistic analysis of the blade thermal design, we used a deterministic model that was approximately calibrated to the field data. As a result of this we observe a good match between the characteristic life from the single blade MCS with the field data. In an ideal situation, we should have used a deterministic model for a blade row that is calibrated to the field data. However, such a thing is not possible unless a MCS is performed on the blade row. Hence, the absolute value of the characteristic life is not of concern here as it is a matter of how the deterministic model is calibrated. Rather, it is the change in the characteristic value from the single blade analysis to the blade row analysis that is of importance.

Table 3 Blade row to blade row variability and blade-to-blade variability blade-to-blade variability

Variability to blade row (global parameters)	Variability to individual blade (local parameters)
P_{Trel}, T_{Trel},	CT_{Dim}, FF_{Dim}, RF_{Dim}, P_{feed}, T_{feed}
Spanwise radial profile parameters	

3.4.2 Effect of Separating Blade-to-Blade Variability From Row-to-Row Variability. The disadvantage in the approach of the previous section is that it relies on a single blade MCS. By doing so, we imply that each blade in a blade row sees a different random value of all the input random parameters considered. This, however, is not true in a realistic situation. Some of the input parameters remain the same for all the blades and some vary from blade to blade. Typically, the gas path parameters such as the relative total pressure and relative temperature are practically the same for all the blades, whereas the feed pressure and the cooling flows vary from blade to blade. Table 3 below lists the specific parameters that remain constant and vary from blade to blade.

In order to account for the effect of these parameters in a realistic way, one needs to perform a Monte Carlo simulation of the whole blade row. Since the blade row has several blades, it amounts to executing the thermal analysis and lifing analysis models several times for a single blade row and that needs to be repeated several hundred times to obtain the population for a fleet of engines. However, this is very time consuming. In order to simplify the problem a response surface approximation technique was considered. This approximation takes the inputs and calculates outputs based on a calibrated polynomial.

The response surface approximation [9] in its generic form is

$$F_1(X) = a_0 + \sum_{i=1}^{N} b_i x_i + \sum_{i=1}^{N} c_{ii} x_i^2 + \sum_{ij(i<j)}^{N} c_{ij} x_i x_j$$

where N is the number of input variables, x_i are the set of input variables, and a, b, c are the polynomial coefficients.

The coefficients are obtained through regression analysis. Typically the regression coefficients are determined by performing simulation of the analysis code for a select few points based on design of experiments techniques. However, in the present case the single blade MCS data were already available and, hence, were used instead.

In order to evaluate the validity of the response surface modeling (RSM) approximation, this model was evaluated at a select few points not used in the regression analysis of the input parameter space. Table 4 shows a comparison of the accuracy of the RSM approximation with respect to the effectiveness predicted by the thermal analysis code at one of the critical locations. It can be seen from the figure that the effectiveness predicted by the RSM agrees very well with that from the thermal analysis code. The excellent comparison of the RSM results could also be due to the fact that a large number of data were available for generating a response surface. If the RSM was generated using only a few points, one could expect a lower accuracy. The approximation was

Table 4 Evaluation of response surface approximation technique

Evaluation case	Percent difference from model (%)
Nominal	−0.02
Upper limits	0.05
Lower limits	−0.51

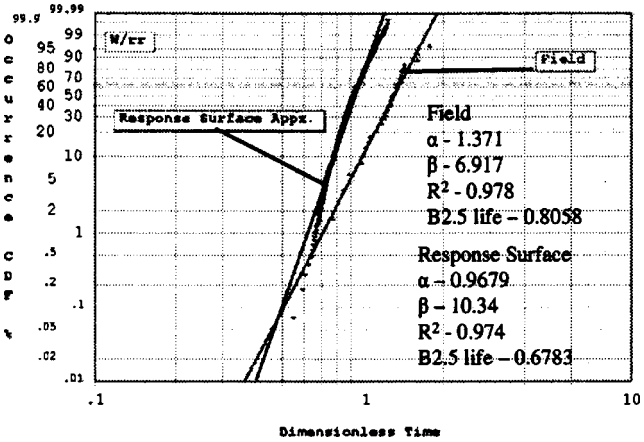

Fig. 13 Blade row results using response surface approximation-Weibull plot of cumulative probability of occurrence of a given life response surface approximation rotor MCS life results

introduced for the thermal model alone while the life model was evaluated in full. With an approximation technique in place for the time consuming thermal analysis, a full simulation of the blade row life considering blade-to-blade variability can be performed.

The results from the RSM simulation are shown in Fig. 13 and are compared to the field data. It should be noted that Fig. 13 differs from Fig. 11 (single blade analysis) and Fig. 12 (blade row analysis from a single blade MCS) in the following ways—(*a*) use of RSM as an approximation of thermal analysis, (*b*) rotor life calculation as opposed to single blade life calculation (Fig. 11), and (*c*) separation of blade-to-blade variation from blade row to blade row variation (see Table 3).

When compared with the field data, the Weibull slope is higher and the characteristic life is lower. The Weibull fit is comparable to that of the field data although some deviations from the Weibull curves are noticeable at extremes. As noted previously, comparison of the characteristic life with the field data is not meaningful and is not critical to this study. The Weibull slope being higher than the field data indicates that this analysis predicts slightly lower level of scatter than the field data. At this point, it is important to remember that the analysis is not expected to predict the exact slope and will not predict the exact slope of the field data unless (*a*) the deterministic model is very accurate and (*b*) all the factors which influence the variability in the life of the blade are accounted for in the simulation. In the current study this is certainly not the case. However, considering the amount of input variability modeled, we believe that the approach presented has predicted the field data reasonably well and can likely be a useful tool in identifying the effect of various parameters on the robustness of a design. Nevertheless, some likely significant parameters are not considered as random variables at all in this exploratory study. Examples include turbulence intensity, surface roughness, radial distribution of the pressure, blade external geometry variation, aircraft mission length, and others. The variability in these parameters are extremely difficult to assess and have been excluded from this exploratory work. It is important to note that these parameters could have some influence on the predicted life and where possible, they should be modelled as well. This will be part of the future work.

Comparing Fig. 13 with Fig. 11, it is possible to conclude that the single blade analysis (Fig. 11), which is the general industrial practice, agrees with the field data. However, as mentioned earlier, it is not a fair comparison as the field data represents the life of a blade row. We believe isolating blade-to-blade variability is important even though Fig. 13 does not demonstrate exceptional correspondence with the field data. Comparing Figs. 13 and 11, it can be seen that the analytical prediction of the characteristic life has come down significantly with the blade row analysis. This was noted earlier through Fig. 12 as well and highlights the importance of modelling a blade row as opposed to a single blade only. The analytically predicted characteristic life though, is higher in Fig. 13 than in Fig. 12. This stresses the importance of modeling the input random variables appropriately as it has a recognizable impact on the characteristic life of the blade row.

4 Conclusions

The probabilistic technique presented has proven to be an effective method for evaluation and analysis of a thermal design. Input variability to the thermal design is obtained from simulation of physics based models of the upstream flow domain. The radial gas path temperature profile has been parameterized by two parabolic curves. This characterization has allowed for implementation of variation in the profile rather than just its mean during simulation. Throughout the probabilistic analysis, the blade thermal effectiveness has been evaluated by a complete thermal analysis. From this effectiveness variation, variation in the life of a single blade has been investigated. In addition, the variation in the life of a blade row has been evaluated using two techniques: (1) direct evaluation from the single blade life MCS and (2)through separating blade-to-blade variability from blade row to blade row variability and using a response surface approximation method.

An overall observation from all the models simulated is that the use of a worst-case approach produces an overly conservative thermal design methodology. Through the use of a probabilistic approach a quantification of the level of over conservatism has been presented. In the most probable worst-case scenario a probability of occurrence of 1.51% (P_{feed}) is observed while in the least probable worst-case scenario it is less than 0.05% (P_{Trel}). The worst-case scenario from the blade row life analysis has a probability of occurrence of 0.055%.

The results from the single blade MCS life simulation show very close agreement with field data in both the Weibull slope and characteristic life. This near perfect match with the field data is likely a coincidence. In comparison the blade row life results derived from the single blade show a similar agreement in the Weibull slope of the field data. In addition the blade row life results have a significantly lower characteristic life compared to single blade results, highlighting the importance of blade row consideration as opposed to just the single blade. The blade row life results obtained considering blade-to-blade variability and using the response surface approximation have both a lower characteristic life and a higher Weibull slope value when compared to the field data. The use of the response surface approximation allowed for an accelerated evaluation time of the thermal analysis. This computational time acceleration is necessary to have the MCS life evaluation separating blade-to-blade variability from blade row to blade row variability completed in a practical time limit.

Discrepancies between the simulation data and the field data may be due to not fully considering the uncertainty in the operating environment. Accounting for uncertainties such as those related to fluid flow may be implicitly included in the flow area geometrical variability. This was demonstrated through use of measured cold flows and three defined geometric parameters. Incorporation of additional uncertainty parameters will be part of future work.

Nomenclature

C = constants used in the radial temperature profile function
CT = cast areas
e = change in response statistic
F = radial temperature profile function
FF = film hole group parameter
RF = film hole group parameter
L = life equation constants

P = pressure
r = radius
R = averaged normalized change in response
tcond = life at a given mission condition
T = temperature
Z = response statistic

Greek Symbols

α = Weibull curve fit mean
β = Weibull curve fit slope
φ = radial temperature profile definition intermediate function
η = thermal effectiveness
σ = standard deviation
θ = nondimensional radial gas temperature

Subscripts

a = upper profile for radial temperature variation
AvgGas = averaged main gas path property used in effectiveness calculation
b = lower profile for radial temperature variation
Dim = area dimension
Feed = coolant feed passage parameter
Peak = parameter at peak of radial temperature profile
Surface = aerofoil external wall
Trel = total relative property

References

[1] Dailey, D., 2000, "Aero-Thermal Performance of Internal Cooling Systems in Turbomachines," VKI Lecture Series 200-03, Feb 28–Mar 3, 2000.
[2] Lykins, C., and Thomson, D., 1994, "Air Force's Application of Probabilistics to Gas Turbine Engines," Proceedings of the 35th AIAA/ASME/ASCE/AHS/ASC Structures, Structural Dynamics and Materials Conference, Apr. 18–20, Hilton Head, SC, No. 2, pp. 1069–1074.
[3] Pomfret, C., 1995, "Probabilistic Concepts for Gas-Turbine Engine Management," Aerospace Engineering, **15**(7), pp. 9–12.
[4] Ghiocel, D. M., and Rieger, N. F., 1999, "Probabilistic High Cycle Fatigue Life Prediction for Gas Turbine Engine Blades," Proceedings of the 1999 AIAA/ASME/ASCE/AHS/ASC Structures, Structural Dynamics and Materials Conference, Apr 12–15, St. Louis, MO, Vol. 4, pp. 2980–2989.
[5] Shen, M. H., 1999, "Reliability Assessment of High Cycle Fatigue Design of Gas Turbine Blades Using the Probabilistic Goodman Diagram," Int. J. Fatigue, **21**(7), pp. 699–708.
[6] Liu, Z., Volovoi, V., and Mavris, D. N., 2002, "Probabilistic Remaining Creep Life Assessment for Gas Turbine Components Under Varying Operating Conditions," AIAA/ASME/ASCE/AHS/ASC structures, Structural Dynamics and Materials Conference, Apr 22–25, Denver, Vol. 1, pp. 587–597.
[7] Garzon, V. E., and Darmofal, D. L., 2003, "Impact of Geometric Variability on Axial Compressor Performance," ASME J. Turbomach., **125**, pp. 692–703.
[8] Sidwell, V., and Darmofal, D., 2003, "Probabilistic Analysis of a Turbine Cooling Air Supply System: The Effect on Airfoil Oxidation Life," Proc. ASME Turbo Expo 2003, June 16–19, GT2003-38119, p. 10.
[9] ISIGHT Reference Guide, Engineous Software Inc, 2001, pp. 271–283.

Effects of Catalytic and Dry Low NO_x Combustor Turbulence on Endwall Heat Transfer Distributions

F. E. Ames

P. A. Barbot

C. Wang

Mechanical Engineering Department,
University of North Dakota,
Grand Forks, ND 58202

Endwall heat transfer distributions taken in a large-scale low speed linear cascade facility are documented for mock catalytic and dry low NO_x (DLN) combustion systems. Inlet turbulence levels range from about 1.0% for the mock catalytic combustor condition to 14% for the mock dry low NO_x combustor system. Stanton number contours are presented at both turbulence conditions for Reynolds numbers based on true chord length and exit conditions ranging from 500,000 to 2,000,000. Catalytic combustor endwall heat transfer shows the influence of the complex three-dimensional flow field, while the effects of individual vortex systems are less evident for the mock dry low NO_x cases. Turbulence scales have been documented for both cases. Inlet boundary layers are relatively thin for both the mock catalytic and DLN combustor cases. Inlet boundary layer parameters are presented across the inlet passage for the three Reynolds numbers and both the mock catalytic and DLN combustor inlet cases. Both midspan and 95% span pressure contours are included. This research provides a well-documented database taken across a range of Reynolds numbers and turbulence conditions for assessment of endwall heat transfer predictive capabilities. [DOI: 10.1115/1.1861923]

Introduction

Low emission combustion systems for power turbines are designed to burn lean combustion mixtures in order to minimize peak combustion temperatures. For the same average temperature the resulting flatter temperature profiles reduce peak gas to vane surface temperature differences but increase local gas to endwall temperature differences. Consequently, the resulting temperature pattern tends to aggravate the endwall cooling problem.

An added complication to the endwall heat transfer problem has been the development of low NO_x combustion systems. Currently, two general types of combustion systems are being developed to produce the lean combustion needed to reduce emissions. These combustion systems, dry low NO_x and catalytic, operate in very dissimilar manners. Dry low NO_x (DLN) combustion systems are more conventional in that they sustain combustion using recirculation zones similar to aeroderivative combustors. They are significantly different than aeroderivative combustors in that they use more of the combustor air in the primary zone and operate at significantly lower equivalence ratios. Catalytic combustion systems use a catalytic surface to initiate and sustain the combustion of a lean mixture of reactants and typically do not require a large-scale recirculation zone. The large-scale recirculation zone produced in aeroderivative and DLN combustors is responsible for the generation of high intensity large-scale turbulence. High turbulence is known to increase heat transfer in the laminar regions of vane leading edges and the pressure surface, cause early transition, and rapidly mix away film cooling coverage. Much lower turbulence levels are expected to be produced by catalytic combustion systems. Consequently, documenting the turbulence characteristics of these low emission combustion systems, as well as their effect on vane and endwall heat transfer, is of significant interest to heat transfer designers.

The research documented in this current paper is part of a larger research effort to investigate endwall heat transfer generated by a range of relevant inlet turbulence conditions. In the current paper, endwall heat transfer rates and inlet boundary layer and turbulence conditions are documented for mock dry low NO_x and catalytic combustion systems. In an earlier paper endwall heat transfer distributions were presented for a mock aeroderivative combustion system and for a base line low turbulence condition. For the present two mock combustor turbulence conditions and the two previously documented conditions, heat transfer rates were documented for true chord exit Reynolds numbers ranging from 500,000 to 2,000,000. Additionally, Rolls Royce of Indianapolis is conducting an analytical effort with a goal of grounding and improving predictive methods for endwall heat transfer using the results of the current experimental study.

Manuscript received December 23, 2003; revised manuscript received October 12, 2004. Review conducted by: P. M. Ligrani.

Background

Secondary Flows. Secondary flows on turbine airfoil endwalls are known to substantially influence endwall heat transfer distributions. A comprehensive review of endwall secondary flows was compiled by Sieverding [2] who presented the secondary flow models of Klein [3] and Langston [4]. Sieverding suggests that Klein identified the complex secondary flows, which develop on endwalls. The importance of secondary flows became clear as aerodynamic loss and heat transfer investigations began to identify the impact of secondary flows on losses and surface heat transfer distributions. Langston's research on secondary flows identified the main vortex systems including the pressure and suction side of the horseshoe vortex and the passage vortex. Additionally, Langston documented counter vortices, which form at the endwall junction with the pressure and suction surfaces. Marchal and Sieverding [5] found the growth in secondary losses increased in regions downstream from the maximum velocity. Ames, Hylton, and York [6] denoted the influence of the inlet boundary layer thickness on secondary losses in unpublished work at Allison Gas Turbine Division of General Motors in a linear vane cascade. Recent cascade investigations show how endwall contouring (Burd and Simon [7]) and leading edge fillets (Zess and Thole [8]) can reduce the effect of secondary flows.

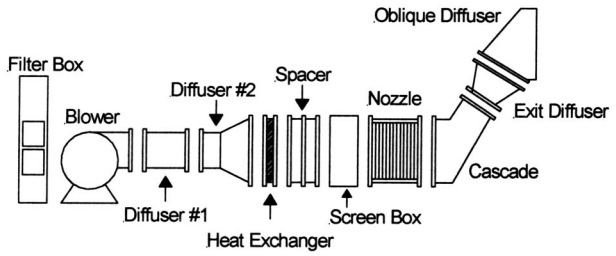

Fig. 1 The large-scale low speed wind tunnel with cascade

Endwall Heat Transfer. Heat transfer studies on the endwalls of vanes and blades generally show increased heat transfer in the stagnation region and downstream off the pressure surface. Vane endwall heat transfer studies include research by York et al. [9], Harasgama, and Wedlake [10], Spencer et al. [11], Arts and Heider [12], Radomsky and Thole [13], and Ames, Barbot, and Wang [14]. Blade endwall heat transfer studies include research by Goldstein and Spores [15] and Giel et al. [16]. Harasgama and Wedlake investigated endwall heat transfer in a compressible annular cascade finding heat transfer distributions were influenced by the endwall curvature on the hub and tip. Spencer et al. studied the influence of high turbulence finding similar results. Radomsky and Thole compared the influence of low and high turbulence on endwall convection rates and found augmentation levels up to 40% in the low velocity inlet regions and increases of around 10% in higher velocity regions. Ames, Barbot, and Wang found increasing Reynolds numbers moved higher heat transfer rates forward in the vane passage. Boyle and Lucci [17] concluded that endwall heat transfer predictions are dependent on the turbulence model and agreement between predictions and experiment can vary from case to case for a given model. These studies suggest a comprehensive database of endwall heat transfer distributions with relevant and well documented inlet conditions is needed to test the soundness of turbulence models for the predictions of endwall heat transfer and secondary flows.

Experimental Approach

The present endwall heat transfer investigation was conducted in a large-scale low speed cascade facility. This research was part of an effort, which documented endwall heat transfer levels for four inlet turbulence conditions over a four to one range in Reynolds number. The first paper, Ames, Barbot, and Wang [14] documented endwall heat transfer distributions and inlet boundary layer and turbulence parameters for two turbulence conditions. The initial low turbulence condition had an inlet turbulence intensity of about 0.7%. The other previous inlet condition consisted of a mock aeroderivative combustor, which produced an inlet turbulence level of about 13.5% and an inlet energy scale, Lu, of about 7 cm. The present paper documents endwall heat transfer distributions for a mock catalytic combustor and a mock dry low NO_x combustor, which are described in this section.

The large-scale low speed wind tunnel was designed to incorporate a cascade test section and is shown schematically in Fig. 1. The wind tunnel entrains air through an inlet filter into the blower, which is capable of moving 6.6 m^3/s of air with a static pressure rise of 5000 Pa. A two-stage diffuser connects the blower to the heat exchanger with a cooling water recirculation system that enables a steady and controllable cascade inlet temperature. This feature is of particular importance in developing accurate endwall heat transfer distributions using liquid crystal paints. A rectangular section spacer connects the heat exchanger to a four-section screen box. The screen box is used to reduce any variations in the velocity distribution prior to the two-dimensional 3.6–1 area ratio contraction nozzle. The nozzle connects with the cascade test section but was replaced by the mock combustor turbulence-generator for the current tests. The large static pressure rise across the blower accommodates the pressure loss in the mock combustion systems, which provide relevant inlet boundary conditions for the endwall heat transfer studies. A diffuser is located at the exit of the cascade test section for static pressure recovery and allows the tunnel to operate over a wider Reynolds number range. An oblique diffuser directs the exhausting air away from ceiling lights.

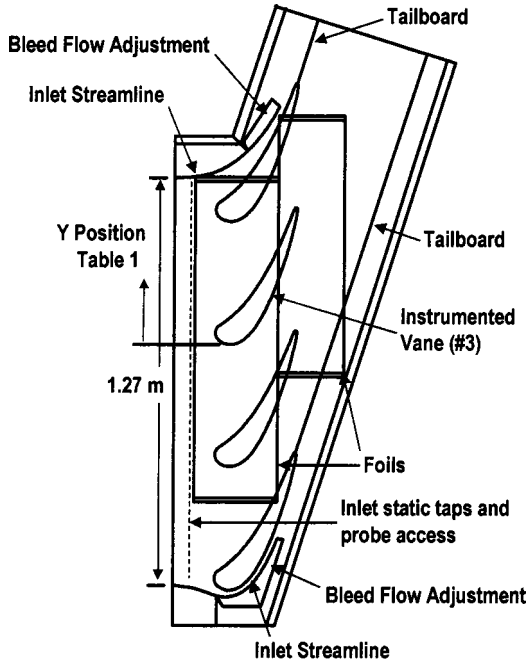

Fig. 2 Schematic of the large-scale low speed cascade facility

The linear cascade facility shown schematically in Fig. 2 has some unique design features to enhance its aerodynamics. The facility uses an 11 times scale vane, which has a midspan loading profile consistent with a fully loaded first vane design in a modern industrial gas turbine. The vane was specially designed for incompressible flow. Consequently, the pressure loading distribution was designed to be consistent with actual vane pressure distributions rather than preserving the exact geometry. The cascade is configured with four vanes producing three full passages. The cascade has inlet bleed flow adjustments, which were designed along calculated streamlines to ensure the flow around the top and bottom vanes is uniform. The cascade also has tailboards extending from the trailing edge of the top and bottom vanes to enable the development of periodic flow from the three passages at the cascade exit. The cascade has inlet and exit static pressure taps to facilitate setting the bleed flows and tailboards and to monitor the experimental condition. A row of access ports is located in a plane 7 cm upstream from the leading edge plane of the vanes and was used to allow documentation of inlet boundary layers, velocities, and turbulence characteristics.

The endwall heat transfer distributions in this study were investigated at exit Reynolds numbers based on true chord 500,000, 1,000,000, and 2,000,000. These conditions are consistent with small to medium sized industrial and propulsion engines. The true chord of the 11 times scale vane is 47.8 cm and the axial chord is 25.0 cm. The vanes are spaced at 38.4 cm and have a height of 25.4 cm. The vanes are set at a stagger angle of 55.1 deg and produce a calculated air exit angle of 73.4 deg. The vane leading edge diameter is 5.59 cm and the trailing edge diameter is 0.98 cm. The aspect ratio of the current vane is 0.53 compared with a ratio of 0.68 for the engine vane geometry. However, the aspect ratio has little influence on the endwall flow based on the 95% pressure distributions.

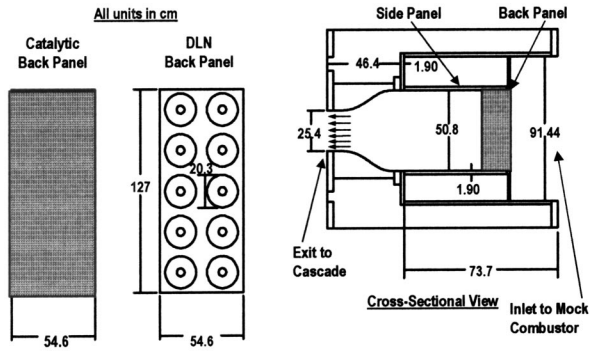

Fig. 3 Schematic of mock low NO_x combustor turbulence generator

Turbulence Generators. The objective of this investigation is to characterize the turbulence generated in low NO_x combustion systems and document its influence on endwall heat transfer. Two mock low NO_x combustion systems have been developed to generate turbulence with characteristics, which are representative of catalytic and DLN combustors. The mock combustor configuration is shown schematically in Fig. 3. Looking at the cross-sectional view, flow enters from the right and is forced through the back panel, which contains either the mock catalytic combustor panel or the mock DLN swirler system. These panels are pictured in Figs. 4 and 5. The flow then leaves the mock combustor through the 2–1 area ratio contraction nozzle on the left of the cross-sectional view and immediately enters the cascade.

Vane Pressure Distribution. The vane pressure distribution was acquired along the midline of the third vane using an epoxy airfoil with integral surface pressure taps. The pressure taps are fabricated by casting a 1.6 mm brass tube near the surface of the vane. A small perpendicular hole is then drilled from the surface of the vane to the center of the tube. The present vane has 82 taps cast into the surface with a small concentration near the leading edge. The pressure or heat transfer vane can be inserted through a machined hole in the endwall and is secured using a flange to the endwall with machine screws. The low turbulence pressure distribution is shown in Fig. 6 for an exit chord Reynolds number of 2,000,000 with a two-dimensional (2D) viscous prediction made using FLUENT [18]. The data are presented as P_s/P_t versus surface distance. Here, positive surface distance is measured from the predicted stagnation point along the suction surface and negative surface distance is measured along the pressure surface. The experimental pressure distribution compares favorably with the prediction. This level of agreement indicates that the midspan aerodynamics on the vane are consistent with the ideal 2D periodic flow represented by the vane geometry. Developing a flow field, which has good consistency with the ideal blade-to-blade solution is critical in producing a heat transfer database useful for predictive comparisons.

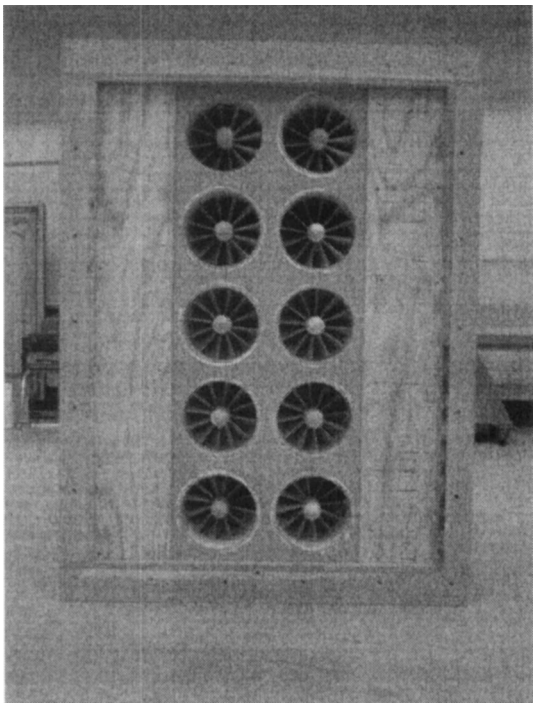

Fig. 4 Digital photo of dry low NO_x swirlers installed in mock combustor liner

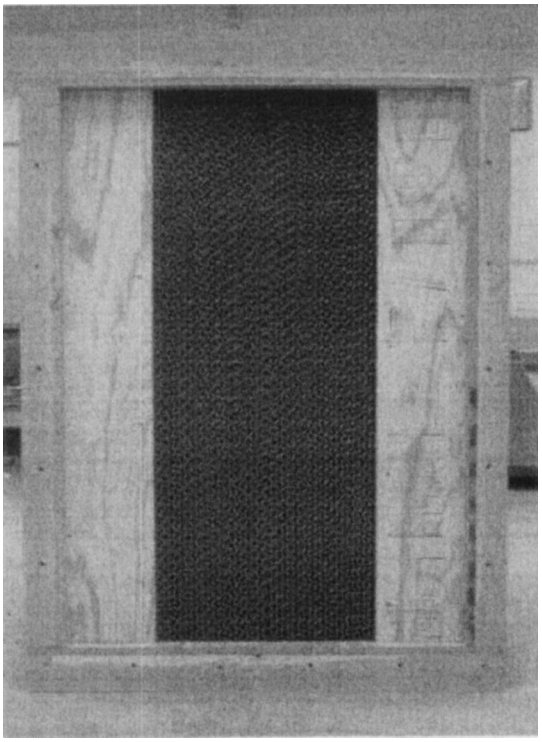

Fig. 5 Digital photo of catalytic combustor surface installed in mock combustor liner

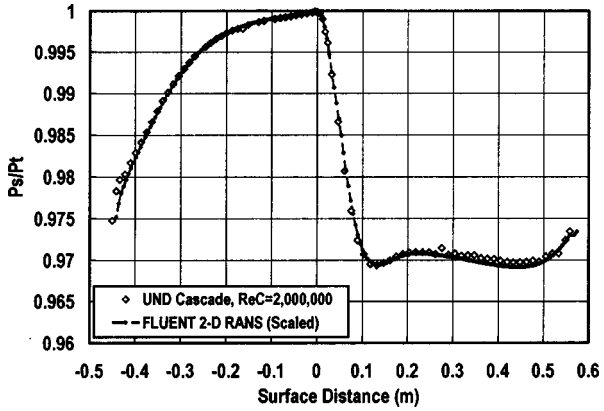

Fig. 6 Comparison between measured and predicted vane midspan pressure distribution, Re_C

Endwall Heat Transfer Distributions. Endwall heat transfer distributions were acquired using a constant heat flux boundary condition with the use of narrow-band thermochromic liquid crystal paint. The constant heat flux was generated on the endwall surface using two 0.025-mm-thick Inconel foils with a copper buss bar soldered to each end. A constant heat flux was generated using a large direct current provided by two power supplies. The foil was backed by a 0.125-mm-thick Kapton film, which was adhered to the endwall surface using a high temperature acrylic adhesive. The endwall surface was fabricated from a 2.54-cm-thick piece of polyisocyanurate foam, which was covered by a 0.4-mm-thick sheet of epoxy board. The epoxy board was secured to the foam using a film of epoxy. As indicated by the test section schematic, Fig. 2, the foils covered an area that preceded the leading edge plane of the vane by 6.35 cm and largely heated the surface between vanes 2 and 4. The foil heaters extended 14 cm axially past the vane trailing edge plane. Since the foil heaters were continuous, they passed underneath vane 2–4. Consequently, the heat flux generated under the vane footprint was conducted away using a vane shaped endwall cooler that was imbedded into the surface of the foam. These endwall coolers were feed air controlled to set the cooler temperature a few degrees below the temperature of the liquid crystal paint in order to minimize the impact of the heat sinks on the surface isotherms. In order to maintain a consistent thermal boundary condition between the endwall and the vane, the surface of the third vane in the cascade was heated in the same manner to a flux consistent with the endwall foils.

The microencapsulated narrow band liquid crystal paint used in these measurements was designed to provide a 1°C bandwidth with a 37°C start. The hue angle of the paint was calibrated as a function of temperature to enable the accurate resolution of surface temperature. The hue angle of the paint was determined from red, green, and blue intensities and provided a monotonic increase from 0° to 360° between the peak red intensity and the peak blue intensity of the visible temperature variation. The procedure used for the calibration is outlined in Ames, Barbot, and Wang [14] and the paint provided a sensitivity of 229°/°C near 37°C. The sensitivity of the paint at the highest green intensity was found to be very high and allowed a resolution of surface temperature within ±0.2°C.

The surface heat transfer coefficient along the isotherms was determined from the net surface heat flux divided by the temperature difference, the surface temperature (at the selected hue angle) less the inlet total air temperature. The heat transfer coefficient was reported in terms of a Stanton number based on the exit velocity, density, and specific heat at constant pressure. Here, exit velocity, U_∞, is determined from the inlet total and average exit static pressure. The net surface heat flux was determined as the heat flux generated within the foil less the radiative loss

$$\mathrm{St} = \frac{(q'' - q''_{\mathrm{rad}})}{(T_{\mathrm{green}} - T_{T,\mathrm{IN}})\rho U_\infty Cp}$$

The radiative heat loss was estimated to be

$$q''_{\mathrm{rad}} = \varepsilon\sigma(T^4_{\mathrm{green}} - T^4_{T,\mathrm{IN}})$$

The radiative loss was slightly overestimated due to the view factor of the endwall surface to the heated vane. Since the conduction loss was found to be less than the uncertainty band of the radiation loss, it was ignored.

The initial surface Stanton number value was found by increasing the heat flux on the endwall until the first green color appeared on the surface. The surface heat flux was then increased until the next incremental Stanton number was achieved. After the test surface had achieved steady state, the isotherms on the surface of the endwall were mapped using a series of pictures acquired with a digital camera. The camera was set in the manual mode to achieve the most repeatable hue angle possible. Subsequent to mapping the initial iso-Stanton number over the entire endwall, the procedure to change the heat flux, wait for steady state, and then acquire digital images was repeated until the last incremental iso-Stanton number was achieved.

At the lowest heat transfer coefficient on the surface, the radiative loss was estimated to be 21% of the net surface heat flux. At this condition, the uncertainty in the Stanton number was estimated to be ±10% at 20–1 odds. At the highest Reynolds number the maximum uncertainty in Stanton number was estimated to be ±5% at 20–1 odds. The largest source of error was due to the uncertainty in the radiative loss.

Data Acquisition. Inlet total and surface static pressures were acquired using two Rosemount smart pressure transmitters with spans of 250 and 5000 Pa full scale. Pressures were ported with a miniature solenoid scanner. Voltage outputs from the pressure transmitters and the EMFs generated by the type *K* thermocouples were scanned and read using an HP 3497A data acquisition unit. The integral voltmeter in the HP 3497A has a sensitivity of 1 μV. The thermocouples were connected using a passive constant temperature junction box, which was referenced using an ice bath. Hot wires were powered using a TSI ISA-300 constant temperature anemometer. Hot wire outputs were offset and amplified in the ISA-300 prior to sampling using a high-speed data acquisition board with 12 bits of resolution. Mean velocities were determined using 8192 samples, which were acquired at a time spacing exceeding two to three integral time scales. Power spectral density functions of the turbulence were averaged over 40 realizations calculated from velocity time records of 8192 points.

Experimental Uncertainties. Estimates for experimental uncertainties were made using the root sum square method discussed by Moffat [19]. Uncertainties in the static pressure were estimated to be 2.5% of the local dynamic pressure. Uncertainty in the exit velocity and Reynolds number was estimated to be 2%. The uncertainty in the reported turbulence level was estimated to be 3% of the value determined by the single wire. The energy scale had an estimated uncertainty level of 11%. All uncertainty levels were based on a 95% confidence interval.

Inlet Boundary Conditions. Inlet boundary layer parameters, turbulence levels, and turbulence scales were determined for both the mock catalytic combustor and the mock DLN combustor to provide comprehensive inlet boundary conditions for predictive comparisons. Data are documented for the three Reynolds numbers for both combustor conditions in Tables 1(*a*) and 1(*b*). Initially, span averaged inlet turbulence parameters are reported (Tu, U_∞, Lu, L_x, and ε). Subsequently, inlet boundary layer parameters taken 7 cm upstream from the vane leading edge plane are reported at five circumferential positions as referenced from the cascade test section schematic. Inlet boundary layer parameters include free-stream or peak velocity (U_∞), displacement and momentum thickness (δ_1 and δ_2), shape factor (H), skin friction coefficient ($Cf/2$), turbulence intensity referenced to U_∞, and the momentum thickness Reynolds number ($\mathrm{Re}_{\delta 2}$).

Experimental Results

Endwall Stanton number distributions taken over three Reynolds numbers for both the mock catalytic and DLN combustors are documented in this paper. Supporting fluid dynamic measurements, which include inlet turbulence conditions, inlet boundary layers conditions, and 95% span pressure distributions, are also presented. Inlet turbulence characteristics and boundary layer parameters were developed from single wire measurements taken 7 cm upstream from the leading edge plane of the cascade at five circumferential locations. The probe access positions are spaced evenly at 1/5th vane spacing in order to provide a representative picture of the inlet boundary condition. Ninety-five percent span pressure distributions were taken for the six conditions but a comparison at only one Reynolds number is shown since the influence of the blockage was not large. In order to provide a method to

Table 1 (*a*) **Endwall inlet boundary layer parameters, catalytic combustor (CC) condition.** (*b*) **Endwall inlet boundary layer parameters, DLN combustor condition.**

Catalytic Combustor (CC)

Re_C	Tu_∞	U_∞ (m/s)	Lx (cm)	Lu (cm)	ε (m^2/s^3)
500000	0.0103	4.95	5.26	3.83	0.0052
1000000	0.0153	9.46	0.62	5.15	0.0931
2000000	0.0102	19.63	0.89	1.75	0.6796

Catalytic Combustor (CC) Re_C = 500,000

Pos	Y (cm)	U_∞ (m/s)	δ_2 (cm)	δ_1 (cm)	H	Cf/2	Tu_∞	$Re_{\delta 2}$
4	16.90	4.32	0.075	0.153	2.041	0.0018	0.0111	206
5	9.22	4.09	0.110	0.213	1.942	0.0019	0.0133	285
6	1.54	4.94	0.089	0.188	2.118	0.0016	0.0092	279
7	-6.14	5.69	0.079	0.152	1.922	0.0019	0.0083	287
8	-13.82	5.08	0.080	0.165	2.066	0.0016	0.0092	259

Catalytic Combustor (CC) Re_C = 1,000,000

Pos	Y (cm)	U_∞ (m/s)	δ_2 (cm)	δ_1 (cm)	H	Cf/2	Tu_∞	$Re_{\delta 2}$
4	16.90	8.72	0.0740	0.1331	1.797	0.0019	0.0160	411
5	9.22	7.50	0.1058	0.1728	1.634	0.0023	0.0169	506
6	1.54	9.22	0.0643	0.1116	1.734	0.0023	0.0144	378
7	-6.14	10.73	0.0557	0.1047	1.881	0.0018	0.0138	380
8	-13.82	9.49	0.0675	0.1233	1.828	0.0017	0.0152	408

Catalytic Combustor (CC) Re_C = 2,000,000

Pos	Y (cm)	U_∞ (m/s)	δ_2 (cm)	δ_1 (cm)	H	Cf/2	Tu_∞	$Re_{\delta 2}$
4	16.90	18.16	0.0776	0.115	1.484	0.0021	0.0114	918
5	9.22	16.44	0.1043	0.165	1.583	0.0017	0.0135	1115
6	1.54	19.56	0.0897	0.127	1.420	0.0020	0.0097	1131
7	-6.14	22.90	0.0844	0.113	1.340	0.0022	0.0081	1247
8	-13.82	20.56	0.1111	0.141	1.270	0.0024	0.0090	1470

(*a*)

Dry Low NOx Combustor

Re_C	Tu_∞	U_∞ (m/s)	Lx (cm)	Lu (cm)	ε (m^2/s^3)
500000	0.1342	5.17	4.57	8.78	5.60
1000000	0.1433	9.65	4.34	8.95	43.73
2000000	0.1417	19.11	4.47	10.77	274.5

Dry Low NOx Combustor (CC) Re_C = 500,000

Pos	Y (cm)	U_∞ (m/s)	δ_2 (cm)	δ_1 (cm)	H	Cf/2	Tu_∞	$Re_{\delta 2}$
4	16.90	4.40	0.115	0.173	1.492	0.00370	0.1550	319
5	9.22	4.44	0.128	0.192	1.506	0.00345	0.1590	355
6	1.54	5.16	0.111	0.167	1.506	0.00314	0.1305	364
7	-6.14	5.81	0.092	0.135	1.466	0.00353	0.1146	341
8	-13.82	4.57	0.137	0.193	1.413	0.00347	0.1665	394

Dry Low NOx Combustor (DLN) Re_C = 1,000,000

Pos	Y (cm)	U_∞ (m/s)	δ_2 (cm)	δ_1 (cm)	H	Cf/2	Tu_∞	$Re_{\delta 2}$
4	16.90	8.66	0.111	0.153	1.414	0.00333	0.1552	549
5	9.22	8.48	0.124	0.179	1.437	0.00280	0.1666	661
6	1.54	9.73	0.114	0.161	1.406	0.00275	0.1332	695
7	-6.14	10.78	0.107	0.145	1.358	0.00288	0.1165	722
8	-13.82	8.38	0.093	0.135	1.460	0.00303	0.1734	486

Dry Low NOx Combustor (DLN) Re_C = 2,000,000

Pos	Y (cm)	U_∞ (m/s)	δ_2 (cm)	δ_1 (cm)	H	Cf/2	Tu_∞	$Re_{\delta 2}$
4	16.90	16.18	0.092	0.122	1.316	0.00290	0.1587	949
5	9.22	16.78	0.243	0.313	1.314	0.00206	0.1612	2299
6	1.54	19.35	0.100	0.137	1.367	0.00230	0.1323	1229
7	-6.14	21.93	0.084	0.110	1.317	0.00254	0.1150	1166
8	-13.82	17.11	0.188	0.236	1.253	0.00234	0.1721	2042

(*b*)

understand and discuss the secondary flow on the surface a lampblack and oil flow visualization taken on a similar cascade is presented. The six endwall Stanton number distributions documented in this paper provide a contrasting picture of the influence of the varying turbulence levels and the impact of Reynolds number. Taken together, these results are expected to provide a useful database for grounding endwall heat transfer predictive tools using relevant geometries across a range of engine relevant inlet conditions.

Inlet Boundary Layer and Turbulence Characteristics. Boundary layer measurements were taken at five circumferential locations at the inlet to the cascade and are documented in Tables 1(*a*) and 1(*b*) over the three Reynolds numbers for the two turbulence conditions. Initially the average inlet turbulence characteristics are given for the particular condition and Reynolds number prior to reporting the boundary layer parameters for each Reynolds number. The circumferential position of each boundary layer survey is given in the tables and is referenced to the bottom most circumferential position of the instrumented vane as shown in Fig. 2. The inlet boundary layer for the mock catalytic combustor is relatively thin due to both the uniform flow exiting the mock catalytic surface and the two to one area decrease across the inlet nozzle. Although the inlet turbulence level is low and the boundary layers are relatively thin ($Re_{\delta 2} \cong 260$) for the 500,000 Reynolds number case, the boundary layers have a significant level of turbulence, and a relatively low shape factor ($H \cong 2.02$) indicating transitional flow. An example of these velocity profiles is given in Fig. 7 where a profiles are presented as U^+ vs Y^+ for 500,000 and 2,000,000 Reynolds numbers for both catalytic and DLN inlet conditions. The 1,000,000 exit chord Reynolds number case also has relatively thin boundary layers ($Re_{\delta 2} \cong 420$), a significant level of turbulence, and a relatively low shape factor ($H \cong 1.78$) again indicating the inlet boundary layers are transitional or in an early stage of turbulent flow. At an exit chord Reynolds number of 2,000,000, the boundary layers are clearly turbulent, as shown in Fig. 7, having grown noticeably ($Re_{\delta 2} \cong 1180$), and with a shape factor ($H \cong 1.42$) and distribution consistent with turbulent flow. Determining the skin friction coefficients for the transitional flow was quite uncertain, probably by up to 20%, due to the lack of near wall velocity measurements.

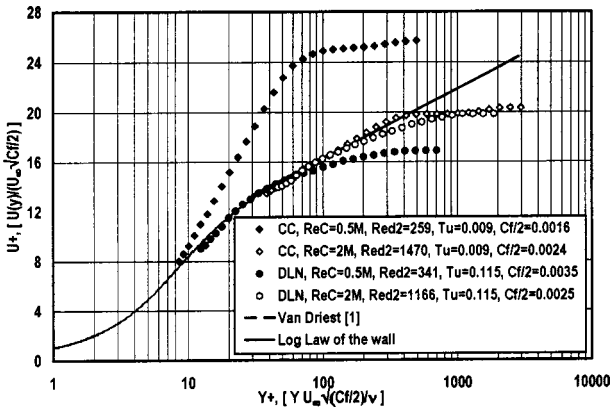

Fig. 7 Comparison between CC and DLN inlet boundary layers, Re_C=500,000 and 2,000,000

Inlet turbulence conditions and boundary layer parameters are presented for the DLN combustor inlet in Table 1(*b*) for the three Reynolds numbers. In contrast to the aeroderivative combustor, which has velocity profiles that peaked in midchannel, the inlet boundary layers for the DLN configuration were relatively thin turbulent boundary layers. Also, unlike canonical turbulent boundary layers, which show an upward departure from the log law in the outer intermittent or wake-like region of the boundary layer, no wake-like behavior was exhibited due to the aggressive mixing action of the high turbulence intensity. This high turbulence behavior is quite evident in the two DLN velocity profiles presented in Fig. 7. Additionally, the skin friction was significantly augmented above the low turbulence level for a similar momentum thickness Reynolds number. However, due to the action of the combustor flow with the swirler generated vorticity, there was a significant variation of velocity at mid channel changing from a deficit at positions 5 and 6 to a peak at position 8.

Nintey-Five Percent Pressure Distributions. Pressure distributions taken at a chord exit Reynolds number of 2,000,000 are shown for 95% span in Fig. 8 for the catalytic and DLN inlet conditions. The pressure distributions are plotted in terms of

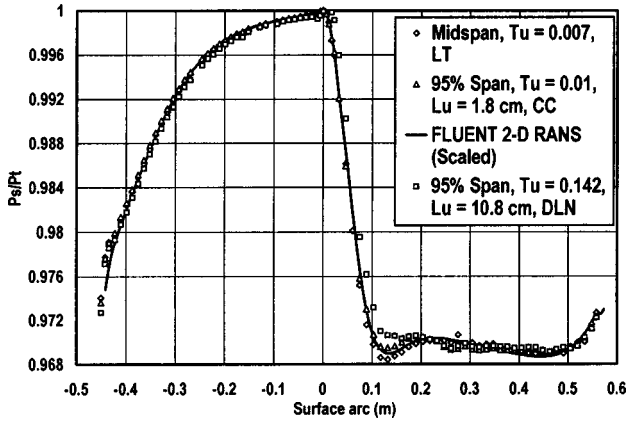

Fig. 8 Comparison of 95% span pressure distribution with midspan values, Re_C=2,000,000

P_s/P_t versus surface arc. The pressure distributions shown for the 2,000,000 Reynolds number case are representative of the pressure profiles for the lower and higher Reynolds number cases. The catalytic inlet condition shows only a very small change in pressure at 95% span indicating little effect of secondary flows. The DLN case at first appears to see a somewhat larger effect. However, the difference between the 95% DLN data and the midline data is likely due to a change in the near wall angle of attack caused by inlet swirl originating in the mock combustor. Even with the effect of the inlet swirl, the net effect on the pressure distribution is small.

Endwall Flow Visualization. Endwall secondary flows have a significant and identifiable influence on endwall heat transfer distributions for low inlet turbulence conditions. Figure 9 presents an endwall flow visualization using lampblack and oil for an endwall cascade with a geometry reasonably consistent with the present cascade (see Ames, Hylton, and York [6]). This visualization was produced by distributing an oil and lampblack mixture upstream of the leading edge plane in a compressible cascade before starting the flow for several minutes. The exit chord Reynolds number for this measurement was 2,000,000 with an exit Mach number of 0.6. The inlet momentum thickness Reynolds number was about 3800 with an inlet turbulence level of 6.5%. The flow visualization shows the mean direction of the wall shear for the incoming endwall flow highlighting the separation saddle point and the separation line in the passage above the pressure surface as well as the suction surface separation line that wraps around the leading edge and is pushed up onto the suction surface. This visualization shows how the incoming flow with low momentum is pushed away from the vane due to the inertial pressure gradients and bunches up below the suction surface. Compared to the present measurements, the inlet turbulence level for the flow visualization is bracketed by the two turbulence generators, while the inlet momentum thickness is roughly three times that of the present conditions.

Endwall Stanton Number Distributions. Endwall heat transfer visualizations showing contours of iso-Stanton numbers are displayed in Figs. 10–15 for the catalytic and DLN combustor inlet conditions. The iso-Stanton numbers are based on exit conditions and are shown at three exit chord Reynolds numbers ranging from 500,000 to 2,000,000. Side-to-side comparisons are shown for a single Reynolds number for both mock combustor configurations. In the first comparison, Figs. 10 and 11, iso-Stanton number contours are shown for a Reynolds number of 500,000 for the mock catalytic and DLN combustors, respectively. The center vane in the figure has the same constant heat flux boundary condition as the endwall heaters. However, the top and bottom vanes, vanes 2 and 4, are unheated. In Fig. 10, high heat

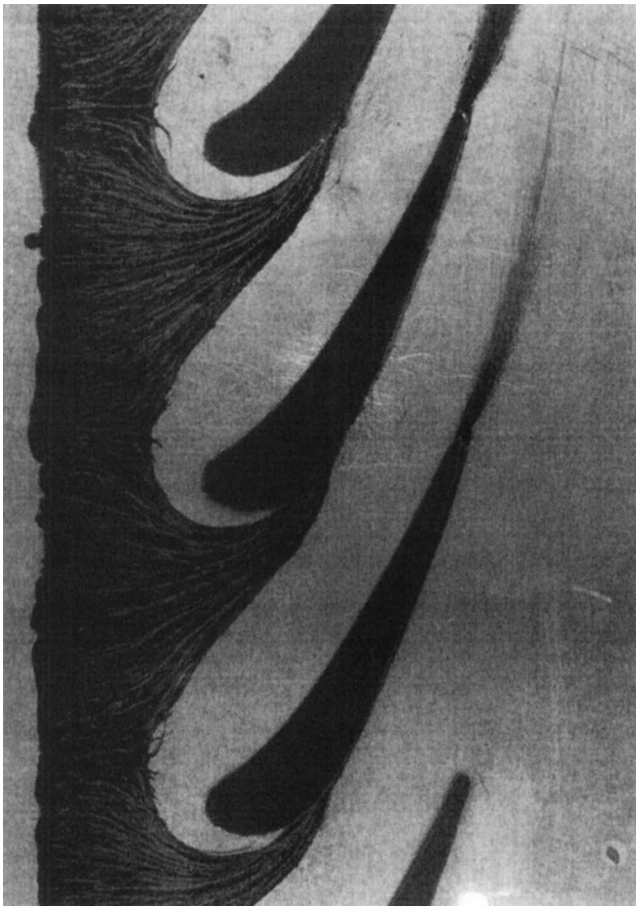

Fig. 9 Endwall flow visualization using lampblack and oil showing separation saddle point and pressure and suction surface separation lines (see Ref. [6])

transfer rates are seen at the beginning of heating, upstream of the cascade, due to the thin thermal boundary layers. Over the majority of the inlet passage, the heat transfer levels first diminish then remain constant as the flow accelerates through the passageway. However, high heat transfer rates are seen on the endwall near the stagnation region of the vane due to the horseshoe vortex, which wraps around the leading edge. Some evidence of the horse vortex system is seen by the jaggedness of contours off the pressure surface near the leading edge. Just below the suction surface, where the flow is entering the passage, a low heat transfer region is observed where the combination of passage vortex pushing fluid away from the pressure surface and suction leg of the horseshoe vortex cause low momentum fluid to converge. The general area of the separation line above the passage vortex can be seen by the variation in the 0.0014 iso-Stanton number underneath of the near suction surface. Within the vane passage, low heat transfer levels persist in spite of the relatively high velocities due the strong acceleration in this region. The level of heat transfer in this region is consistent with laminar flow. Higher heat transfer levels are seen along the suction surface, downstream of the expected liftoff location of the combined passage and horseshoe vortices, possibly due to a counter vortex. Downstream from the vane trailing edge, high heat transfer levels are seen due to turbulence generated by the wake. This high heat transfer region is pushed in the circumferentially upward direction. This trajectory is consistent with the characteristic over turning along the endwall, which is due to the endwall pressure gradients acting on the low momentum fluid accumulating along the surface. Generally, the heat

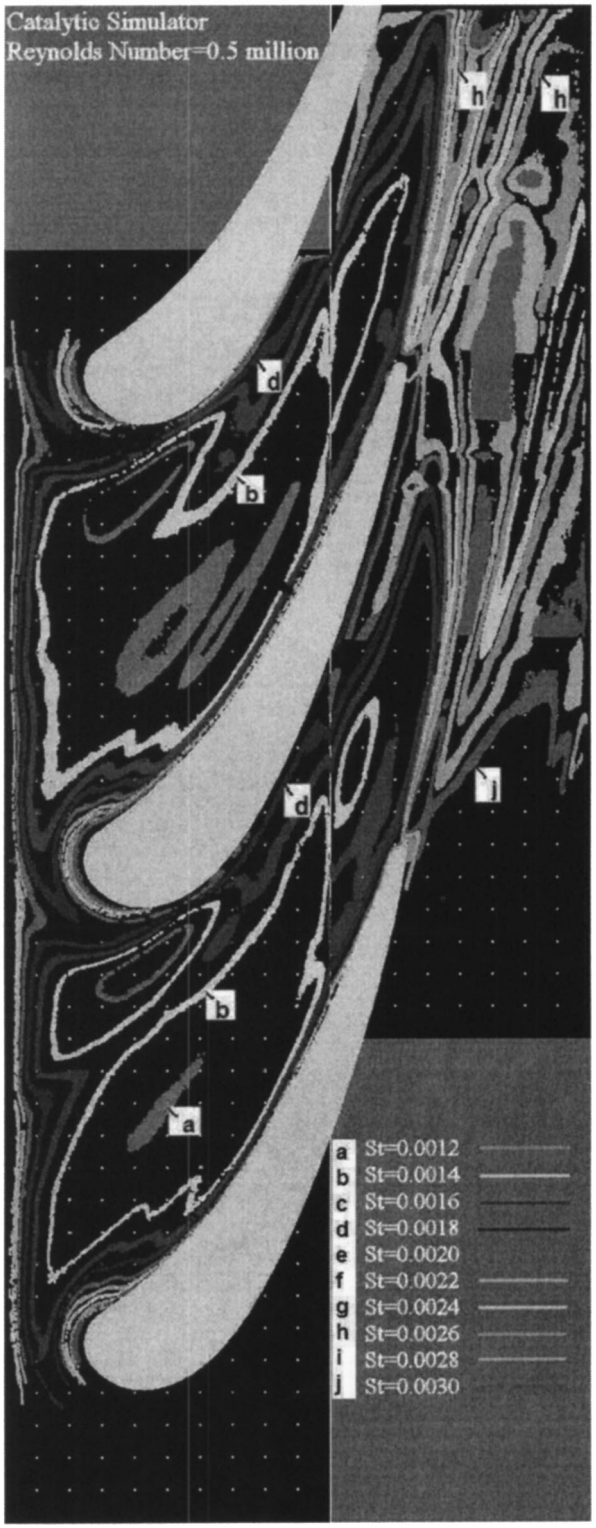

Fig. 10 Endwall Stanton number contours, CC, Tu=0.01, Lu =3.8 cm, Re_C=500,000

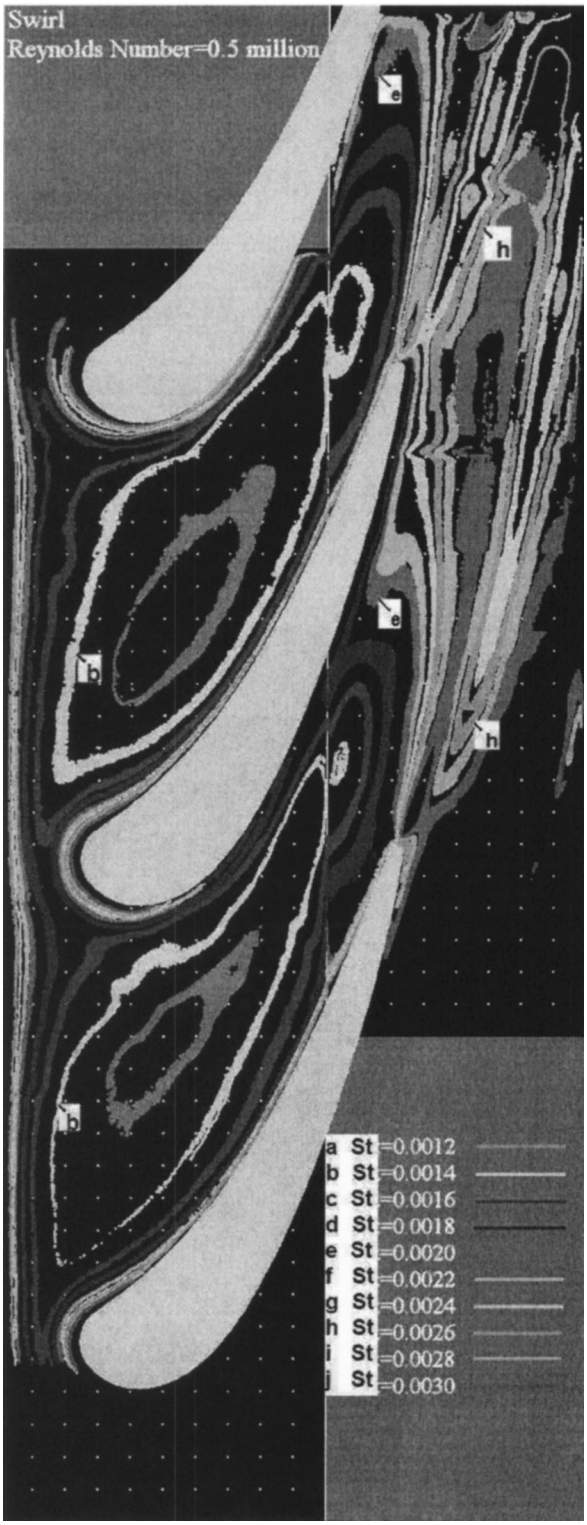

Fig. 11 Endwall Stanton number contours, DLN, Tu=0.134, Lu=8.8 cm, Re_C=500,000

transfer distributions acquired over this low turbulence catalytic combustor condition are strongly influenced by the secondary flows and vortices present in the passage.

The levels of heat transfer do not seem to be strongly influenced by the presence of the heated middle vane, except in the region directly downstream from the vane trailing edge. This difference can be seen by comparison between the upper trailing edge, which is the heated vane, and the lower trailing edge, which is the unheated vane. Generally flow moves up off the endwall onto the suction surface so we would not expect this region to be affected noticeably by the heated vane. However, flow moves down off the vane onto the endwall in the stagnation region and off the pressure surface. Comparison between Stanton number levels off the pressure side of the middle and bottom vanes exhibit

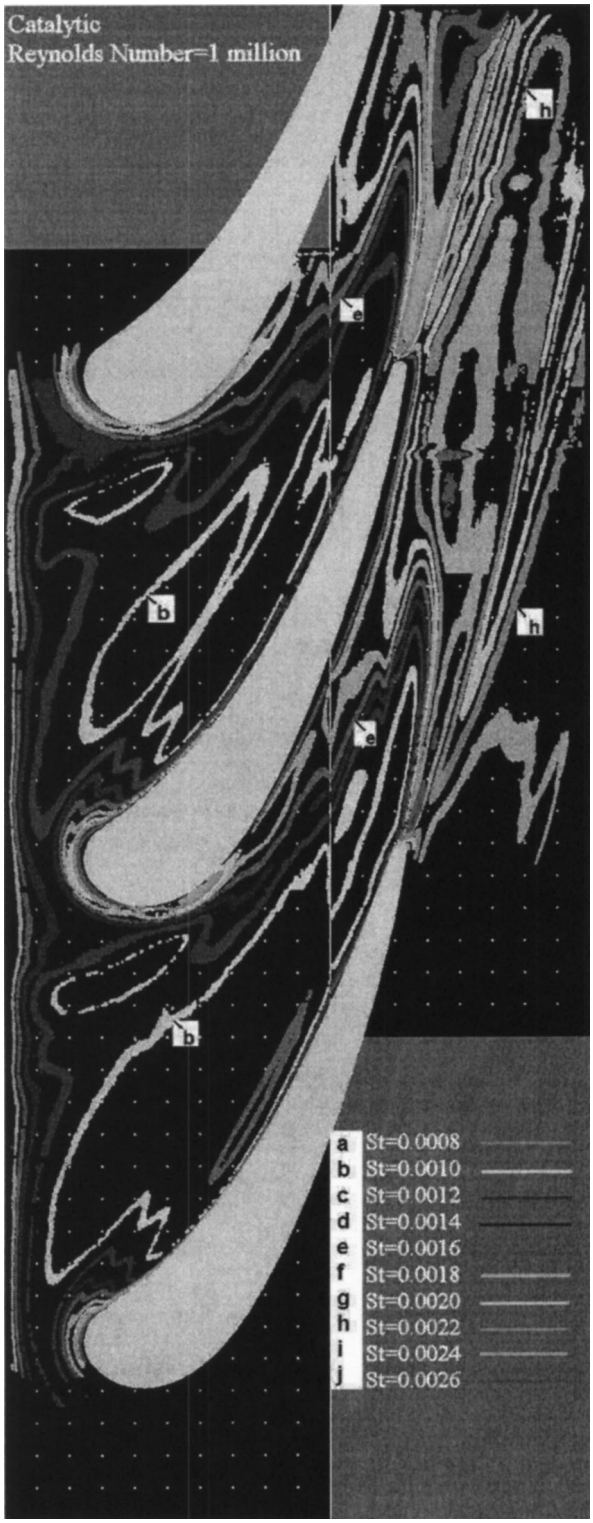

Fig. 12 Endwall Stanton number contours, CC, Tu=0.015, Lu =5.2 cm, Re_C=1,000,000

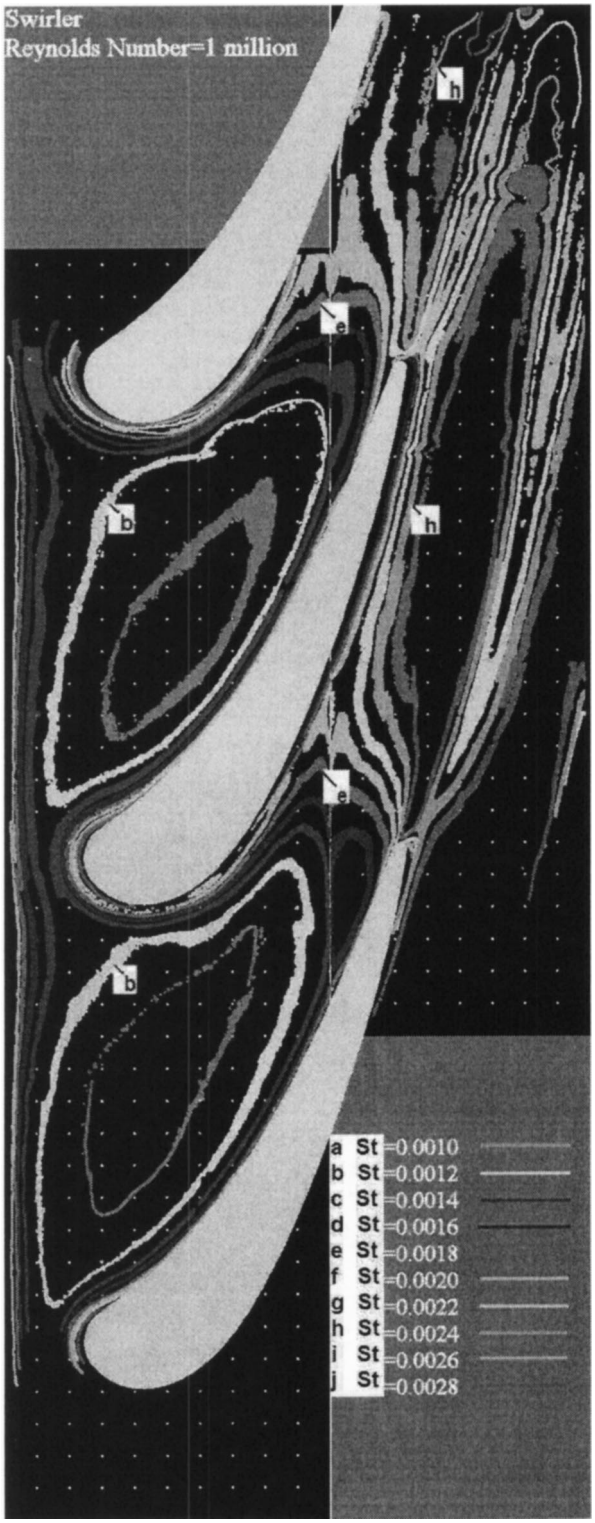

Fig. 13 Endwall Stanton number contours, DLN, Tu=0.143, Lu=9.0 cm, Re_C=1,000,000

little difference. This small difference is likely due to the very thin boundary layer, which forms on the vane in this region.

The endwall Stanton number distributions for the mock DLN combustor configuration shown in Fig. 11 appear to be much less affected by the discrete vortex systems seen on the endwall. High heat transfer rates can be seen adjacent to the stagnation region and downstream from the trailing edge similar to the catalytic combustor figure. However, no low heat transfer island is seen below the suction surface. Also, the contours are much smoother and do not exhibit the waviness produced by the discrete vortices. We can attribute this difference to the high intensity large-scale turbulence, which not only enhances the turbulence transport but also tends to push the discrete structures around. The heat transfer levels for the mock DLN combustor are a bit higher than the mock CC combustor in the region of the endwall which includes the region upstream of the vane leading edge through the first quarter

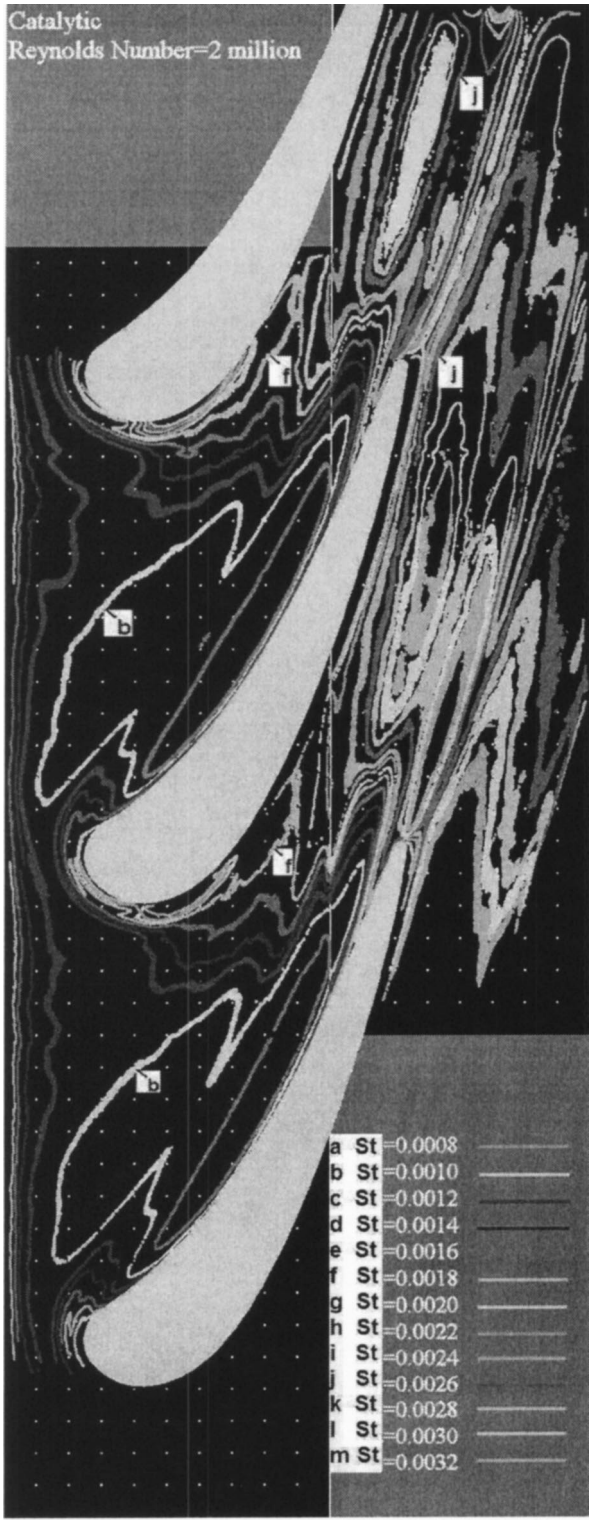

Fig. 14 Endwall Stanton number contours, CC, Tu=0.01, Lu =1.8 cm, Re_C=2,000,000

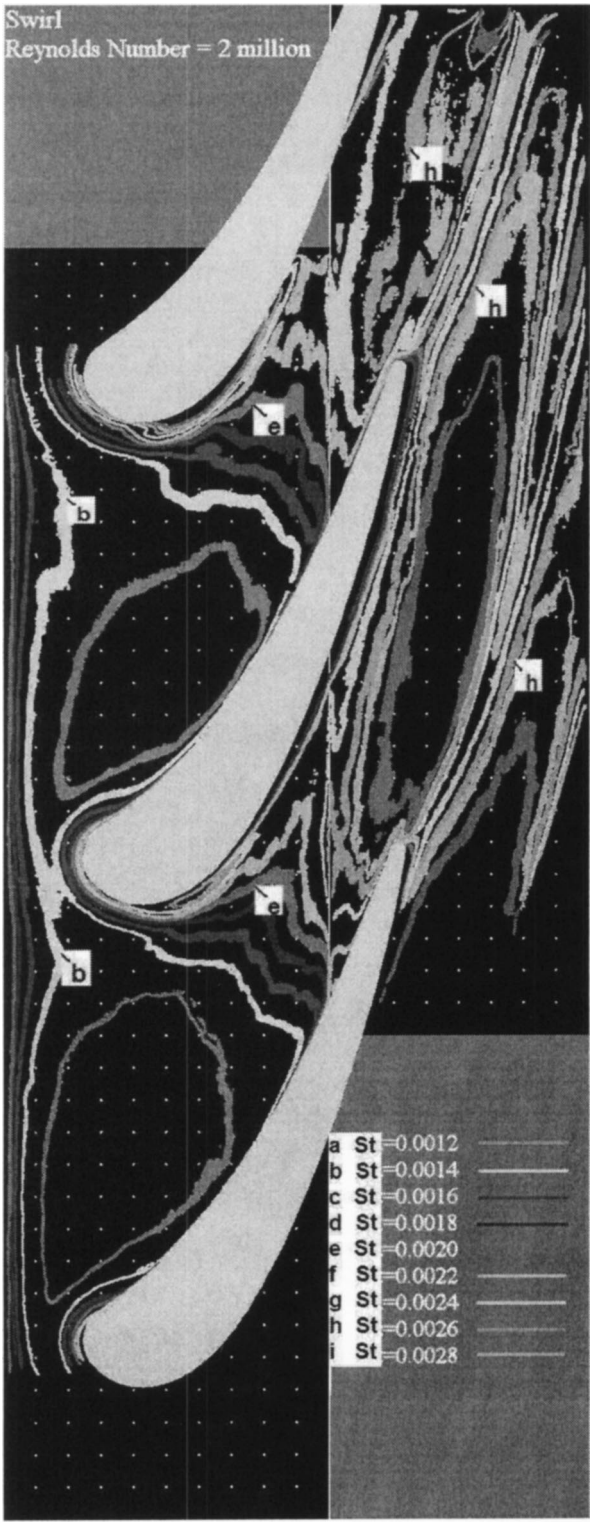

Fig. 15 Endwall Stanton number contours, DLN, Tu=0.142, Lu=10.8 cm, Re_C=2,000,000

of the passage. Also, for the DLN case there is no jaggedness in the contours off the pressure surface near the leading edge and no evidence of the effect of the pressure side separation streamline on the intrapassage contours. High heat transfer rates are present downstream from the trailing edge, which are slightly higher and more diffused or spread out than the catalytic combustor case. Heat transfer levels in the passage off the pressure surface and in the wake of the heated vane are slightly lower than off the unheated vane.

Stanton number patterns taken at a Reynolds number of 1,000,000 are presented for the mock catalytic combustor in Fig. 12 and show many similarities to the 500,000 Reynolds number case. However, at this Reynolds number the influence of the discrete vorticity is much more evident off the pressure surface. Here a low heat transfer region appears off the pressure surface of the vane where a laminar boundary layer has formed. Elevated heat transfer levels appear off the suction surface downstream of where

Table 2 Comparison of conditions and results of other vane endwall heat transfer studies

Ref	* E-6	* E-6	Exit	%	%			min	max
[#]	$Re_{C,MIN}$	$Re_{C,MAX}$	Ang	$Tu_{,MIN}$	$Tu_{,MAX}$	St, min	St, max	δ_2/C_{ax}	δ_2/C_{ax}
[9]	0.91	2.83	71	6.5	6.5	0.00095	0.00253	0.0125	0.05
[11]	3.4	3.4	73	13	13	0.00084	0.00273	0.0038	0.0038
[13]	1.1	1.1	72	0.6	19	0.00083	0.00292	0.0242	0.0246
[14]	0.5	2	73.4	1	14	0.0008	0.003	0.0029	0.019
[*]	0.5	2	73.4	1	14	0.0008	0.003	0.0033	0.005

the combined passage and horseshoe vortex are expected to liftoff and may be affected by a counter vortex in that region. High heat transfer rates are again seen downstream from the trailing edge. However, now two distinct regions are present. One high heat transfer region is just downstream from the wake and the other is further off of the pressure surface. This second region appears just downstream of the trailing edge plane and may be due to transitioning of the boundary layer.

Endwall Stanton number contours taken at a Reynolds number of 1,000,000 are shown for the DLN combustor in Fig. 13. Augmentation levels between the DLN and catalytic conditions in the inlet of the passageway are lower than those found by Radomsky and Thole [13] and may be due to differences in the inlet boundary layers. The average inlet momentum thickness Reynolds number is 622 for the DLN case and 416 for the catalytic simulator. The 1,000,000 Reynolds number DLN case shows many similarities with the 500,000 Reynolds number case. The iso-Stanton number contours are quite smooth and very little evidence of discrete vorticity is shown other than the relatively high heat transfer levels, which occur near the leading edge. Unlike the catalytic case, there is only one high heat transfer region downstream from the vane trailing edge. However, the width of this region is significantly larger than for the 500,000 Reynolds number DLN case and may be due to transitional effects within the passage.

Endwall Stanton number contours are shown in Fig. 14 for the catalytic combustor case at an exit Reynolds number of 2,000,000. The effects of secondary flows are evident in the heat transfer patterns in the leading edge region and off the suction surface. A low heat transfer region is evident off the pressure surface presumably where laminar flow is swept onto the endwall surface. High heat transfer regions exist downstream from the tailing edge in two very distinct regions. One region is clearly influenced by the wake and the other region is due to the thin turbulent boundary layer in the high velocity region of the passage. Heat transfer levels in the wake are lower downstream from the heated vane compared to the unheated vane. While some similarities are present between the catalytic combustor cases, the low heat transfer island below the suction surface is no longer present and higher heat transfer levels are present in the passage due to turbulent flow.

Endwall Stanton number contours taken at a Reynolds number of 2,000,000 are presented in Fig. 15 for the mock DLN combustor. Again, the Stanton number contours are much smoother than the mock catalytic combustor case and show little evidence of the discrete secondary flows. Stanton numbers through the passage are a strong function of the local velocity suggesting turbulent flow throughout the passage. The high heat transfer region downstream from the trailing edge has further enlarged from the lower Reynolds number cases and is likely the result of both the scrubbing of the wake and high velocities and thin turbulent boundary layers present in this region. The high intensity turbulence has likely caused enough buffeting to remove any delineation between the two high heat transfer regions. The endwall heat transfer patterns show many similarities to the lower Reynolds number cases except for the higher Stanton number levels within the passage.

Comparison with Previous Studies. A brief comparison of the conditions and results of other vane heat transfer studies is presented in Table 2. The Reynolds and Stanton numbers have been reported at exit conditions for consistency while the turbulence level and momentum thickness to axial chord ratio were based on inlet conditions. York, Hylton, and Mihelc [9] made endwall heat transfer measurements in a compressible linear cascade by calculating heat transfer through a thick solid metal endwall using a finite element technique and input from 85 thermocouples placed along the top and bottom surface. They acquired data at exit Reynolds numbers based on true chord ranging from $0.91E6$ to $2.83E6$. Their inlet turbulence level was 6.5% and they looked at inlet momentum thickness to axial chord ratios of 0.0125 and 0.05. For a typical case run at a chord Reynolds number of $0.91E6$ their Stanton numbers recalculated for exit conditions ranged from 0.00095 to 0.00253. They found an enhancement of endwall heat transfer near the vane stagnation region but their relatively sparse array of thermocouples could not resolve it well. Spencer, Jones, and Lock [11] acquired data in an isentropic light piston rig with an annular cascade using a transient liquid crystal technique. They acquired data at an exit Reynolds number based on midspan chord of approximately $3.4E6$. Their inlet turbulence level was determined to be 13% with an integral scale equal to about 37% of their inlet span. Their inlet momentum thickness to mean axial chord ratio was 0.0038. Their data showed no discernable enhancement on either hub or tip endwall in the vicinity of the stagnation region, probably due to endwall contouring. The highest heat transfer rates were generally downstream from the throat off the pressure surface. They reported heat transfer contours equivalent to Stanton numbers based on exit conditions ranging from 0.00084 to 0.00273. Radomsky and Thole [13] acquired endwall heat transfer measurements using a constant heat flux plate painted black with an infrared camera to obtain surface temperature measurements. They acquired their data in a large scale low speed cascade rig using a 9 times scale vane at an exit Reynolds number of $1.1E6$. They developed inlet turbulence levels of 0.6% and 19.5% and their reported integral scale for the high turbulence case was 12% of their inlet span. Their inlet momentum thickness to mean axial chord ratio was 0.025 for both the low and high turbulence cases. In spite of a rather blunt leading edge they reporting enhanced heat transfer in the leading edge with the highest values occurring downstream of the trailing edge in the wake and off of the pressure surface. They measured up to a 40% increase in Stanton number in the inlet region between the low and high turbulence level due to the relatively thick inlet boundary layers. They reported Stanton numbers based on inlet conditions, which when rescaled to exit conditions ranged from 0.00083 to 0.00292 excluding values along their tailboard. Detailed comparisons are impossible between the different studies due to very significant differences in geometries, measurement techniques, and inlet conditions. However, the range of the Stanton numbers reported is surprisingly consistent.

Conclusions

The present paper documents endwall surface heat transfer distributions taken in a linear cascade facility using two inlet turbulence conditions, which are representative of new low NO_x combustor configurations. One configuration has been developed to simulate turbulence generated in a catalytic combustion system and produced a turbulence level of one percent and a scale of about 2 cm. The other configuration is representative of a DLN geometry producing a turbulence level of 14% and a scale of about 9.5 cm. The boundary layers developing downstream of both combustor simulators have been investigated and are relatively thin. Heat transfer distributions and inlet conditions have been documented at Reynolds numbers of 500,000, 1,000,000, and 2,000,000.

The catalytic combustor condition had iso-Stanton number contours, which were strongly influenced by the secondary flows on the endwall. The horseshoe and passage vortex clearly affected the heat transfer distribution seen on the surface. The highest levels of

heat transfer were seen near the leading edge, downstream from the wake, and in the passage at the trailing edge plane.

The DLN combustion configuration did not show significant influence from the secondary flows on the endwall surface except in the near leading edge region. The high intensity large-scale turbulence created relatively smooth heat transfer contours on the endwall due to the enhanced transport of the turbulence its ability to push the vortex structures around on the surface. High heat transfer levels were produced on the surface downstream from the trailing edge due to the wake as well as at the trailing edge plane due to thin high velocity boundary layers. Heat transfer levels generated by DLN configuration were slightly higher than levels generated by the catalytic configuration.

The constant heat flux boundary condition developed on the surface of the middle vane had a noticeable influence in lowering heat transfer levels downstream from the trailing edge and a lesser influence in the passage above the pressure surface. Increasing Reynolds number caused higher Stanton number levels within the vane passage. However, overall Stanton number levels at the inlet and exit decreased with increasing Reynolds number.

The heat transfer level and distribution for the mock catalytic combustor was surprisingly similar to heat transfer generated by the low turbulence condition documented in Ames, Barbot, and Wang [14]. Similarly, the heat transfer level and distribution for the mock DLN combustor was quite similar to the heat transfer generated by the mock aeroderivative combustion system.

The heat transfer database documented in this paper and in (Ames, Barbot, and Wang [14]) is expected to be useful in grounding predictive methods for endwall heat transfer.

Acknowledgments

The authors gratefully acknowledge the support from the Advanced Gas Turbine System Research (AGTSR) consortium, which is administrated by the South Carolina Institute for Energy Studies and largely funded through DOE's National Energy Technology Laboratory. The authors would also like to acknowledge the help of Rolls Royce of Indianapolis for providing the vane geometry used in this study. Additionally, the facility used in this project was funded through a seed grant from the North Dakota EPSCoR. In addition, the authors are indebted to the University of North Dakota for providing additional support and laboratory space. Finally, the authors would like to acknowledge the work of Dan Pelarski, Robert Stengel, Scott Ciocetto, Jeremy Stocke, and Bobby Shimpa who helped design and fabricate the original test section as a senior design project and to Troy Lassle, Mark Hettwer, Brad Wall, and Scott Lindfors who worked as summer research assistants on this project.

Nomenclature

C = vane true chord length, m

C_{ax} = vane axial chord length, m

$Cf/2$ = skin friction coefficient, $Cf/2=\tau_w/\rho U_\infty^2$

Cp = specific heat at constant pressure, J/kg K

h = heat transfer coefficient, W/m^2/K, based on T_{green} and T_∞

H = shape factor, $H=\delta_1/\delta_2$

Lu = energy scale, Lu$=1.5|u'|^3/\varepsilon$

Lx = longitudinal integral scale of u' fluctuation

P = pressure, Pa

q'' = surface heat flux

Re_C = Reynolds number based on true chord and exit conditions

$\mathrm{Re}_{\delta 2}$ = momentum thickness Reynolds number, $\mathrm{Re}_{\delta 2}=U_\infty \delta_2/\nu$

St = Stanton number, St$=h/(\rho Cp U_{exit,\infty})$

T = temperature, K

Tu = turbulence level, Tu$=|u'|/U_\infty$

U_∞ = freestream velocity, m/s

$U+$ = velocity nondimensionalized on inner variables, $U+=U(y)/[U_\infty \cdot (Cf/2)^{1/2}]$

u', $|u'|$ = streamwise component root mean square fluctuation velocity, m/s

Y = normal distance from test surface, m

$Y+$ = wall normal distance nondimensionalized on inner variables, $Y+=y\cdot[U_\infty \cdot (Cf/2)^{1/2}]/\nu$

Greek Symbols

δ_1 = displacement thickness, Eq. (6.5) Kays and Crawford [1]

δ_2 = momentum thickness, Eq. (6.6) Kays and Crawford [1]

ε = emissivity

ε = turbulent dissipation rate, m^2/s^3

ν = kinematic viscosity, m^2/s

ρ = fluid density, mass per unit of volume, kg/m^3

σ = Stefan–Boltzman's constant

τ = shear stress, N/m^2

Subscripts

exit = refers to conditions at the nozzle exit plane

green = refers to peak in green intensity condition

rad = refers to radiative mode of heat transfer

s = refers to static condition

t = refers to total or stagnation condition

∞ = evaluated in the free stream

References

[1] Kays, W. M., and Crawford, M. E., 1993, *Convective Heat and Mass Transfer*, 3rd ed., McGraw-Hill, New York.

[2] Sieverding, C. H., 1985, "Recent Progress in the Understanding of Basic Aspects of Secondary Flow in Turbine Blade Passages," ASME J. Eng. Gas Turbines Power, **107**, pp. 248–257.

[3] Klein, A., 1966, "Investigation of the Entry Boundary Layer on the Secondary Flows in the Blading of Axial Turbines," BHRA T 1004.

[4] Langston, L. S., Nice, M. L., and Hooper, R. M., 1977, "Three-Dimensional Flow Within a Turbine Cascade Passage," ASME J. Eng. Power, pp. 21–28.

[5] Marchal, P., and Sieverding, C. H., 1977, "Secondary Flows Within Turbomachinery Bladings," Secondary Flows in Turbomachines, AGARD CP 214.

[6] Ames, F. E., Hylton, L. D., and York, R. E., 1986 (unpublished).

[7] Zess, G. A., and Thole, K. A., 2001, "Computational Design and Experimental Evaluation of Using an Inlet Fillet on a Gas Turbine Vane," ASME Paper No. 2001-GT-404.

[8] Burd, S. W., and Simon, T. W., "Flow Measurements in a Nozzle Guide Vane Passage with a Low Aspect Ratio and Endwall Contouring," ASME J. Turbomach., **122**, pp. 659–666.

[9] York, R. E., Hylton, L. D., and Milelc, M. S., 1984, "An Experimental Investigation of Endwall Heat Transfer and Aerodynamics in a Linear Vane Cascade," ASME J. Eng. Gas Turbines Power, **106**, p. 159.

[10] Harasgama, S. P., and Wedlake, E. T., 1989, "Heat Transfer and Aerodynamics of a High Rim Speed Turbine Nozzle Guide Vane Tested in the RAE Isentropic Light Piston Cascade," ASME J. Turbomach., **113**, pp. 384–391.

[11] Spencer, M. C., Jones, T. V., and Lock, G. D., 1996, "Endwall Heat Transfer Measurements in an Annular Cascade of Nozzle Guide Vanes at Engine Representative Reynolds and Mach Numbers," Int. J. Heat Fluid Flow, **17**, pp. 139–147.

[12] Arts, T., and Heider, R., 1994, "Aerodynamic and Thermal Performance of a Three Dimensional Annular Transonic Nozzle Guide Vane, Part I—Experimental Investigation," Paper No. 1994-31, 30th AIAA/ASME/SAE/ASEE Joint Propulsion Conference.

[13] Radomsky, R., and Thole, K. A., 2000, "High Freestream Turbulence Effects in the Endwall Leading Edge Region," ASME J. Turbomach., **122**, pp. 699–708.

[14] Ames, F. E., Barbot, P. A., and Wang, C., 2003, "Effects of Aeroderivative Combustor Turbulence on Endwall Heat Transfer Distributions Acquired in a Linear Vane Cascade," ASME J. Turbomach., **125**, pp. 210–220.

[15] Goldstein, R. J., and Spores, R. A., 1988, "Turbulent Transport on the Endwall in the Region Between Adjacent Turbine Blades," ASME J. Heat Transfer, **110**, pp. 862–869.

[16] Giel, P. W., Thurman, D. R., Van Fossen, G. J., Hippensteele, A. A., and Boyle, R. J., 1996, "Endwall Heat Transfer Measurements in a Transonic Turbine Cascade," ASME Paper No. 96-GT-180.

[17] Boyle, R. J., and Lucci, B. L., 1996, "Predicted Turbine Heat Transfer for a Range of Test Conditions," ASME Paper No. 96-GT-304.

[18] FLUENT 5.5, 2000, FLUENT 5.5 User's Guide, Fluent, Inc., Lebanon, NH.

[19] Moffat, R. J., 1988, "Describing the Uncertainties in Experimental Results," Exp. Therm. Fluid Sci., **1**, pp. 3–17.

Computational Analysis of Heat Transfer Enhancement in Square Ducts With V-Shaped Ribs: Turbine Blade Cooling

R. Jia
e-mail: rongguang.jia@vok.lth.se

B. Sundén
e-mail: bengt.sunden@vok.lth.se

Division of Heat Transfer,
Lund Institute of Technology,
P.O. Box 118,
221 00 Lund, Sweden

M. Faghri
e-mail: faghri@egr.uri.edu
Mechanical Engineering & Applied Mechanics,
University of Rhode Island,
Kingston, Rhode Island 02881

Experimental studies have revealed that both downstream and upstream pointing V-shaped ribs result in more heat transfer enhancement than transverse straight ribs in ducts. However, based on the available experimental results, contradiction exists whether the upstream or the downstream pointing V-shaped ribs orientation is superior for better enhancement in heat transfer. Further investigations are thus needed concerning the heat transfer and fluid flow phenomena in ducts with V-shaped ribs to clarify this. In the present investigation a numerical approach is taken and the heat and fluid flow is numerically simulated by a multi-block parallel 3D solver. For turbulence modeling, the $\overline{v^2}$ *f-k*ε *model is employed but results from previous EASM calculations are also considered in analyzing and attempting to understand the various experimental data. Large eddy simulations (LES) are also carried to evaluate the accuracy and reliability of the results of Reynolds-averaged Navier-Stokes (RANS) methods and to understand the underlying physical phenomena. It is suggested that the discrepancy between the various experiments most probably is due to the measurement methods, or the number of sampling points. With the TC (thermocouples) technique, a few sampling points are not sufficient to represent the heat transfer behavior in V-shaped ribs, due to the uneven distribution of the heat transfer coefficients.* [DOI: 10.1115/1.1865220]

1 Introduction

In order to allow the gas turbine designer to increase the turbine inlet temperature while maintaining an acceptable material temperature, sophisticated cooling methods are essential. For the internal cooling of the blades, ribbed ducts are usually used. The presence of ribs, also called roughness or turbulators, enhances the heat transfer coefficients by redevelopment of the boundary layer after flow reattachment between the ribs and because of induced secondary flows. The rib layouts and configurations can be varied and include 90, 60, and 45° parallel ribs and 45 and 60 deg V-shaped ribs.

It is essential to be able to accurately predict the enhancement of heat transfer generated by the roughness elements to ensure good design decisions. Accordingly, the heat transfer and fluid flow in ribbed ducts have been extensively studied both experimentally [1–15] and numerically [16–27].

As reviewed by Sundén [10], several conclusions can be drawn from the previous experimental studies:

- The rib height is important, and, for solid ribs, pitch to height ratio, $P/e=10$, is appropriate for effective heat transfer.
- The rib shape affects the pressure drop more than the heat transfer.
- The average heat transfer coefficients and friction factors increase with the blockage ratio, while the goodness factor $[(j/j_0)/(f/f_0)]$ decreases with the blockage ratio (e/D_h).
- Angled ribs or inclined ribs were found to be favorable for both heat transfer and pressure drop considerations.
- To study the mechanisms for the momentum and heat transfer processes, detailed measurements of flow and temperature fields are desirable.

Besides the above findings, there exist contradictions, for which clarification is necessary:

- The reattachment length reported by Webb et al. [6] and Rau et al. [8] are 6–8 rib heights and 3.5–4 rib heights downstream of the separation point, respectively.
- V-shaped ribs pointing in the upstream direction (≪) have been found to be superior as the volume goodness factor and the flow area goodness factor were considered by Han et al. [2] and Olsson and Sundén [9], while the downstream pointing V-shaped (≫) ribs are deemed to be better by Taslim et al. [4] and Gao and Sundén [15].

For the selection of turbulence models, the following conclusions are drawn based on the numerical investigations:

- Low-Re turbulence models are necessary to predict the heat transfer in ribbed ducts properly [16], and low-Re RSM yields thermal predictions superior to those of the low-Re eddy viscosity models [16,18].
- The $\overline{v^2}$ f-kε model is a promising turbulence model for accurate heat transfer predictions in the near-wall region. The $\overline{v^2}$ f-kε model predicts very well the heat transfer on the ribbed side wall of transverse-ribbed ducts. But for the smooth side wall of 3D ribbed ducts, the prediction is not good, mainly due to the presence of stress-induced strong secondary flow [24].
- However, for heat transfer in inclined-ribbed 3D ducts, the $\overline{v^2}$ f-kε model has a very good prediction, according to the study of Hermanson et al. [25]. This might be because the secondary flow is mainly driven by the inclined ribs, instead of by anisotropy of Reynolds stresses.
- At low-Reynolds numbers, the wall function approach is not capable of resolving the flow field between the ribs where both separation and reattachment points exist [16,26].
- Large-eddy simulation (LES) becomes a more reliable and feasible turbulence model with further developments in computational power [23,27].

In a previous study [28] using a low-Re EASM model [29], the authors found that sidewall heating could be a reason for the dis-

Manuscript received February 27, 2004; revision received October 21, 2004. Review conducted by: S. Acharya.

Table 1 Comparison of the four experiments (TC: thermocouple, LC: liquid crystal thermography)

Study	Han et al. [2]	Taslim et al. [4]	Olsson and Sundén [9]	Gao and Sundén [15]
Thermal measurement	TC	LC	TC	LC
Thermal uncertainty	±8%	±6%	±4%	±7.2%
Pressure uncertainty	±8%	±8%	±6%	···
Side wall heating	Yes	No	Yes	No
Wall heating method	Constant heat flux	Constant heat flux	Constant wall temperature	Constant heat flux
$\overline{Nu}$ calculation method	Average over the whole test section	Area averaged between two successive ribs	Average over the whole test section	Area averaged between two successive ribs
Local Nu provided	No	Yes	No	Yes
Rib heating	Yes (Metal ribs)	No (Plastic ribs)	Yes (Metal ribs)	No (Plastic ribs)
Duct aspect ratio	1	1	8	8
Re	15,000–90,000	5000–30,000	500–15,000	1000–6000
Rib arrangement	Inline	Staggered	Staggered	Staggered
Rib angle	30, 45, 60	45	60	60
e/D_h	0.0625	0.0833, 0.125, 0.167	0.0562	0.06
P/e	10	10	50	10
Conclusions	≪ Ribs provide higher heat transfer and lower pressure drop	≫ Ribs provide higher goodness factor	≪ Ribs provide higher goodness factor	≫ Ribs provide higher heat transfer coefficients

crepancy between various results. However, the validity of the EASM is sometimes questionable for complex turbulent flows and it would be appropriate to apply other models as well. Based on the successful prediction of heat transfer for inclined-ribbed 3D ducts [25], the $\overline{v^2}$ f-kε model is employed in the present study. In addition, a more universal modeling method such as LES is employed to further evaluate the RANS methods.

In this study, the conditions of the four experimental investigations, which resulted in contradictory conclusions, are first compared in Table 1. Then, the applied RANS models are validated with the available experimental data of Rau et al. [8]. The computations are carried out for the 45 deg V-shaped ribs for both inline and staggered arrangements. The rib heights to hydraulic diameters (e/D_h) are 0.0625 and 0.125. The geometry of all the cases is shown in Fig. 1. Finally, LES is carried out for the 60 deg V-shaped inline ribs for Re=4000 to validate the results from the RANS methods, and contribute to suggest an explanation and the possible reasons for the discrepancy between the experiments.

2 Analyses of the Four Experiments

Four experiments are compared in Table 1 to find out the different experimental conditions and the possible reasons for the discrepancy.

Due to the large aspect ratio in the study of Olsson and Sundén [9], and Gao and Sundén [15], the comparison hereafter is made with the other two experiments [2,4]. By comparing the different configurations, the following possible reasons should be examined:

- heating of the sidewalls
- inline or staggered rib arrangements
- effect of rib size, e/D_h
- definition of the average Nu
- experimental techniques

3 Method of Computational Analysis

3.1 Basic Equations. The fluid flow and heat transfer is solved using the filtered incompressible Navier-Stokes equations, with periodic boundary conditions. The filtered continuity, momentum, and energy equations are as follows:

$$\frac{\partial \overline{u_j}}{\partial x_j} = 0 \tag{1}$$

$$\frac{\partial \overline{u_i}}{\partial t} + \frac{\partial}{\partial x_j}(\overline{u_i}\,\overline{u_j}) = \frac{\partial}{\partial x_j}\left[\overline{\nu}\left(\frac{\partial \overline{u_i}}{\partial x_j} + \frac{\partial \overline{u_j}}{\partial x_i}\right) + \tau_{ij}\right] - \frac{1}{\overline{\rho}}\left(\frac{\partial \overline{p^*}}{\partial x_i} - \beta\right) \tag{2}$$

$$\frac{\partial \overline{t^*}}{\partial t} + \frac{\partial}{\partial x_j}(\overline{u_j}\,\overline{t^*}) = \frac{\partial}{\partial x_j}\left[\frac{\overline{\nu}}{\mathrm{Pr}}\frac{\partial \overline{t^*}}{\partial x_j} + \varphi_j\right] - \delta_{1j}\overline{u_j}\gamma \tag{3}$$

The appearance of τ_{ij} and φ_j is due to the convection terms, and they are modeled by the RANS or LES method.

In the RANS method, the turbulent stresses, $\tau_{ij} = -\overline{u_i' u_j'}$, and the turbulent heat fluxes, $\varphi_j = \overline{t' u_j'}$, are modeled by the $\overline{v^2}$ f-kε model and by the simple eddy diffusivity (SED) model, respectively.

In LES, $\tau_{ij} = -(\overline{u_i u_j} - \overline{u_i}\,\overline{u_j})$ and $-\varphi_j = \overline{u_j t} - \overline{u_j}\,\overline{t}$ are the subgrid scale (SGS) stresses and fluxes, respectively. The SGS stresses are modeled by the Smagorinsky model [30], and the fluxes are modeled by the SED model.

The assumption of fully developed periodic conditions is applicable for ribbed ducts in many cases. It has been shown experimentally that after a number of ribs, periodic fully developed flow prevails in which the mean velocity and thermal fields are periodically repeated with a constant shift. Moreover, the periodicity is pointed out and proved by experimental evidence in the cases considered by Rau et al. [8], Han et al. [2], and Taslim et al. [4]. The procedure chosen here to handle periodicity is addressed by Patankar et al. [31]. The pressure is divided up into a periodic part $\overline{p^*}$ in the main flow direction and a nonperiodic part $-\beta x$, i.e.,

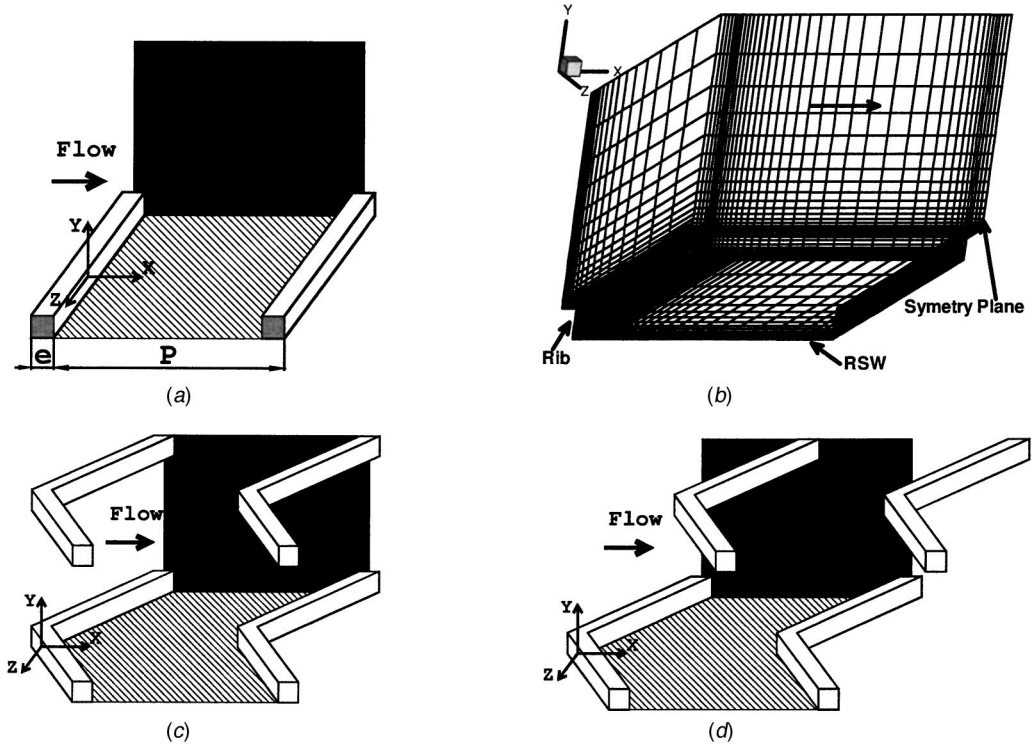

Fig. 1 Geometry of a straight square duct (*a*) with one-sided transverse ribs, (*b*) grid for the inline V ribs, (*c*) with two-sided inline V ribs, and (*d*) with two-sided staggered V ribs

$\overline{p}=\overline{p}^*-\beta x$, where β resembles the nonperiodic pressure gradient. Inserting this decomposition in the momentum equation leads to Eq. (2).

In the energy equation a constant heat flux boundary condition is applied because of the experimental conditions in [2,4]. Similar to the treatment of pressure, the temperature is divided up into a periodic part $\overline{t}^*$ in the main flow direction and a nonperiodic part γx, i.e., $t=\overline{t}^*+\gamma x$, where γ resembles the nonperiodic temperature linear increase rate, calculated as

$$\gamma=\frac{\dot{Q}}{\dot{m}c_pP} \tag{4}$$

where Q is the rate of heat input (over one pitch length) to the fluid. $\overline{t}^*$ is the periodic part of the temperature field. Inserting this decomposition in the energy equation leads to Eq. (3).

3.2 The RANS Methods. In the RANS methods, the unsteady terms are zero, and the filtered variables are equivalent to the Reynolds' averaged mean values, e.g., $\overline{u_i}\equiv U_i$.

3.2.1 The $\overline{v^2}$ f-kε Model. The $\overline{v^2}$ f-kε model by Durbin [32] is employed in the present study. The following two equations are solved for the turbulent kinetic energy and dissipation rate,

$$\frac{\partial}{\partial x_j}(U_jk)=\frac{\partial}{\partial x_j}\left[\left(\nu+\frac{\nu_t}{\sigma_k}\right)\frac{\partial k}{\partial x_j}\right]+P_k-\varepsilon, \tag{5}$$

$$\frac{\partial}{\partial x_j}(U_j\varepsilon)=\frac{\partial}{\partial x_j}\left[\left(\nu+\frac{\nu_t}{\sigma_\varepsilon}\right)\frac{\partial \varepsilon}{\partial x_j}\right]+\frac{C_{\varepsilon1}P_k-f_\varepsilon C_{\varepsilon2}\varepsilon}{T}, \tag{6}$$

where $P_k=-\overline{u_iu_j}\partial U_i/\partial x_j$ is the turbulent production.

This model extends the k-ε model by incorporating near-wall turbulence anisotropy and nonlocal pressure-strain effects, while retaining a linear eddy viscosity assumption. Two additional equations are solved. The first determines the stream-normal velocity fluctuation, $\overline{v^2}$:

$$\frac{\partial}{\partial x_j}(U_j\overline{v^2})=\frac{\partial}{\partial x_j}\left[(\nu+\nu_t)\frac{\partial \overline{v^2}}{\partial x_j}\right]+kf-\frac{\varepsilon}{k}\overline{v^2}, \tag{7}$$

where kf represents redistribution of turbulence energy from the streamwise to the wall-normal component.

The second transport equation is solved to obtain the nonhomogeneous effects produced by the presence of walls, which in turn avoids the need for damping functions. This is an elliptic relaxation equation for f:

$$f=L^2\frac{\partial}{\partial x_j}\left[\frac{\partial f}{\partial x_j}\right]+\frac{C_1}{T}\left[\frac{2}{3}-\frac{\overline{v^2}}{k}\right]+C_2\frac{P_k}{k}, \tag{8}$$

where the time and length scales are

$$T=\min\left[\max\left[\frac{k}{\varepsilon},6\sqrt{\frac{\nu}{\varepsilon}}\right],\frac{0.6k}{\sqrt{6}C_\mu\overline{v^2}S}\right], \tag{9}$$

$$L=C_L\max\left[\min\left[\frac{k^{3/2}}{\varepsilon},\frac{k^{3/2}}{\sqrt{6}C_\mu\overline{v^2}S}\right],C_\eta\frac{\nu^{3/4}}{\varepsilon^{1/4}}\right], \tag{10}$$

where $S=\sqrt{S_{ij}S_{ij}}$.

The Reynolds stresses are modeled as

$$\overline{u_iu_j}=\tfrac{2}{3}k\delta_{ij}-2\nu_tS_{ij}. \tag{11}$$

The turbulent eddy viscosity is modeled as

$$\nu_t=C_\mu\overline{v^2}T. \tag{12}$$

The coefficients are chosen as $f_\varepsilon=1$, $\sigma_\varepsilon=1.3$, $C_{\varepsilon2}=1.9$, $C_1=0.4$, $C_2=0.3$, $C_L=0.3$, $C_\mu=0.19$, $C_\eta=70$, and $C_{\varepsilon1}=1.3+0.25/[1+(C_L\varsigma/2L)^2]^4$, where ς is the nearest normal distance to the walls. The wall boundaries are set as

$$k_w=0, \quad \overline{v_w^2}=0, \quad \varepsilon_w=\frac{2\nu k_1}{s_1^2}, \quad f_w=-\frac{20\nu^2\overline{v_1^2}}{\varepsilon_w s_1^4}, \qquad (13)$$

where the subscript 1 represents the first grid point adjacent to walls.

3.2.2 The EASM Model. An EASM model was used in a previous investigation [28] and in this work some results will be used and further analyzed. For details of the model the reader is referred to [28].

3.2.3 Modeling of Turbulent Heat Fluxes. A simple eddy diffusivity (SED) model, based on the Boussinesq assumption, is employed in the present study,

$$\overline{u_i t}=\frac{\nu_t}{\sigma_T}\frac{\partial T}{\partial x_j}, \qquad (14)$$

where the turbulent Prandtl number is $\sigma_T=0.89$.

3.3 The LES Method. LES is a computational method in which the large eddies are computed, and the smallest, subgrid-scale (SGS) eddies are modeled. The underlying premise is that the largest eddies are directly affected by the boundary conditions, carrying most of the Reynolds stresses, anisotropic, and must be computed. The small-scale turbulence is weaker, contributing less to the turbulent Reynolds stresses, nearly isotropic, and has nearly universal characteristics. Therefore, it is less critical and more amenable to model. In many cases, the numerical diffusion plays a very important role in SGS stresses, thus there are no general rules to choose a SGS model. Actually, the SGS stresses contribute much less to the turbulent Reynolds stresses than the resolved scales. Therefore, for the sake of simplicity and robustness, $\tau_{ij}=-(\overline{u_i u_j}-\overline{u_i}\,\overline{u_j})$ are modeled by the Smagorinsky [30] model, and $-\varphi_j=\overline{u_j t}-\overline{u_j}\,\overline{t}$ are modeled by the SED model. This model assumes the SGS stresses follow a gradient-diffusion process, similar to molecular motion. Consequently, τ_{ij} is given by

$$\tau_{ij}=2\nu_t S_{ij}, \qquad (15)$$

where

$$S_{ij}=\frac{1}{2}\left(\frac{\partial\overline{u_i}}{\partial x_j}+\frac{\partial\overline{u_j}}{\partial x_i}\right)$$

is called the "resolved strain rate," and ν_t is the Smagorinsky eddy viscosity given by

$$\nu_t=(C_S\Delta)^2\sqrt{S_{ij}S_{ij}}, \qquad (16)$$

where Δ and C_S are the filter width (grid spacing) and the Smagorinsky constant, respectively, which must be specified prior to a simulation, varying from flow to flow. It is set as $C_S=0.1$ in this simulation.

3.4 Numerical Method. An in-house multi-block parallel computer code, CALC-MP [33,34], is applied to solve the governing equations. The code has been validated against many heat transfer and fluid flow cases, e.g., the channel flow, duct flow, impinging jets, and ribbed duct flow. It uses a collocated mesh arrangement and employs the improved Rhie and Chow interpolation [35] to calculate the velocities at the control volume faces. The SIMPLEC algorithm couples the pressure and velocity. An algorithm based on TDMA is used for solving the equations. In the RANS method, QUICK scheme is used for the discretization of the convection terms for the momentum equations, while the hybrid scheme is used for the convection terms in other equations. In LES, a second-order central scheme is used for the discretization of all the terms. Under-relaxation is applied for all equations and the source terms of the turbulence equations, and the proper values of the relaxation parameters for good convergence behavior were found from some test calculations.

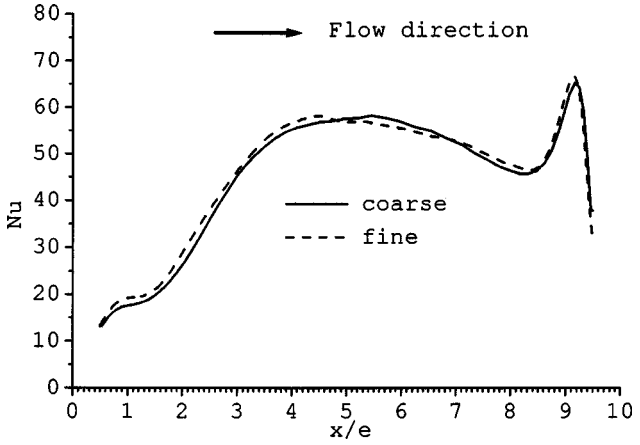

Fig. 2 Grid independence test for LES of the 90° ribbed case

For LES, nonuniform grids were generated, and grid refinement close to the wall was applied. To study grid independence, a 0.6M (coarse) and a 1.88M (fine) grid are used for the 90 deg case. The Nusselt number (Nu) distribution at the symmetry line on the ribbed wall is shown in Fig. 2. The largest difference in the local Nusselt number is less than 2%. Therefore, the coarse grid was deemed sufficient and subsequently used for the calculation for the 90 deg case. Body-fitted grids with the same number of cells as the 90 deg case are generated consequently.

For the RANS method, as a low Reynolds number (Re) formulation is applied, it is important that the y^+ value of the grid points closest to the wall be of the order of unity. In this work the y^+ values were less than unity in all the cases considered. Several successive grid refinements have been carried out in every case to make sure that negligible effects of the mesh on the solutions prevail. Figure 3 shows the thermal results for the one-sided transverse ribbed ducts with two grids of $82\times82\times32$ and $115\times115\times32$. The largest difference in the local Nu is less than 1.8%. Further increase of the number of grid points did not change the results significantly. Therefore, $82\times82\times32$ grid points were deemed sufficient and subsequently used for the validation case with one-sided ribs, while for the ducts roughened with inline V (IV) ribs $82\times56\times32$ grid points were used, due to the symmetry characteristics in both the *y*- and *z*-directions. A $98\times118\times32$ grid was used for the staggered V (SV) ribs cases.

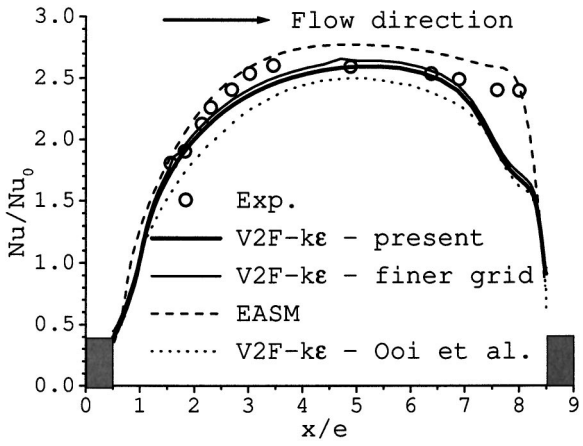

Fig. 3 Normalized Nusselt number at the ribbed wall in comparison with the experiments of Rau et al.

4 Results and Discussion

4.1 Validation of the Present Code With the One-Sided (1S) Ribs. Basically, the present code has been validated by Saidi and Sundén [21,22] with the detailed data of Rau et al. [8], including the 1S cases with $P/e=9$ and 12, and the two-sided-ribbed (2S) case with $P/e=9$ for the test Re of 30,000. The overall thermal and flow field features were predicted reasonably well. In this paper, only the simulation results, of the 1S case with $P/e=9$, Re=30,000, are presented in comparison with the experimental data of Rau et al. [8], because similar comparison results are obtained for the other cases (2S, $P/e=9$ case, and 1S, $P/e=12$ case). The geometry configuration is depicted in Fig. 1(*a*). The duct has a square cross section with ribs on the bottom wall only. The pitch to rib height ratio is 9 ($P/e=9$), and the rib height to hydraulic diameter is equal to 0.1 ($e/D_h=0.1$).

Figure 3 shows the local Nu distribution at the symmetry line on the ribbed sided-wall (RSW) normalized by that of a smooth duct, in comparison with the experiments. As shown, the agreement is good in both the shape and magnitude. However, the EASM slightly overpredicts the heat transfer, which might be due to the overprediction of the turbulent Reynolds stresses. The $\overline{v^2}$ f-kε model slightly underpredicts the Nu. The study of Ooi et al. [36] is also included, but it gives lower values than the present simulation. They used a slightly lower Prandtl number and they used a different version of the $\overline{v^2}$ f-kε model by Parneix and Durbin [37].

In general, the present simulations are in relatively good agreement with the experiments. Therefore, the numerical solution procedure is employed in the study of V ribs.

4.2 Straight Duct With Two-Sided V Ribs. The mean thermal-hydraulic characteristics of inline V (IV) ribs are presented first to obtain which pointing orientation is better for heat transfer enhancement. Then, the computations are conducted to find which of the following parameters lead to contradictory conclusions:

- rib arrangements, inline or staggered
- rib size, e/D_h
- the heating or not heating of the smooth side-wall (SSW)
- experimental techniques.

4.2.1 Inline V Ribs (e/Dh=0.0625). The flow configuration was a straight duct with IV ribs mounted on two opposite walls periodically, as shown in Fig. 1(*c*). The angle α is 45 deg. The ratio of pitch to rib height (P/e) is 10, and the ratio of rib height to hydraulic diameter (e/D_h) is 0.0625, which are chosen in accordance with Han et al. [2]. The computational grid is a multiblock body-fitted mesh, and it is shown in Fig. 1(*b*). Re is in the range of 10,000 to 32,000, which is typically employed in turbine blade cooling. Both the ribbed and smooth walls were set at constant wall heat flux condition.

Figure 4(*a*) shows the normalized averaged Nu and the Fanning friction factor for SSW and RSW versus Re for IV ribs. The ribbed-side normalized Nu is the averaged value of the entire RSW over one period. Similarly, the SSW Nu is the averaged value over a period.

The thermal results predicted by EASM show that the $\ll$ ribs provide higher Nu than $\gg$ ribs, on both the SSW and RSW. This finding is consistent with the experiments of Han et al., although the levels of values are not all in good agreement. However, the thermal results predicted by the $\overline{v^2}$ f-kε model show that the $\gg$ ribs provide higher Nu than $\ll$ ribs on RSW, while the $\gg$ ribs provide lower Nu than $\ll$ ribs on SSW. In the experiments by Han et al., 40 TCs were used to measure the temperature on the walls of ten periods, i.e., four TCs for each period, and one on each surface. The accuracy of the measurements depends on the location of the TCs. In addition, if one checks the local Nu distribution for $\ll$ and $\gg$ ribs in the paper of Han et al. [2], there is a steep

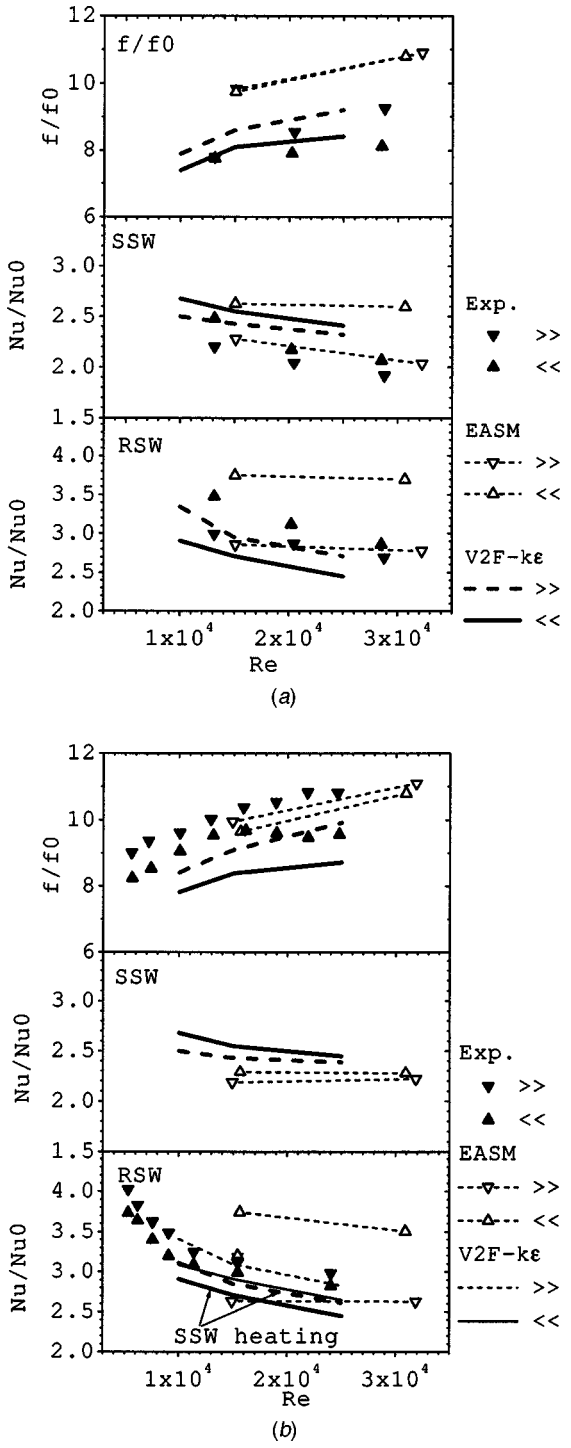

Fig. 4 Normalized Fanning friction factors, average Nusselt numbers of different rib configurations and Reynolds number at the ribbed and smooth side-walls: (*a*) The inline V ribs with $e/D_h=0.0625$, and the lines with open symbols are from the numerical solution, while the solid symbols are from the experimental data of Han et al. [2]. (*b*) The staggered V-ribs with $e/D_h=0.0625$, and the experimental data are from Taslim et al. [5] for $e/D_h=0.083$.

increase downstream of $x/D_h=16$, which is explained by the authors as an effect of favorable secondary flow induced by the rib orientation. This means that the flow considered is still in the developing region, and the Nu will be further increased downstream until the secondary flow is fully periodic developed. Con-

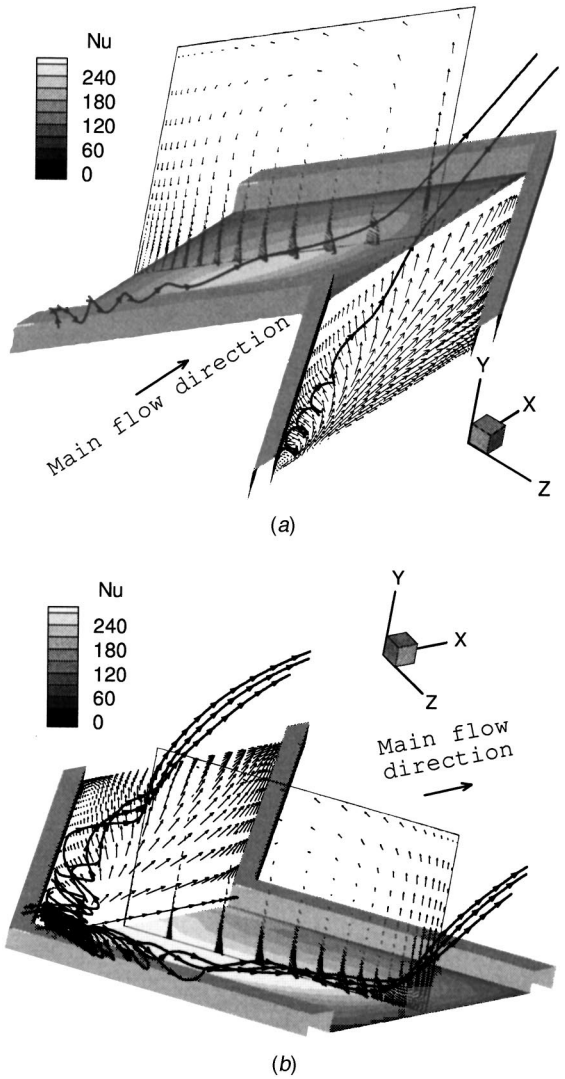

Fig. 5 The simulated fluid flow and heat transfer structure in ducts ribbed with inline V ribs at Re=15,000: (*a*) ≫ ribs and, (*b*) ≪ ribs

sequently, the average of the Nu of a more downstream period should be larger than the averaged value presented in the paper by Han et al., which is in accordance with the predicted larger Nu by the present numerical simulation using EASM.

Concerning the Fanning friction factor, the ≫ ribs induced a larger friction factor or higher-pressure drop. This is detected both by the experiments and the $\overline{v^2}$ f-kε model. However, the EASM severely over predicts the friction factor, and almost missed the difference between the two pointing directions. It is mainly caused by the up-flow at the middle of the ≫ ribs, as shown in Fig. 5(*a*). This up-flow induces a recirculation downstream, like the recirculation downstream of a cylinder, which consequently causes a larger drag force.

Figure 5 shows the flow structure and heat transfer coefficients on the RSW. The fluid flow is dominated by counter-rotating vortices induced by the ribs. The ≪ ribs induce an inflow vortex pair. The inflow vortex pair will stretch and thin the boundary layer between the two vortices, resulting in higher heat transfer coefficients at the center region, as shown in Fig. 5(*b*). However, the secondary flow induced by ≫ ribs acts in a contrary manner, inducing outflow. Therefore, the heat transfer coefficients are lower at the center region, as shown in Fig. 5(*a*).

According to the $\overline{v^2}$ f-kε model results, the ≫ ribs provide a higher Nu on the RSW, while ≪ ribs provide a higher Nu on the SSW, and a lower pressure drop than the ≫ ribs. Discrepancy exists on Nu on the RSW between the EASM and $\overline{v^2}$ f-kε models. This will be further discussed in the following sections.

Table 2 Measured Nu on the RSW for ‖ ribs by Han et al. [2] and Taslim et al. [4]

Authors	Rib	Re	Nu_{rib}/Nu_0
Han et al. [2]	Inline arrangement	14,476	2.5309
	$e/D_h=0.0625$	22,473	2.3062
Taslim et al. [4]	Staggered arrangement	15,623	2.2053
	$e/D_h=0.083$	24,748	2.0452

4.2.2 The Staggered V-Shaped Ribs (SV) ($e/D_h=0.0625$). The geometry for the staggered ribs with 45° angle is shown in Fig. 1(*d*).

As shown in Table 2, the experimental data of Han et al. [2] are compared with those of Taslim et al. [4]. There is about a 13% decrease of heat transfer coefficients in the staggered arrangement, although the e/D_h is increased, which should usually result in a higher Nu, because Nu increases with the increase of blockage ratio. Here the decrease of heat transfer is unlikely, because for flow in transverse ribbed ducts, an inline arrangement of the ribs gives approximately the same results as a staggered arrangement, which is stated in the paper of Han et al. [1]. Their conclusion is based on a case of Re=16,000, with $e/D_h=0.076$, $P/e=5$. So here the difference should be the heating of the SSWs in the experiments of Han et al., while this was not the case by Taslim et al. This will be further discussed in Sec. 4.2.4. Another possible reason is the sampling area. The mean value of the heat transfer coefficients of Han et al. is the average over the whole channel, including the developing region (where the heat transfer coefficients are high due to the underdeveloped boundary layer) and fully developed region. In Taslim et al., the average is over one period at the fully developed region.

As shown in Fig. 4(*b*), generally speaking, there is no large difference in the numerical results of the Nu on the RSWs for the inline and staggered ribs.

With both $\overline{v^2}$ f-kε model and EASM, the predicted friction factors for SV ribs are very similar to those of IV ribs, although the influence of the rib pointing directions is a little larger. They are also in relatively good agreement with the experiments of Taslim et al. For the staggered arrangement, the agreement between the numerical prediction of the friction factor and that of the experiments seems much better. However, one should bear in mind that the geometric parameters are a little different in the experiments of Taslim et al. If the change of the blockage ratio is taken into account, the friction factors are overpredicted, because the present blockage ratio (0.0625) is lower than that of Taslim et al. (0.083), and a lower blockage ratio should result in lower friction factors. Besides the geometric difference between the experiments of Taslim et al. and Han et al., the difference in the measured friction factor could also be due to the uncertainties in their experiments, because both authors claimed an uncertainty of order of 8%.

Overall, the numerical results are very similar for inline and staggered arrangement. Therefore, the rib arrangement is not the reason for the contradictory conclusions.

4.2.3 Effect of the Rib Size (Staggered, e/Dh=0.125). With EASM calculations, the increase of the rib size has a larger effect on the ≫ ribs than on the ≪ ribs. As shown in Fig. 6, the heat transfer coefficients on the SSW of the ≫ ribs is higher than those of the RSW. In addition, the heat transfer coefficients on the SSW of the ≫ ribs are higher than those of the ≪ ribs. However, the trends of the results from the $\overline{v^2}$ f-kε model are very similar to

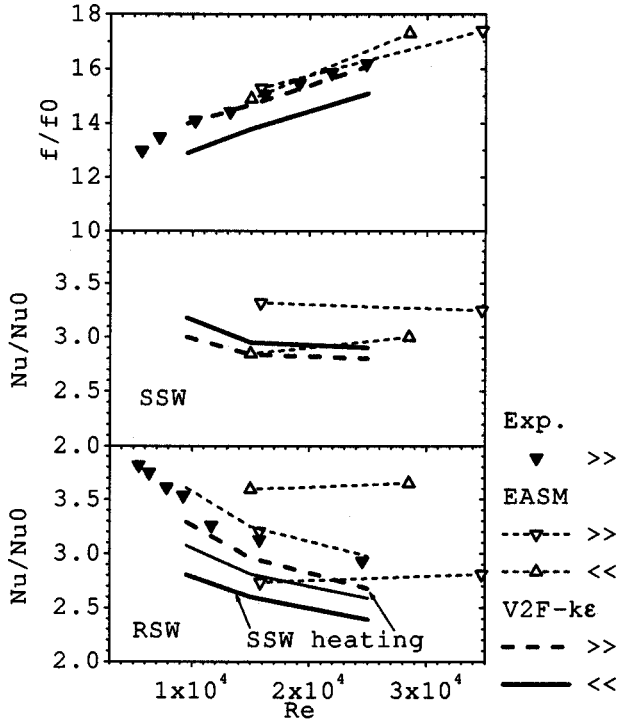

Fig. 6 Normalized Fanning friction factors, average Nusselt numbers of different rib configurations, and Reynolds number at the ribbed and smooth side-walls of the staggered V ribs with $e/D_h=0.125$

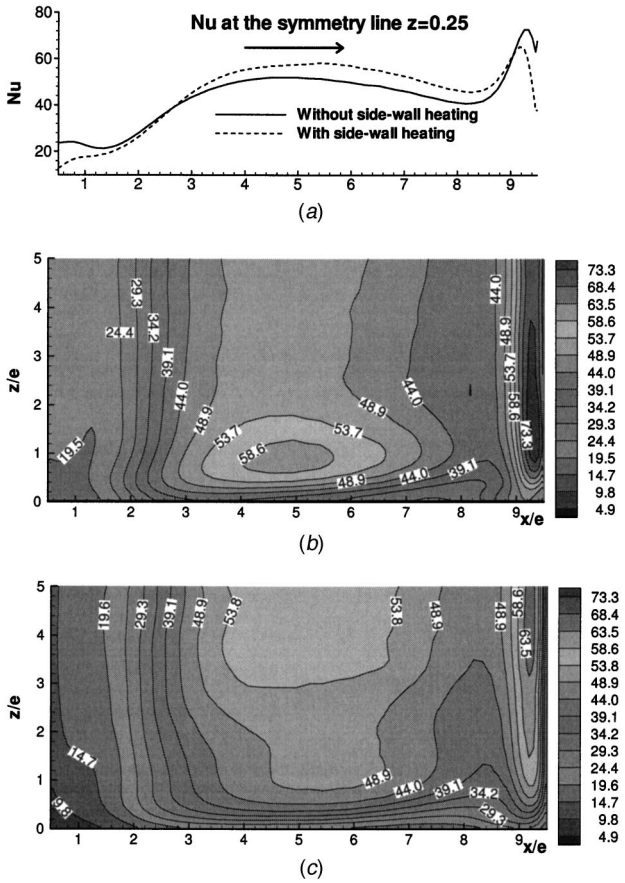

Fig. 7 Effect of SSW heating on the RSW Nu: (*a*) the comparison at the symmetry line, (*b*) no SSW heating, and (*c*) with SSW heating

those of the case with smaller rib size. Based on these findings it is likely that the rib size is not the main reason for the discrepancy between the various experiments.

4.2.4 The Effect of Heating of SSWs. SSW heating could be the reason for the contradictory conclusions, because the two experiments [2,9] with SSW heating demonstrated the superiority of the ⋘ ribs, while contrary conclusions are reached with the two experiments [4,15] without SSW heating. In fact, the SSW heating does have a large effect on the heat transfer coefficient, as shown in Fig. 7. With the $\overline{v^2}$ f-kε model, however, the SSW heating does not affect which pointing direction provides the higher heat transfer coefficient.

Here we want to explain how the SSW heating affects the heat transfer by LES calculations for the 90 deg case with $e/D_h=0.1$, $P/e=10$, and Re=4000. Figure 7 shows the Nu distributions on the RSW with and without SSW heating.

Figure 7(*b*) shows the Nu distribution on the RSW without SSW heating. A high Nu region occurs around the reattachment line. An island of very high heat transfer coefficient occurs around the point ($x/e=5$ and $z/e=1$) which is induced by the downwash fluid from the secondary flow. The largest heat transfer coefficient occurs around the corner upstream the rib. The basic reason is the very strong vortex induced around the corner. This strong vortex results in very high mean shear stress, which stretches the boundary layer to be very thin. Consequently, high heat transfer is induced. Normally, RANS models seriously underpredict this vortex intensity. Consequently, a serious underprediction occurs here, as was shown in Fig. 3.

Figure 7(*c*) shows the Nu distribution on the RSW with SSW heating. The flow field is the same as that without SSW heating. However, the heat transfer pattern is very different. The basic difference is that the high heat transfer regions are generally shifted toward the symmetry plane. The reason is two fold: (1) The SSW heating will generally increase the temperature of the fluid. This is especially true for the fluid close to the SSW, while the fluid close to the symmetry plane will be less influenced. In general, the bulk temperature T_b will be higher due to energy conservation. (2) Higher fluid temperature results in higher wall temperature T_w. The increase of the wall temperature close to the symmetry plane is less than that close to the SSW. Therefore, concerning the computation of $\mathrm{Nu}=q_w D_h/k(T_w-T_b)$, the Nu is decreased at regions close to the SSW, while it is increased at regions far from the SSW or close to the symmetry plane, as shown in the line-plot of Fig. 7(*a*).

Due to the fact that the $\overline{v^2}$ f-kε model and the EASM provide contradictory results, LES is employed to further clarify this.

4.3 Straight Duct With Two-Sided V Ribs. Table 3 shows the results from the present LES for $e/D_h=0.1$, 60 deg ribs with inline arrangement, and Re=6240. The results are in agreement with the experimental data [4,15]. The ⋙ ribs produce a higher Nu on the RSW, both with and without SSW heating, and induce higher friction factor, around 10%. The ⋘ ribs produce a higher Nu on the SSW. The SSW heating decreases the Nu on the RSW

Table 3 Results from the LES for $e/D_h=0.1$, 60 deg ribs with inline arrangement, and Re=6,240

Rib	Without SSW heating RSW Nu/Nu_0	With SSW heating RSW Nu/Nu_0	With SSW heating SSW Nu/Nu_0	f/f_0
⋘	3.331	2.746	2.751	11.63
⋙	3.696	3.168	2.523	13.31

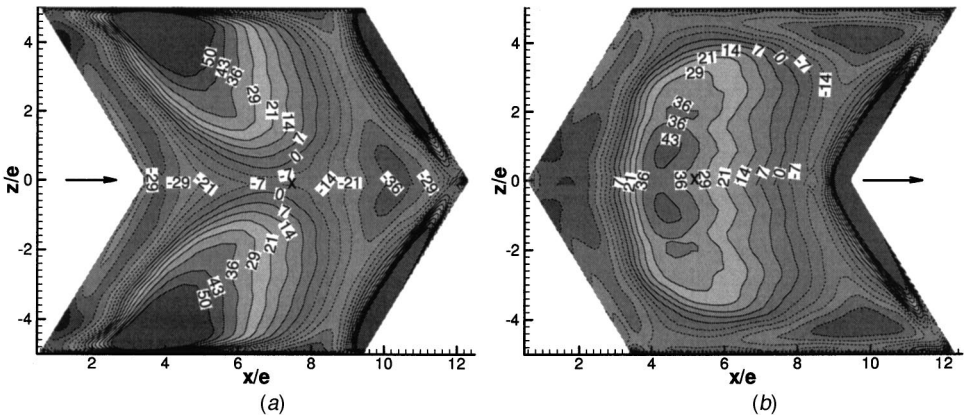

Fig. 8 Deviation (%) from the average Nu for (*a*) ≫ ribs and (*b*) ≪ ribs

for both ≫ and ≪ ribs. These results are in agreement with those from the $\overline{v^2}$ f-kε model and thus the LES supports the $\overline{v^2}$ f-kε model.

4.4 Analysis of the Experimental Data. Figure 8 shows the deviation of the local Nu from the average Nu. The reason for the experimental contradiction can be explained from this picture. If we use one TC (thermocouple) to measure the temperature representing the surface, ideally, we should put the TC at the places, where the averaged value is located, i.e., the 0%-deviation contour lines. For the ≫ ribs, if one puts the TC at the center of the surface, one will obtain a reasonably accurate average value [Fig. 8(*a*)], because the value at the center of the surface is very close (around −5% underprediction) to the average value. For the ≪ ribs, however, if one puts the TC at the center of the surface, one will obtain an overpredicted averaged value [Fig. 8(*b*)], because the value at the center of the surface is far (around 30% overprediction) from the averaged value.

If one checks the averaged values shown in Table 3, one can see that the averaged Nu on the RSW of the ≫ ribs is around 10% larger than that of the ≪ ribs. This larger percent is far less than the effect of TC location (30%), as shown in Fig. 8 and as discussed in the above paragraph. Combining the two effects, one can get up to 20% larger Nu on the RSW of the ≪ ribs than for the ≫ ribs, as shown in Fig. 4(*a*). Consequently, contradictory results are obtained between the experimental results with the TC technique and those with the LC (liquid crystal) technique.

Therefore, we conclude that the experimental data of [4,15] are more reliable than those of [2,9]. The main reason is that the information of the precise temperature distribution is important.

Concluding Remarks

The present solver and applied turbulence models were validated against experiments successfully. Local heat transfer and fluid flow characteristics have been achieved in straight square ducts with transverse and V-shaped ribs for Re ranging from 4000 to 32,000. The main conclusions are as follows:

Generally the results of the $\overline{v^2}$ f-kεmodel agree reasonably well with experimental data while some results from the EASM model appear less convincing. The LES calculations support the $\overline{v^2}$ f-kε method.

The ≫ ribs provide higher heat transfer coefficients on the RSW, while the ≪ ribs provide higher heat transfer coefficient on the SSW. The ≫ ribs induce a higher friction factor.

The SSW heating is not the main reason for the contradiction between the experiments, but it does have a large effect on the Nu of the RSW. This also means that the conclusion drawn in [28] was not completely correct.

An analysis of the experimental investigations suggests that the discrepancy between the experiments is probably because of the measurement methods or the number of sampling points. With the TC technique, a few sampling points are not sufficient to represent the heat transfer behavior. The two experiments [2,9] underestimate the heat transfer on the RSW for ≫ ribs, while they overestimate the heat transfer on the RSW for ≪ ribs. In the two experiments [4,15] with the LC technique, the numbers of the sampling points are enough to correctly present the heat transfer behavior. Therefore, the findings should be reliable.

In the design of cooling passages for turbine blades, ≫ ribs are recommended for application as high heat transfer enhancement is provided. However, one should note that this is accompanied by a high-pressure drop penalty.

It is also found that for analyzing and evaluating the heat transfer phenomena in gas turbine related applications, experimental investigations and numerical simulations are complementary and benefit from each other. However, development and careful handling are important.

Acknowledgments

The Swedish Energy Agency (STEM) financially supported this research work. The collaboration between Lund University and University of Rhode Island is financially supported by Wenner-Gren Foundation.

Nomenclature

e = Rib width and height (square rib)
D_h = Hydraulic diameter
f = Fanning friction factor, $f=\beta D_h/(2\rho U_b^2)$
f_0 = Fanning friction factor of a smooth circular tube (DB), $f_0=0.046\,\mathrm{Re}^{-0.2}$
j = Colburn j factor, $j=\overline{\mathrm{Nu}}/(\mathrm{Re}\,\mathrm{Pr}^{1/3})$
k = Turbulent kinetic energy
Nu = Nusselt number, $\mathrm{Nu}=q_w D_h/(\lambda(T_w-T_b))$
$\overline{\mathrm{Nu}}$ = Average Nu, $\overline{\mathrm{Nu}}=\int \mathrm{Nu}\,dA/\int dA$
Nu_0 = Nusselt number in a smooth circular tube $\mathrm{Nu}_0=0.023\,\mathrm{Re}^{0.8}\mathrm{Pr}^{0.4}$
P = Pitch of rib location
Re = Reynolds number, $\mathrm{Re}=U_b D_h/\nu$
Re_t = Turbulent Reynolds number, $\mathrm{Re}_t=k^2/(\nu\varepsilon)$
T_b = Bulk temperature, $T_b=\int T|U|dA/\int|U|dA$
U_b = Bulk velocity, $U_b=\int U dA/\int dA$
y^+ = Dimensionless distance to the wall
β = Nonperiodic pressure gradient
ε = Eddy dissipation rate
γ = Nonperiodic temperature gradient
ν = Kinematic viscosity
ν_τ = Turbulent kinematic viscosity
σ_T = Turbulent Prandtl number

ς = Normal distance to the nearest wall

Abbreviations.

$\parallel$ ribs = Inline two-sided transverse ribs
$\gg$ ribs = V-shaped ribs pointing downstream
$\ll$ ribs = V-shaped ribs pointing upstream
1s = One-sided transverse ribs
IV ribs = Inline V-shaped ribs
RSW = Ribbed side-wall
SSW = Smooth side-wall
SV ribs = Staggered V-shaped ribs
V ribs = V-shaped ribs

References

[1] Han, J. C., Glicksman, L. R., and Rohsenow, W. M., 1978, ''Investigation of Heat-Transfer and Friction for Rib-Roughened Surfaces,'' Int. J. Heat Mass Transfer, **21**(8), pp. 1143–1156.

[2] Han, J. C., Zhang, Y. M., and Lee, C. P., 1991, ''Augmented Heat Transfer in Square Channels With Parallel, Crossed, and V-Shaped Angled Ribs,'' ASME J. Heat Transfer, **113**, pp. 590–596.

[3] Metzger, D. E., Fan, C. S., and Yu, Y., 1990, ''Effects of Ribs Angle and Orientation on Local Heat Transfer in Square Channels With Angled Roughness Ribs,'' in *Compact Heat Exchangers*, edited by R. K. Shah, A. D. Kraus, and D. E. Metzger, Hemisphere Publishing Corporation, New York, pp. 151–167.

[4] Taslim, M. E., Liu, T., and Kercher, D. M., 1996, ''Experimental Heat Transfer and Friction in Channels Roughened With Angled, V-Shaped, and Discrete Ribs on Two Opposite Walls,'' ASME J. Turbomach., **118**(1), pp. 20–28.

[5] Liou, T. M., Hwang, J. J., and Chen, S. H., 1993, ''Simulation and Measurement of Enhanced Turbulent Heat Transfer in a Channel With Periodic Ribs on One Principal Wall,'' Int. J. Heat Mass Transfer, **36**(2), pp. 507–517.

[6] Webb, R. L., Eckert, E. R. G., and Goldstein, R. J., 1971, ''Heat Transfer and Friction in Tubes With Repeated-Rib Roughness,'' Int. J. Heat Mass Transfer, **14**, pp. 601–617.

[7] Kukreja, R. T., and Lau, S. C., 1998, ''Distribution of Local Heat Transfer Coefficient on Surfaces With Solid and Perforated Ribs,'' J. Enhanced Heat Transfer, **5**, pp. 9–21.

[8] Rau, M., Cakan, M., Moeller, D., and Arts, T., 1998, ''The Effect of Periodic Ribs on the Local Aerodynamics and Heat Transfer Performance of a Straight Cooling Channel,'' ASME J. Turbomach., **120**, pp. 368–375.

[9] Olsson, C. O., and Sundén, B., 1998, ''Experimental Study of Flow and Heat Transfer in Rib-Roughened Rectangular Channels,'' Exp. Therm. Fluid Sci., **16**(4), pp. 349–365.

[10] Sundén, B., 1999, ''Enhancement of Convective Heat Transfer in Rib-Roughened Rectangular Ducts,'' J. Enhanced Heat Transfer, **6**, pp. 89–103.

[11] Liou, T. M., Chen, M. Y., and Wang, Y. M., 2003, ''Heat Transfer, Fluid Flow, and Pressure Measurements Inside a Rotating Two-Pass Duct With Detached 90 deg Ribs,'' ASME J. Turbomach., **125**(3), pp. 565–574.

[12] Al-Hadhrami, L., Griffith, T., and Han, J. C., 2003, ''Heat Transfer in Two-Pass Rotating Rectangular Channels (AR=2) With Five Different Orientations of 45 deg V-Shaped Rib Turbulators,'' ASME J. Heat Transfer, **125**(2), pp. 232–242.

[13] Iacovides, H., Kelemenis, G., and Raisee, A., 2003, ''Flow and Heat Transfer in Straight Cooling Passages With Inclined Ribs on Opposite Walls: An Experimental and Computational Study,'' Exp. Therm. Fluid Sci., **27**(3), pp. 283–294.

[14] Chandra, P. R., Alexander, C. R., and Han, J. C., 2003, ''Heat Transfer and Friction Behaviors in Rectangular Channels With Varying Number of Ribbed Walls,'' Int. J. Heat Mass Transfer, **46**(3), pp. 481–495.

[15] Gao, X., and Sundén, B., 2001, ''Heat Transfer and Pressure Drop Measurements in Rib-Roughened Rectangular Ducts,'' Exp. Therm. Fluid Sci., **24**(1–2), pp. 25–34.

[16] Iacovides, H., and Raisee, M., 1999, ''Recent Progress in the Computation of Flow and Heat Transfer in Internal Cooling Passages of Turbine Blades,'' Int. J. Heat Fluid Flow, **20**(3), pp. 320–328.

[17] Jang, Y. J., Chen, H. C., and Han, J. C., 2001, ''Flow and Heat Transfer in a Rotating Square Channel With 45 deg Angled Ribs by Reynolds Stress Turbulence Model,'' ASME J. Turbomach., **123**(1), pp. 124–132.

[18] Bonhoff, B., Parneix, S., Leusch, J., Johnson, B. V., Schabacker, J., and Bölcs, A., 1999, ''Experimental and Numerical Study of Developed Flow and Heat Transfer in Coolant Channels With 45 deg Ribs,'' Int. J. Heat Fluid Flow, **20**(3), pp. 311–319.

[19] Shih, T. I.-P., and Sultanian, B. K., 2001, ''Computations of Internal and Film Cooling,'' in *Heat Transfer in Gas Turbines*, B. Sundén and M. Faghri, Eds. pp. 175–226.

[20] Jia, R., Rokni, M., and Sundén, B., 2001, ''Impingement Cooling in a Rib-Roughened Channel With Cross Flow,'' Int. J. Numer. Methods Heat Fluid Flow, **11**(7), pp. 642–662.

[21] Saidi, A., and Sundén, B., 2000, ''Numerical Simulation of Turbulent Convective Heat Transfer in Square Ribbed Ducts,'' Numer. Heat Transfer, Part A, **38**(1), pp. 67–88.

[22] Saidi, A., and Sundén, B., 2001, ''On Prediction of Thermal-Hydraulic Characteristics of Square-Sectioned Ribbed Cooling Ducts,'' ASME J. Turbomach., **123**(3), pp. 614–620.

[23] Murata, A., and Mochizuki, S., 2001, ''Large Eddy Simulation of Turbulent Heat Transfer in an Orthogonally Rotating Square Duct With Angled Rib Turbulators,'' ASME J. Turbomach., **123**(5), pp. 858–867.

[24] Ooi, A., Iaccarino, G., and Durbin, P. A., 2002, ''Reynolds Averaged Simulation of Flow and Heat Transfer in Ribbed Ducts,'' Int. J. Heat Fluid Flow, **23**(6), pp. 750–757.

[25] Hermanson, K., Parneix, S., Wolfersdorf, J., and Semmler, K., 2000, ''Prediction of Pressure Loss and Heat Transfer in Internal Blade Cooling Passages,'' Turbine-2000, Int. Symp. on Heat Transfer in Gas Turbine Systems, 13–18 August, Cesme, Turkey.

[26] Abdon, A., 2001, ''Numerical Simulation of Cooling Concepts Related to Gas Turbine Combustors,'' Ph.D. thesis, Division of Heat Transfer, Dept. Heat and Power Engineering, Lund Institute of Technology, Lund, Sweden.

[27] Saha, A. K., and Acharya, S., 2003, ''Flow and Heat Transfer in Internally Ribbed Duct With Rotation: An Assessment of LES and URANS,'' ASME paper no. GT2003-38619.

[28] Jia, R., Saidi, A., and Sundén, B., 2003, ''Heat Transfer Enhancement in Square Ducts With V-Shaped Ribs,'' ASME J. Turbomach., **125**(4), pp. 788–791.

[29] Rokni, M., 2000, ''A New Low-Reynolds Version of an Explicit Algebraic Stress Model for Turbulent Convective Heat Transfer in Ducts,'' Numer. Heat Transfer, Part B, **37**(3), pp. 331–363.

[30] Smagorinsky, J., 1963, ''General Circulation Experiments With the Primitive Equations. I. The Basic Experiment,'' Mon. Weather Rev., **91**, pp. 99–164.

[31] Patankar, S. V., Liu, C. H., and Sparrow, E. M., 1977, ''Fully Developed Flow and Heat Transfer in Ducts Having Streamwise-Periodic Variations of Cross-Sectional Area,'' ASME J. Heat Transfer, **99**, pp. 180–186.

[32] Durbin, P. A., 1995, ''Separated Flow Components With $k-\varepsilon-v^2$ Model,'' AIAA J., **33**(4), pp. 659–664.

[33] Jia, R., and Sundén, B., 2004, ''Parallelization of a Multi-Blocked CFD Code Via Three Strategies for Fluid Flow and Heat Transfer Analysis,'' Comput. Fluids, **33**, pp. 57–80.

[34] Jia, R., and Sundén, B., 2003, ''A Multi-Block Implementation Strategy for a 3D Pressure-Based Flow and Heat Transfer Solver,'' Numer. Heat Transfer, Part B, **44**(5), pp. 457–472.

[35] Rhie, C. M., and Chow, W. L., 1983, ''Numerical Study of the Turbulent Flow Past an Airfoil With Trailing Edge Separation,'' AIAA J., **21**, pp. 1525–1532.

[36] Ooi, A., Iaccarino, G., and Behnia, M., 1998, ''Heat Transfer Predictions in Cavities,'' *Annual Research Briefs of Center for Turbulence Research* (1998) Stanford University, CA, pp. 185–196.

[37] Parneix, S., and Durbin, P. A., 1997, ''Numerical Simulation of 3D Turbulent Boundary Layers Using the V2F Model,'' *Annual Research Briefs of Center for Turbulence Research*, NASA/Stanford Univ., pp. 135–148.

Journal of Heat Transfer

Technical Note

This section contains shorter technical papers. These shorter papers will be subjected to the same review process as that for full papers.

Film Effectiveness Downstream of a Row of Compound Angle Film Holes

M. E. Taslim and A. Khanicheh
Mechanical and Industrial Engineering Department,
Northeastern University, Boston, MA 02115

Effects that two different compound-angle film-hole configurations have on film cooling effectiveness are investigated. Effectiveness measurements have been made downstream of a single row of compound-angle cylindrical holes with a diameter of 7.5 mm, and a single row of compound-angle, diffuser-shaped holes with an inlet diameter of 7.5 mm. Both geometries were inclined with respect to the coverage surface at an angle α of 25 deg. The cylindrical holes, however, were oriented perpendicular to the high-temperature airflow direction while the diffuser-shaped holes had a compound angle of 45 deg with respect to the high temperature air flow direction. Both geometries were tested over a blowing ratio range of 0.7 to 4.0 Surface temperatures were measured along four longitudinal rows of thermocouples covering the downstream area between two adjacent holes. The results showed that the best overall protection over the widest range of blowing ratios was provided by the diffuser-shaped film cooling holes, particularly at high blowing ratios. The increased cross-sectional area at the shaped hole exit lead to a reduction of the momentum flux of the jet exiting the hole. Therefore, the penetration of the jet into the main flow was reduced, resulting in an increased cooling effectiveness. CFD analyses were also performed to study the film cooling effectiveness downstream of the row of holes. Comparisons between the test and numerical results showed a reasonable agreement between the two, thus CFD can be considered a viable tool to predict the cooling performance of different film cooling configurations in a parametric study. [DOI: 10.1115/1.1865222]

Introduction

For film cooling with compound-angle injection, higher and more uniform film cooling effectiveness is expected due to the reduced axial momentum and the enhanced lateral momentum of the secondary flow. Ligrani et al. [1,2] tested cases of $\phi=30$ deg and $\phi=50.5$ deg for both a single row and staggered double row of holes with compound-angle injection. Their results showed that the compound-angle injection configuration significantly improved the film cooling protection. Studies by Ekkad et al. [3,4], Sen et al. [5], and Schmidt et al. [6], provided film cooling effectiveness and heat transfer coefficient distribution over a flat surface with one row of inclined holes for different compound angles. Similar to previous studies, they found that compound-angle injection provides higher effectiveness values than injection without a compound angle. In another attempt to further improve the cooling process, attention has been turned to adapting shaped holes, such as holes with enlarged exits. Using these shaped holes, better cooling performance can be obtained due to the reduction in penetration of coolant jets into the hot gases and improved lateral spread of coolant. Overall improvements in film effectiveness were found in the studies conducted by Goldstein et al. [7,8], Papell [9], Makki and Jakubowski [10], and Gritsch et al. [11], for a variety of shaped holes. These studies have shown that expanding the exit of the cooling hole improves film cooling performance relative to that for a cylindrical hole. One further step in improving the performance of film cooling is the combination of compound angle holes with shaped holes producing noncylindrical holes oriented away from the streamwise direction. Less work has documented film cooling effectiveness for the compound-angle shaped hole. In a recently published paper, Bell et al. [12] investigated the film cooling effectiveness and the Stanton number ratio downstream of different cooling hole configurations, such as cylindrical, round, simple angle; laterally diffused, simple angle; laterally diffused, compound angle; forward-diffused, simple angle; and forward-diffused, compound angle. The best overall protection was provided by laterally diffused, compound-angle holes, followed by forward diffused, compound-angle holes. Early computational studies of film cooling were limited to simplified geometries with coarse grids. Bergeles et al. [13] used a finite dif-

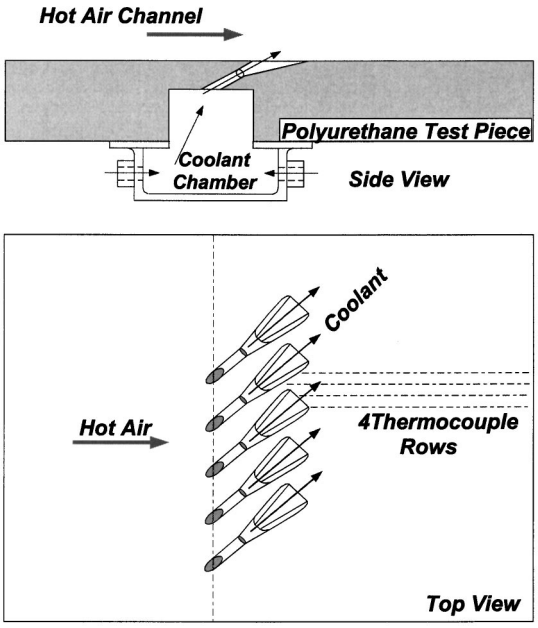

Fig. 1 Schematics of the test apparatus

Contributed by the Heat Transfer Division for publication in the JOURNAL OF HEAT TRANSFER. Manuscript received by the Heat Transfer Division February 10, 2004; revision received December 15, 2004. Associate Editor: P. M. Ligrani.

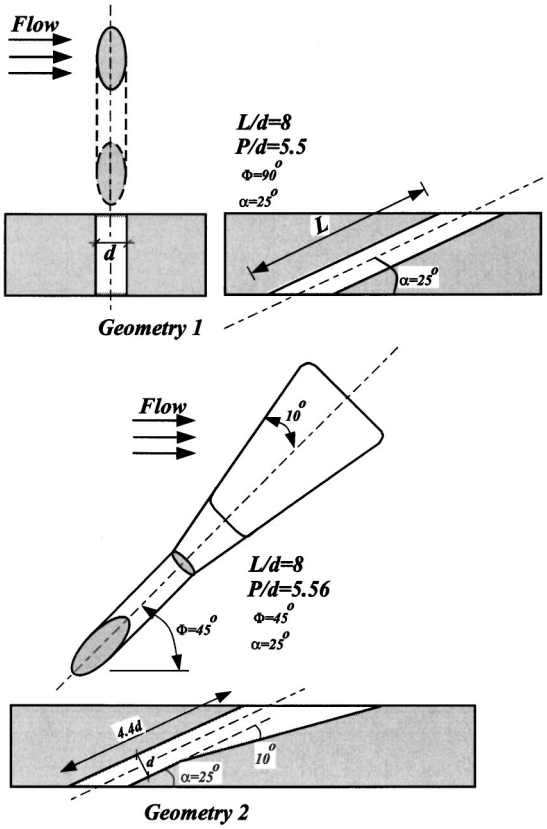

Fig. 2 Film-hole geometries

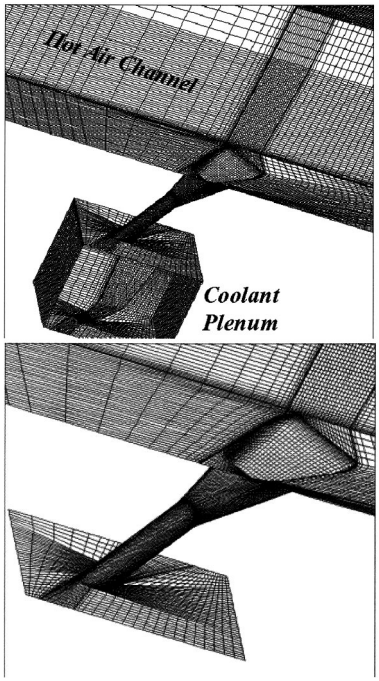

Fig. 4 Schematics of the mesh arrangements for the shaped film hole

ference scheme with a ''partial parabolic'' scheme of flowfield in the neighborhood of the injection holes with poor agreement between numerical results and experimental data. Much finer meshes, as well as more accurate discrete schemes, were needed to improve the accuracy of results. Demuren [14] showed that for identical grid meshes a higher-order discretization scheme performed better than a first-order hybrid scheme. Leylek and Zerkle [15] showed that the computational model must include the film-hole and plenum regions to capture the physics of the jet cross-flow interaction accurately. Of the recent investigations that employ numerical techniques, Walters and Leylek [16], McGovern and Leylek [17], Hyams and Leylek [18], and Brittingham and Leylek [19] performed computational simulations with comparison to experimental data to obtain the effects of streamwise injection and compound angle with cylindrical and shaped holes.

In this study, film cooling effectiveness distributions are measured downstream of two different hole geometries: a row with compound-angle cylindrical hole configuration and a row with compound-angle, shaped holes. To the best of the authors' knowledge, no similar comparisons of experimental data exist in the open literature. Thus, there is significant need for experimental film effectiveness measurements downstream of these two compound-angled geometries, both for the design of gas turbine components, as well as for the development of numerical models. A numerical study was also conducted and numerically calculated film effectiveness distributions are compared with the corresponding measured results.

Experimental Setup

Figure 1 shows the schematics of the test apparatus, consisting of hot and cold air circuits. The mainstream air was directed to an

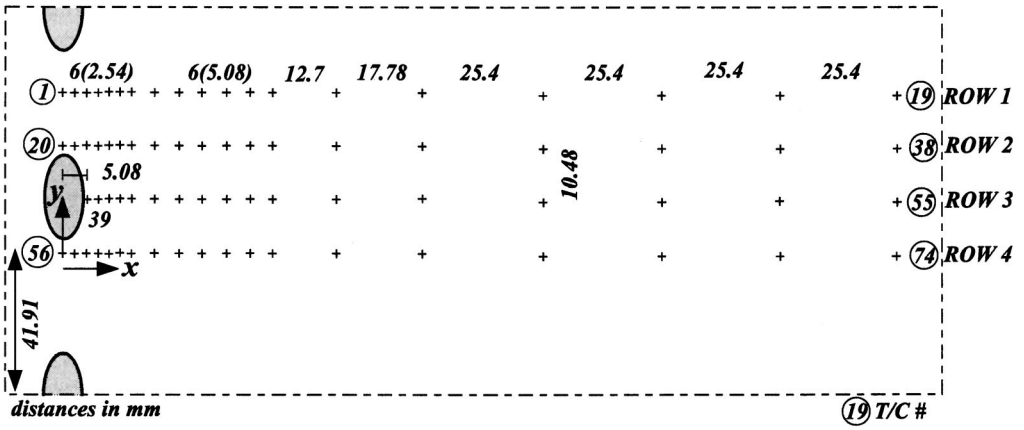

Fig. 3 Thermocouple arrangement downstream of the film holes

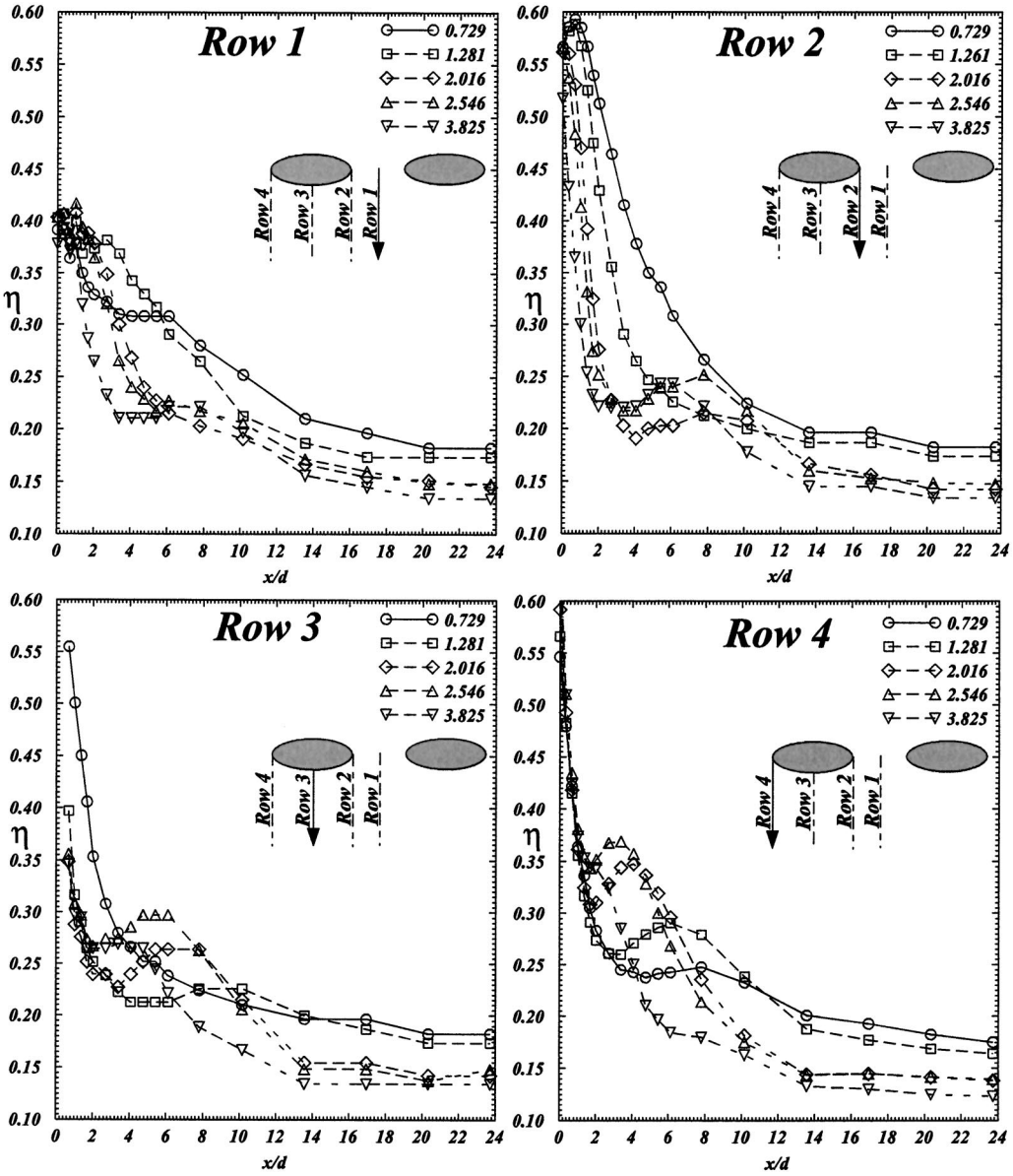

Fig. 5 Film effectiveness versus normalized distance downstream of the compound-angle cylindrical film holes

electric heater where its temperature was raised to about 55°C then into a plenum chamber as two opposing jets for proper mixing, through a wire mesh and then to the mainstream channel via a bell-mouth opening. The film cooling air was directed to a dryer and then to a copper coil immersed in an ice-water box in order to reduce its temperature to about 0°C, and then into the coolant plenum chamber. The mainstream plenum and channel were made of an aluminum shell with polyurethane-slab inserts. A removable test piece, made out of a 7.62-cm-thick polyurethane slab of relatively low conductivity ($k = 0.35$ W/mK), was the part of the test apparatus that had the relevant film-hole geometry for each test. In this study, two instrumented test pieces with two different compound angle film hole configurations were tested: a single row of five compound-angle cylindrical holes, and a single row of five compound-angle forward-lateral-diffused holes. Coolant was injected through these cooling holes from a fiberglass plenum, which was installed on the back of the test piece. Details of the hole geometries are shown in Fig. 2. All holes had a diameter of 7.5 mm at their inlet, and were separated 5.56 diameters in the lateral direction (center-to-center). The total axial length of each hole was eight times its inlet diameters. Both film hole geometries made a 25 deg angle with the coverage surface. Cylindrical holes were oriented perpendicular to the high temperature airflow while the shaped holes had a compound angle of 45 deg with respect to the hot air flow. Surface temperatures were measured at discrete locations using 74 *K*-type thermocouples mounted flush with the coverage surface. The thermocouples were oriented along four longitudinal rows covering the downstream area between two adjacent holes. Figure 3 shows the thermocouple arrangements downstream of the cylindrical film holes. Similar arrangement was set for the shaped holes. A rake of 10 thermocouples oriented in a plane immediately upstream of the film hole outlets and perpendicular to the hot air flow measured the hot air temperature profile. These thermocouples were unevenly spaced with more thermocouples close to the coverage surface. The first one was about 0.2 mm above the surface. Air temperature variation across the hot air channel was insignificant. Coolant temperature was measured immediately upstream of the film hole outlet. Two criti-

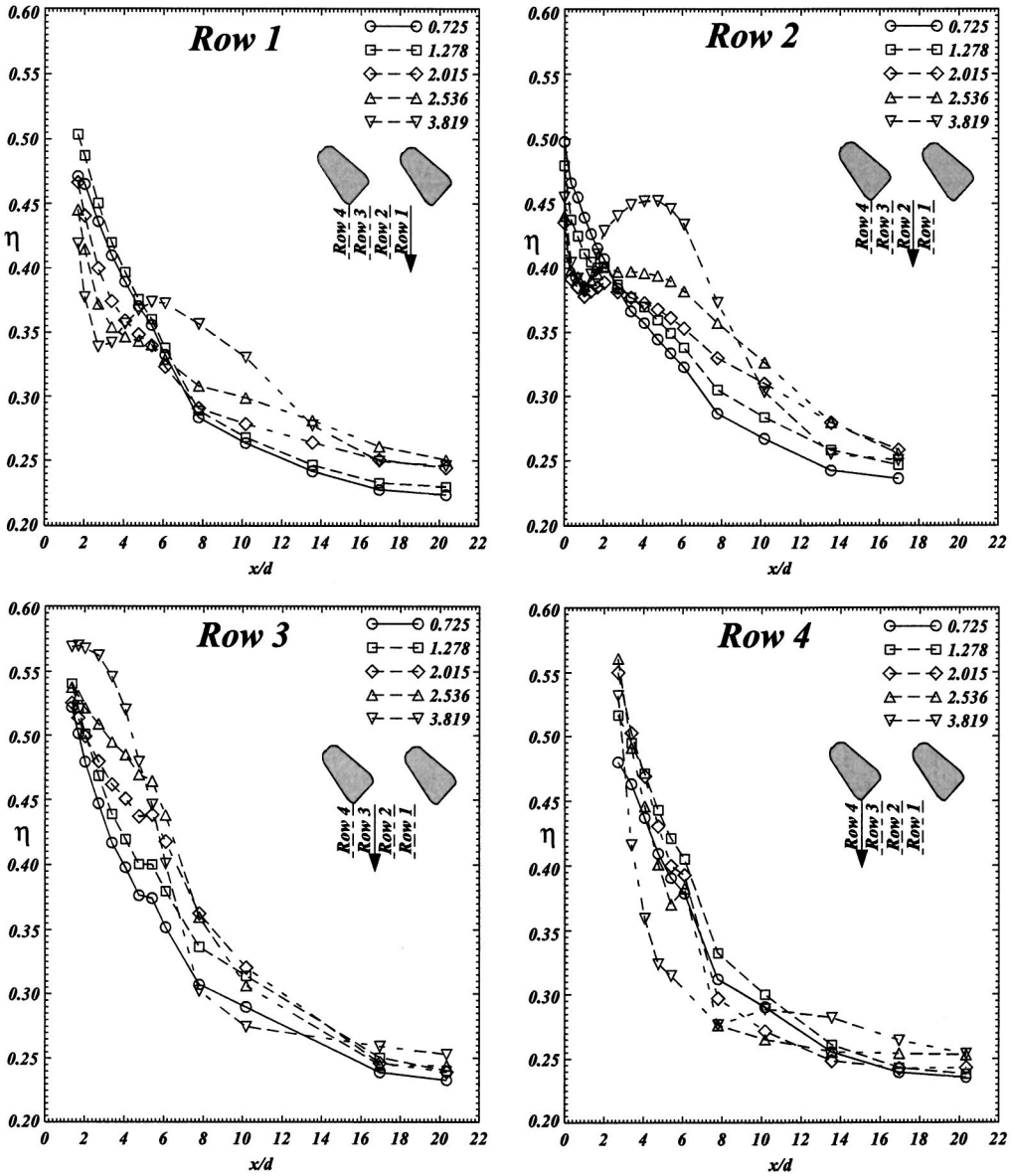

Fig. 6 Film effectiveness versus normalized distance downstream of the compound-angle forward-lateral-diffused film holes

cal venturis measured the hot and cold air mass flow rate. For each test, the blowing ratios (M) was varied between 0.7 and 4. Film effectiveness was calculated directly from the experimental data as:

$$\eta = \frac{T_h - T_{aw}}{T_h - T_c} \tag{1}$$

Experimental uncertainties for the film effectiveness values, following the method of Kline and McClintock varied from ±2% around the film-hole exit to about ±7% for the last thermocouple on each row. Blowing ratio uncertainty varied from ±2% to ±4.3%. To account for the conduction losses, a solid model of the test piece for each film-hole geometry was meshed and solved for the test boundary conditions [20]. It was found that only for the cylindrical hole case, due to a shorter conduction path, the first two thermocouple readings on each row had to be corrected for a maximum error of 1.2°C. The shaped hole conduction analyses showed insignificant errors in thermocouple readings.

Numerical Models

The computational model simulated a row of compound-angle cylindrical film cooling holes and a row of compound-angle, forward-lateral-diffused film cooling holes using the assumption of repeating boundary conditions between holes. For accurate representation of the jet crossflow interaction, it is necessary to model the hot channel, film cooling hole, and cold plenum regions simultaneously. Figure 4 shows this representative domain for the compound angle, forward-lateral-diffused film cooling hole geometry and details of the numerical grid. The CFD analysis was performed using the *Fluent/UNS* solver by *Fluent*, Inc., a pressure-correction-based, multiblock, multigrid, and unstructured/adaptive solver. The standard k-ε turbulence model in conjunction with the generalized wall function was used for turbulence closure. Other available options, short of the two-layer model which required a remeshing of the numerical models, were tried without any significant changes in the final results. Mesh independence was achieved at about 350,000 cells for compound

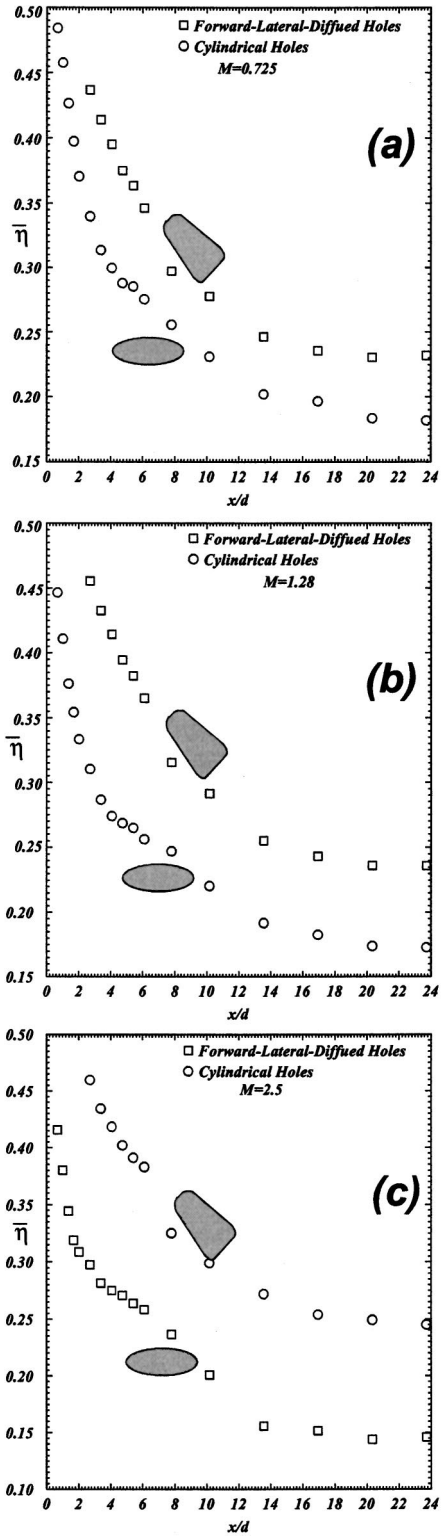

Fig. 7 Laterally averaged film effectiveness for small (a), medium (b), and large (c) blowing ratios

angle cylindrical configuration, and at about 450,000 cells for the compound angle, forward-lateral-diffused configuration with the majority of cells in the film cooling hole and near the bottom wall channel. Cells in both models were entirely hexagonal, a preferred choice for CFD analysis, and were varied in size bigeometrically from the boundaries to the center of the computational domain in order to have finer mesh around the film-hole boundaries. Mesh size for the first row of cells on the wall was varied such that the overall average y^+ for the first row of cells was less than 20. All boundary conditions matched the experimental values. Mass flow rate boundary conditions were specified at the inlet of the hot channel and the cold plenum. At both the hot channel and the cold plenum inlet planes, turbulence intensity was set to 1%, and the length scale was taken as 1/10th of the hydraulic diameter of that inlet. Adiabatic boundary conditions were assumed for all walls. A constant pressure condition was applied at the outlet, with all other flow variables upwinded.

Results and Discussion

Figure 5 shows the film effectiveness versus x/d for all four rows of thermocouples downstream of the cylindrical film holes. Representative results for five blowing ratios, ranging from 0.729 to 3.83, show that beyond $x/d=8$ the film effectiveness decreases as the blowing ratio increases. This is an indication of the coolant penetration into the main flow as its momentum increases with the increasing blowing ratio. A local increase in film effectiveness with the blowing ratio, consistently observed in the interval between $x/d=3$ and $x/d=8$ depending on spanwise location, is attributed to the coolant jet reattachment to the surface after its detachment immediately downstream of the film hole exit.

Representative results of the measured film effectiveness for the shaped film holes are shown in Fig. 6 for the same blowing ratios as those for the cylindrical film holes. Several observations are made. Film effectiveness values, especially further downstream of the film holes are higher than those of the cylindrical holes. For the same amount of coolant, increased exit area has reduced the coolant momentum and increased the coverage area both contributing to the increased film effectiveness. Contrary to the cylindrical film holes, for these shaped holes, the film effectiveness increases with the blowing ratio. Again, increased exit area reduces the coolant exit velocities to levels much lower than those of the cylindrical film holes, thus reducing the rate of penetration of the coolant into the mainstream. Local peaks in film effectiveness for the first and second rows of the thermocouples in the vicinity of $x/d=4-8$ is again attributed to the reattachment of the coolant to the surface after its initial detachment immediately downstream of the exit area.

Figure 7 compares the laterally averaged film cooling effectiveness in the mainstream direction for the two film hole geometries. Results are presented for three blowing ratios. As expected by the individual row results of Figs. 5 and 6, the shaped holes are producing much higher film effectiveness, especially at high blowing ratios. The improvement in laterally averaged film cooling effectiveness when using shaped film holes is caused mainly by the increased lateral spreading of the injected cooling air and better coverage of the surface. Compared with the cylindrical film holes, the laterally averaged film effectiveness of the shaped film holes increased by about 25% for the lowest blowing ratio, 35% for the medium blowing ratio, and up to 45% for the highest blowing ratio.

CFD Results

Results from computational simulation are presented in the form of comparison with experiments for downstream laterally averaged film effectiveness values. These comparisons showed good agreement with experiments, and served to validate the computational method. CFD models identical to the tested geometry for each case were run on PC Pentium4™, 1.6 GHz machines with 512 MB memory. A typical case took about 2000 iterations and about one full day to converge. Figure 8 shows the computed versus measured laterally-averaged film effectiveness values downstream of the film holes. For the compound-angle cylindrical film holes, the most significant disagreement occurs immediately downstream of the jet exit in the near-hole region ($x/d<5$). The numerical models consistently predicted lower effectiveness values in this region. These deviations are attributed partly to insuf-

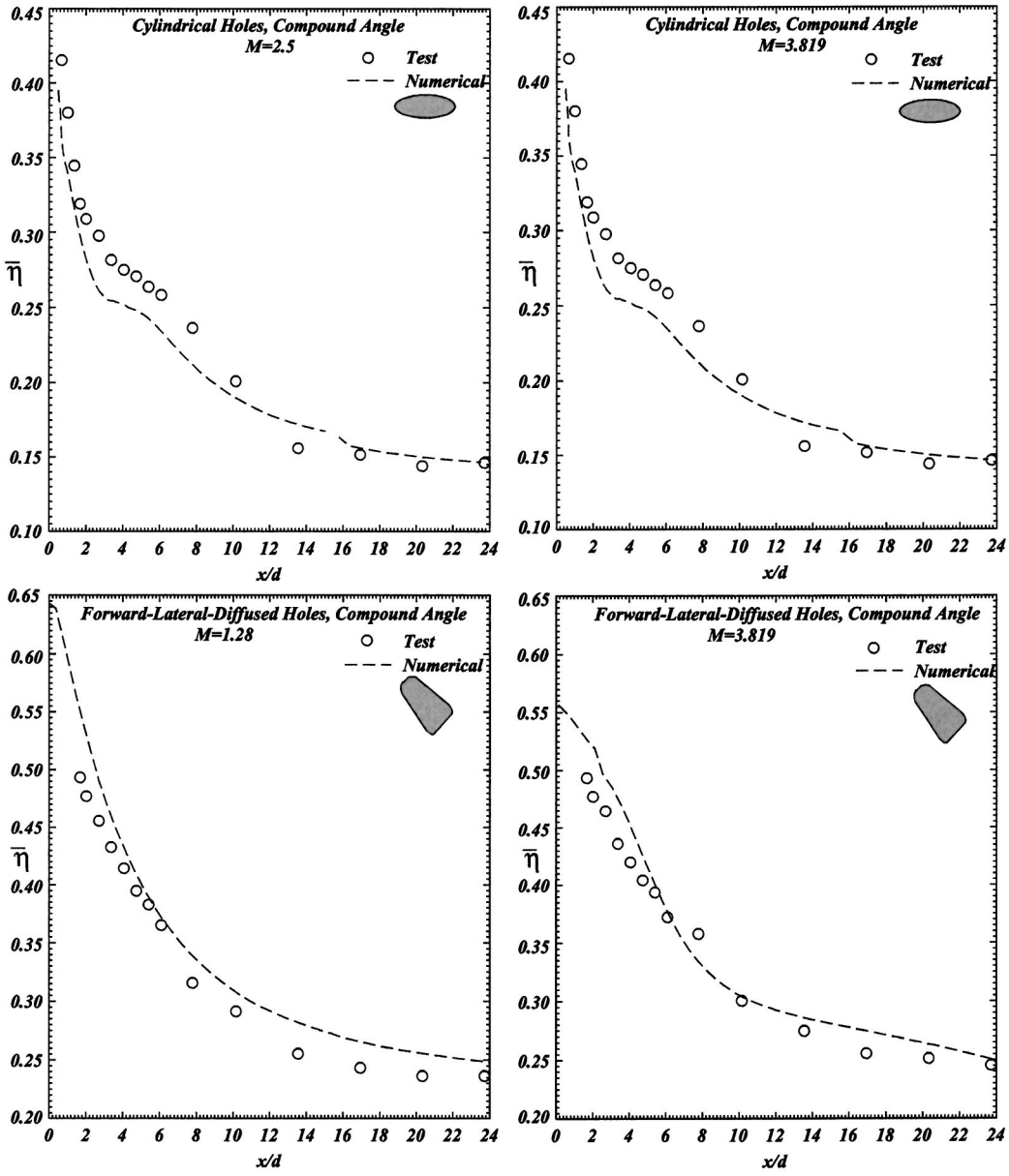

Fig. 8 Comparison between the experimental and numerical laterally averaged film effectiveness

ficient spreading in the computations and also the limited ability of creating perfectly adiabatic surfaces in the experiments. As x/d increases, the agreement between predicted and measured film effectiveness values becomes very good. For the compound-angle forward-lateral-diffused film hole, in the near-hole region ($x/d < 3$) effectiveness is somewhat over-predicted, presumably because of a hypothesized recirculation region immediately downstream of the film hole exit; the use of wall functions in the simulations does not allow the grid resolution necessary to capture such a phenomenon. As the coolant moves further downstream, the numerical model seems to slightly overpredict the film effectiveness. The maximum difference, however, is about 10%.

Conclusions

Film effectiveness values were measured and compared for two film-hole geometries: a single row of compound-angle cylindrical holes and a single row of compound-angle forward-lateral-diffused holes. A combination of several factors, including less jet penetration into the mainstream, cooling flow diffusion, lower velocity gradient because of increased exit area, increased lateral spreading, and greater injectant concentration near the coverage surface results in a better cooling performance for the forward-lateral-diffused film holes, particularly at high blowing ratios. Computations were performed using *Fluent* software to study film cooling effectiveness downstream of the hole geometries used in the experiments. Comparisons between the experimentally measured and numerically calculated film effectiveness distribution showed that the computed results, especially for the shaped holes, are in good agreement with the measured results. Therefore, CFD can be used as a viable tool to predict cooling performances for different film cooling configurations in a parametric study.

Nomenclature

A = cross-sectional area perpendicular to the flow direction
L = film-hole length
M = blowing ratio, $(\rho U)_c/(\rho U)_h = (m/A)_c/(m/A)_h$
P = film-hole pitch

T = temperature
d = film-hole diameter in the cylindrical portion
k = thermal conductivity
m = air mass flow rate
x = distance downstream of the cooling hole in the hot air flow direction (Fig. 3)
y = lateral direction (Fig. 3)
α = injection angle (angle between the film hole axis and the coverage plane)
$\underline{\eta}$ = film cooling effectiveness, $(T_h - T_{aw})/(T_h - T_c)$
$\bar{\eta}$ = laterally averaged film cooling effectiveness
ρ = air density
ϕ = compound angle (Fig. 2)

Subscripts

aw = adiabatic wall
c = property value at injection hole (cold) conditions
h = property value at mainstream air (hot) conditions

References

[1] Ligrani, P., Wigle, J., Ciriello, S., and Jackson, S., 1994, ''Film Cooling From Holes With Compound Angle Orientations, Part I: Results Downstream of Two Staggered Rows of Holes With 3D Spanwise Spacing,'' ASME J. Heat Transfer, **116**, pp. 341–352.

[2] Ligrani, P., Wigle, J., Ciriello, S., and Jackson, S., 1994, ''Film Cooling From Holes With Compound Angle Orientations, Part I: Results Downstream of a Single Row of Holes With 6D Spanwise Spacing,'' ASME J. Heat Transfer, **116**, pp. 353–362.

[3] Ekkad, S., Zapata, D., and Han, J., 1997, ''Heat Transfer Coefficient Over a Flat Surface With Air and CO_2 Injection Through Compound Angle Holes Using a Transient Liquid Crystal Image Method,'' ASME J. Turbomach., **119**, pp. 580–586.

[4] Ekkad, S., Zapata, D., and Han, J., 1997, ''Film Effectiveness Over a Flat Surface With Air and CO_2 Injection Through Compound Angle Holes Using a Transient Liquid Crystal Image Method,'' ASME J. Turbomach., **119**, pp. 587–593.

[5] Sen, B., Schmidt, D. L., and Bogard, D. G., 1996, ''Film Cooling With Compound Angle Holes: Heat Transfer,'' ASME J. Turbomach., **118**, pp. 800–806.

[6] Schmidt, D. L., Sen, B., and Bogard, D. G., 1996, ''Film Cooling With Compound Angle Holes: Adiabatic Effectiveness,'' ASME J. Turbomach., **118**, pp. 807–813.

[7] Goldstein, R. J., Eckert, E. R. G., and Burggraf, F., 1974, ''Effects of Hole Geometry and Density on Three-Dimensional Film Cooling,'' Int. J. Heat Mass Transfer, **17**, pp. 594–605.

[8] Goldstein, R. J., and Jin, P., 2001, ''Film Cooling Downstream of a Row of Discrete Holes With Compound Angle,'' ASME J. Turbomach., **123**, pp. 222–230.

[9] Papell, S., 1984, ''Vortex Generating Flow Passage Design for Increased Film Cooling Effectiveness and Surface Coverage,'' ASME Paper No. 84-HT-22.

[10] Makki, Y. H., and Jakubowski, G. S., 1986, ''An Experimental Study of Film Cooling From Diffused Trapezoidal Shaped Holes,'' AIAA Paper No. AIAA-86-1326.

[11] Gritsch, M., Schulz, A., and Witting, S., 1998, ''Adiabatic Wall Effectiveness Measurements of Film Cooling Holes With Expanded Exits,'' ASME J. Turbomach., **120**, pp. 549–556.

[12] Bell, C. M., Hamakawa, H., and Ligrani, P. M., 2000, ''Film Cooling From Shaped Holes,'' ASME J. Heat Transfer, **122**, pp. 224–232.

[13] Bergeles, G., Gosman, A. D., and Launder, B. E., 1978, ''The Turbulent Jet in a Cross Stream at Low Injection Rates: A Three-Dimensional Numerical Treatment,'' Numer. Heat Transfer, **1**, pp. 217–242.

[14] Demuren, A. O., 1982, ''Numerical Calculation of Steady Three-Dimensional Turbulent Jets in Cross Flow,'' Rep. SFB 80/T/129, Sonderforschungsbereich 80, University of Karlsruhe, Germany.

[15] Leylek, J. H., and Zerkle, R. D., 1994, ''Discrete Jet Cooling: A Comparison of Computational Results With Experiments,'' ASME J. Turbomach., **113**, pp. 358–368.

[16] Walters, D. K., and Leylek, J. H., 1997, ''A Systematic Computational Methodology Applied to a Three-Dimensional Film Cooling Flowfield,'' ASME J. Turbomach., **119**, pp. 777–785.

[17] McGovern, K. T., and Leylek, J. H., 2000, ''A Detailed Analysis of Film Cooling Physics: Part II Angle Injection With Cylindrical Holes,'' ASME J. Turbomach., **122**, pp. 113–121.

[18] Hyams, D. G., and Leylek, J. H., 2000, ''A Detailed Analysis of Film Cooling Physics: Part III Streamwise Injection With Shaped Holes,'' ASME J. Turbomach., **122**, pp. 122–132.

[19] Brittingham, R. A., and Leylek, J. H., 2000, ''A Detailed Analysis of Film Cooling Physics: Part IV Angle Injection With Shaped Holes,'' ASME J. Turbomach., **122**, pp. 133–145.

[20] Khanicheh, A., 2002, ''An Experimental and Computational Investigation on the Film Cooling Effectiveness of a Single Row of Cylindrical and Shaped Holes,'' Northeastern University, M.S. thesis.

Journal of Heat Transfer

Technology Review

A Review of Shaped Hole Turbine Film-Cooling Technology

Ronald S. Bunker
General Electric Global Research Center, Niskayuna, NYA Review of Shaped Hole Turbine Film-Cooling Technology

Film cooling represents one of the few game-changing technologies that has allowed the achievement of today's high firing temperature, high-efficiency gas turbine engines. Over the last 30 years, only one major advancement has been realized in this technology, that being the incorporation of exit shaping to the film holes to result in lower momentum coolant injection jets with greater surface coverage. This review examines the origins of shaped film cooling and summarizes the extant literature knowledge concerning the performance of such film holes. A catalog of the current literature data is presented, showing the basic shaping geometries, parameter ranges, and types of data obtained. Specific discussions are provided for the flow field and aerodynamic losses of shaped film hole coolant injection. The major fundamental effects due to coolant-to-gas blowing ratio, compound angle injection, cooling hole entry flow character, and mainstream turbulence intensity are each reviewed with respect to the resulting adiabatic film effectiveness and heat transfer coefficients for shaped holes. A specific example of shaped film effectiveness is provided for a production turbine inlet vane with comparison to other data. Several recent unconventional forms of film hole shaping are also presented as a look to future potential improvements. [DOI: 10.1115/1.1860562]

Introduction

Film cooling is one of the major technologies allowing today's gas turbines to obtain extremely high turbine firing temperatures, subsequent high efficiencies, and longer life parts. The art and science of film cooling concerns the bleeding of internal component cooling air through the external walls to form a protective layer of cooling between the hot gases and the component external surfaces. The application of effective film-cooling techniques provides the first and best line of defense for hot gas path surfaces against the onslaught of extreme heat fluxes, serving to directly reduce the incident convective heat flux on the surface. Because of its high importance and widespread application, research into the many aspects of film cooling has seen a tremendous increase in the last 10–15 years. The publications relating directly or indirectly to film cooling are far too numerous to recount here, but they deal with the major effects of film hole internal fluid dynamics, interactions with the mainstream gas flow, turbulence and vorticity production, effects of approach flows prior to the hole entry, hole shaping, orientation, and spacing, hole length-to-diameter ratio, density ratio, blowing strength, momentum flux ratio, effects of mainstream turbulence intensity, mainstream acceleration, external surface curvature, and external surface roughness. Indeed, by one unpublished bibliography of film-cooling technical references performed by Kercher [1], the known literature consists of nearly 2700 manuscripts, most of which have appeared in the period of 1970 to the present.

Over the past 30+ years, investigations have been performed by a broad spectrum of researchers to understand the fundamental physics of film cooling, and to improve the state of the art. The primary focus of most research has been on the use of discrete film holes, or rows of film holes, on the hot gas path surfaces of the turbine. Virtually all aspects of film cooling have been explored, some in great depth and others to a lesser extent, both experimentally and computationally. One of the goals of film cooling in gas turbines has been the achievement of ideal cooling films, such as those from two-dimensional (2D) continuous slots with uniformly distributed cooling supply. Due to the many competing constraints of turbine design (e.g., aerodynamics, thermal and mechanical stress, fabrication), it is generally impractical to place such slots into the high temperature surfaces of the turbine components. As a consequence, film cooling is performed almost exclusively through the use of discrete holes and rows of evenly spaced holes. In practical applications, both commercial and military, all film cooling holes are either round or shaped.

Considering the extent and diversity of research into film cooling, it is somewhat surprising to realize that only one primary advancement in this technology has been put into widespread practice over these many years. That single improvement has been the change from round film holes to shaped film holes. Furthermore, the use of the term ''shaped,'' while allowing a potentially vast number of geometries, is actually limited again to a single class of geometry. Shaped holes are composed of round metering or throat sections with a uniform and symmetric expanded exit region on the hot gas surface. Most commonly, all shaped holes applied in practice have fan diffuser exits with divergence angles between 10 and 15 deg on each lateral side as well as on the side into the surface. It is as simple as that.

It is the purpose of this review to examine the origins of shaped film cooling and to summarize the current state of knowledge concerning this technology. What is our current understanding of this cooling technique? What are the limitations and assumptions of our design knowledge? How much real benefit is actually obtained from the use of shaped film cooling? Do the various shapes of cooling holes perform equally well, or is there an optimal shaping? This review will look at the flow field, heat transfer coefficients, and adiabatic film effectiveness associated with shaped film cooling. Several special forms of film hole shaping will also be summarized.

The Case for Shaped Film Cooling

Most of the early studies into film cooling were driven by applications other than gas turbine cooling, such as the high-

Manuscript received by the Heat Transfer Division January 4, 2004; revision received May 15, 2004. Review conducted by: S. Acharya.

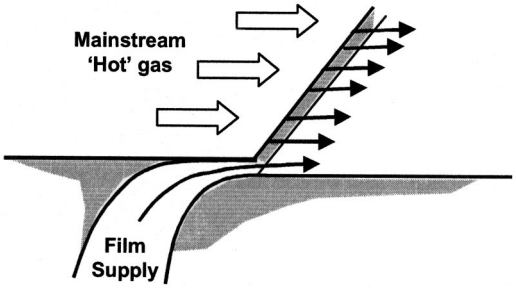

Fig. 1 Ideal tangential slot film cooling

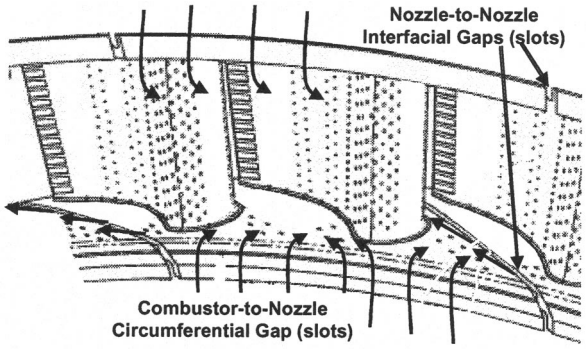

Fig. 2 Schematic of slot-like film cooling regions in turbine

temperature gaseous environments around reentry vehicles, surfaces containing plasma jets, rockets, or flame tube devices. In many examples, the protective film cooling may be introduced in the form of a two-dimensional or slot-type jet. These slot jets can take many forms, including tangential injection layers, angled slots to the surface, or porous strips of material that allow transpiration cooling. An excellent review of the early film-cooling research and modeling associated with these basic film geometries can be found in Goldstein [2]. In all cases, it is the goal of discrete geometry film cooling to approach the formation of an ideal tangential slot injection leading to a continuous layer of film over the surface as shown in Fig. 1. A common definition for the local adiabatic film effectiveness on the surface is

$$\eta = (T_{\text{recovery}} - T_{\text{adiabatic wall}})/(T_{\text{recovery}} - T_{\text{coolant}})$$

The mainstream (hot) gas recovery temperature is a local value, but is in some cases taken to be a constant, or assumed equal to the gas total temperature. The coolant temperature is typically taken to be equal to the coolant exit bulk temperature at the injection point into the mainstream, though in compressible flows it may be more appropriate to use the coolant recovery or total temperature. The adiabatic wall temperature is the local mixed fluid temperature that drives heat transfer to or from the wall. It is this adiabatic wall temperature that is primarily dependent on many parameters of the fluid streams, both local and developing, as well as the surfaces and geometry. Even for a so-called ideal tangential slot film cooling, the parameters of note include blowing ratio, momentum flux ratio, velocity ratio, density ratio, temperature ratio, slot height, surface curvature, slot lip thickness, free-stream Mach number, and free-stream turbulence intensity. These parameters and their relative strengths and interactions determine the initial film effectiveness level at the injection point and also the rate of effectiveness decay downstream.

As complex as this type of film cooling is, gas turbine cooling can seldom ever take advantage of the high effectiveness levels obtained with continuous or semi-continuous slots. While many instances of slot cooling can be found in turbines, these are mostly associated with leakages at free interfaces, which may or may not be treated as reliable cooling flows. Depicted in the schematic of Fig. 2, the endwalls of turbine nozzles have two such applications that may be treated roughly as two-dimensional normal cooling slots: first, the interface leakage gap between the combustor liner and the forward edge of the endwall, and second, the nozzle-to-nozzle interface leakage gaps. Similar interfacial slots are found around the shrouds and the bucket platforms. Another common application of cooling slots is in the combustor system design, where cooling layers are used to protect the liner walls in the combustion zones.

The most highly stressed components of the turbine engine, the high-pressure turbine airfoils, cannot yet take advantage of slot film cooling owing to the need for structural integrity and life of the parts. Mechanical, centrifugal, pressure, and thermal loads all dictate that penetrations through the component walls must be discrete, with reasonably low stress concentration factors. Only in very limited regions, such as the very trailing edge of airfoils, may short slots be used, and even then, cracking issues are common. As a consequence, the standard in film cooling for these airfoils over the past 30 years has been the round film hole, machined at as shallow an angle as possible to the surface, and spaced apart at least two hole diameters on center. Formed as individual holes or rows of holes, round film holes are economical, being readily drilled by laser, electrodischarge machining (EDM), or water-jet methods. Round holes may be formed with virtually any angle, size, and location by laser, except as restricted by line-of-sight access and surface bounce or tunneling issues associated with angle, material, and laser power. Though more costly, EDM hole drilling can work around all these issues. In most highly cooled turbine airfoils, such as the example aeroengine vane and blade shown in Fig. 3, film holes will typically be found with radial angles in the leading-edge stagnation region, compound angles in the high surface curvature regions, and axial angles (relative to the bulk hot gas flow direction) over the remainder of the airfoil and end walls.

The move to shaped film holes, first in military engines and then in commercial engines, is a natural extension of the round film hole toward a more slotlike behavior, especially in the case of a row of film holes. The shaped film hole contains some initial round entry length that acts as the metering or throat section (though not necessarily choked), followed by an expanded diffuser-type exit intended to spread the coolant flow laterally and/or into the surface. This shaping is usually confined to the near-surface region, perhaps the outer 20–50% of the wall thickness, to maintain acceptable hole and hole-to-hole stress concentrations. The target for shaped film holes is to expand the exit area in the plane of the surface of the injection jet by a factor of 2–3 times that of the round jet without separation. Depending on the flow conditions, this may or may not correspond to an equivalent diffusion of the jet itself. This jet diffusion can lead to lower blowing ratios, lower aerodynamic mixing losses, and greater lateral coolant coverage, all of which may benefit cooling effectiveness and turbine efficiency. For holes that are spaced about two throat diameters apart, lateral shaping can result in a merging of the footprints at the downstream portion of the surface geometry. While most shaped holes are still machined by EDM, either in part (shaped footprint only) or in total, pulsed laser or water-jet techniques may eventually allow rapid and controlled drilling of shapes and angles. Shaped film holes have limitations, however, requiring available wall thickness and surface distance to form the geometry. They must also be amenable to the application of protective coatings for oxidation resistance and thermal insulation. There are also places where shaping adds little or no value, for example on some airfoil pressure side regions where destabilizing effects may override shaped benefits. If possible though, nearly every film hole applied in practice today would be a shaped hole, or a modification of a shaped hole.

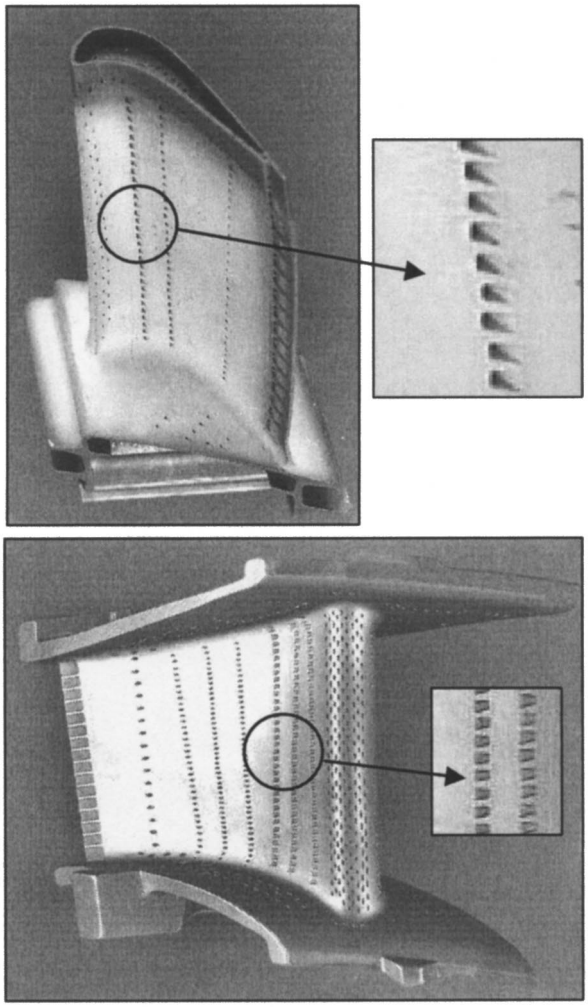

Fig. 3 Modern HPT film cooled blade and vane

Catalog of Shaped Film Literature

A partial catalog of literature concerning the aerothermal effects of shaped film cooling holes is presented in Fig. 4. This list is not intended as a complete bibliography, but does constitute the bulk of existing literature data. The majority of the studies noted deal with the fundamental understanding of shaped film cooling in flat plate wind tunnel environments. Such research has been conducted over the past 30 years, with an increasing level of investigation over the last decade as the use of shaped holes has become common and even prevalent. Very recent research, including new data presented in this paper, focuses more on shaped film cooling in airfoil cascade environments that seek a closer similarity to engine conditions. All of the references included here concern film effectiveness, heat transfer coefficients (HTC), flow fields, or CFD predictions for single shaped holes or rows of holes with various parametric or design effects.

Virtually all shaped film hole studies can be classified into one of four hole geometries as depicted in Fig. 5. Geometry A is the classic shaped film hole that includes both lateral expansion, also known as fan-shaped, and expansion into the surface, also known as laidback. Geometry B contains only lateral exit expansion, while geometry C contains only laidback expansion. Geometry D is a conical film hole that expands from inlet to exit equally in each direction around its centerline. In actual applications, geometry A is the most common, in part due to performance, but also because manufacturing methods will usually produce diffusion in both directions. It is more difficult to produce the pure single expansion directions of B and C. Type D holes are not widely used, and the data pertaining to this type of shape are extremely limited. For all but one of the studies in Fig. 4, literature research has been performed exclusively on film holes with precision shapes, sharp edges, and constant throat sections. Very limited data are available for shaped film holes produced by actual manufacturing methods, or for the variability of shapes produced by these methods.

Examining Fig 4 it is clear that most shaped film hole studies have utilized axial holes containing no radial direction component in the geometry. Only a few cases have considered compound angle (CA) shaped holes, and, in fact, these are less common in practice. Most diffusion angles for exit expansions fall in the 10–15 deg range. The great majority of axial film hole data also focuses on centerline angles of 30–35 deg relative to the surface tangent. These factors are common in practice.

Seminal Study

The study of Goldstein et al. [3] is recognized as the first to demonstrate and quantify the film cooling effects due to shaped holes. As noted in Fig 4, this research used an axial film hole of type B shaping having lateral exit fan diffusion of 10 deg on each side. Goldstein et al. postulated that an alteration in the film jet exit area and geometry from the circular metering section might allow the jet to remain closer to the surface. They noted two possible mechanisms for this improvement, one being the reduction in momentum flux ratio at the exit of the hole leading to a decreased penetration of the jet into the mainstream flow, and the other being a Coanda effect causing the jet to hug the surface. Both flow visualization and adiabatic wall temperature tests were performed with comparisons to a row of round film holes. Simple flow visualization showed a remarkable ability of the shaped film hole jet to resist separation from the surface. The basic comparison of adiabatic film effectiveness between round and shaped holes can be summarized by examining Figs. 6 and 7 as reproduced from [3]. In Fig. 6, the centerline effectiveness is shown for single round or shaped film holes having nominal blowing ratios of 0.5, 1.0, and 2.0 based on the same common throat diameter. Several observations can be made from this comparison that will carry through all subsequent research on shaped film cooling. (i) Shaped hole film effectiveness shows relatively little variation with blowing ratio, tending to remain at the highest level of the mass flow equivalent round film hole effectiveness. (ii) The overall magnitude of the shaped film hole effectiveness, at least under the test conditions of [3], approaches that of two-dimensional film cooling. (iii) The far-field effectiveness for shaped film holes tends toward negligible cooling at essentially the same nondimensional distance downstream as that for round film holes. In Fig. 7, the centerline film effectiveness for a row of holes is shown as a function of blowing ratio for two discrete locations on the surface, one very near the film row at X/D of 6.7, and the other far downstream at X/D of 82.7. For the blowing ratio range shown, shaped film effectiveness is seen to exhibit no distinct local maximum with blowing ratio, whereas round film hole effectiveness displays characteristic near-field jet separation (partial and eventually total) known as blowoff beginning at about $M=0.5$. Up to this blowing ratio, round and shaped film holes lead to very similar cooling effectiveness. As the blowing ratio is raised, shaped film-cooling effectiveness becomes increasingly better by comparison. It should be noted that the relative behavior due to shaped film-cooling holes discussed here becomes very important in actual engine applications where most instances of component design lead to blowing ratios of 0.5 and greater.

Shaped Film Flow Field

The hydrodynamic behavior of round film-cooling jets injected at a shallow angle relative to the surface (ie., 20–40 deg) is well documented in the literature. Detailed flow measurement studies, such as that of Lopez-Peña and Arts [4], provide data on the

Reference Study	Type	L/D	LT / D	α	β	δ	Film Row Type	Hole Spacing	M	Data Type
Goldstein et al. [3]	B	5.2	1.7	35	10	0	Axial	3D, 6D	0.5 - 2.2	Discrete centerline and lateral effectiveness
Makki & Jakubowski [22]	A	~6	~3	35	~10	~10	Axial	3D	0.5 - 4	LA ratio of HTC with and without film cooling
Sen et al. [24]	C	4	2.1	35	0	15	CA 60-deg	3D, 6D	0.4 - 2.0	HTC enhancements
Schmidt et al. [16]	C	4	2.1	35	0	15	CA 60-deg	3D, 6D	0.4 - 2.0	Discrete centerline, lateral, and LA effectiveness
Thole et al. [5]	A, B	6	2	30	14	15, 0	Axial	Infinite	1	Exit flow field
Kohli & Thole [29]	A	4	2	35	15	15	Axial	Infinite	1, 2	CFD effectiveness map
Gritsch et al. [11]; Gritsch et al. [23]	A, B	6	2	30	14	15, 0	Axial	Infinite	0.5 - 2.0	Local and LA effectiveness; HTC's
Haven et al. [6]	A, B, D	~6	~2.5,2.5,0	35	15	15,0,10	Axial	Unknown	1	Flow visualization
Yu et al. [12]	A, C	10	8.4	30	10, 0	10	Axial	3D	0.5, 1.0	Local film and LA effectivenness; HTC's
Kohli & Bogard [38]	A	2.8	0.9	55	15	15, 25	Axial	3D	0.4 - 1.0	Centerline and LA effectiveness
Jackson et al. [39]	D	2.3	0	35	10	10	Axial	4D	0 - 0.65	Simulated airfoil aero loss
Reiss & Boelcs [18]	B, C	3.7	1.7	45	15,0	0,15	CA 30-deg	3.7D	0.6 - 1.5	Multi-row showerhead film effectiveness and HTC
Ganzert et al. [8]; Hildebrandt et al. [40]	A, B	5	1.9	30	10	10, 0	Axial	5D	0.5 - 2.0	Airfoil cascade flow field and HTC's; CFD
Bunker [13]	A	5.7	3.2	30	10	10	Axial	3.6D	0.9 - 1.3	Centerline effectiveness with and w/o blockage
Saumweber et al. [28]	B	6	2	30	14	0	Axial	4D	0.5 - 2.5	Local and LA effectiveness with entrance effects
Takeishi & Aoki [31]	A	~5	~2	30, 35	9, 12	12,20,24	Axial	2.5D, 3D	0.75	Vane and blade cascade pressure and suction side effectiveness
Barthet & Bario [41]	C	~5	~2	50	0	~25	Axial	6D	1	Airfoil cascade flow field
Chen et al. [17]	C	3.5	~1	35	0	~15	Axial, CA 45-deg	3D	0.5 - 2.0	Concave and convex wall effectiveness
Sargison et al. [15]	B	6	2	35	25	0	Axial	3.5D	0.5, 1.0	LA effectiveness and HTC
Yuen et al. [14]	B	6	2	30	14	0	Axial	3D	0 - 1.7	Local and LA effectiveness
Dittmar et al. [19]	B	6	2	45	14	0	Axial; CA 35-deg	4D	0 - 3	Local and LA effectiveness; HTC's
Ferguson et al. [21]; McGrath et al. [20]	A	5.2	~3.5	~50	~15	~15	Axial; CA ~45-deg	5D	1.5, 3, 4.5	CFD for airfoil cascade pressure side; LA data
Ferguson et al. [21]; McGrath et al. [20]	A	10	~5	~30	~15	~15	Axial; CA ~45-deg	4.4D	1, 1.5, 2	CFD for airfoil cascade suction side; LA data
Saumweber et al. [30]	B	6	2	30	14	0	Axial	4D	0.5 - 2.5	Local and LA effectiveness with varied freestream Tu
Saumweber & Schulz [42]	B	6	2	30	14	0	Axial	4D	0.5 - 2.0	Local and LA effectiveness for double row of holes
Bohn et al. [43]	B, C	5	2, 4	30	14,0	0,10	Axial	3D	2	Conjugate analyses

Fig. 4 Catalogue (partial) of shaped film literature [38–43]

distributions of mean velocity, velocity component fluctuations, and shear stresses at various locations from the injection site, and for varying blowing conditions. Many studies using laser Doppler velocimetry (LDV), planar laser-induced fluorescence (PLIF), or particle image velocimetry (PIV) measurements have demonstrated the formation of the main paired, counter-rotating vortices from the jet injection interaction with the mainstream flow. Other features, such as the minor adjacent vortices and the upstream horseshoe vortex, have also been characterized. It has been shown that these primary vortices formed at injection tend to draw the hot mainstream fluid to the surface and even under the cooling jet, thereby leading to potentially severe degradation of film effectiveness. These findings have also been heavily investigated through many numerical studies.

Thole et al. [5] performed a similar wind tunnel experiment to that of [4], but with two geometries of shaped film holes as noted in Fig. 4. LDV measurements were used to determine mean velocity vectors, streamwise and lateral velocity components, turbulence intensities, and turbulent shear stresses in the formative regions of fluid interaction at the hole exits for a blowing ratio of unity. Figure 8 shows the turbulence intensity level maps from [5] for both (a) the hole centerline plane and (b) a transverse plane located at $X/D=4$ downstream. The data are indicative of the study's findings that both hole shapes lead to less shear mixing of the injection jet with the mainstream, less penetration of the shaped jet fluid, and a much higher degree of lateral spreading of the coolant jet relative to that of a round hole. Turbulent shear stress measurements show high positive values on the windward side of round jets, but negative values for the corresponding locations of the shaped jets, the latter showing positive shear stresses in the leeward region of the hole exits. Further evidence of the developing flow structure for shaped film injection has been shown in the PLIF measurements made by Haven et al. [6]. Figure 9 shows the images for planar sheets over and just downstream of shaped film hole exits, again for blowing ratios of unity. The shaped hole of type A demonstrates a so-called anti-kidney flow structure with vortices developing in the opposite sense to those associated with round jet injection. In this example, the anti-kidney vortices actually separate the cooling fluid layer, potentially leading to lower film effectiveness downstream. The shaped hole of type B also demonstrates this behavior, but to a lesser degree. Both [5] and [6] conclude that the laterally and forward expanded hole shape A can lead to lower film effectiveness than the laterally expanded hole shape B due to excessive diffusion of the injection jet and the subsequent mainstream interactions. Further evidence of the near surface streamline behavior around film injection is shown in the oil and dye traces obtained by Wilfert and Fottner [7] for round holes and Ganzert et al. [8]

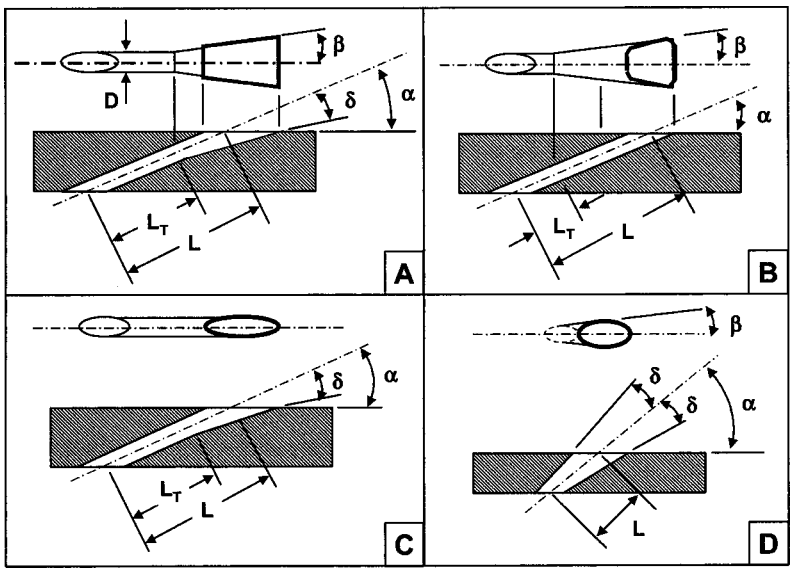

Fig. 5 Defined geometries for four types of shaped film holes

for two types of shaped holes. These studies utilized film rows with 30 deg axial injection on the midchord suction side of cascade airfoils. Images of these oil and dye traces are shown in Fig. 10. Round film hole injection shows a clear horseshoe rollup vortex at the upstream point of interaction, which then wraps around the jet. The immediate effect of the vortex pair is seen just after the hole exit where the two branches meet and lift with a separation zone, as well as downstream with the trailing centerline trace. In contrast, the Type B shaped hole shows a smaller horseshoe vortex that does not wrap completely around the jet. Instead, the vortex ends where it meets the diffused jet, showing a nearly uniform region of streamlines downstream. A small separation is still apparent, as well as the development of intermediate vortices between film jets. The Type-A-shaped hole exhibits no horseshoe vortex as the laidback diffusion allows the diffused jet to sit down on the surface better. There is also no separation shown at the hole exit. Small jet-mainstream interactions are observed to initiate about halfway along the sides of the shaped footprints, which are quickly absorbed by the diffused jet downstream. Both [5] and [8] speculate that the Type-A-shaped hole may allow some hot gas ingestion in its upstream region due to the laidback expansion effect, but considering the internal film hole cooling magnitude and the unsteady nature of such flows this may be entirely acceptable. In fact, engine experience in general shows no such detrimental effect in Type-A-shaped holes.

Aerodynamic Losses Due to Shaped Film Hole Injection

The primary use of shaped film holes is to achieve greater film-cooling effectiveness, but care must be taken in this objective because there are penalties and design trade-offs to be made in the use of such film holes. Aside from the considerations of cost, fabrication, and repair, the principal detriment associated with shaped film holes is their aerodynamic efficiency penalty. This penalty is most commonly referred to as the mixing loss. Mixing losses are usually characterized by some form of the Hartsel mixing box model [9], which assumes mixing of coolant and mainstream at constant pressure near the injection point. Since the goal of the shaped hole is to diffuse the coolant over the surface for greater protection, this leads to a lower momentum jet being injected and mixed into a high-energy working fluid, which can detract from aerodynamic efficiency by increasing total pressure

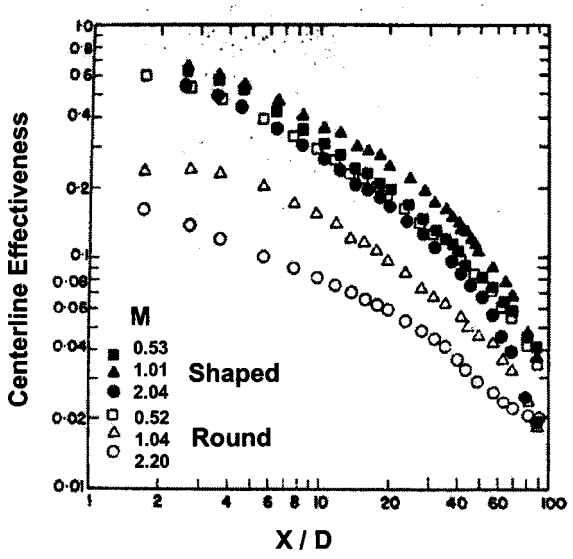

Fig. 6 Centerline effectiveness downstream of single round or shaped hole (reprinted from [3] with permission from Elsevier)

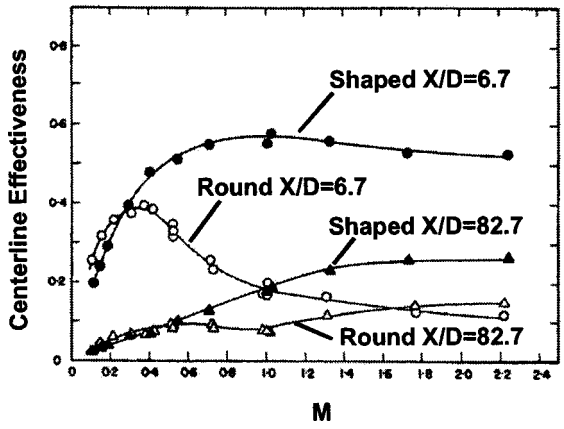

Fig. 7 Centerline effectiveness as a function of blowing rate; row of holes three-dimensional spacing (reprinted from [3] with permission from Elsevier)

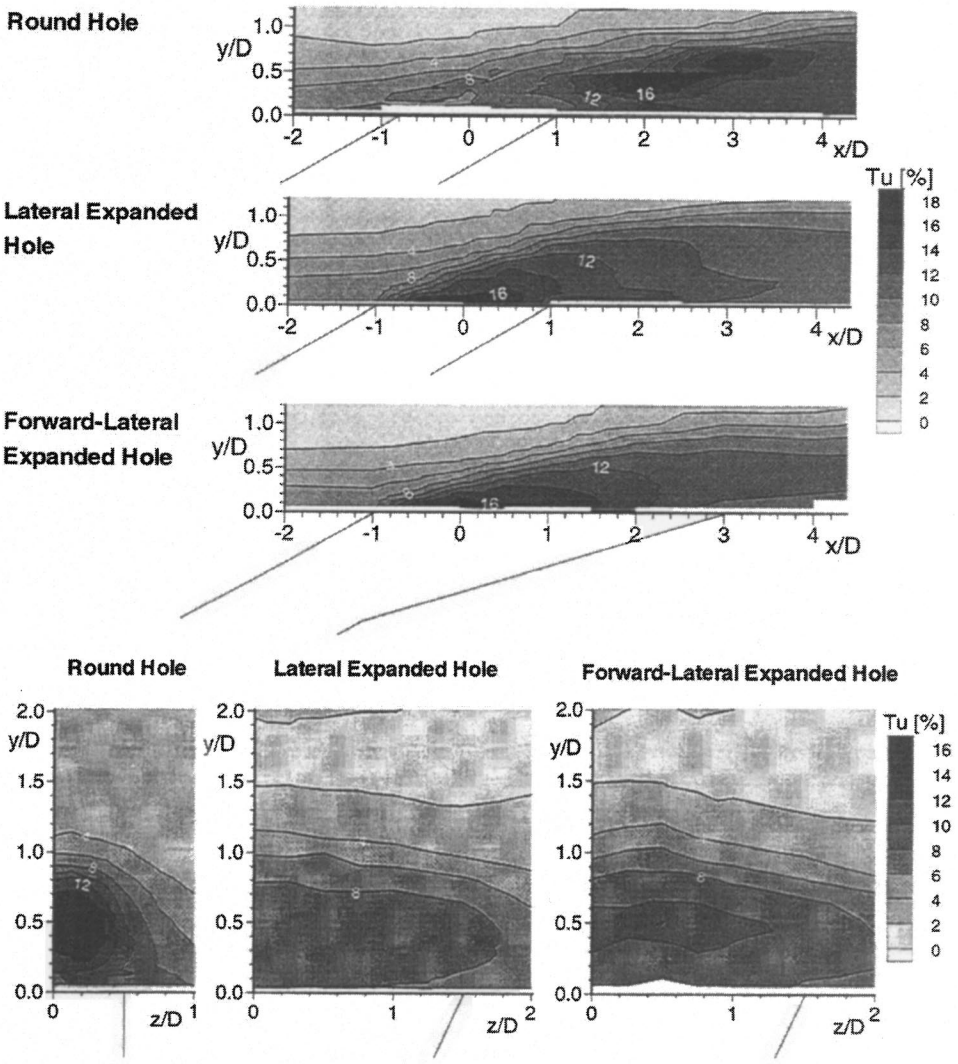

Fig. 8 Turbulence intensity for hole centerline plane (top) and transverse location $X/D=4$ plane (bottom); reproduced from [5]

losses. The use of shaped holes can actually cut in either direction, relative to the use of round holes, in terms of aerodynamics. In regions of low Mach number flows, such as the forward portions of vanes and vane end walls, shaped holes may reduce the coolant injection momentum down to the level of the mainstream, thereby improving aerodynamic efficiency over the use of round film holes. In regions of high Mach number flows, such as the mid-chord and aft portions of airfoil suction surfaces, the opposite can occur, leading to high mixing losses. To some degree, film hole shaping can be used to tailor mixing losses for the best advantage in differing locations of the flow path. This is usually achieved in conjunction with engineering of the internal component pressure losses. Surface location in the sense of mainstream Mach number may also be traded off with the resulting cooling effectiveness downstream and the mixing loss to achieve workable solutions.

The regions of most concern with regard to mixing losses are the airfoil suction sides and the aft portions of the end walls or platforms, since these contribute the majority of the total mixing losses due to discrete film-cooling injection. Ganzert et al. [8] measured the integrated total pressure loss coefficients for a row of holes located midway along the suction surface of a blade in a subsonic cascade test. They tested three hole shapes, one with lateral expansion only (Type B), one with both lateral and laid-back expansion (Type A), and a third with the addition of compound angle to the Type A shaping. The Type-A-shaped hole resulted in about a 10% lower loss coefficient than the Type B hole over the range of blowing ratios from 0 to 1.8 (a reduction in loss coefficient from 4% to 3.6%). Above a blowing ratio of 1.8, the hole shapes yielded the same results. The addition of a 45 deg compound angle served to increase the loss coefficient to the Type B level for blowing ratio up to 1, and drastically higher for greater blowing ratios, indicating mixing losses due to the turning of the injected coolant. Unlike the single film row test of [8], Day et al. [10] examined the mixing losses associated with wholesale changes in several turbine inlet vane film rows from round to shaped holes. Using a transonic vane cascade airfoil with 14 rows of film cooling on the airfoil (six showerhead/gill film rows, four pressure side rows, and four suction side rows), total changes in aerodynamic efficiency were measured with the last four film rows on both sides changed from round to shaped. The shaping was Type B with lateral angle of about 15 deg. The film row locations were typical of a highly cooled turbine inlet vane. They found the use of shaped film rows to essentially double the decrement in stage efficiency over that associated with the use of only round film holes (from -0.27% to -0.60% relative to the uncooled vane).

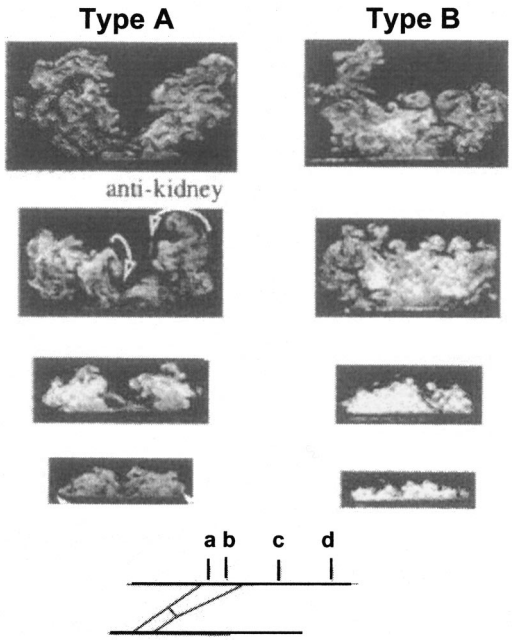

Fig. 9 Shaped film hole LIF images at transverse planes (reproduced from [6])

Fundamental Cooling Effects Due to Shaping

While it is an accepted fact that most shaped film holes provide higher centerline and laterally averaged film effectiveness than round holes given the same flow rate and hole spacing, there are surprisingly few published studies containing data on any one type of shaped geometry with similar parameters. For example, flat plate Type-A-shaped hole effectiveness experimental data listed in Fig. 4 is limited to the studies of [11,12], and [13], and even then parameters, such as L/D, spacing, and diffusion angle are different. Type-B-shaped hole effectiveness data is limited to the studies of [3,11,14], and [15]. One parameter not listed in Fig. 4 is that of the coolant-to-mainstream density ratio (DR). Among most film-cooling studies, DR takes on either very low values near 1.0, or more engine representative values approaching 2.0. Since DR has a strong effect on the resulting film effectiveness, this presents additional difficulties in comparing data sets. Studies are also typically divided into two subgroups depending on the extent of downstream data in terms of X/D, either near hole data with $X/D<20$, or full field data out to $X/D\sim100$. Observations about film-cooling parametric effects must then be drawn individually from studies on the basis of general and relative relationships, but not on the basis of absolute effectiveness magnitudes.

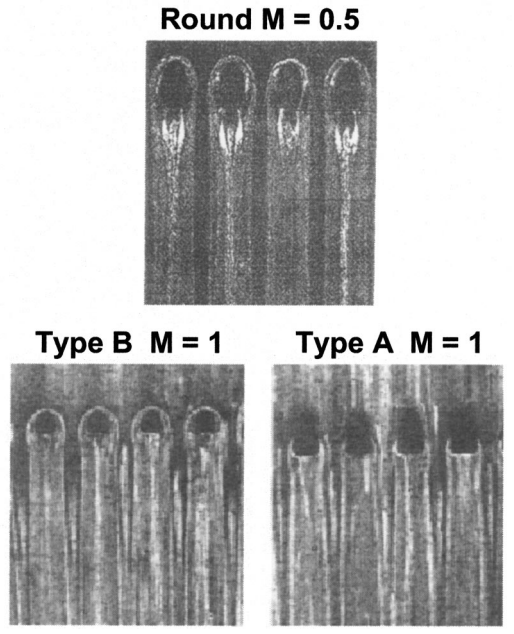

Fig. 10 Oil and dye surface traces for round and shaped film holes (reproduced from [7] and [8], respectively)

Blowing (Mass Velocity) Ratio. The basic effect of blowing ratio for shaped film holes has been shown in Figs. 6 and 7, from the study of [3], for a single geometry of film hole. But, do other shaped film holes perform in the same manner and magnitude? One of the more extensive investigations is that of Gritsch et al. [11] for both Type A and B shapes, using a DR of 1.85. This research is limited to $X/D\leqslant10$, focusing only on the developmental region of jet interaction. This data is also for a single film hole, however, the study of [3] showed little difference between single hole and row of holes results. Over the range of blowing ratio from 0.5 to 1.5, they find the Type B centerline film effectiveness to continuously decay downstream from peak levels of about 0.7, showing no signs of blowoff. Type A centerline effectiveness is very similar for the higher blowing ratios, but is severely degraded at $M=0.5$. The fan-shaped Type B holes resulted in higher centerline effectiveness at each blowing ratio compared to the laidback Type A holes. This improvement amounted to as much as 40–50% increases at $M=0.5$ and $M=1.5$, but only about 10% or less for $M=1$. In examining blowing ratios from 0.25 to 1.75, the fan-shaped Type B holes exhibited optimal effectiveness for blowing ratios of about 1–1.2, while the Type A holes showed no optimal blowing ratios, but instead increasing steadily as blowing ratio increased. From this study, it can be concluded that Type B film holes provide the highest centerline film effectiveness over the broad blowing ratio range up to about 1.5, but that Type A holes are more robust to very high blowing ratios. This latter observation is likely due to the greater diffusion volume provided by the laidback holes. The Type-A-shaped holes of both [12] and [13] also exhibit increasing centerline effectiveness levels as blowing ratio is increased over their more limited ranges. The Type B film hole data of [3], referring back to Figs. 6 and 7, show little sensitivity to blowing ratio changes from 0.5 to 2, with similar peak magnitudes to the data of [11]. In contrast, the investigation of Yuen et al. [14], using the same Type B geometry as in [11], but with a DR of 1.5, shows constantly increasing centerline and laterally averaged film effectiveness values as blowing ratio is increased from 0.33 up to 1.67. Laterally averaged film effectiveness is nearly 1 in this study at the highest blowing ratio, a result which has no independent verification as yet. The Type B data of Sargison et al. [15] is very much in agreement with that of [3] and [11].

Compound Angle (CA) Holes With Shaping. In the application of film cooling to turbine airfoils, it is generally preferred to orient holes in the axial direction to reduce mixing with the mainstream gases for better effectiveness, and to hold mixing losses to a minimum. There are regions of the airfoils, however, where the machining of axial holes would require the use of steep angles to the surface, perhaps as much as 60–70 deg, which would yield unacceptable cooling effectiveness. These regions are the high curvature areas of the aerodynamic profile on both the pressure and suction sides, typically in the forward portion of the airfoils, just aft of the showerhead radial film holes. These regions see the application of compound angle film holes, sometimes referred to as gill holes. The compound angle imposes both axial and radial components to the hole centerline relative to the surface tangent in the axial direction (or relative to the radial tangent,

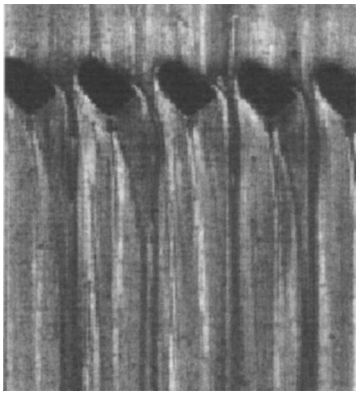

Fig. 11 Oil and dye surface traces for compound angle, shaped film holes (reproduced from [8])

though this is not the usual definition). The compound angle allows the hole centerline angle to the local surface to remain in the range of 20–40 deg for shallow injection and best effectiveness. Most Type-C-shaped holes using only diffusion in the laidback sense will be found in these regions, which is why there is little flat plate data on Type C holes. Only the study of [12] shows Type C data without compound angle on a flat plate, with results showing negligible improvement in effectiveness over round film holes. The research of Schmidt et al. [16] used a Type-C-shaped hole with a 60 deg radial compound angle on a flat plate surface and compared to a round hole of the same orientation. Their results showed the addition of the shaping to yield better uniformity of effectiveness laterally in downstream locations and to increase laterally averaged film effectiveness in the $X/D<10$ region by 20–50% for blowing ratios of 0.6 and 1.25, respectively. Both CA holes, shaped or not, showed improvements over the axial round hole effectiveness.

Shaping provides a much needed improvement to compound angle holes, albeit one that is difficult to manufacture with consistency. The natural tendency of the film injection from a CA hole is to lose much of its cooling potential in the process of turning and mixing with the mainstream flow. Shaping allows the film to remain closer to the surface for a more benign turning, one with lower mixing and greater film coverage. Figure 11 shows the oil and dye surface streamline traces obtained by Ganzert et al. [8] for a Type-A-shaped, 45 deg CA film hole with blowing ratio of 1.0. As noted above, the mixing losses are greater for this hole, but the traces indicate a very uniform and laterally dispersed coverage with turning confined to the hole exit region. A fundamental study of Type-C-shaped CA film holes by Chen et al. [17] investigated the application of such film rows to general concave and convex surfaces in a wind tunnel, with comparison to axial shaped holes. On a concave surface, the addition of compound angle of 45 deg made no improvement at low blowing ratio (0.5), but provided nearly a 30% improved laterally averaged effectiveness for $X/D<10$ at high blowing ratio of 2. On a convex surface, the addition of CA improved average effectiveness by 30% for the low blowing ratio, again in the $X/D<10$ region, and drastically improved effectiveness at high blowing ratio by preventing blowoff. The general benefit of hole shaping that was noted early is seen again here, that of more robustness in cooling effectiveness at high blowing ratios.

At least three studies have looked specifically at the airfoil leading-edge application of compound angle-shaped film holes. Reiss and Boelcs [18] investigated the use of both Type-B- and Type-C-shaped holes as improvements to the typically round compound angled holes in the stagnation showerhead region of the airfoil. They applied the changes to the stagnation film row and two additional showerhead film rows and tested two approach mainstream Mach numbers to represent vanes or blades. At the lower mainstream Mach number of 0.14, the Type C laidback film hole performed the best overall, especially at higher blowing ratios of 1 or greater, showing a 10–20% averaged effectiveness benefit over round CA holes. The Type B shaping showed in essence no improvement. At the higher mainstream Mach number of 0.26, the results are much more mixed. The Type C shaping does as well, and sometimes very much better than the round holes, but the improvements are much more localized to specific rows of film. Again, the Type B shaping shows little or no improvement. The research of Dittmar et al. [19] modeled a single row of gill holes using Type B shaping with and without compound angle. It is important to note that the tests of [19] used a small circular tube to supply the film rows rather than a large plenum, creating an additional internal coolant supply directional effect. The shaped film holes provided higher laterally averaged effectiveness in all cases, and particularly so at high blowing ratio. Improvements over round holes were 10–30%. The effect of compound angle on the shaped hole in this study was minor, and seen mostly in a less uniform distribution of cooling near the hole exit due to the internal supply mechanism. In a CFD study, McGrath et al. [20] show effectiveness predictions and details of flow for compound angled Type A holes on both pressure- and suction-side models (gill holes) and compare effectiveness to data obtained in a linear cascade of the same geometry. Laterally averaged effectiveness on the pressure side (concave) compared well with test data, showing effectiveness levels from peaks of 0.6 with well-behaved decay far downstream, similar to [17]. Increased blowing ratios from 1.5 to 4.5 resulted in increased effectiveness with no signs of blowoff. Similar results were found on the suction side (convex), but with much lower overall effectiveness levels for blowing ratios from 1 to 2, again similar to [17]. Axial-shaped hole data obtained by Ferguson et al. [21] for the same cascade exhibit lower film effectiveness on the pressure-side surface, showing signs of blowoff that the CA holes tend to resist. In contrast, axial shaped hole data on the suction side show significantly better film effectiveness than their CA-shaped counterparts, the latter being degraded from crossflow interaction effects and according to the CFD also hot gas ingestion.

Effect of Shaping on Heat Transfer Coefficients. In reviewing the various studies that have measured heat transfer coefficients with film injection, one key factor becomes immediately evident, that the resulting heat transfer coefficients are highly dependent on the state of the boundary layer approaching the film holes. This would appear to be an obvious point, and, in fact, the disturbance of the boundary layer, whether small or great, also depends greatly on the film hole blowing rate (velocity and momentum ratios to the mainstream), as well as the hole spacing or coverage in the direction transverse to the mainstream. Two main arguments can be made with respect to film injection effects, and either one can be true depending on the situation. On one end of the spectrum, a developed boundary layer, typically turbulent for cooled airfoils, will not be as disturbed by film hole injection as a thin or new boundary layer. At low blowing rates, or low coolant velocity relative to the mainstream, the film injection presents little effect on the turbulent boundary layer, and even serves to thicken it to the extent that the heat transfer coefficient is lower than that of the noninjected case. Only at sufficiently high blowing rates does the injection result in heat transfer coefficient enhancement over the undisturbed level. At the other end of the spectrum, a fresh or very thin boundary layer (relative to the film hole diameter) will feel the disturbance of the film injection for virtually all blowing rates, less for low blowing rate and greater for high blowing rate, but always yielding a heat transfer coefficient enhancement greater than unity. Such thin boundary layers may be found in the region of the airfoil leading edge and, generally, all along an airfoil that has significant numbers of film cooling rows (see Fig. 3) that serve to continuously disrupt the reforming boundary layer. The coverage of the film row, a somewhat loosely defined quantity representing the physical or fluid-

dynamic percentage of lateral spatial injection, plays a role in determining if the injection disturbance is localized (low coverage) or total (full coverage). For example, shaped film holes with close spacing may have merging exit regions leading to 100% coverage, which in a thin boundary layer could cause a fresh start to the boundary layer. Research into the heat transfer coefficients for shaped film hole coolant injection tends to fall into these two categories of boundary layer flows, either injection into thick boundary layers or injection into thin boundary layers. The former cases may represent isolated film cooling rows for components receiving limited total cooling, for example, the second- or third-stage airfoils of the turbine. The latter cases are more representative of those experienced in most highly cooled turbine airfoils.

In the category of relatively thick boundary layers compared to the injection jet size ($\delta/D > 0.5$), Makki and Jakubowski [22] measured the heat transfer coefficient (HTC) enhancement for shaped holes on a flat plate, as the ratio of HTC with film cooling to that without film cooling. For blowing ratios from 1 to 3 and a density ratio of 1.59, they observed a fairly constant HTC enhancement of about 0.8 compared to enhancement levels between 0.9 and 1 for round holes. These levels held out to nearly X/D of 100. At low density ratio of 1.15, there was more distinction of blowing ratio effect, showing enhancement of 0.9 at $M=0.9$ and increasing to 1.2 at $M=2.5$. Under this condition, most cases showed a rise or decay to enhancement approaching 1 downstream. In the flat plate study of Gritsch et al. [23], using a density ratio of 1.85, laterally averaged HTC enhancements of 0.8–1.2 were measured as blowing ratio increased from 0.25 to 1.75, with gradual change toward enhancement of 1 downstream. Their Type-B-shaped holes showed much less range of initial enhancement from 0.7 to 0.85, all rising toward enhancement of 1 at $X/D=10$ at essentially the same rate. Similarly for Type-A-shaped holes, the initial enhancements ranged from 0.6 to 0.75, again rising up to level at $X/D=10$. As a function of blowing ratio, the shaped holes exhibited a minimum HTC enhancement at $M\sim 1.0$, with both lower and higher M leading to greater initial enhancements. The less extensive tests of Yu et al. [12] also showed initial enhancements of 0.7 rising to 1 at about $X/D=10$ for the blowing ratios of 0.5 and 1.0. The study of Sen et al. [24] employed a somewhat thinner boundary layer with $\delta/D\sim 0.23$ at injection, with a density ratio of 1.6. Their HTC enhancement for a CA-shaped hole was about 1.4 initially with decay to about 1 at $X/D=25$, representing a higher and more prevalent effect.

Several studies have employed relatively thin boundary layers of $\delta/D \leqslant 0.12$ at injection either through design or because of the model geometry and flow. Chen et al. [17] performed concave and convex wall-shaped film injection with density ratio of 0.98. They found HTC enhancements of 1.4–1.6 on the concave surface for $M=0.5$, which was the same as that of a round hole. Increasing the blowing ratio to 2, however, caused enhancement to rise to 1.5–2 or more, with levels persisting far downstream, especially for the CA-shaped holes. On the convex surface, enhancements ranged from 1.4 to 3 at $M=0.5$ as well as $M=2$, again with the higher blowing ratio case elevated far downstream. The airfoil leading-edge investigation of Reiss and Boelcs [18] with density ratio of 1.6, which naturally has a fresh boundary layer, showed mixed results of sometimes lower or higher HTC enhancements due to shaped holes, but generally averaging about a 1.2 factor overall. Dittmar et al. [19] obtained enhancements for shaped gill holes on a leading-edge model using density ratio 1.3. At low blowing ratio of $M\sim 0.5$, HTC enhancements were 1.2–1.4, while at $M\sim 1.5$ these were 1.4–1.8, and at $M\sim 3$ values were from 1.2 to 1.6. In all cases the enhancements decayed to about 1 at $X/D\sim 30$. In a blade cascade test, Ganzert et al. [8] observed shaped row enhancement of about 1.6 initially with only a limited decay for $M=1$ and 2. Because the suction-side injection caused the boundary layer to remain turbulent rather than transitioning to laminar flow, downstream enhancement was as much as 3 at $X/D=20$. In a vane cascade test with density ratio 1.7, Abuaf et al. [25] measured suction-side-shaped film HTC enhancement of 1.5, but in this case, decay was rapid to 1 at $X/D\sim 20$. The vane cascade retained a turbulent condition even without film injection.

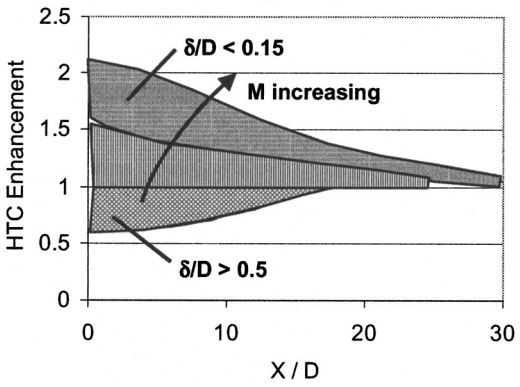

Fig. 12 Summary of heat transfer coefficient enhancements with shaped film holes

Figure 12 attempts to summarize the ranges of HTC enhancements observed for shaped film holes. The indicated regions may overlap, grow, or shrink depending on specific parameters, and there will always be circumstances that exceed these regions in terms of magnitude and extent. The studies noted employed film row hole spacing ranging from $2.5D$ to $5D$ based on the throat diameters, which with shaping will result in approximate geometric coverage values from 80% to 40%, respectively. The reported HTC enhancements results were by and large laterally averaged values such that any coverage effect is already included. One additional measure of film injection effect is the net heat flux reduction (NHFR), or simply the ratio of heat flux with film to that without film. This depends, of course, and can be derived from, the film effectiveness, the HTC enhancement, the gas and coolant temperatures, and the surface temperature, as per Sen et al. [24]. Film effectiveness is generally the dominant player in NHFR, with typical values of 0.8–0.5 just downstream of the film injection; but when injection disrupts the boundary layer severely, the NHFR can be greater than unity (i.e., higher heat flux with film cooling).

Effect of Film Hole Entry and Internal Conditions. Although much attention is paid to the outward results of adiabatic film effectiveness and heat transfer coefficients, relatively little notice has been given to the effects of the internal coolant feed mechanism or the interior of the holes themselves. It has become apparent in the last few years that effectiveness and heat transfer resulting from plenum-fed experiments do not necessarily represent true data for real airfoil cooling. This is especially true for film holes with length-to-diameter ratios of $\leqslant 6$, which make up the majority of those used in practice. Issues of channel-fed film, internal channel flow velocity and orientation, resulting generation of turbulence within the film holes, and even internal surface features of channels and film holes can all significantly affect the external cooling. Gritsch et al. [26] assessed the discharge coefficients for round and shaped film holes under various conditions of internal channel Mach number as well as parallel or perpendicular cross flow feeding the film holes. Drastic reductions in discharge coefficients were observed for all hole types as the internal channel Mach number was raised from 0 to 0.6. Similar large reductions were noted when film holes were fed by perpendicular cross flow rather than parallel cross flow for a given internal channel Mach number. Likewise, the work of Bunker and Bailey [27]

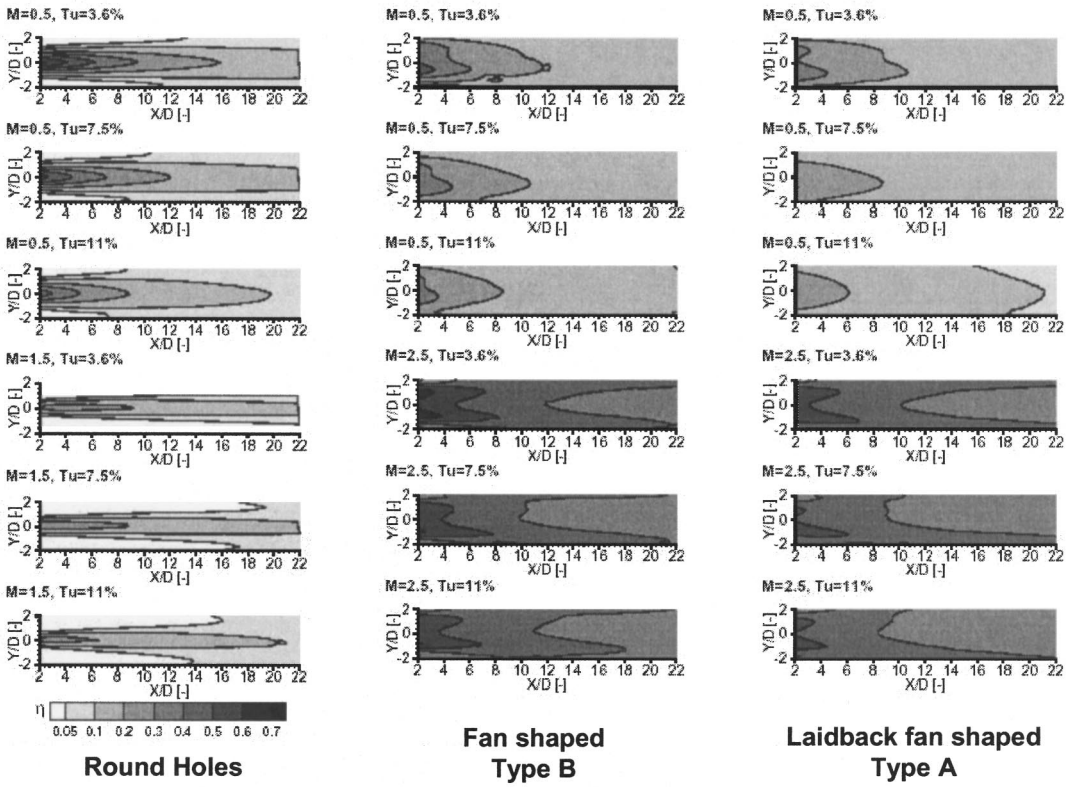

Fig. 13 Effect of freestream turbulence intensity (reproduced from [31])

showed significant discharge coefficient changes due to the relative placement of film hole entries near internal channel turbulators.

Carrying such effects into the associated film effectiveness and heat transfer measurements, Gritsch et al. [11] showed that increased internal channel Mach number up to 0.6 served to increase round hole laterally averaged effectiveness by about 30% for the region of $X/D<10$, but had impacts in decreasing near-hole responses for shaped holes by 15 to 20% at $M=1$. Gritsch et al. [23] showed the companion effects on heat transfer coefficients of about 10% increase for round holes, 15% increase for Type-B-shaped holes, and 30% increase for Type-A-shaped holes. Both studies used parallel coolant channels to the hole entry. Saumweber et al. [28], also using $M=1$, showed the effect of perpendicular internal channel cross flow on Type-B-shaped holes to be a 10–20% reduction in effectiveness compared to parallel feed, with a skewing of the local surface effectiveness distribution due to the altered flow into the holes. The CFD study of Kohli and Thole [29] came to the same conclusions regarding the effects of internal channel Mach number and cross flow on shaped holes and showed even stronger effects at $M=2$. This and other CFD studies, such as those of [20] and [21], provide predictions of the detailed flow within shaped holes showing entry jetting and recirculation regions affecting the ultimate issue of the film cooling. In the more specific case of a tube supply chamber feeding a row of shaped gill film holes, Dittmar et al. [19] found that the direction of coolant flow within the supply tube drastically affected both the film effectiveness and heat transfer coefficients for CA-shaped holes. Supply of the coolant in the direction leading to a shallow angle of entry into the film holes resulted in 25–50% higher effectiveness and also somewhat higher HTC than supply requiring a greater than 90 deg turn into the holes. The interaction of coolant supply means with the film holes and their shapes is obviously a very complex process with nearly unlimited possible configurations, but also potential for advantage in performance. Finally, while film holes are today manufactured and coated by several means, resulting in differing internal surface morphologies, there is so far only one published study looking at the change in film effectiveness due to any such interior surfaces. Bunker [13] examined the effect of partial coating blockage on film effectiveness for round and shaped holes. For EDM film holes with actual plasma-sprayed protective coatings applied as in a land-based power turbine, the potential for severely reduced effectiveness is present in round holes with as much as 50% loss. Shaped holes of Type A were found to much more tolerant of partial blockages from applied coatings.

Effect of Freestream Turbulence (Tu) Level. The majority of the aforementioned studies into shaped film holes utilized relatively low freestream turbulence intensities, generally less than 4%. Research into the effects of freestream turbulence on round film hole effectiveness has shown that elevated intensity levels can quite severely reduce effectiveness. The investigation of Saumweber et al. [30] presents both effectiveness and heat transfer coefficient enhancement data for Type A and B shaped holes with variations in freestream turbulence intensity from 3 to 11%. Figure 13 shows the detailed effectiveness distributions downstream of both round and shaped holes for low and high blowing ratios. This data also depicts many of the general differences between round and shaped hole effectiveness noted earlier. With regard to the effect of Tu at low blowing ratio, round holes experience a 20–40% reduced effectiveness as Tu is increased, while shaped holes show only a 10–20% reduction. At high blowing ratio, there is very little effect of Tu to be seen in round or shaped holes, as the jet strength and jet turbulence levels dominate the responses. The two shaped-hole types show essentially the same effectiveness under similar conditions. The HTC enhancements for round and shaped holes with low Tu are those noted in [23] and discussed above. At high free-stream Tu levels, enhancements for round holes increase for all blowing ratios to about 1.1. En-

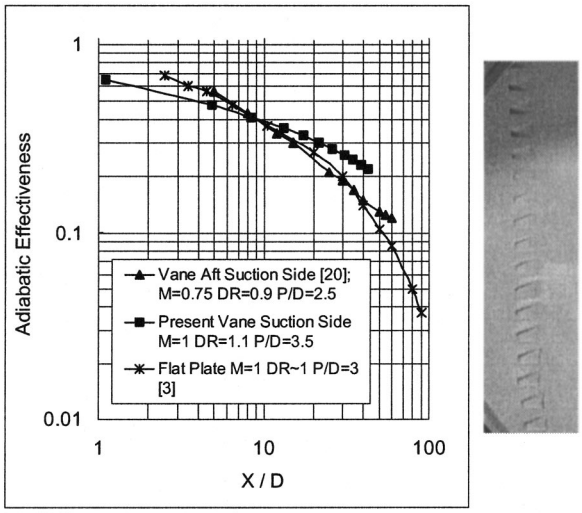

Fig. 14 Cascade suction side film effectiveness with shaped film (present test surface photo)

hancements for shaped holes at high blowing ratios of $M=1.5$ and 2.5 also increase with Tu, but much higher to about 1.7 initially, followed by decay to about 1.4 by $X/D=20$. Under low blowing ratio of $M=0.5$, this response is lessened to that of the round holes. Shaped film hole injection effectiveness shows less sensitivity to freestream turbulence levels, though reduction is observed, but also demonstrates a substantial magnification of the heat transfer coefficients.

Cascade Shaped Film Data

The primary purpose in using shaped film holes is the resulting increase in adiabatic film effectiveness over that obtained with round film holes. The database of literature concerning shaped film effectiveness rests mostly on flat plate experiments, but is this data useful for design? There have been several airfoil cascade tests using shaped film holes for one or more film rows, but most of these investigations do not show the isolated effectiveness due to shaped film holes in the cascade environment, making it difficult to assess individual row effectiveness. Two cascade tests do provide data on a single shaped film row on the suction side of a vane. Takeishi and Aoki [31] provide data for a row of Type-A-shaped holes midway down the suction side issuing prior to the passage throat in a low-speed cascade. Their airfoil was made of a low-conductivity insulating material. Recent cascade test data from the present author also utilized a single row of Type-A-shaped film holes placed midway on the suction side prior to the throat, but in a high-speed transonic cascade. This cascade used an actual production heavy frame turbine airfoil with film holes machined by standard methods. Figure 14 shows the centerline film effectiveness for both cascades, as well as the shaped hole data of [3] at a similar blowing ratio of $M=1$. Also shown is a close-up view of the film row tested in the present research. It is notable that all three film curves shown agree fairly well despite the differences in test environments. This is not altogether unexpected though, since the suction side of the airfoil will see an effective low free-stream turbulence intensity. The use of a single film row in such a location also means that the boundary layer will be thicker than otherwise expected if typical upstream film row injections were present to disrupt and restart the boundary layer. These factors, in essence, level the playing field between the tests and result in good agreement. The main point behind this comparison is that fundamental film effectiveness data can be highly useful for turbine design purposes when it is performed under compatible enginelike conditions for those parameters most affecting film-cooling performance. Under noncompatible conditions the data are not of design use, but rather point to relative results that might distinguish between hole geometries.

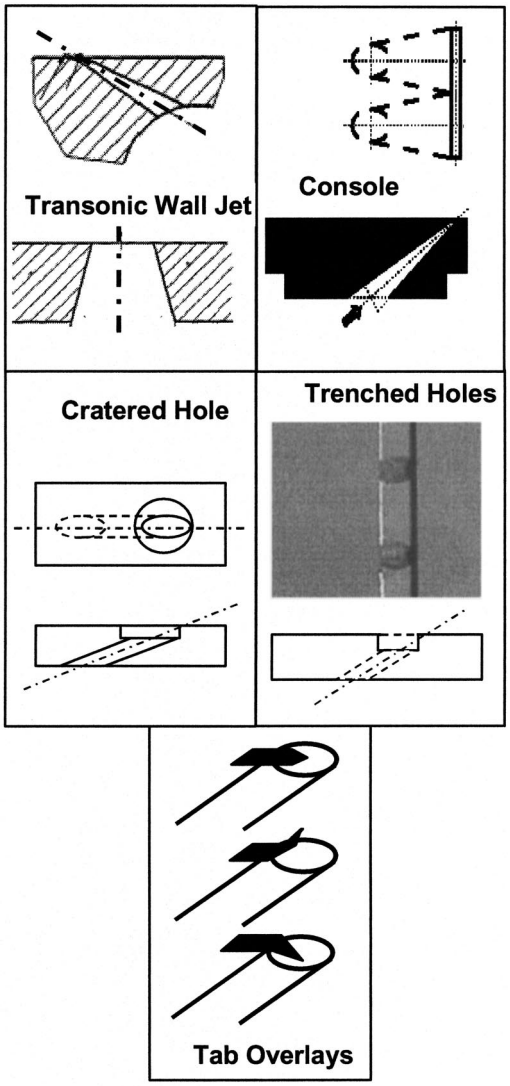

Fig. 15 Proposed alternative film holes shapes

Special Shapes Shown to Improve Effectiveness

Several alternate geometries of film-cooling holes have been proposed within the last few years that have in some form demonstrated at least equivalent film effectiveness performance to the shaped holes discussed above. These differing film holes may have specific form and function, either of limited or widespread potential, but each must also ultimately face the challenges of manufacturing, operability, and cost effectiveness. Figure 15 shows five such geometries that will be briefly explained here.

Moser et al. [32] analyzed a transonic wall jet geometry in which the film hole transitions from some interior cross section, perhaps circular, to a surface slit. This transition is such that the hole converges in both the axial and lateral directions. The basic principle of this design is the creation of a choked flow and underexpanded jet that will conform to the exterior curved surface via the Prandtl-Meyer effect for expansion waves. Their analysis shows that such film jets are very insensitive to angle and show no lift-off from the surface. Because the jet is underexpanded, the local film effectiveness according to the conventional definition

exceeds unity at the exit. Such a jet requires a heavy pressure ratio to be realized, however. The analysis did not evaluate aerodynamic losses.

Sargison et al. [33] and [34] demonstrated a converging slot-hole, or Console, geometry in both flat plate and cascade testing. In this geometry, the hole transitions from circular to slot with convergence in the axial direction and divergence laterally. The hole area does diminish to cause the flow to accelerate, though not necessarily to a choked condition. The exit is the metering section. This accelerated flow is speculated to have lower jet turbulence and more stability. Flat plate tests show the effectiveness and HTC enhancement to be on par with fan-shaped holes, while the aerodynamic loss is less. Transonic cascade tests comparing Console to fan-shaped holes showed higher effectiveness and HTC on the accumulated suction-side film cooling from multiple rows and about equivalent effectiveness with higher HTC on the pressure side accumulated film. The cascade aerodynamic losses were much decreased.

Fric and Campbell [35] investigated a so-called cratered film hole in which the circular hole exits into a shallow right circular surface cup or depression. The flow actually impinges on the edge of this depression causing it to deflect and fill the depression prior to issuing onto the external surface. Flat plate tests show about a 50% improved effectiveness over round holes at $M=1$ and a greater increase as blowing ratio increases. Effectiveness improvement of 100% and more was observed at $M=5$. A suggested application in [35] is the full coverage film cooling of combustor liners.

Bunker [36] extended the work of [35] to a two-dimensional version, or trench film geometry. The intention of this geometry is the same, to cause the film-cooling flow to spread into the trench prior to issuing on the surface. The particular advantage of this geometry is that it can be formed using the protective coatings applied to the surface, without machining the trench into the substrate. Film effectiveness improvements of 50–75% over round holes were measured in flat plate tests, putting this on par with shaped holes.

Finally, Nasir et al. [37] tested round film holes with the addition of triangular tabs covering the upstream edge of the holes, either turned upward, downward, or flat. The flat and downward tabs modified the exit flow and vortex structure in a manner that kept the coolant from lifting off. Their data showed effectiveness consistent with shaped holes, but much higher HTC enhancement level of about 2.

Conclusions

Shaped hole film-cooling technology has become the standard in today's highly cooled gas turbine airfoils. This review has examined the origins of shaped film cooling and summarized the current state of knowledge concerning this technology, including the flow field, heat transfer coefficients, and adiabatic film effectiveness. The benefits of shaped film holes using expanded exits of fan and/or laidback geometries may be summarized as follows:

- higher centerline and laterally averaged adiabatic film effectiveness, in some cases approaching that of two-dimensional slot film
- little variation in effectiveness over blowing ratios from 0.5 to 2
- virtually no susceptibility to film blow-off under typical conditions
- continuously increasing effectiveness with blowing ratio
- low variability in heat transfer coefficient enhancement with blowing ratio
- low sensitivity to free-stream turbulence intensity variations
- amenable to use with compound angles

Shaped film holes also have some drawbacks, however, including higher aerodynamic mixing losses for the most common regions of use and more sensitivity (negative) to variations in entry flow orientations and strengths.

Of the 2500+ publications dealing with film cooling, only 50 or so specifically examine shaped, expanded exit film hole aerodynamics and thermal performance. The current understanding of shaped film parametric effects and physics is relatively sparse, however, the acceptance of shaped film technology is based largely on the foundation of round film hole data. The benefits of shaped hole film cooling are real and substantial, so much so that these types of film holes are used whenever possible in the practice of cooling gas turbines. No single shaping of film hole stands out as an optimal geometry, as long as the general guidelines of diffusion angles and sufficient depth/length of transition are followed. As manufacturing methods progress further, additional unconventional shapes of film holes will become viable, possibly leading to even higher performance and the ability to cool components with less air.

Nomenclature

D = film hole throat internal diameter
DR = density ratio $=\rho_{jet}/\rho_{gas}$
I = momentum flux ratio $=\rho_{jet}V_{jet}^2/\rho_{gas}V_{gas}^2$
L = film hole length
L_T = film hole throat section length
M = blowing ratio, $=\rho_{jet}V_{jet}/\rho_{gas}V_{gas}$
P = spanwise pitch between film hole centerlines
PR = film hole pressure ratio=Coolant total/Mainstream static pressure
Re = jet Reynolds number based on film hole diameter, $\rho_{jet}V_{jet}D_{jet}/\mu_{jet}$
$T_{coolant}$ = film hole exit static temperature
T_{gas} = freestream gas temperature prior to film row
$T_{recovery}$ = local recovery temperature of gas
$T_{surface}$ = local surface temperature with film cooling
Tu = mainstream turbulence intensity
V_{jet} = velocity of film jet based on throat diameter
V_{gas} = velocity of freestream gas
x = axial distance measured along surface from film hole exit
z = lateral distance from film row centerline
δ = boundary layer thickness
η = adiabatic local film cooling effectiveness, $=(T_{recovery}-T_{surface})/(T_{recovery}-T_{coolant})$
μ_{jet} = dynamic viscosity of film jet at exit
ρ_{jet} = density of film jet at exit
ρ_{gas} = density of freestream gas

Acronyms.

CA = compound angle
HTC = heat transfer coefficient
LA = laterally averaged value
LDV = laser Doppler velocimetry
PIV = particle image velocimetry
PLIF = planar laser-induced fluorescence

References

[1] Kercher, D. M., 2000, "A Bibliography of Film Cooling" (personal communication, unpublished).
[2] Goldstein, R. J., 1971, "Film Cooling," *Advances in Heat Transfer*, Academic Press, San Diego, Vol. 7, pp. 321–379.
[3] Goldstein, R. J., Eckert, E. R. G., and Burggraf, F., 1974, "Effects of Hole Geometry and Density on Three-Dimensional Film Cooling," Int. J. Heat Mass Transfer, **17**, pp. 595–607.
[4] Lopez-Peña, F., and Arts, T., 1993, "On the Development of a Film Cooling Layer," *Heat Transfer and Cooling in Gas Turbines*, AGARD-CP-527, pp. 36-1 thru 36-12.
[5] Thole, K., Gritsch, M., Schulz, A., and Wittig, S., 1996, "Flowfield Measurements for Film Cooling Holes With Expanded Exits," *IGTI Turbo Expo*, Birmingham, UK, Paper 96-GT-174.
[6] Haven, B. A., Yamagata, D. K., Kurosaka, M., Yamawaki, S., and Maya, T.,

1997, ''Anti-Kidney Pair of Vortices in Shaped Holes and Their Influence on Film Cooling Effectiveness,'' *IGTI Turbo Expo*, Orlando, Paper 97-GT-45.
[7] Wilfert, G., and Fottner, L., 1996, ''The Aerodynamic Mixing Effect of Discrete Cooling Jets With Mainstream Flow on a Highly Loaded Turbine Blade,'' ASME J. Turbomach., **118**, pp. 468–478.
[8] Ganzert, W., Hildebrandt, T., and Fottner, L., 2000, ''Systematic Experimental and Numerical Investigations on the Aerothermodynamics of a Film Cooled Turbine Cascade With Variation of the Cooling Hole Shape, Part 1, Experimental Approach,'' *IGTI Turbo Expo*, Munich, Paper 2000-GT-295.
[9] Hartsel, J. E., 1972, ''Prediction of Effects of Mass Transfer Cooling on the Blade Row Efficiency of Turbine Airfoils,'' *AIAA Aerospace Sciences Meeting*, San Diego, Jan. 17–19, AIAA Paper 72-11.
[10] Day, C. R. B., Oldfield, M. L. G., Lock, G. D., and Dancer, S. N., 1998, ''Efficiency Measurements of an Annular Nozzle Guide Vane Cascade With Different Film Cooling Geometries,'' *IGTI Turbo Expo*, Stockholm, Paper 98-GT-538.
[11] Gritsch, M., Schulz, A., and Wittig, S., 1997, ''Adiabatic Wall Effectiveness Measurements of Film-Cooling Holes With Expanded Exits,'' *IGTI Conference*, Orlando, Paper 97-GT-164.
[12] Yu, Y., Yen, C.-H., Shih, T. I.-P., Chyu, M. K., and Gogineni, S., 1999, ''Film Cooling Effectiveness and Heat Transfer Coefficient Distributions Around Diffusion Shaped Holes,'' *IGTI Conference*, Indianapolis, Paper 99-GT-34.
[13] Bunker, R. S., 2000, ''Effect of Partial Coating Blockage on Film Cooling Effectiveness,'' *IGTI Conference*, Munich, Paper 2000-GT-244.
[14] Yuen, C. H. N., Martinez-Botas, R. F., and Whitelaw, J. H., 2001, ''Film Cooling Effectiveness Downstream of Compound and Fan-Shaped Holes,'' *IGTI Turbo Expo*, New Orleans, Paper 2001-GT-0131.
[15] Sargison, J. E., Guo, S. M., Oldfield, M. L. G., and Rawlinson, A. J., 2001, ''The Variation of Heat Transfer Coefficient, Adiabatic Effectiveness, and Aerodynamic Loss With Film Cooling Hole Shape,'' Ann. N.Y. Acad. Sci., **934**, pp. 361–368.
[16] Schmidt, D. L., Sen, B., and Bogard, D. G., 1994, ''Film Cooling With Compound Angle Holes: Adiabatic Effectiveness,'' *IGTI Turbo Expo*, The Hague, Netherlands, Paper 94-GT-312.
[17] Chen, P. H., Hung, M. S., and Ding, P. P., 2001, ''Film Cooling Performance on Curved Walls With Compound Angle Hole Configuration,'' Ann. N.Y. Acad. Sci., **934**, pp. 353–360.
[18] Reiss, H., and Boelcs, A., 1999, ''Experimental Study of Showerhead Cooling on a Cylinder Comparing Several Configurations Using Cylindrical and Shaped Holes,'' *IGTI Turbo Expo*, Indianapolis, Paper 99-GT-123.
[19] Dittmar, J., Schulz, A., and Wittig, S., 2002, ''Assessment of Various Film Cooling Configurations Including Shaped and Compound Angle Holes Based on Large Scale Experiments,'' *IGTI Turbo Expo*, Amsterdam, Paper GT-2002-30176.
[20] McGrath, E. L., Leylek, J. H., and Buck, F. A., 2002, ''Film Cooling on a Modern HP Turbine Blade Part IV: Compound Angle Shaped Holes,'' *IGTI Turbo Expo*, Amsterdam, Paper GT-2002-30521.
[21] Ferguson, J. D., Leylek, J. H., and Buck, F. A., 2002, ''Film Cooling on a Modern HP Turbine Blade Part III: Axial Shaped Holes,'' *IGTI Turbo Expo*, Amsterdam, Paper GT-2002-30522.
[22] Makki, Y. H., and Jakubowski, G. S., 1986, ''An Experimental Study of Film Cooling From Diffused Trapezoidal Shaped Holes,'' *AIAA/ASME 4th Joint Thermophysics and Heat Transfer Conference*, Boston.
[23] Gritsch, M., Schulz, A., and Wittig, S., 1998, ''Heat Transfer Coefficients Measurements of Film-Cooling Holes With Expanded Exits,'' *IGTI Conference*, Stockholm, Paper 98-GT-28.
[24] Sen, B., Schmidt, D. L., and Bogard, D. G., 1994, ''Film Cooling With Compound Angle Holes: Heat Transfer,'' *IGTI Turbo Expo*, The Hague, Netherlands, Paper 94-GT-311.
[25] Abuaf, N., Bunker, R., and Lee, C. P., 1997, ''Heat Transfer and Film Cooling Effectiveness in a Linear Airfoil Cascade,'' ASME J. Turbomach., **119**, pp. 302–309.
[26] Gritsch, M., Saumweber, C., Schulz, A., Wittig, S., and Sharp, E., 2000, ''Effect of Internal Coolant Crossflow Orientation on the Discharge Coefficient of Shaped Film Cooling Holes,'' ASME J. Turbomach., **122**, pp. 146–152.
[27] Bunker, R. S., and Bailey, J. C., 2001, ''Film Cooling Discharge Coefficient Measurements in a Turbulated Passage With Internal Cross Flow,'' ASME J. Turbomach., **123**, pp. 774–780.
[28] Saumweber, C., Schulz, A., Wittig, S., and Gritsch, M., 2001, ''Effects of Entrance Cross-Flow Directions to Film Cooling Holes,'' Ann. N.Y. Acad. Sci., **934**, pp. 401–408.
[29] Kohli, A., and Thole, K. A., 1998, ''Entrance Effects on Diffused Film Cooling Holes,'' *IGTI Turbo Expo*, Stockholm, Paper 98-GT-402.
[30] Saumweber, C., Schulz, A., and Wittig, S., 2002, ''Free-Stream Turbulence Effects on Film Cooling With Shaped Holes,'' *IGTI Turbo Expo*, Amsterdam, Paper GT-2002-30170.
[31] Takeishi, K. I., and Aoki, S., 2001, ''Contribution of Heat Transfer to Turbine Blades and Vanes for High Temperature Industrial Gas Turbines: Part 1, Film Cooling,'' Ann. N.Y. Acad. Sci., **934**, pp. 305–312.
[32] Moser, S., Ivanisin, M., Woisetschlaeger, J., and Jericha, H., 2000, ''Novel Blade Cooling Engineering Solution,'' *IGTI Turbo Expo*, Munich, Paper 2000-GT-242.
[33] Sargison, J. E., Guo, S. M., Oldfield, M. L. G., Lock, G. D., and Rawlinson, A. J., 2001, ''A Converging Slot-Hole Film Cooling Geometry Part 1: Low-Speed Flat Plate Heat Transfer and Loss,'' *IGTI Turbo Expo*, New Orleans, Paper 2001-GT-0126.
[34] Sargison, J. E., Guo, S. M., Oldfield, M. L. G., Lock, G. D., and Rawlinson, A. J., 2001, ''A Converging Slot-Hole Film Cooling Geometry Part 2: Transonic Nozzle Guide Vane Heat Transfer and Loss,'' *IGTI Turbo Expo*, New Orleans, Paper 2001-GT-0127.
[35] Fric, T. F., and Campbell, R. P., 2002, ''Method for Improving the Cooling Effectiveness of a Gaseous Coolant Stream Which Flows Through a Substrate, and Related Articles of Manufacture,'' US Patent No. 6,383,602.
[36] Bunker, R. S., 2002, ''Film Cooling Effectiveness Due to Discrete Holes Within a Transverse Surface Slot,'' *IGTI Turbo Expo*, Amsterdam, Paper GT-2002-30178.
[37] Nasir, H., Acharya, S., and Ekkad, S., 2001, ''Film Cooling From a Single Row of Cylindrical Angled Holes With Triangular Tabs Having Different Orientations,'' *IGTI Turbo Expo*, New Orleans, Paper 2001-GT-0124.
[38] Kohli, A., and Bogard, D. G., 1999, ''Effects of Hole Shape on Film Cooling With Large Angle Injection,'' *IGTI Turbo Expo*, Indianapolis, Indiana, Paper 99-GT-165.
[39] Jackson, D. J., Lee, K. L., Ligrani, P. M., Johnson, P. D., and Soechting, F. O., 1999, ''Transonic Aerodynamic Losses Due to Turbine Airfoil Suction Surface Film Cooling,'' *IGTI Turbo Expo*, Indianapolis, Paper 99-GT-260.
[40] Hildebrandt, T., Ganzert, W., and Fottner, L., 2000, ''Systematic Experimental and Numerical Investigations on the Aerothermodynamics of a Film Cooled Turbine Cascade With Variation of the Cooling Hole Shape, Part 2, Numerical Approach,'' *IGTI Turbo Expo*, Munich, Paper 2000-GT-298.
[41] Barthet, S., and Bario, F., 2001, ''Experimental Investigation of Film Cooling Flow Induced by Shaped Holes,'' Ann. N.Y. Acad. Sci., **34**, pp. 313–320.
[42] Saumweber, C., and Schulz, A., 2003, ''Interaction of Film Cooling Rows: Effects of Hole Geometry and Row Spacing on the Cooling Performance Downstream of the Second Row of Holes,'' *IGTI Turbo Expo*, Atlanta, Paper GT2003-38195.
[43] Bohn, D., Ren, J., and Kusterer, K., 2003, ''Conjugate Heat Transfer Analysis for Film Cooling Configurations With Different Hole Geometries,'' *IGTI Turbo Expo*, Atlanta, Paper GT2003-38369.